ARPA 6155

Program Code 7410

Program Title
Environmental Effects in Niobium
Base Alloys and Other Selected
Intermetallic Compounds

Sponsored by
Defense Advanced Research Projects Agency
DARPA Order No. 6155

Monitored by AFOSR Under Contract No. F49620-88-C-0013

Contractors
Department of Materials Science and Engineering
University of Pittsburgh

Department of Metallurgical Engineering and Materials Science
Carnegie Mellon University

Principal Investigators

G.H. Meier
412-624-9741
University of Pittsburgh

A.W. Thompson
412-268-2700
Carnegie Mellon University

Period Covered
November 1, 1987 - October 31, 1990

Final Report
April 30, 1991

SECURITY CLASSIFICATION OF THIS PAGE

REPORT DOCUMENTATION PAGE

Form Approved
OMB No. 0704-0188

1a. REPORT SECURITY CLASSIFICATION: UNCLASSIFIED	1b. RESTRICTIVE MARKINGS
2a. SECURITY CLASSIFICATION AUTHORITY	3. DISTRIBUTION/AVAILABILITY OF REPORT: UNCLASSIFIED/UNLIMITED
2b. DECLASSIFICATION/DOWNGRADING SCHEDULE	
4. PERFORMING ORGANIZATION REPORT NUMBER(S)	5. MONITORING ORGANIZATION REPORT NUMBER(S): F49620-88-C-0013
6a. NAME OF PERFORMING ORGANIZATION: Dept. of Materials Science Engineering, Univ. of Pittsburgh	6b. OFFICE SYMBOL (If applicable)
6c. ADDRESS (City, State, and ZIP Code): 848 Benedum Hall, Pittsburgh, PA 15261	7a. NAME OF MONITORING ORGANIZATION: Air Force Office of Scientific Research
	7b. ADDRESS (City, State, and ZIP Code): Bolling AFB, Washington, DC 20332
8a. NAME OF FUNDING/SPONSORING ORGANIZATION: Defense Advanced Research Projects Agency	8b. OFFICE SYMBOL (If applicable)
8c. ADDRESS (City, State, and ZIP Code): 1400 Wilson Boulevard, Arlington, VA 22209-2308	9 PROCUREMENT INSTRUMENT IDENTIFICATION NUMBER: F49620-88-C-0013
	10. SOURCE OF FUNDING NUMBERS: PROGRAM ELEMENT NO. 62712E; PROJECT NO. Darpa; TASK NO; WORK UNIT ACCESSION NO.

11. TITLE (Include Security Classification)
Environmental Effects in Niobium Base Alloys and Other Selected Intermetallic Compounds

12. PERSONAL AUTHOR(S)
Meier, G. H., Univ. Of Pittsburgh and Thompson, A. W., Carnegie Mellon University

13a. TYPE OF REPORT	13b. TIME COVERED	14. DATE OF REPORT (Year, Month, Day)	15. PAGE COUNT
Final	FROM 11/1/87 TO 10/31/90	4/30/91	186 pages

16. SUPPLEMENTARY NOTATION

17. COSATI CODES			18. SUBJECT TERMS (Continue on reverse if necessary and identify by block number)
FIELD	GROUP	SUB-GROUP	Niobium Base Alloys, Intermetallics, Oxidation, Hydrogen, Mechanical Properties

19. ABSTRACT (Continue on reverse if necessary and identify by block number)

Niobium aluminides and silicides as well as other intermetallic compounds have potential for use in advanced gas turbines where increased operating temperatures are necessary to obtain the targeted performance goals. These materials will be subjected to a variety of environments over a range of temperatures. Two of the principal reactants in these environments are oxygen and hydrogen. This program has been concerned with the effects of oxygen and hydrogen on niobium alloys and other selected intermetallic compounds. It consists of two parts. Part I involves the effects of oxygen and was performed at the University of Pittsburgh by Professors G.H. Meier and F.S. Pettit. Part II is concerned with hydrogen effects and was performed at Carnegie Mellon University by Professor A.W. Thompson.

The investigations involving oxygen examined the mechanisms by which intermetallic compounds are degraded in oxidizing environments. Emphasis was placed upon the conditions which must be achieved in order to obtain sufficient oxidation resistance for use at temperatures above about 1100°C. Specific intermetallics studied included $NbAl_3$, $NbSi_2$, $TaSi_2$, TiAl and $MoSi_2$. The oxidation of these intermetallics was investigated at temperatures between 500° and 1400°C

20. DISTRIBUTION/AVAILABILITY OF ABSTRACT: ☑ UNCLASSIFIED/UNLIMITED ☐ SAME AS RPT ☐ DTIC USERS	21. ABSTRACT SECURITY CLASSIFICATION: UNCLASSIFIED
22a. NAME OF RESPONSIBLE INDIVIDUAL: R Goldstein	22b. TELEPHONE (Include Area Code): 202-767-4933 / 22c. OFFICE SYMBOL: NE

DD Form 1473, JUN 86 — Previous editions are obsolete — SECURITY CLASSIFICATION OF THIS PAGE

in oxygen and in air. In this report it is shown that intermetallics in the Nb-Al, Nb-Si and Ta-Si systems do not have sufficient oxidation resistance for use at temperatures above 800°C. The intermetallic TiAl can be oxidation resistant up to temperatures as high as 1000°C but its oxidation behavior is affected by nitrogen in the environment and aluminum concentration. The compound $MoSi_2$ is extremely oxidation resistant over a range of temperatures up to 1400°C, however its oxidation properties at temperatures near 500°C can result in unacceptable oxidation rates under certain conditions. Mechanisms applicable to the oxidation of intermetallics in general are presented in this report.

The investigations involving hydrogen have emphasized brittle fracture, crack growth and the behavior of hydrides in Ti-24Al-11Nb (at. %). Some work of this type was also performed on TiAl. The mechanical properties of these alloys were determined after exposure to hydrogen. The mechanical tests included simple tensile and compression tests, and notched bend and precracked compact tension specimens. Properties such as yield and ultimate tensile strength, ductility, and fracture toughness have been determined as a function of both hydrogen (hydride) content and temperature.

Table of Contents

Introduction 1

Part I

Oxidation of Niobium Base Alloys and Selected Intermetallics 2

Introduction 2
Mechanisms for the Oxidation of Intermetallics 3

- Effects of Temperature 6
- Effects of Alloying Elements 8
- Effects of Atmosphere Composition 9

Summary 10
References 12
Publications Related to Support Under This Program 14
Table
Figures
Appendix I

- Oxidation Resistance of Intermetallic Compounds Containing Niobium or Tantalum
- Oxidation Behavior of γ Ti-Al
- Oxidation of $MoSi_2$

Part II

Hydrogen in Titanium Aluminides 15

Publications Sponsored Under This Program 17
Appendix II

- Effects of Hydrogen as a Temporary Stabilizer on Microstructure and Brittle Fracture Behavior in a Titanium Aluminide Alloy
- Effects of Grain Size on Yield Strength in TiAl
- Environmental Effects In Titanium Aluminide Alloys
- Effect of Grain Size and Hydrides on Mechanical Behavior of TiAl
- Hydrogen Solubility in a Titanium Aluminide Alloy

Introduction

Niobium aluminides and silicides as well as other intermetallic compounds have potential for use in advanced gas turbines where increased operating temperatures are necessary to obtain the targeted performance goals. These materials will be subjected to a variety of environments over a range of temperatures. Two of the principal reactants in these environments are oxygen and hydrogen. This program has been concerned with the effects of oxygen and hydrogen on niobium alloys and other selected intermetallic compounds.

This program consists of two parts. Part I is involved with the effects of oxygen and has been performed at the University of Pittsburgh by Professors G.H. Meier and F.S. Pettit. Part II is concerned with hydrogen effects and has been performed at Carnegie Mellon University by Professor A.W. Thompson.

The investigations involving oxygen were directed towards describing the conditions which must be achieved in order to have continuous, protective Al_2O_3 or SiO_2 scales developed on niobium-based alloys and compounds, and other selected intermetallics, at temperatures between 600° and 1400°C. The studies concerned with hydrogen effects were directed towards determining solubility limits, hydrogen uptake and permeation rates, and the effect and degree to which hydrogen degrades the properties of these materials.

Part I

Oxidation of Niobium Base Alloys And Other Selected Intermetallics

Introduction

Nickel-and cobalt-base superalloys cannot be used for extended periods of time above 1100° to 1200°C. An objective of this program is to determine the alloys that may have adequate oxidation resistance for use at temperatures above this range. Furthermore, the currently available titanium base alloys cannot be used above about 600°-650°C because of creep and oxidation limitations. Intermetallic compounds are currently being considered for a variety of high temperature applications because some of these compounds offer possible improved creep resistance along with in some cases low density compared to state-of-the-art, coated superalloys. However, the achievement of adequate oxidation resistance in the systems which possess high specific strengths is a matter of concern. In Figure 1 some of the systems with potential for meeting these requirements are identified. The current program has been involved with investigating the oxidation of the following intermetallics: $NbAl_3$, $NbSi_2$, $TaSi_2$, TiAl and $MoSi_2$. Subsequent sections of this report contain papers which have been submitted for publication and describe the oxidation of these intermetallics. In the following the basic mechanisms important to the oxidation properties of intermetallics will be presented and key unanswered questions will be pointed out.

Mechanisms For The Oxidation of Intermetallics

The development of oxidation resistance in any alloy is based on the addition of an element which will oxidize selectively and produce a protective surface oxide. The formation of this surface layer requires that the oxide be more stable than the lowest oxide of the base metal. Figure 2 indicates the free energies of formation of a few selected oxides. The oxides Al_2O_3, SiO_2, and BeO are of principal interest because they exhibit low diffusivities for both cations and anions as well as being highly stable. Thus the addition of Al to Ni, as in the case of aluminide coatings on nickel-base alloys, or Si to Mo, as in the case of $MoSi_2$ heating elements, clearly satisfy the stability requirements. However, in the case of Nb- or Ti-base alloys the oxides of the base metal are nearly as stable as those of Al, Si, or Be. This results in conditions for which selective oxidation is not possible. It should be emphasized that the determination of which oxide is more stable must take into account the prevailing metal activities. Detailed analysis of this situation are presented by Rahmel and Spencer[1] for Ti-Al and Ti-Si alloys and Luthra[2] for Ti-Al alloys. These analyses predict that alumina scales are not stable in contact with Ti-Al alloys containing less than 50 at% Al. This prediction has been verified experimentally by Misra[3] and results obtained in the present investigation[4].

A second requirement is that the concentration of the element added for oxidation resistance is sufficient for the formation of its oxide as a continuous external layer rather than as internal precipitates. The two possibilities for the simple case where the oxygen partial pressure is too low to oxidize the base metal are illustrated in Figure 3. Alloys with low solute concentrations allow inward diffusion of oxygen which results in internal oxidation,

Figure 3a, while for high solute contents the outward diffusion of solute results in the formation of a continuous external layer of oxide, Figure 3b. The critical solute concentration for the transition from internal to external oxidation has been expressed by Wagner[5] as

$$N_B^* = \left(\frac{\pi g^* N_o D_o V_M}{2 D_B V_{ox}} \right)^{1/2} \quad (1)$$

Here N_oD_o is the oxygen permeability in A, D_B is the solute diffusivity, g^* is a factor determined by the volume fraction of oxide required for the transition (often near 0.3), and V_M and V_{ox} are the molar volumes of the alloy and oxide, respectively. The solute content required for external scale formation is seen to increase with the solubility and diffusivity in the alloy. However, for most systems of interest, the oxide of the base metal can also form in the ambient atmosphere and grows until the more stable oxide of the solute B becomes continuous and stops the growth of the "transient oxide". This situation is illustrated schematically in Figure 4. The effect of transient oxidation on the transition from internal to external oxidation of B has been analyzed by Gesmundo and Viani[6] who found that an excess of solute above that predicted by equation 1 is required in the presence of transient oxides. The amount of excess solute required is predicted to increase as the growth rate of the transient oxide increases. The conditions assumed in the derivation of equation (1) do not apply rigorously to the oxidation of intermetallics for several reasons which will become apparent. Nevertheless, the above analysis provides a useful qualitative method to evaluate the effects of variables such as temperature, composition, and atmosphere on the selective oxidation process.

Long term stability of the protective scale requires that the flux of solute to the alloy/scale interface remains large enough to prevent oxides of A from becoming stable. Pettit[7], for example, found there were two critical concentrations for the formation of alumina scales on Ni-Al alloys: one required for development of the alumina scale and a larger one required to maintain its stability. Wagner[8] has derived an approximate equation for the concentration of solute required to maintain the growth of an external scale as:

$$N_B = \frac{V_M}{16 z_B} \left(\frac{\pi k_p}{D_B} \right)^{1/2} \qquad (2)$$

Here k_p is the parabolic rate constant for the growth of the protective scale and z_B is the valence of B in BO. Thus, the long term stability of a protective scale depends on the thermodynamic and diffusional properties of the alloy immediately beneath the scale. This can be particularly significant for the oxidation of intermetallic compounds with small homogeneity ranges. Here the removal of the scale-forming element to form an external layer immediately results in the formation of a layer of the next lower compound adjacent to the oxide. This situation, which is in contrast to the smooth concentration gradient in the alloy depicted in Figure 4(b), means that the properties of the lower compound determine the ability of the alloy to maintain the growth of the protective oxide. Apparently some compounds, such as Mo_5Si_3[9], provide a sufficient flux of Si to the oxide/alloy interface to maintain the growth of a silica layer on $MoSi_2$, as is illustrated schematically in Figure 5. This is not the case, however for many systems as is illustrated for the oxidation of $NbAl_3$[10] in Figure 5. The initial exposure of this compound results in the formation of a continuous

alumina layer on the surface but the depletion of Al causes the next lower aluminide, Nb_2Al, to form beneath the oxide. This compound has been shown to be incapable of forming continuous alumina[11] and, indeed, the alumina breaks down and then begins to reform under the Nb_2Al layer and envelops it. This enveloped metal is eventually converted to a Nb-Al oxide in the scale. Repetition of these processes results in a layered scale. This process has been studied by Steinhorst and Grabke[12] and in the present investigation[10] using acoustic emission which indicated cracking associated with each successive layer. It is not yet clear, however, if the cracking is the cause of the breakdown of the alumina layer or the result of the formation of Nb-Al mixed oxides which have become more stable in contact with the alloy as Al is depleted.

EFFECTS OF TEMPERATURE

The effect of temperature on the selective oxidation process is determined by the temperature dependence of all of the terms in equations 1 and 2 and that of the growth rate of the transient oxides. Therefore, some systems form protective external scales more readily at higher temperatures while others form them more efficiently at lower temperatures. For example, Ni-Al alloys form protective alumina scales more readily at high temperatures[7] whereas γ-TiAl forms alumina scales at low temperatures in oxygen but forms mixed Ti-Al scales above about 1000°C[4,13].

The refractory-metal di-silicides generally form protective silica scales more readily at high temperatures. For example, the oxidation rates of $MoSi_2$ at temperatures between 600° and 1200°C are extremely slow as the result of the formation of a protective silica film[9].

However, the oxidation rates at 500°C show rapid, breakaway kinetics. This breakaway can result in disintegration of the specimen. This disintegration was first studied for $MoSi_2$ by Fitzer[14] who termed it "pesting". The pest effect has been studied most extensively for $MoSi_2$, particularly by Berkowitz and coworkers[15,16] but the review compiled by Aitken[17], indicates its occurrence in a wide range of intermetallic compounds. The basic characteristics of the pest effect may be summarized as follows:

1. Attack is predominantly intergranular, often associated with grain boundary hardening.
2. Exposure to a reactive gas, particularly O_2, is required.
3. Rapid attack is preceded by an incubation period.
4. Disintegration occurs over a limited temperature range which varies from one compound to the next.
5. Some compounds appear to be immune.
6. Defects such as cracks in the starting material appear to be required.
7. The detailed mechanism is still not fully understood.

The effect of temperature cycling can also have substantial effects on the selective oxidation process. The rates of oxidation are generally comparable to the isothermal rates for short times but scale spalling caused by thermal stresses which result from the thermal expansion mismatch between the oxide and alloy and which become larger as the scale thickens eventually produce weight losses. The amount of degradation under cyclic conditions generally is substantially greater than under isothermal conditions. Cyclic oxidation data for intermetallic compounds are limited but those available for NiAl in diffusion aluminide coatings on Ni-base alloys[18], Fe-silicides[19], and Ni-silicides[20] indicate similar behavior to that described above.

EFFECTS OF ALLOYING ELEMENTS

The beneficial effects of third element additions on the selective oxidation process are best typified by additions of Cr to Ni-Al alloys which promote external Al_2O_3 scale formation at substantially lower Al contents than those indicated by equation 1. The effects of Cr additions are summarized in the isothermal[21,22] oxidation maps in Figure 6. The explanation of these effects requires consideration of the influence of Cr on all of the parameters in equation 1 and on the growth rate of the transient oxide. The predominant effect of Cr is generally thought to involve reduction of the oxygen solubility, N_o, but other factors must be important. For example, Si additions to Ni-Al alloys, which should decrease N_o in a similar manner to Cr, actually retards the development of external Al_2O_3 scales for certain ranges of Al contents[23]. The cause of this retardation appears to be associated with Si stabilizing phases in which Al diffusion is slower. Regardless of the exact mechanism, these data indicate the need to consider all of the important parameters in analyzing third element effects. Again, data for most intermetallic compounds are lacking but Cr and V additions to Ti-aluminides[24] and Ti and Cr additions to Nb-aluminides[25,26] have been shown to promote external Al_2O_3 scale formation at much lower Al contents than those required for the binary alloys. Figure 7[27] illustrated the beneficial affect Cr additions on the formation of protective alumina scales on Ti-Al alloys.

Additional effects of alloying involve changes in the melting points of the alloys and the oxide scales which form on them. For example, Figure 1 indicates that the amount of alloying elements required to produce the Nb-Ti-Cr-V-Al alloys, which are marginal alumina formers[26], has lowered the melting point well below that of binary NiAl. The melting

temperature of the transient oxide scales which form on the alloys can also be greatly affected by alloying additions as the selected list of oxide melting points and eutectic temperatures in Table 1 indicates.

EFFECTS OF ATMOSPHERE COMPOSITION

The pressure and composition of the reactive gas atmosphere can have substantial effects on the oxidation behavior of many intermetallic compounds. Figure 8, taken from the work of Perkins and Packer[28], shows the effect of oxygen partial pressure on the formation of continuous silica films on $MoSi_2$ as a function of temperature. The silica film forms in an intermediate pressure range at each temperature. This type of behavior may be understood by considering the vapor species diagrams for the Mo-O and Si-O systems, Figure 9, which indicate the stable condensed phases and the partial pressures of the important vapor species as a function of oxygen pressure. The "active" oxidation at high oxygen pressures is associated with the formation of MoO_3 in the scales which grows rapidly, being liquid above 701°C, and prevents the formation of a continuous silica film. The "active" region at low oxygen pressures, which also occurs for pure Si[29], results from the high pressure of SiO over SiO_2 which leads to reactive volatilization of Si oxides rather than the formation of a protective film. The high volatility of MoO_3 indicated in Figure 8 results in $MoSi_2$ being able to develop protective silica films at temperatures as low as 600°C[9] whereas $TaSi_2$ and $NbSi_2$ only form protective scales at temperatures well above 1000°C because of the low volatility of transient Ta- and Nb-oxides.

Additional effects of the atmosphere can occur if it contains a second reactive component, even the nitrogen in air. This effect is most striking for the oxidation of Ti-aluminides. Protective alumina scales were formed on Ti-Al, exposed in oxygen, up to temperatures near 950°C. However, the same exposures conducted in air result in the formation of TiO_2-rich scales which grow at rates orders of magnitude faster than the alumina scales[4]. This effect was originally shown by Choudhury et al.[30] to be associated with the presence of nitrogen as opposed to any other variable pressure. The detailed mechanisms of the effect of nitrogen and the extent that it applies to other intermetallic systems is in need of further study. However, it appears that the effect involves the nucleation and initial growth of the scale on TiAl since preoxidation in pure oxygen develops an alumina scale which remains protective when nitrogen is added to the gas[4]. Kobayashi et al. have also[31] reported that such preformed scales remain protective even under cyclic oxidation conditions, although the frequency of thermal cycles was not severe.

Summary

Figure 10 presents an overview of the temperature to which alloy systems containing intermetallic phases can maintain reasonable oxidation resistance. This diagram, which has been updated from that published by Aitken[17] by the inclusion of data on Fe-Si and Ni-Si[32], is based on an approximate oxidation rate of 20 mg/cm^2 in 100 hours for the most oxidation resistant compound in each system. This representation obviously oversimplifies a very complex body of data. The results from the present investigation[10] show that intermetallics in the Nb-Si, Nb-Al and Ta-Si do not possess adequate oxidation resistance to be used at

temperatures above 800°C. Under certain conditions the intermetallic TiAl is oxidation resistant[4], and $MoSi_2$ is very oxidation resistant over a range of temperatures but this compound can undergo acceleration oxidation under certain conditions[9]. Figure 10 is useful for qualitative comparisons. The temperature ranges where breakdown phenomena, such as "pesting", have been reported are crosshatched in the Figure.

The basic concepts of selective oxidation apply to intermetallic compounds. However, the details of the selective oxidation process for the compounds of major interest for high temperature applications differ as a result of:

a. Generally low permeabilities for interstitials in the alloy.
b. Smaller differences in the stabilities of the oxides of the components.
c. Tight stoichiometry of many compounds.
d. Transient oxides which grow with linear or rapid parabolic kinetics.

The effects of oxidation temperature and alloying on the selective oxidation process varies from one compound to the next depending on their relative effects on:

a. Solubility and diffusivity of interstitials.
b. Diffusivities of the metallic components.
c. Rate of transient oxidation.
d. Alloy phases stabilized.
e. Vaporization of metallic and oxide species.
f. Oxide and alloy melting.

The oxidation of some compounds is sensitive to the composition of the oxidizing atmosphere e.g. the presence of nitrogen.

References

1. A. Rahmel and P.J. Spencer, Oxidation of Metals, 35, 53 (1991).

2. K.L. Luthra, "A Comparison of the Mechanisms of Oxidation of Ti- and Ni-Base Alloys", to appear in the Proceedings of a TMS/ASM Symposium on Environmental Effects on Advanced Materials, Detroit, MI, Oct., 1990.

3. A.K. Misra, Met. Trans. A., 22A, 715 (1991).

4. G.H. Meier and F.S. Pettit, "Oxidation Behavior of γ-TiAl", Appendix I, this report.

5. C. Wagner, Z. Elektrochem., 63, 772 (1959).

6. F. Gesmundo and F. Viani, Oxid. Metals, 25, 269 (1986).

7. F.S. Pettit, Trans. TMS-AIME, 239, 1296 (1967).

8. C. Wagner, J. Electrochem. Soc., 99, 369 (1952).

9. D.A. Berztiss, F.S. Pettit and G.H. Meier, "Oxidation of $MoSi_2$", Appendix I, this report.

10. R.R. Cerchiara, G.H. Meier and F.S. Pettit, "Oxidation Resistance of Intermetallic Compounds Containing Niobium or Tantalum", Appendix I, this report.

11. R. Svedberg, "Oxides Associated with the Improved Air Oxidation Performance of some Niobium Intermetallics and Alloys", in Properties of High Temperature Alloys, Z.A. Foroulis and F.S. Pettit eds., The Electrochem. Soc., 1976, p. 331.

12. M. Steinhorst and H.J. Grabke, J. Mater. Sci. Eng., A120, 55 (1989).

13. G.H. Meier, D. Appalonia, R.A. Perkins, and K.T. Chiang, "Oxidation of Ti-Base Alloys", in Oxidation of High Temperature Intermetallics, p. 185, (1989).

14. E. Fitzer, Plansee Proc., 2nd Seminar, Reutte/Tyrol, Pergamon Press, 1956, p. 56.

15. J. Berkowitz-Mattuck, P.E. Blackburn, and E.J. Felten, Trans. TMS-AIME, 233, 1093 (1965).

16. J. Berkowitz-Mattuck. M. Rossetti, and D.W. Lee, Met. Trans., 1, 479 (1970).

17. E.A. Aitken, "Corrosion Behavior", in Intermetallic Compounds, J.H. Westbrook ed., Wiley, 1967, Chap. 25.

18. J.H. Wood and E. Goldman, "Protective Coatings", in Superalloys II, C.T. Sims, N.S. Stoloff, and W.C. Hagel eds.,

19. T. Adachi and G.H. Meier, Oxid. Metals, 27, 347 (1987).

20. B.M. Warnes, F.S. Pettit, and G.H. Meier, in preparation for Oxid. Metals.

21. G.S. Giggins and F.S. Pettit, J. Electrochem. Soc., 118, 1782 (1971).

22. G.R. Wallwork and A.Z. Hed, Oxid. Metals, 3 171 (1971).

23. F.S. Pettit and G.H. Meier, in preparation of Oxid. Metals.

24. R.A. Perkins, K.T. Chiang, and G.H. Meier, Scripta Met., 21, 1505 (1987).

25. C.S. Wukusick, "Oxidation Behavior of Intermetallic Compounds in the Nb-Ti-Al System", Report on USAEC Contract No. AT(40-1)-2847, General Electric Corp., July 31, 1963.

26. R.A. Perkins, K.T. Chiang, and G.H. Meier, Scripta Met., 22, 419 (1988).

27. R.A. Perkins and G.H. Meier, "Oxidation Resistant Aluminides for Metal-Matrix Composites" in Proc. Industry-University Advanced Materials Conference II, F. Smith ed., Advanced Materials Inst., 1989, p. 92.

28. R.A. Perkins and C.M. Packer, Private Communication.

29. C. Wagner, Corr. Sci., 5, 751 (1965).

30. N.S. Choudhury, H.C. Graham, and J.W. Hinze, "Oxidation Behavior of Titanium Aluminides", in Properties of High Temperature Alloys, p. 668.

31. E. Kobayashi, M. Yoshihara, and R. Tanaka, High Temp. Tech., 8, 179 (1990).

32. G.H. Meier, "Fundamentals of the Oxidation of High-Temperature Intermetallics" in Oxidation of High-Temperature Intermetallics, T. Grobstein and J. Doychak eds., TMS, Warrendale, PA, 1989, p. 1.

Publications Related to Support Under This Program

1. G.H. Meier, "Fundamentals of the Oxidation of High Temperature Intermetallics", in Oxidation of High Temperature Intermetallics, T. Grobstein, and J. Doychak, eds., The Min., Met., and Materials Soc., 1989, p. 1.

2. G.H. Meier and F.S. Pettit, "High Temperature Oxidation and Corrosion of Intermetallic Compounds", in High Temperature Intermetallics, pp. 66-80, The Royal Society, London, The Institute of Metals, London, UK, (Invited Paper) 1991.

3. R.R. Cerchiara, G.H. Meier and F.S. Pettit, "Oxidation Resistance of Intermetallic Compounds Containing Niobium or Tantalum", submitted for publication.

4. G.H. Meier and F.S. Pettit, "Oxidation Behavior of γ-TiAl", submitted for publication.

5. D.A. Berztiss, F.S. Pettit and G.H. Meier, "Oxidation of $MoSi_2$", submitted for publication.

Table 1

Oxide Melting Points and Eutectic Temperatures

Oxide:	Al_2O_3	SiO_2	TiO_2	Nb_2O_5	Nb_2O_5-Al_2O_3	Nb_2O_5-SiO_2	Nb_2O_5-TiO_2
Temp. (°C)	2050	1723	1857	1510	1400	1448	1467

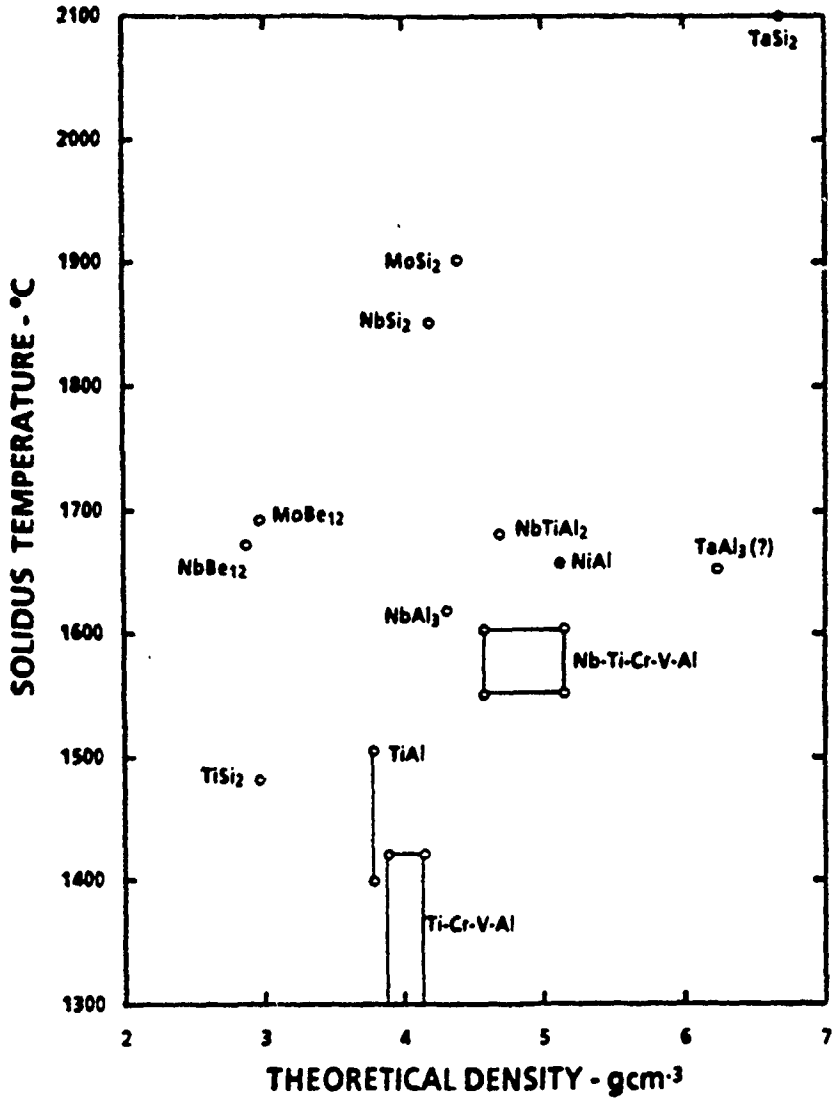

Figure 1. Melting points and densities of selected intermetallics.

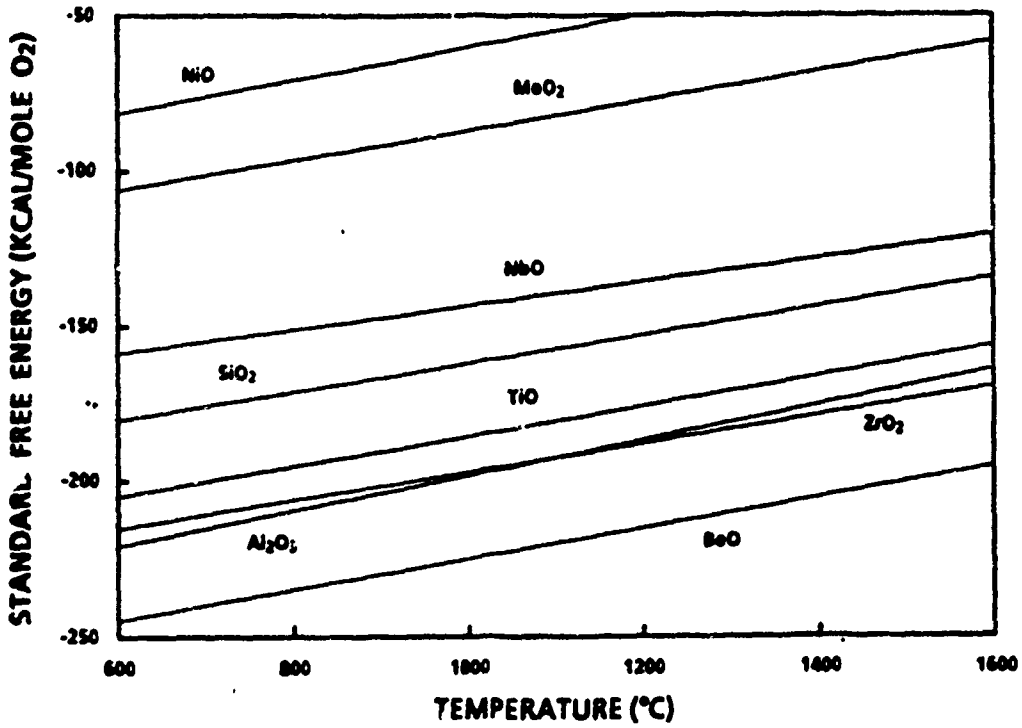

Figure 2. Standard free energies of formation for selected oxides.

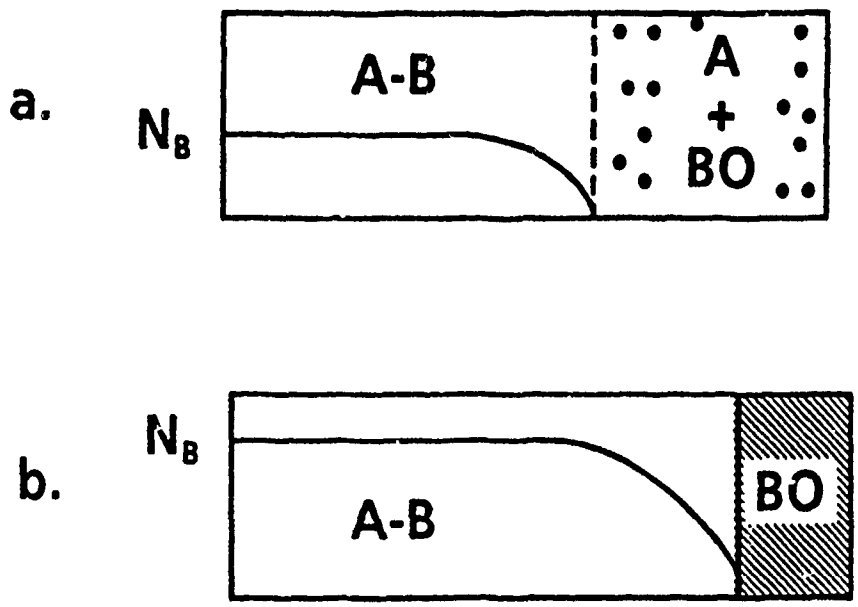

Figure 3. Schematic diagram of the oxidation of a noble metal, A, containing a reactive metal, B. a) Dilute alloy showing internal oxidation of B. b) Concentrated alloy forming an external layer of BO.

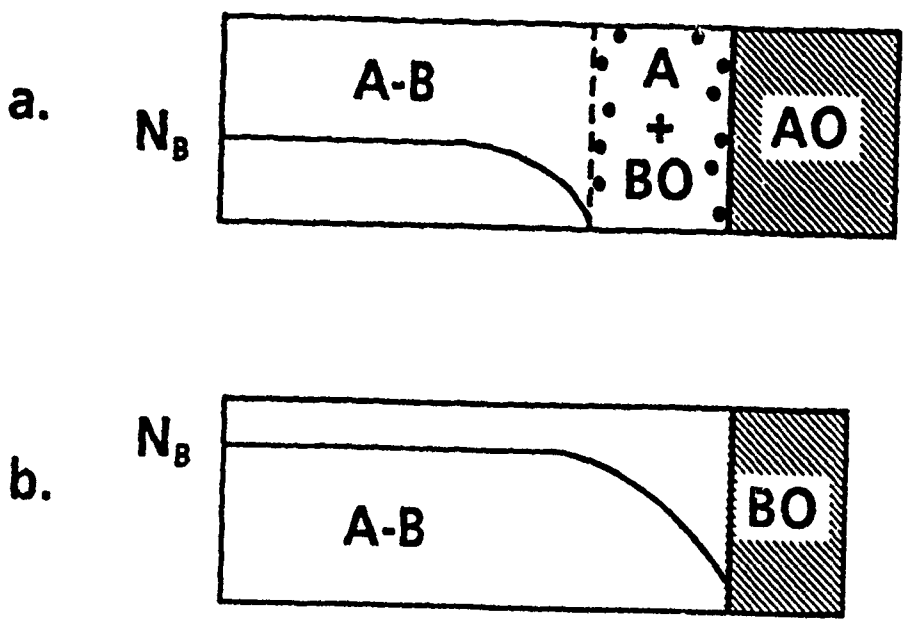

Figure 4. Schematic of oxidation of A-B with both AO and BO stable (BO more stable than AO). a) Dilute alloy showing internal oxidation under external AO. b) Concentrated alloy forming external BO.

Oxidation of Stoichiometric Compounds

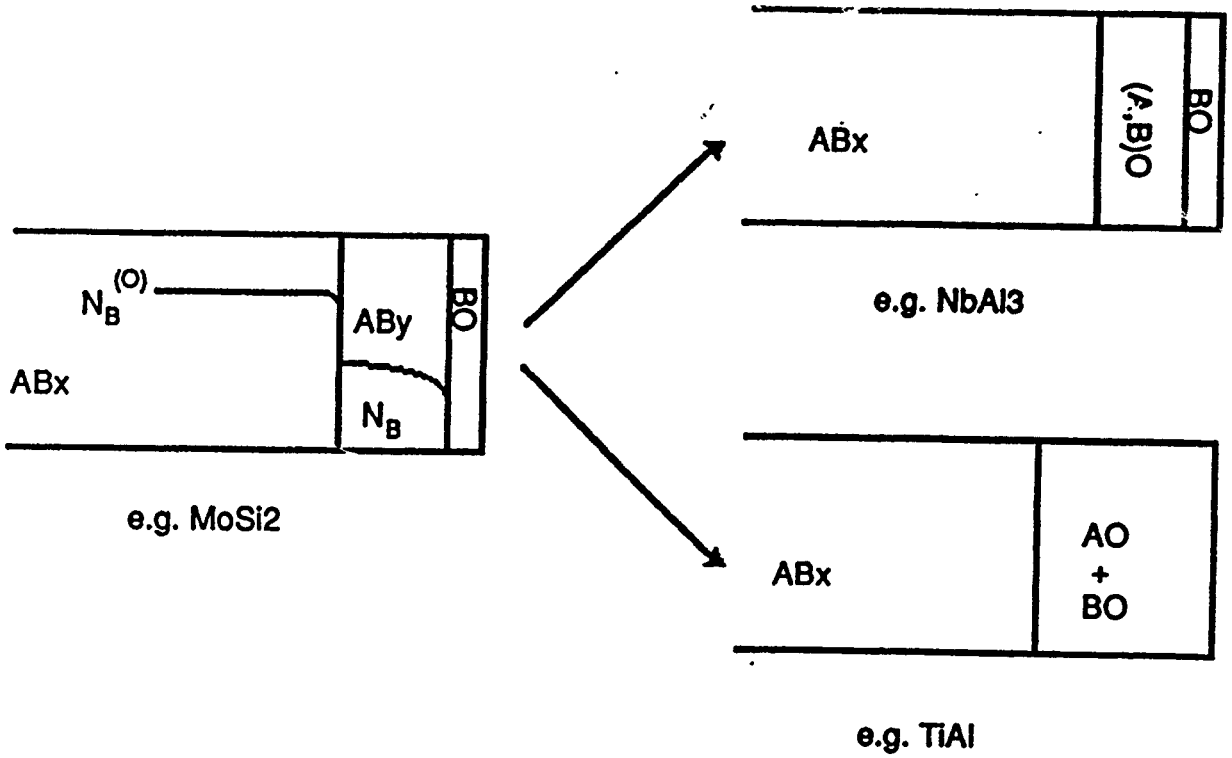

Figure 5. Schematic diagram illustrating the special features involved in the oxidation of intermetallic compounds with narrow ranges of stoichiometry.

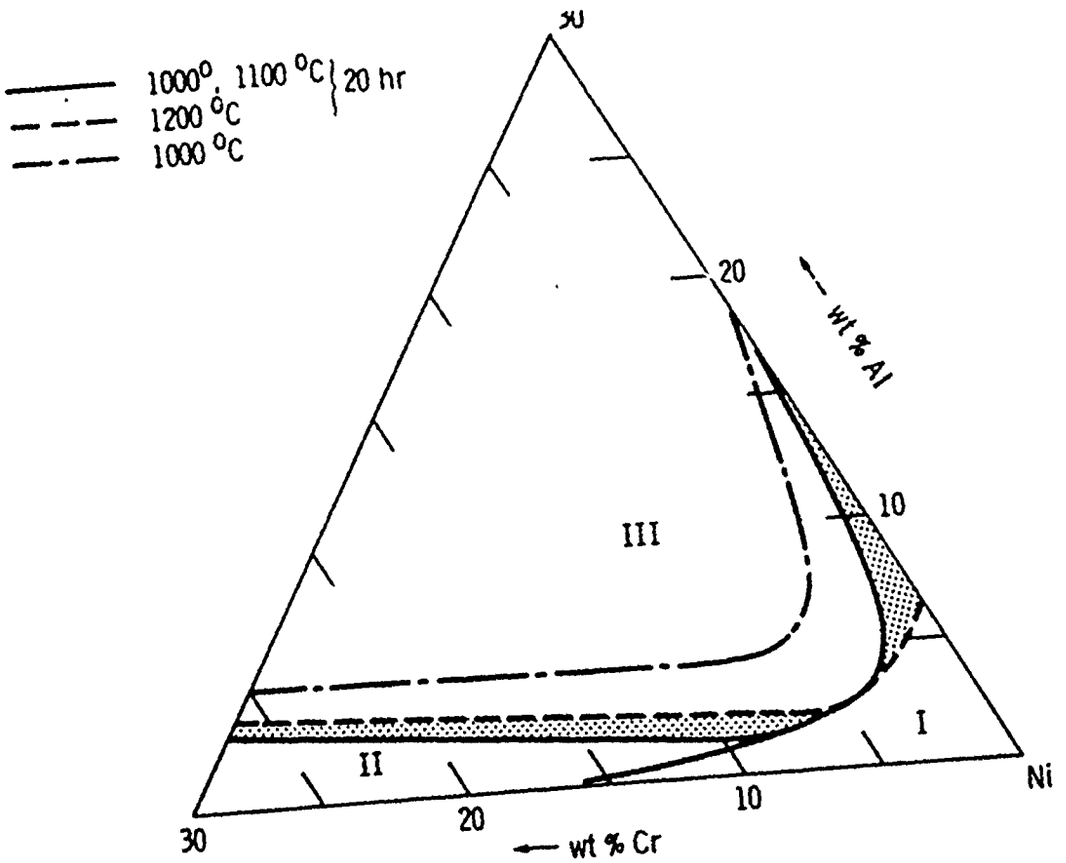

I External NiO, Internal $Cr_2O_3/Al_2O_3/Ni(Al,Cr)_2O_4$

II External Cr_2O_3, Internal Al_2O_3

III External Al_2O_3

Figure 6. Isothermal oxidation map for the Ni-Cr-Al system showing the effect of Cr in developing and maintaining a protective alumina scale.

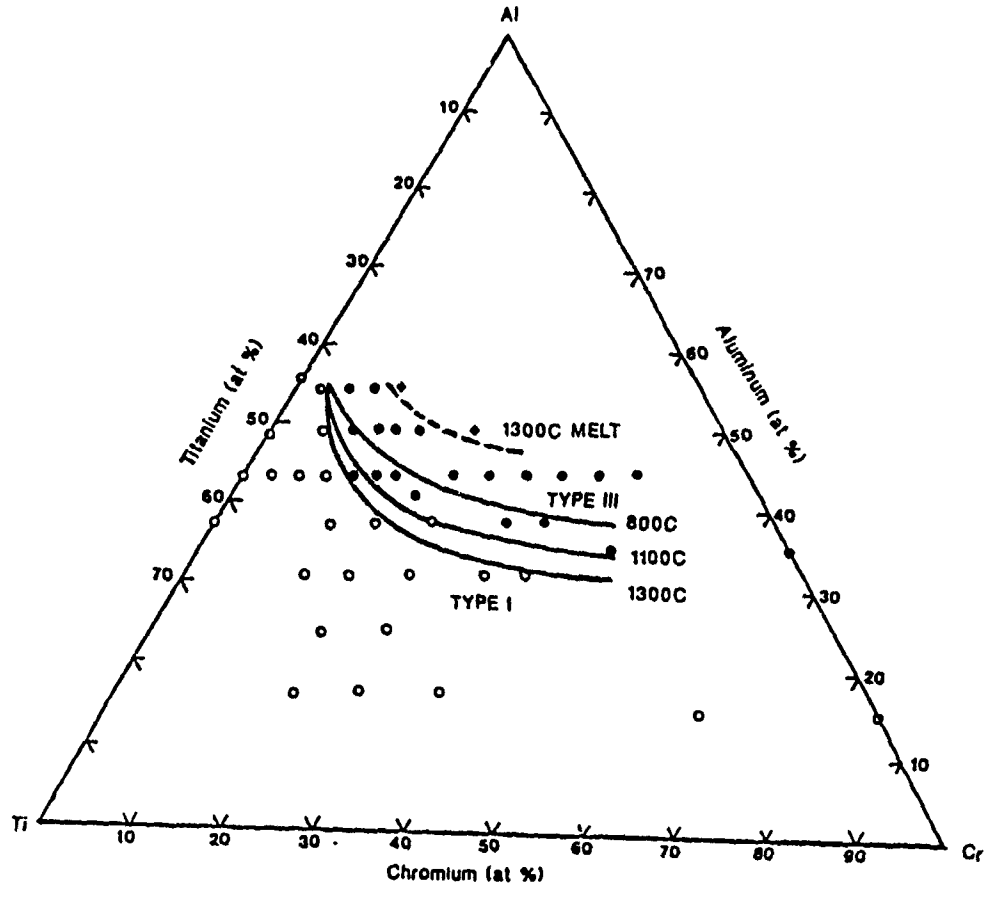

Figure 7. Isothermal oxidation map for the Ti-Cr-Al system showing the effect of Cr on developing a protective alumina scale.

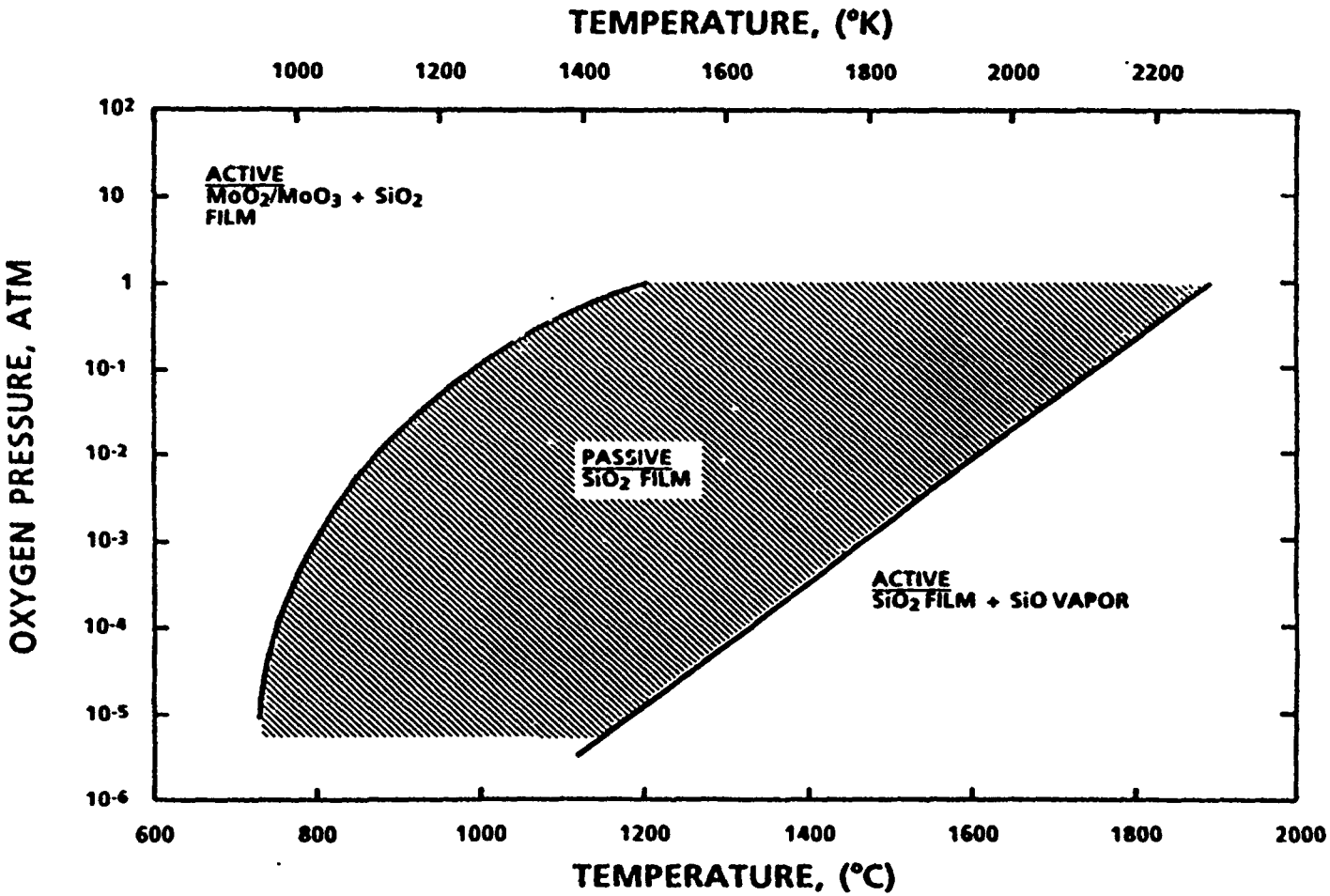

Figure 8. Map of oxygen pressure vs. temperature indicating conditions for the development of a protective silica film on $MoSi_2$ and the importance of volatile species in this process.

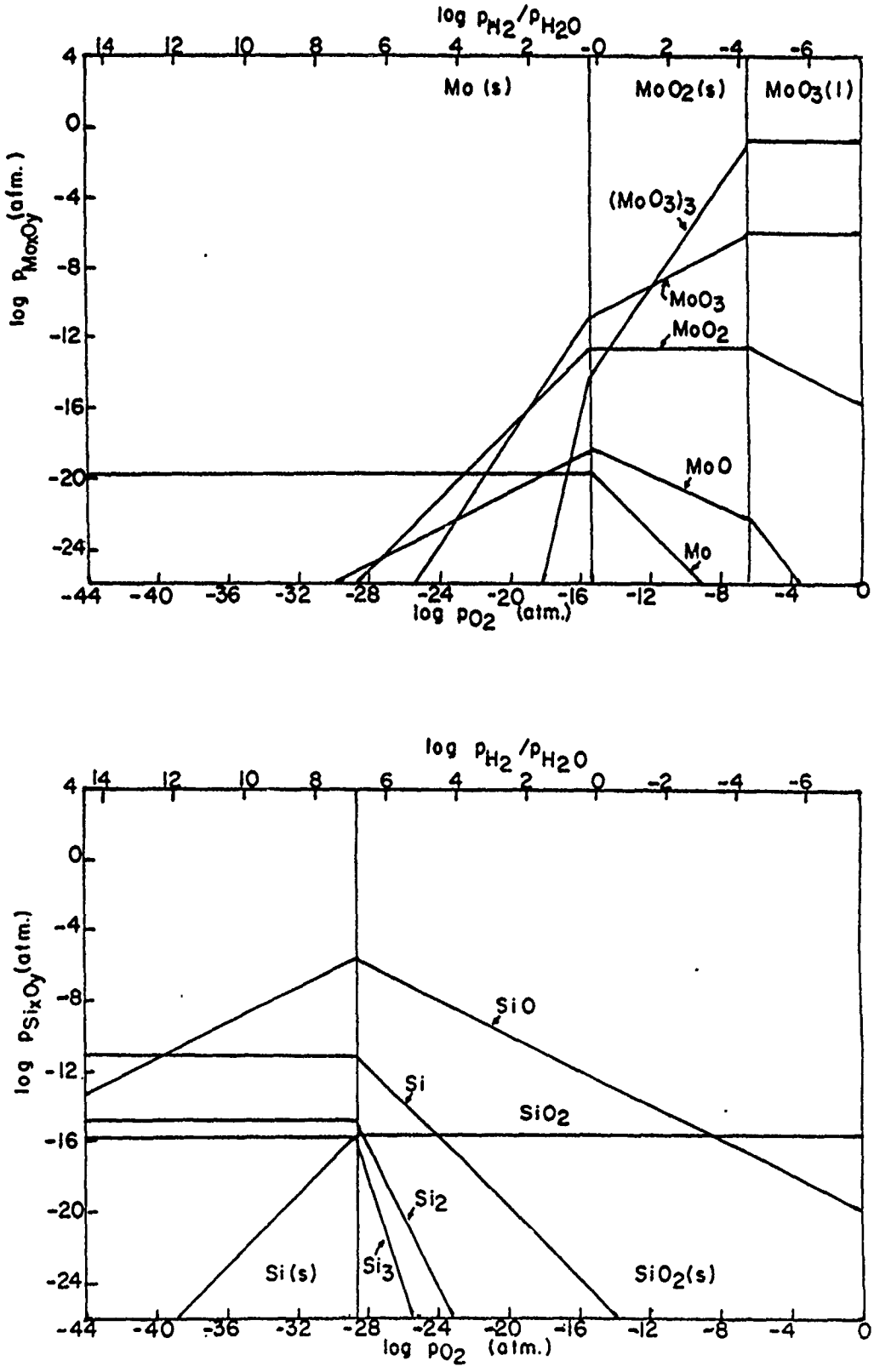

Figure 9. Volatile species for the Mo-O (top) and Si-O (bottom) systems

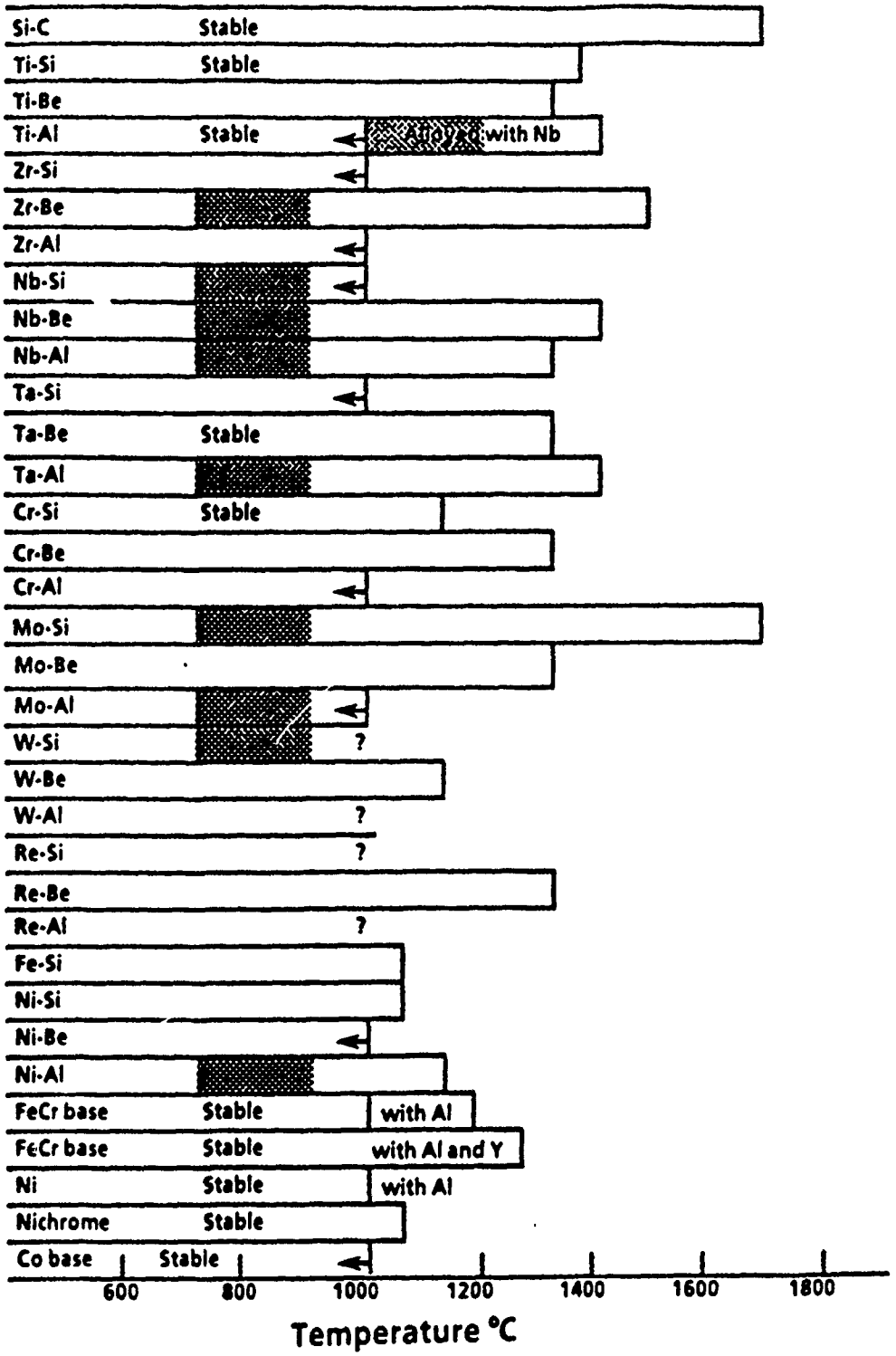

Figure 10. Bar chart summarizing the oxidation behavior of the most resistant compound in each of the indicated systems. The maximum temperature generally corresponds to 20 mg/cm^2 in 100 hours.

Appendix I

Oxidation Resistance of Intermetallic Compounds Containing Niobium or Tantalum

by

R.R. Cerchiara, G.H. Meier and F.S. Pettit
Materials Science and Engineering Department
University of Pittsburgh
Pittsburgh, PA 15261

Abstract

Intermetallic compounds in the Nb-Al, Nb-Si and Ta-Si systems have been oxidized in oxygen and in air at temperatures between 800° and 1400°C. It was not possible to selectively oxidize aluminum or silicon even in the intermetallics most rich in these two elements. At temperatures in the vicinity of 800°C some of the intermetallics degraded via a pest type of oxidation. The oxidation behavior of the intermetallic compounds in these systems is such that adequate oxidation resistance for practical applications cannot be developed at temperatures above about 800°C.

Introduction

A number of intermetallic compounds are being investigated to determine if they possess properties appropriate for consideration at elevated temperatures beyond the temperature limits (~ 1050°-1200°C) of the current nickel-base superalloys. Numerous mechanical properties, such as yield strength, creep strength and fatigue lives, are important. Another important requirement is oxidation resistance. Since niobium and tantalum have high melting points, intermetallic compounds with these elements are candidates for development as high temperature systems. The oxidation resistance of alloys provided by

scales of Nb_2O_5 and Ta_2O_5 is very poor[1] since transport through these oxides is so rapid. Intermetallics based on niobium or tantalum can be oxidation resistant therefore only when another element is present which can be selectively oxidized. Moreover, the oxide of this other element must be one through which transport takes place at rates consistent with acceptable lives. The only elements that satisfy such requirements for temperatures beyond 1050°C are aluminum and silicon. Both of these elements form oxides with large, negative free energies of formation, which is necessary if selective oxidation is to occur, and transport through their oxides takes place slowly compared to most other oxides. Chromium is another element that has been used to develop oxidation resistance in superalloys to temperatures of 1000°C but it is not effective at higher temperatures due to the formation of CrO_3 gas.

The present paper is concerned with the oxidation properties of intermetallics based upon the Nb-Al, Nb-Si, and Ta-Si systems. In attempting to develop alloys in which aluminum or silicon is selectively oxidized, the standard free energies of oxides such as NbO_2 and Ta_2O_5 are still important because they must be substantially less than those of the oxides that are being formed selectively. This is a factor that is less favorable for metals such as niobium and tantalum compared to elements such as nickel or cobalt which are the base elements used in superalloys. Standard free energies of formation as a function of temperature of the oxides relevant to the oxidation the intermetallics of interest in this paper are presented in Figure 1 where the standard free energy of formation for NiO is also included for comparison. The importance of the lack of a substantial difference between the standard free energies of formation of the oxides that can be formed in the intermetallics

of interest will be an important factor which will be discussed in more detail in the discussion section of this paper.

Experimental

The intermetallics $NbAl_3$, $NbSi_2$ and $TaSi_2$ were prepared by arc melting and drop casting. Coupons, approximately 1 cm x 1 cm x 0.2 cm were cut from these castings, polished through 600 grit abrasive paper, and ultrasonically cleaned. The specimens were oxidized in oxygen or air at a number of temperatures between 800° and 1400°C. A microbalance was used to continuously determine weight changes as a function of time. Oxidized specimens were examined using XRD, optical microscopy and scanning electron microscopy.

To attempt to determine if cracking occurred in growing oxide scales, acoustic emission was used. Cumulative counts were measured as a function of exposure time. Previous studies have shown that these counts correlate well with oxide scale cracking[2]. A wave guide was used to transmit the acoustic signal from the specimen to the transducer, as shown schematically in Figure 2. This wave guide was a one millimeter thick, one meter long platinum wire which also served the purpose of suspending the specimen in the furnace. The specimen was attached to the wave guide with a fine spot weld. On the other end of the wave guide a stainless steel cone was permanently welded to allow the transducer to be attached. Platinum was chosen since it does not oxidize under the experimental conditions used and does not undergo any phase transformation which could be a potential source of acoustic emission. (Specimens which contain Si were studied using an alumina waveguide.)

The acoustic emission monitoring system used, was the Dunegan/Endevco, 3000 series. The acoustic emission signal is detected by a high sensitivity PZT transducer (Model S9204) which has a frequency response over the range of 100 - 400 KHz. The transducer signal is preamplified by a fixed gain of 40 dB (100 times) and passed through a 100 KHz highpass filter. The preamplified filtered signal is then processed for count measurements for amplitude analysis. For count measurement, the signal is further amplified and fed to a threshold detector which sends a digital pulse to a digital counter each time the signal exceeds the threshold voltage. The threshold voltage is fixed at one volt so the signal has to be amplified such that the noise level is just below one volt to obtain the maximum sensitivity. The digital counter accumulates all the pulses and displays them on a LED window as AE counts. The digital signal is also converted into an analog signal to plot the counts on a recorder.

Results and Discussion

Oxidation of $NbAl_3$

Several different heats of $NbAl_3$ were studied. The heat identified as Loch/under 75 Al was niobium rich compared to the stoichiometric composition and a typical microstructure is shown in Figure 3. Two phases were present. The major phase was $NbAl_3$ with a small amount of Nb_2Al at grain boundaries of the $NbAl_3$. The heat, West > 75 Al, was just slightly excess aluminum and in the microstructure a very small amount of aluminum could be detected at the grain boundaries of the $NbAl_3$. There was also some Loch/> 75 Al specimens. The final heat, West + Si, contained 7.8 atomic percent Si and 67.2% aluminum.

Since some of the aluminum was replaced with silicon, this heat was also excess niobium.

Results from weight change versus time measurements for the oxidation of the $NbAl_3$ samples in oxygen and in air at temperatures of 800° and 1100°C are presented in Figures 4 and 5, respectively. At 800°C the weight gains for all specimens were much larger than that for growth of protective scales of Al_2O_3. Those specimens with excess aluminum did not oxidize as rapidly as those with excess niobium. The niobium rich specimens usually disintegrated into a fine powder, Figure 6. This type of degradation was occasionally preceded, Figure 4, by an incubation period of very slow oxidation. No disintegration of the aluminum rich samples was observed but the oxidation of these samples was accelerated compared to that for protective alumina scale formation.

Oxidation coupled with the disintegration of specimens has been observed during the oxidation of other intermetallics[3-5] and has been named pesting by Fitzer[3]. Berkowitz and coworkers have investigated the pesting of $MoSi_2$[4,5]. The oxidation of $MoSi_2$ has been studied by Bertziss et al.[6] at temperatures between 500° and 1400°C. It was observed that pesting of $MoSi_2$ occurred in a narrow temperature range near 500°C. Above this temperature a protective layer of SiO_2 was formed and it was extremely oxidation resistant to temperatures in excess of 1400°C. Berkowitz did not observe pesting in single crystals of $MoSi_2$ and more recent work by Meschter[7] has shown that pesting does not occur in polycrystalline $MoSi_2$ which is free of cracks and fabrication defects. It appears that pesting occurs when oxidation takes place at small defects in $MoSi_2$. The oxidation process causes cracks to initiate and grow at these defects. This form of degradation has been observed in a number of intermetallics[8], Figure 7. In the case of $MoSi_2$, its oxidation resistance is

resistance is poorest between 500° - 600°C. In this temperature range much MoO_3 is formed along with SiO_2 and continuous scales of SiO_2 are not formed[6]. The inability of intermetallics to form protective scales may be a necessary condition, but not a sufficient condition, for pesting.

Measurements of acoustic emission were obtained during the oxidation of $NbAl_3$ under conditions that caused pesting. This was an aluminum rich specimen. The results are presented in Figure 8. The number of counts are not very large but they are above background and indicate that the intermetallic is cracking during pesting. Surface photographs and a cross sectional view of this specimen after the acoustic emission measurements are presented in Figure 9. the attack of the specimen is not severe and pesting appears to be in the initiation stage that often precedes the rapid degradation of intermetallics via pesting. The length of this initiation stage varies as can be seen in Figure 4. The duration of the initiation stage depends on the amount of defects which are present in the specimen prior to oxidation.

At 1100°C the weight changes are not extremely large, Figure 5, but still usually larger than that for alumina growth. Results from acoustic emission measurements, Figure 10, showed some cracking may have occurred during oxidation at 1100°C. Cracking of the oxide scale or in the alloy adjacent to the external oxide scale could affect the transient oxidation which takes place prior to the development of a continuous Al_2O_3 scale. The oxide scale that formed upon $NbAl_3$ during oxidation at 1100°C in oxygen and in air was composed of layers of $NbAlO_4$ and Al_2O_3, Figure 11. Grabke and coworkers have also observed such layered oxide scales during oxidation of $NbAl_3$[8]. These investigators have observed

intermittent acoustic emission signals during oxidation of $NbAl_3$ and concluded that the layered scale is formed by the development of a continuous Al_2O_3 scale on this alloy which cracks and the $NbAlO_4$ is formed upon oxidation of the aluminum depleted alloy beneath the cracked Al_2O_3 scale. The results obtained in the current investigation are in agreement with this proposal. The cause of the cracking has not been identified. The sequential layers show that some selective oxidation of the aluminum must occur. The portions enriched in niobium must be formed after the cracking although as discussed subsequently they may cause the cracking.

Weight change data obtained for the oxidation of $NbAl_3$ in oxygen at temperatures between 950° and 1400°C are presented in Figure 12. The rates of oxidation increase with temperature and those at 1250 and 1300 indicate that some cracking of the oxide is occurring. The magnitudes of these weight changes show that selective oxidation of aluminum in these specimens is not occurring. Analyses of specimens from these tests using x-ray diffraction and optical metallography showed that oxides of both aluminum and niobium had been formed. Typical microstructures are presented in Figure 13. In some areas a continuous Al_2O_3 scale appears to have developed beneath oxides that contain both niobium and aluminum. In other areas the oxide is much thicker and alternating layers of oxide rich in aluminum and niobium are evident. Preferential oxidation of the Nb_2Al phase was always observed, Figure 14.

At temperatures where pesting does not occur continuous layers of Al_2O_3 are not developed upon $NbAl_3$. The results indicate that after some amount of transient oxidation, continuous Al_2O_3 scales do begin to develop but cracking of this layer occurs and niobium

rich oxides are formed due to oxidation of the aluminum depleted substrate. Subsequent oxidation leads to selective oxidation of aluminum with eventual cracking of the Al_2O_3 scale. Consequently, the overall scale is composed of alternating layers of aluminum rich and niobium rich oxides. This scale is not protective and the oxidation rate is unacceptably high.

The cause of cracking in the Al_2O_3 scales as they begin to develop continuity is not fully understood. The stoichiometric range of $NbAl_3$ is very small and as aluminum is preferentially oxidized the aluminum concentration cannot be reduced substantially, otherwise Nb_2Al will be formed at the alloy-oxide interface. The microstructures of oxidized specimens show that a layer of Nb_2Al is usually present at the alloy-oxide interface which shows that the oxidation reaction has caused the aluminum concentration to be decreased to levels below those necessary for the stability of $NbAl_3$. The aluminum activity in $NbAl_2$ is not available but preferential oxidation of this phase is always evident. It therefore appears that aluminum cannot be selectively oxidized from $NbAl_2$. Oxides of niobium must develop beneath the Al_2O_3 scale as this scale begins to develop continuity which causes the Al_2O_3 scale to crack.

The results obtained for the oxidation of $NbAl_3$ show that protective scales of Al_2O_3 cannot be developed on niobium-aluminum alloys. Moreover some of the intermetallics in this alloy system will pest when defects are present, such as small cracks. This alloy system does not have sufficient oxidation resistance to be considered for applications at temperatures above those of current state-of-the-art superalloys.

Oxidation of $NbSi_2$

When specimens of $NbSi_2$ were prepared, it was difficult to obtain samples that were completely free of some pores and small cracks. Upon heating such specimens to 800°C in oxidation experiments, the specimens completely disintegrated. Alloys were also prepared close to the composition of $NbSi_2$ but with a small amount of aluminum (i.e. Nb-5Al-62Si, Nb-10Al-57Si, atomic percent). These specimens did not disintegrate upon heating and oxidation experiments were performed in oxygen at 800° and 1100°C. The results are presented in Figures 15 and 16. The weight changes are large and selective oxidation of silicon or aluminum could not have occurred. The oxidized specimens exhibited thick scales containing large amounts of niobium, Figure 17, consistent with the observed large weight increases.

The results obtained with the $NbSi_2$ specimens show that the silicon cannot be selectively oxidized. The results also indicate that there are probably conditions for which pesting will occur in this intermetallic. Intermetallics of the Nb-Si systems do not have adequate oxidation resistance to be considered for use under conditions of the state-of-the-art superalloys.

Oxidation of $TaSi_2$

A photograph showing the microstructure of $TaSi_2$ used in the oxidation experiments is presented in Figure 18. This microstructure consisted of $TaSi_2$ with some pure silicon at grain boundaries. The observed microstructure is consistent with the Ta-Si phase diagram. Results obtained for the oxidation of these specimens are presented in Figures 19 and 20

where weight changes versus time are presented for oxidation in air and oxygen at temperatures of 800° and 1100°C. Data are also presented for a Ta-Si alloy where some of the silicon in $TaSi_2$ was replaced with aluminum (Ta-10%Al-57%Si). The substitution of aluminum for silicon causes the major phase to become Ta_5Si_3 rather than $TaSi_2$ due to the small stoichiometric range of $TaSi_2$. The results obtained at 800°C indicate that pesting may be occurring in $TaSi_2$, Figure 19. Surface photographs and a cross-sectional view of a specimen after oxidation are presented in Figure 21. The specimen is covered with a thick scale containing silicon and tantalum in which large protrusions of a tantalum rich oxide are evident. Acoustic emission results obtained during oxidation are presented in Figure 22. The large number of counts show that cracking of the oxide and/or the alloy is occurring during oxidation.

Inspection of the data presented in Figure 20 show that oxidation of $TaSi_2$ is more severe at 800°C than 1100°C. This is consistent with the specimen pesting at 800°C. The weight change data for oxidation of $TaSi_2$ at 1100°C were small but examination of specimens after oxidation revealed that the oxidation was not uniform. The surface of a specimen after oxidation at 1100°C is shown in Figure 23 and a cross-section is presented in Figure 24. The specimen is covered in numerous areas with a thin layer of SiO_2 but there are numerous nodules of thicker oxide composed of tantalum oxides and silica. Cracks in the oxidized specimen can be seen and oxidation has occurred at these sites, Figure 23. These nodules may have been formed during the transient oxidation period and the silicon could be selectively oxidized at 1100°C in $TaSi_2$. The oxidation kinetics for the specimens with small

amounts of aluminum are very large at 1100°C. This is because the major phase is Ta_5Si_3 and silicon cannot be selectively oxidized in this phase.

The results show that as in the case of $NbAl_3$ and $NbSi_2$, $TaSi_2$ undergoes pesting at temperatures around 800°C. At 1100°C silicon may be selectively oxidized in $TaSi_2$ but not in Ta_5Si_3. If tantalum silicides are to be used for systems more advanced than the superalloys, they must be capable of withstanding some cracking and spalling of the silica scales observed on $TaSi_2$ at 1100°C. Since Ta_5Si_3 will be exposed to oxidation when the oxide cracks or spalls, tantalum silicides do not possess adequate oxidation resistance to be considered as successors to the superalloys.

Concluding Remarks

Niobium silicides, niobium aluminides and tantalum silicides do not have adequate oxidation resistance to be considered for high temperature applications (e.g. above 800) in oxidizing conditions. Many of the intermetallics in these systems can degrade via pesting at temperatures around 800°C. The pest type degradation requires the presence of small cracks for initiation. Defect free materials apparently will not pest. On the other hand many of the intermetallics based upon these elements are brittle and fabrication of defect free alloys is not easily achieved. Moreover, the use of defect free hardware under certain conditions could result in the formation of defects and pesting could occur. While pesting of these intermetallics is not a problem to be ignored, it is not the major obstacle preventing their use at elevated temperatures. These intermetallics cannot be used because selective oxidation of elements such as aluminum and silicon is not possible even in compositions that

are extremely rich in these latter elements. The major factors that appear to prevent the selective oxidation of aluminum and silicon in these intermetallics are the rapid growth rates of oxides such as Nb_2O_5 and Ta_2O_5, the relatively large standard free energies of formation for these oxides, and the low activities of the elements to be selectively oxidized in these intermetallics.

References

1. P. Kofstad, High Temperature Corrosion, pp. 309-319, Elsevier Applied Science, New York, 1988.

2. A. Ashary, G.H. Meier and F.S. Pettit, pp. 105-119, High Temperature Protective Coatings, S.C. Singhal, editor, the Metallurgical Society, Warrendale, PA, 1983, AIME, 239, 1296 (1983).

3. E. Fitzer, Plansie Proc., 2nd Seminar, p. 56, Reutte/Tyrol, 1955, Pergamon Press, London, (1956).

4. J. Berkowitz-Mattuck, P.E. Blackburn, and E.J. Felten, Trans-AIME, 233, 1093 (1965).

5. J. Berkowitz-Mattuck, M. Rosetti, and D.W. Lee, Met. Trans., 1, 479 (1970).

6. D. Berztiss, G.H. Meier and F.S. Pettit, "Oxidation of $MoSi_2$ in Oxygen and Air at Temperatures Between 500° to 1400°C", submitted to Oxidation of Metals for publication.

7. P. Meschter, personal communication.

8. E.A. Aitken, "Corrosion Behavior", in Intermetallic Compounds, J.H. Westbrook ed., J. Wiley, 1967, Chap. 25.

9. M. Steinhorst and H. Grabke, Materials Science and Engineering, A120, 55 (1989).

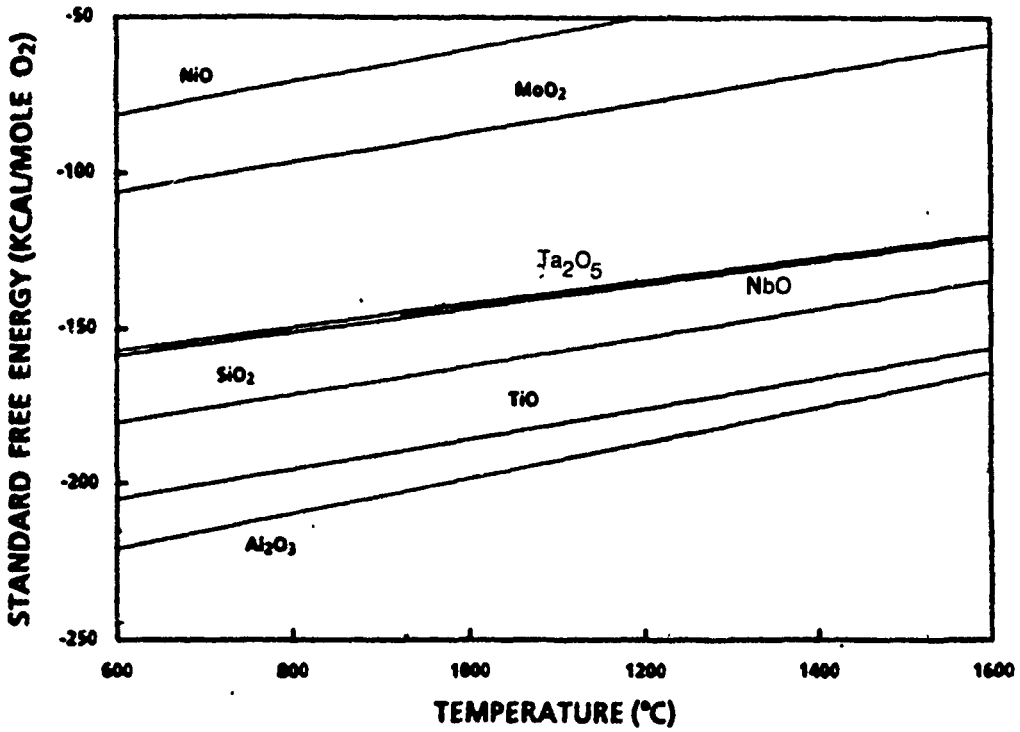

Figure 1. Standard free energies of formation for selected oxides.

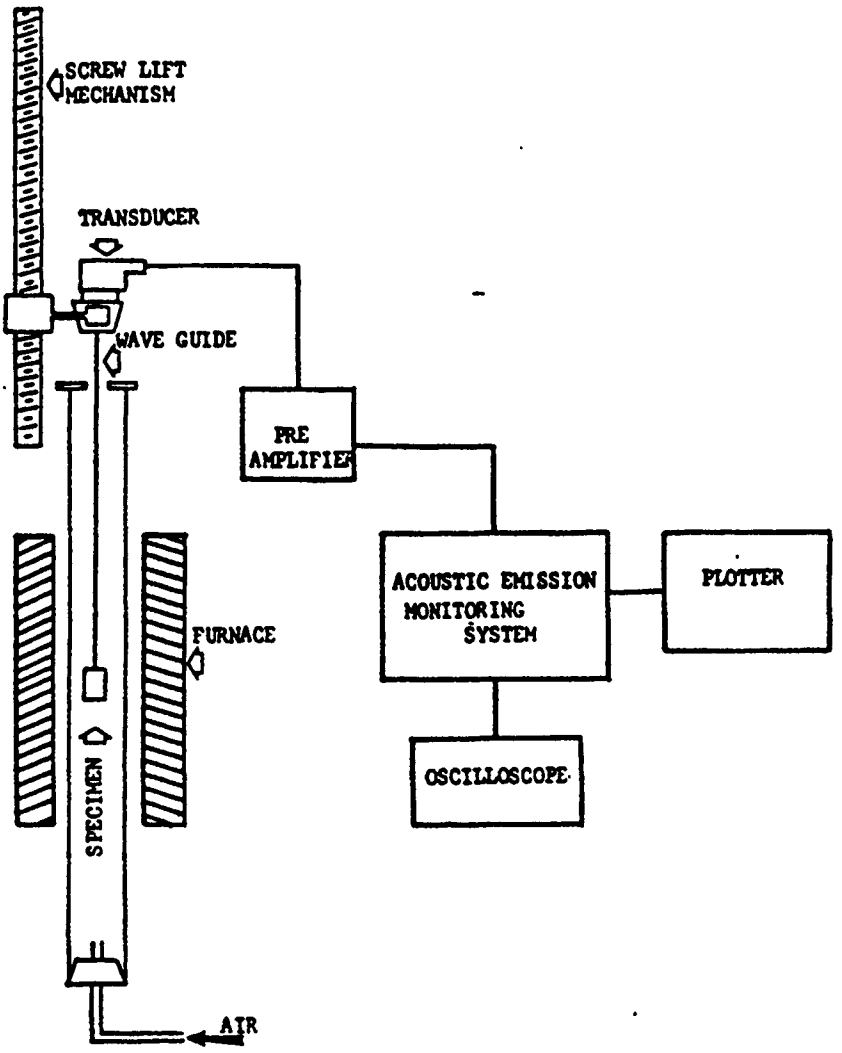

Figure 2. Experimental setup for the acoustic emission study of oxide scale failure.

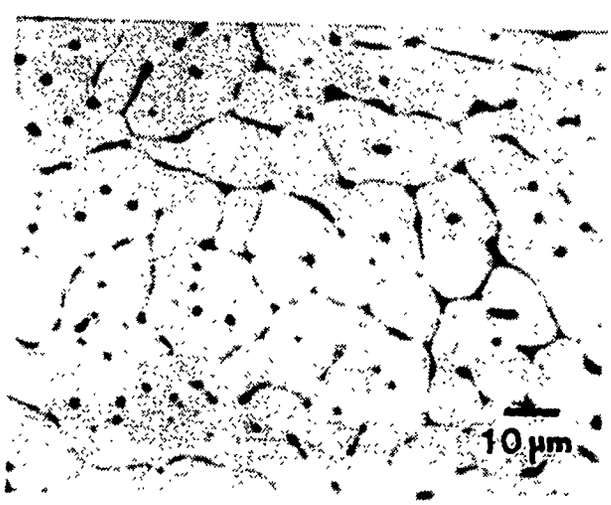

Figure 3. Initial microstructure of $NbAl_3$ (Dark phase is Nb_2Al).

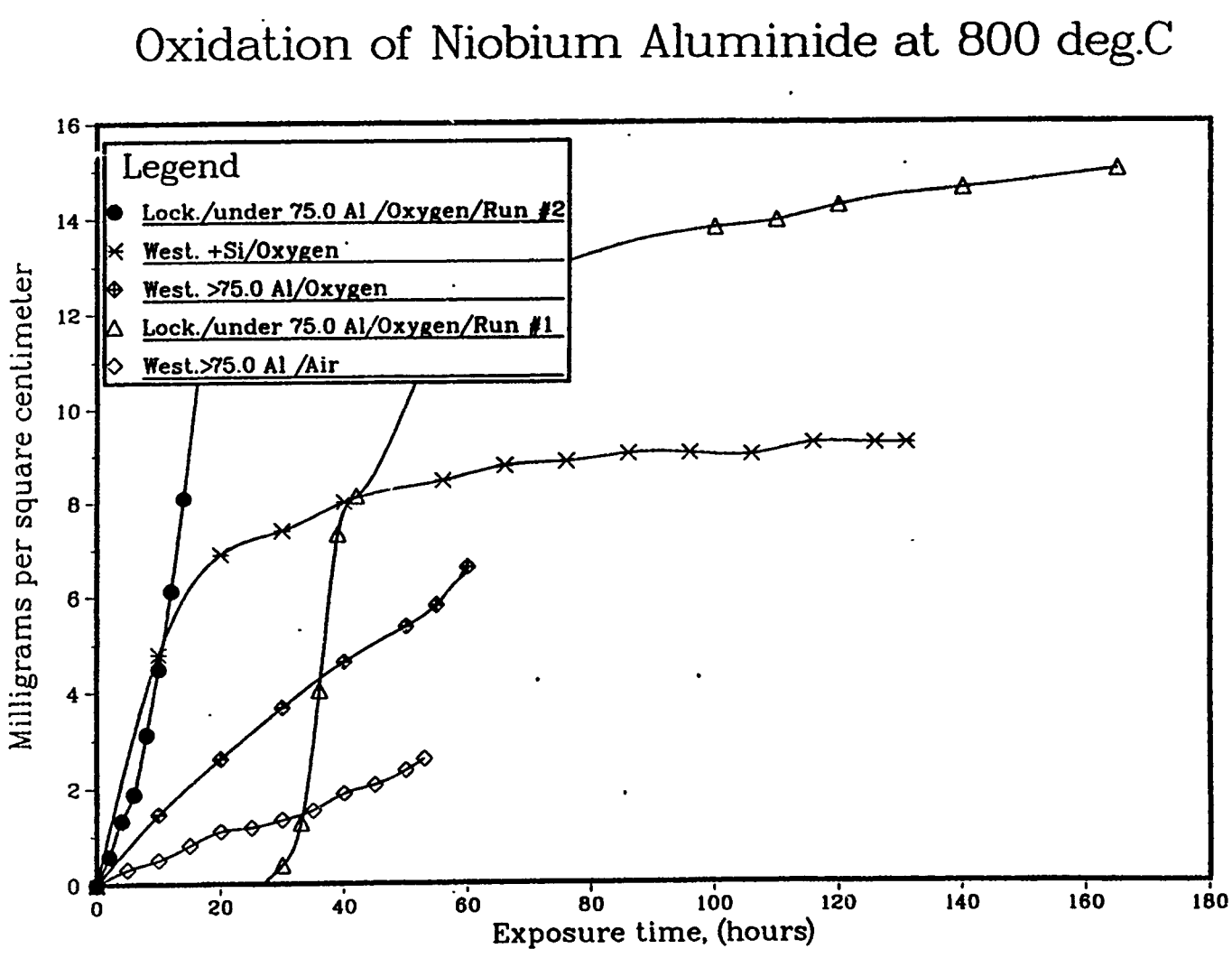

Figure 4. Weight change versus time data for $NbAl_3$ oxidized at 800°C in oxygen and air. The data also indicate the effects of Al content and Si additions.

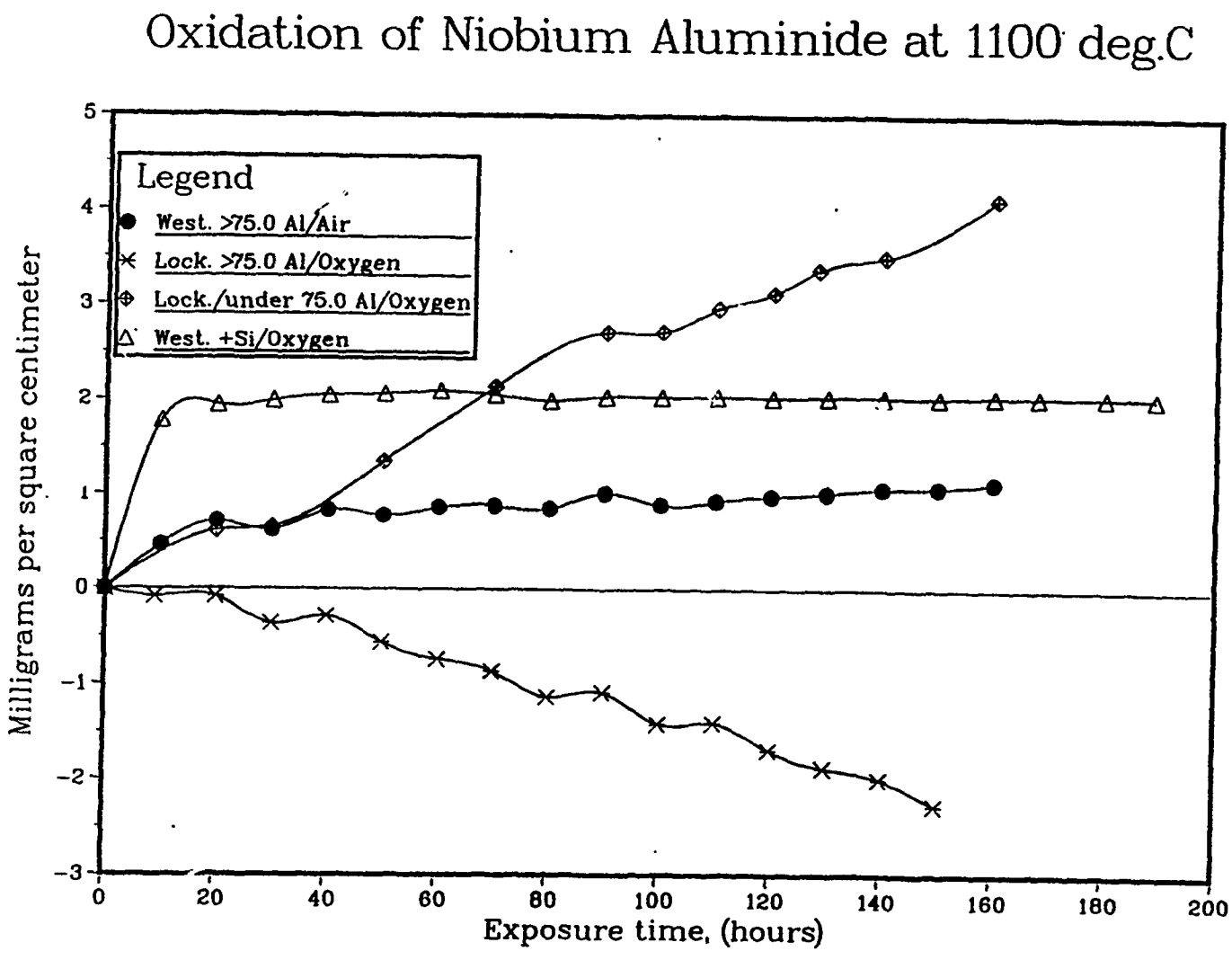

Figure 5. Weight change versus time data for $NbAl_3$ oxidized at 1100°C in oxygen and air. The data also indicate the effects of Al content and Si additions.

$NbAl_3$ 24hr Oxygen 800°C
Shows Result of "Pesting"

Figure 6. Micrograph of $NbAl_3$ showing "pesting" after 24 hrs. oxidation in oxygen at 800°C.

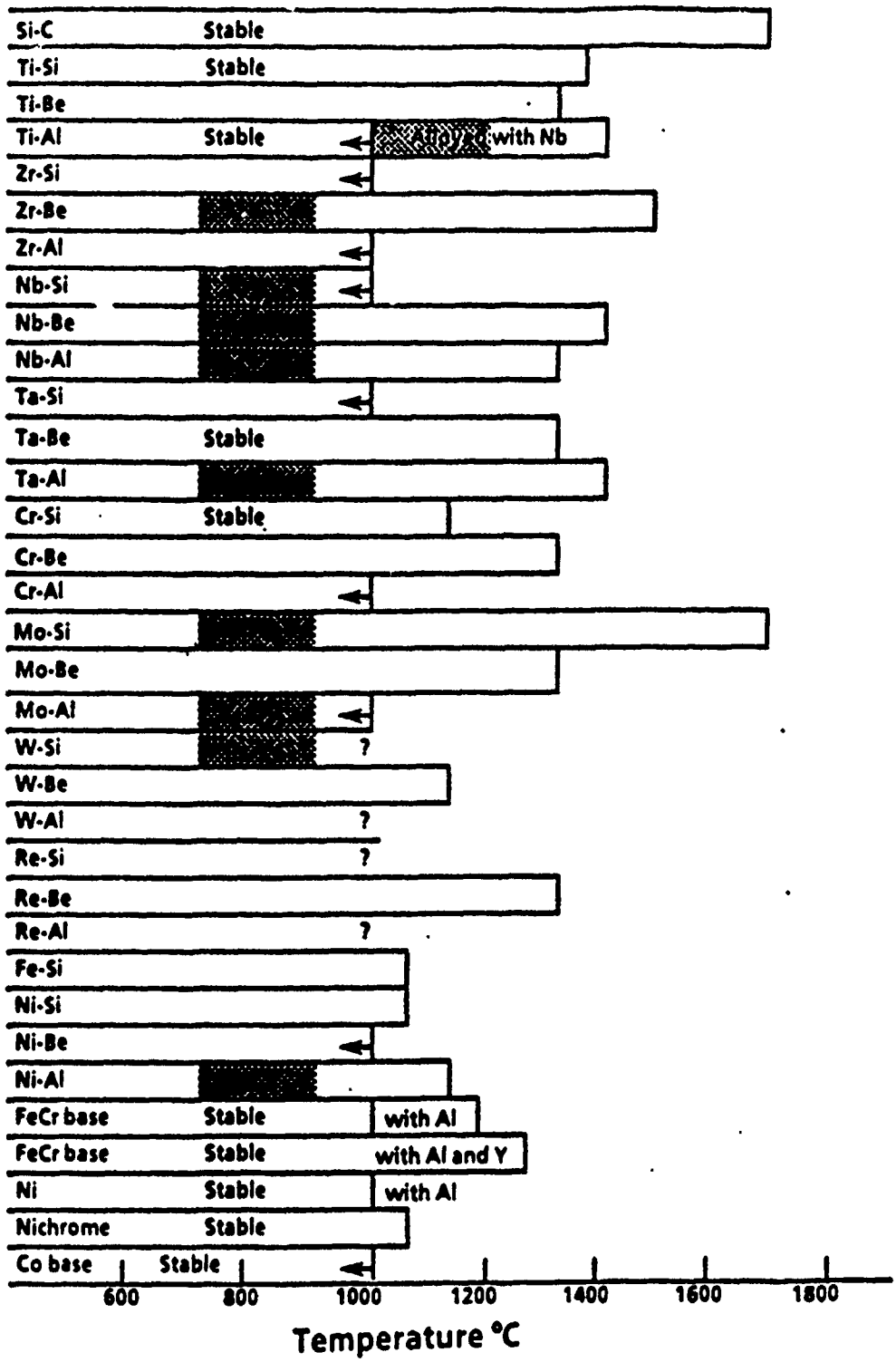

Figure 7. Bar chart summarizing the oxidation behavior of the most resistant compound in each of the indicated systems. The maximum temperature generally corresponds to 20 mg/cm^2 in 100 hours.

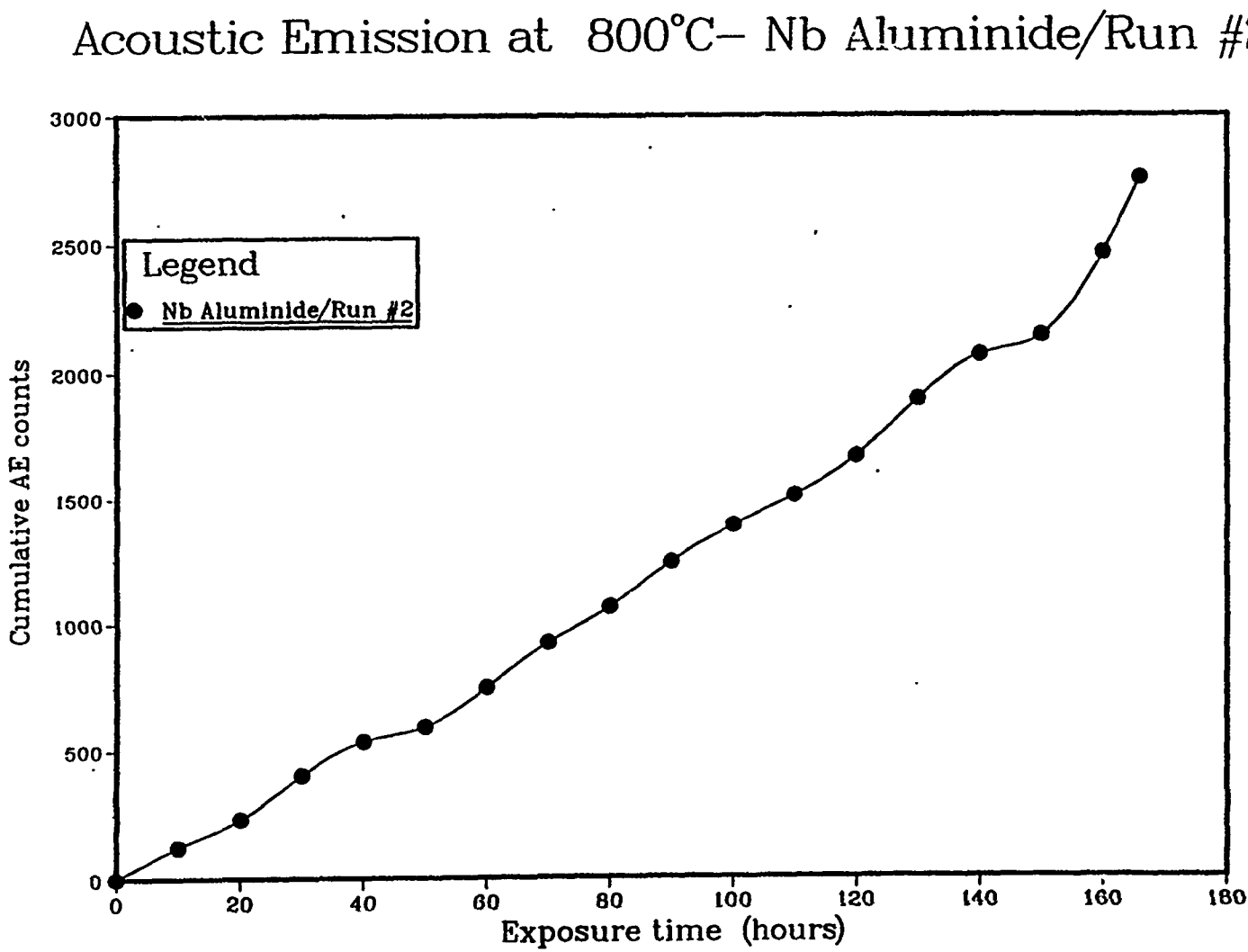

Figure 8. Acoustic emission data obtained during the isothermal oxidation of Al-rich $NbAl_3$ in air at 800°C.

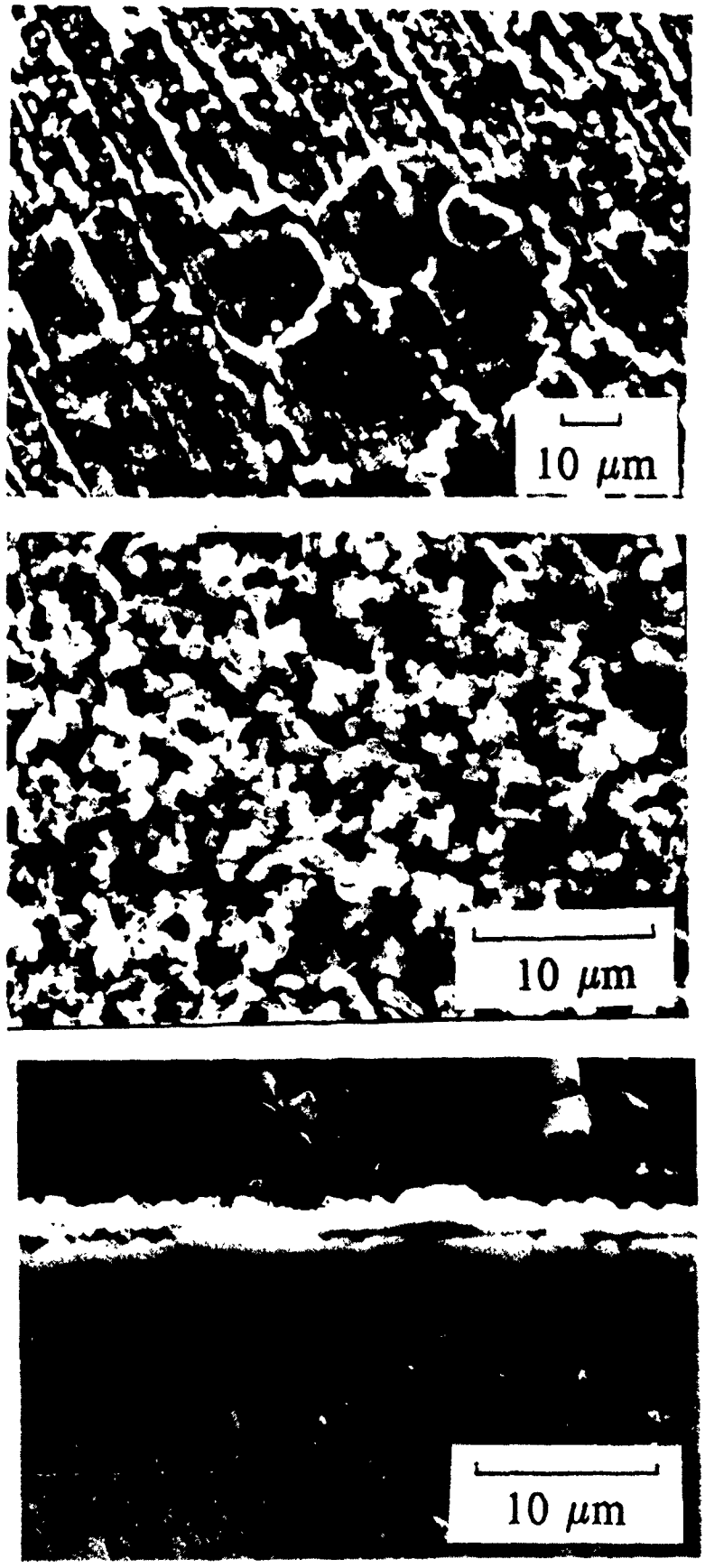

Figure 9. Surface and cross-section micrographs of the acoustic emission specimen from Fig. 8.

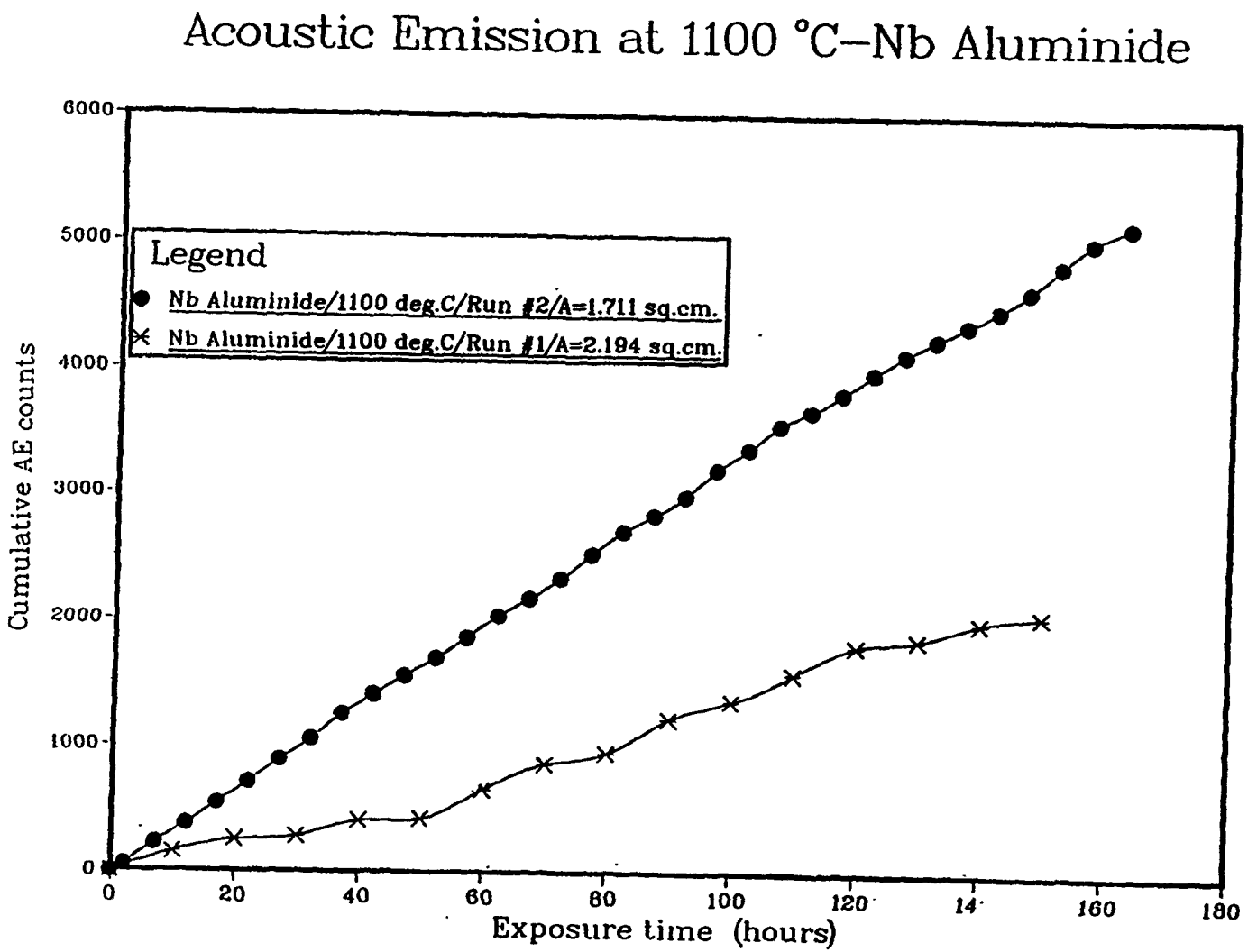

Figure 10. Acoustic emission data obtained during the isothermal oxidation of Al-rich $NbAl_3$ in air at 1100°C.

Figure 11. Cross-section of $NbAl_3$ after 168 hrs. oxidation at 1100°C showing the development of a layered scale of Al_2O_3 and $NbAlO_4$.

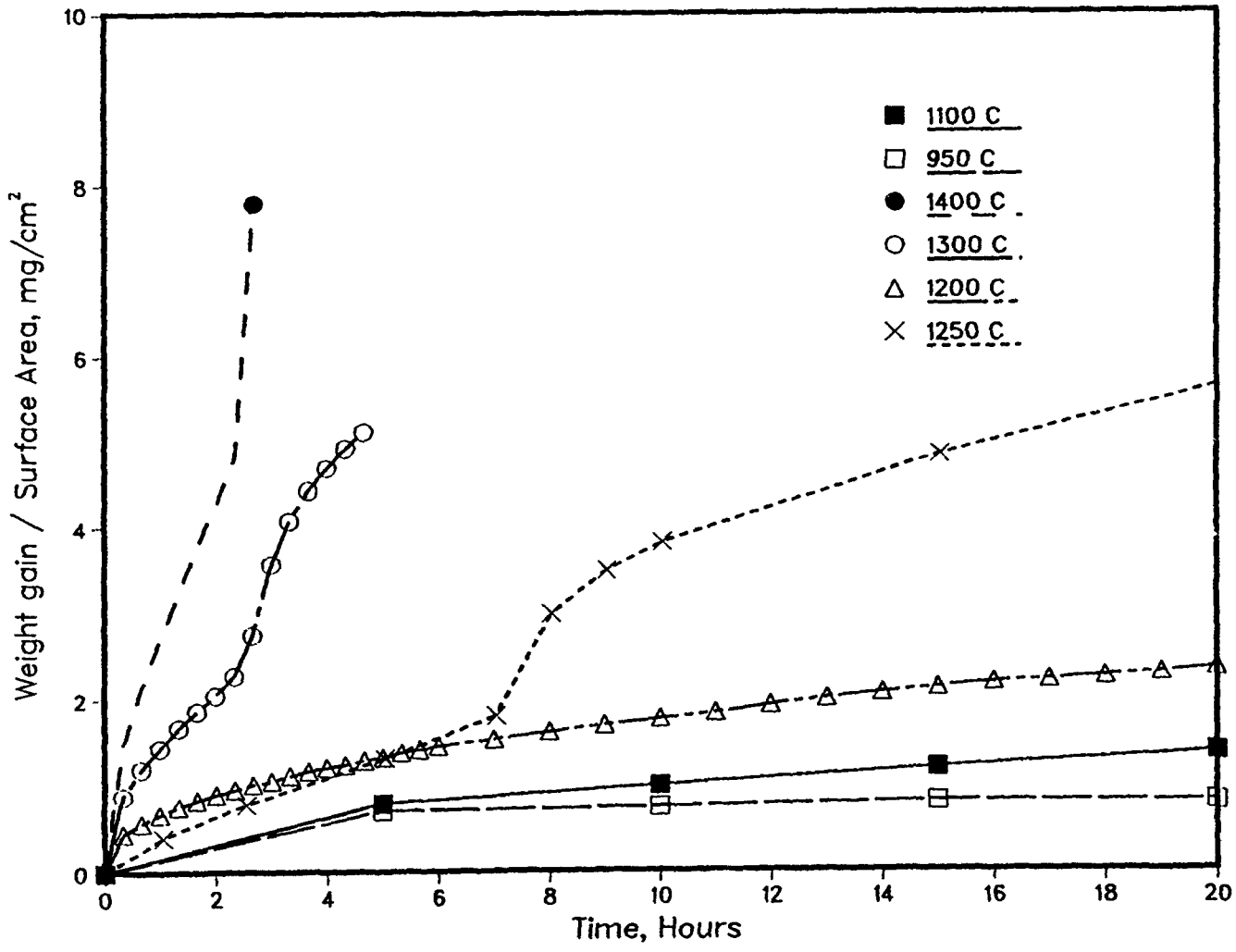

Figure 12: Oxidation of aluminum-rich $NbAl_3$ in O_2

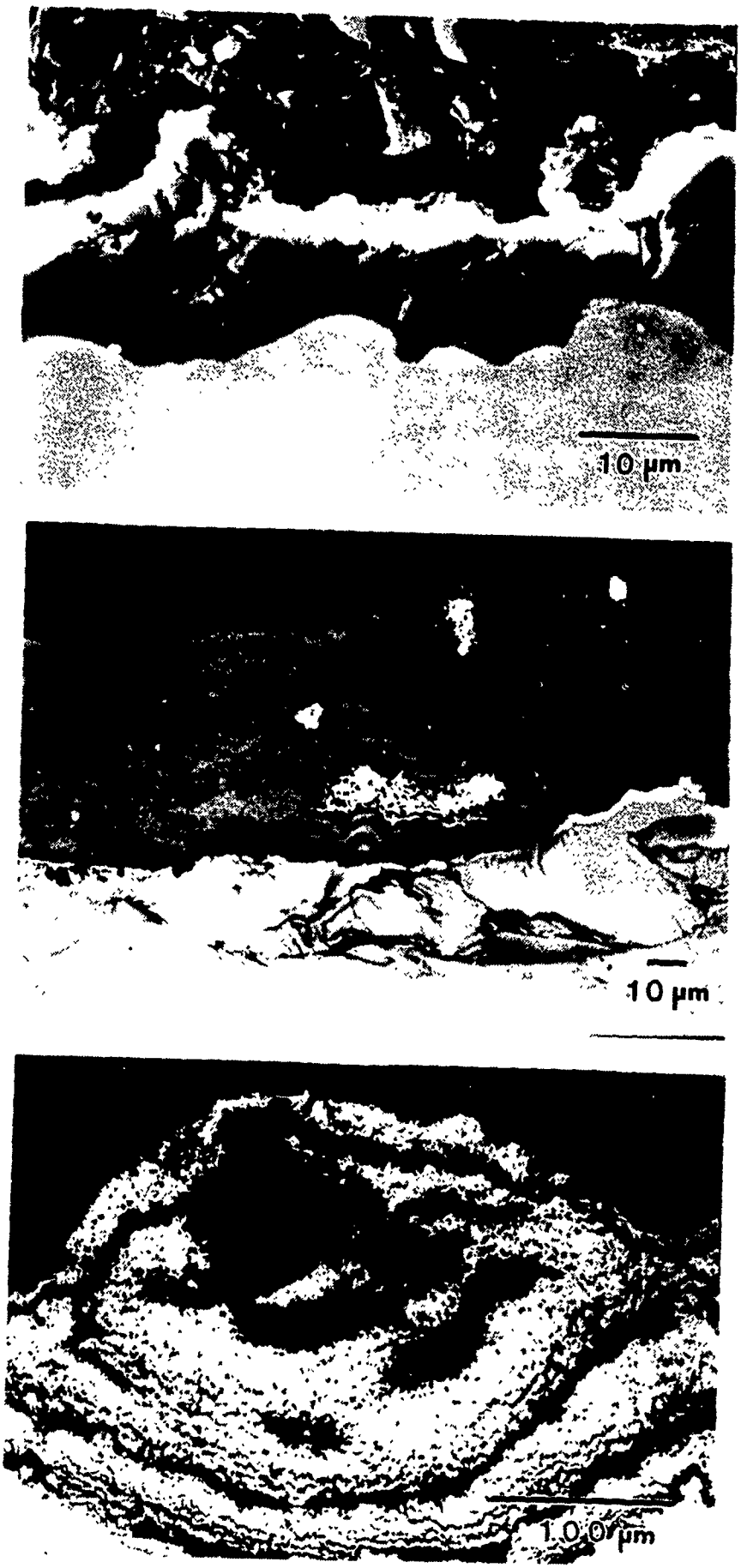

Figure 13. Oxidation of aluminum-rich $NbAl_3$, 1100-1400°C.
Top: 1200°C - predominantly Al_2O_3
Center, bottom: 1300,1400°C - both scales contain Al_2O_3 (dark) and Nb/Al oxide (light)

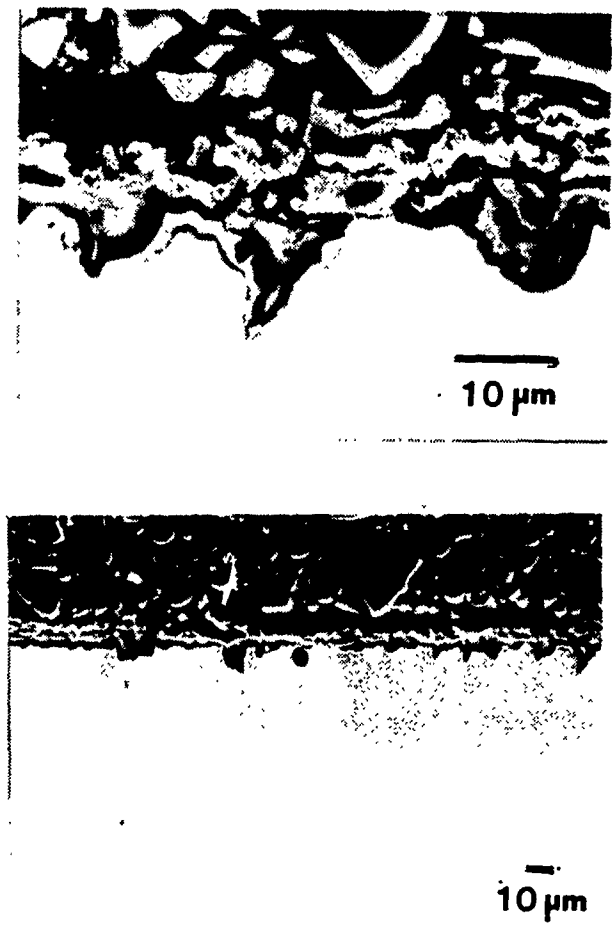

Figure 14: Secondary electron image of the cross-section of $NbAl_3$ after 24 hrs. oxidation at 1100°C (top) showing preferential attack of Nb_2Al at grain boundaries. Backscatterred electron image showing alumina between an outer $NbAlO_4$ and inner Nb_2Al layer.

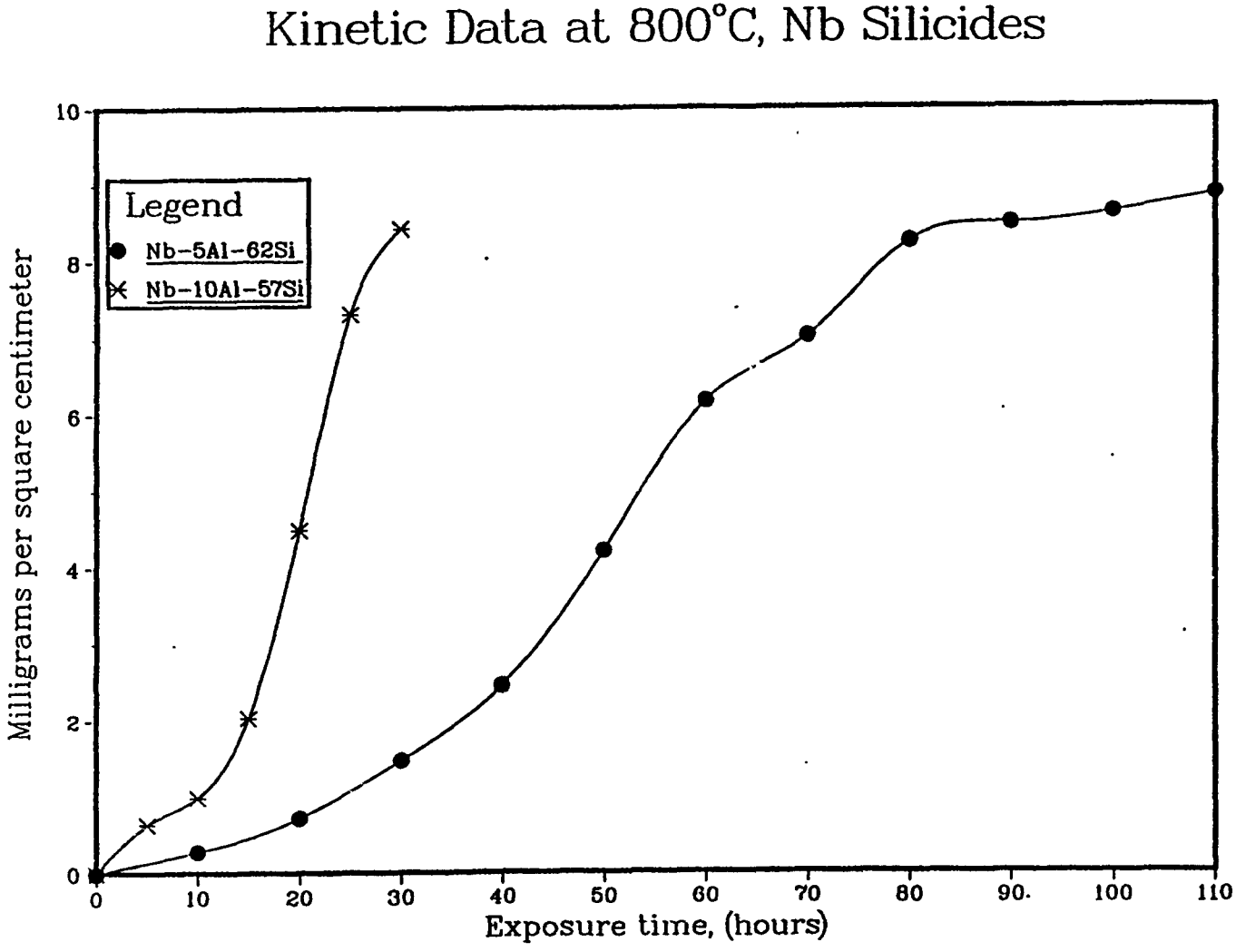

Figure 15. Weight change versus time data for Al-modified $NbSi_2$ oxidized in oxygen at 800°C.

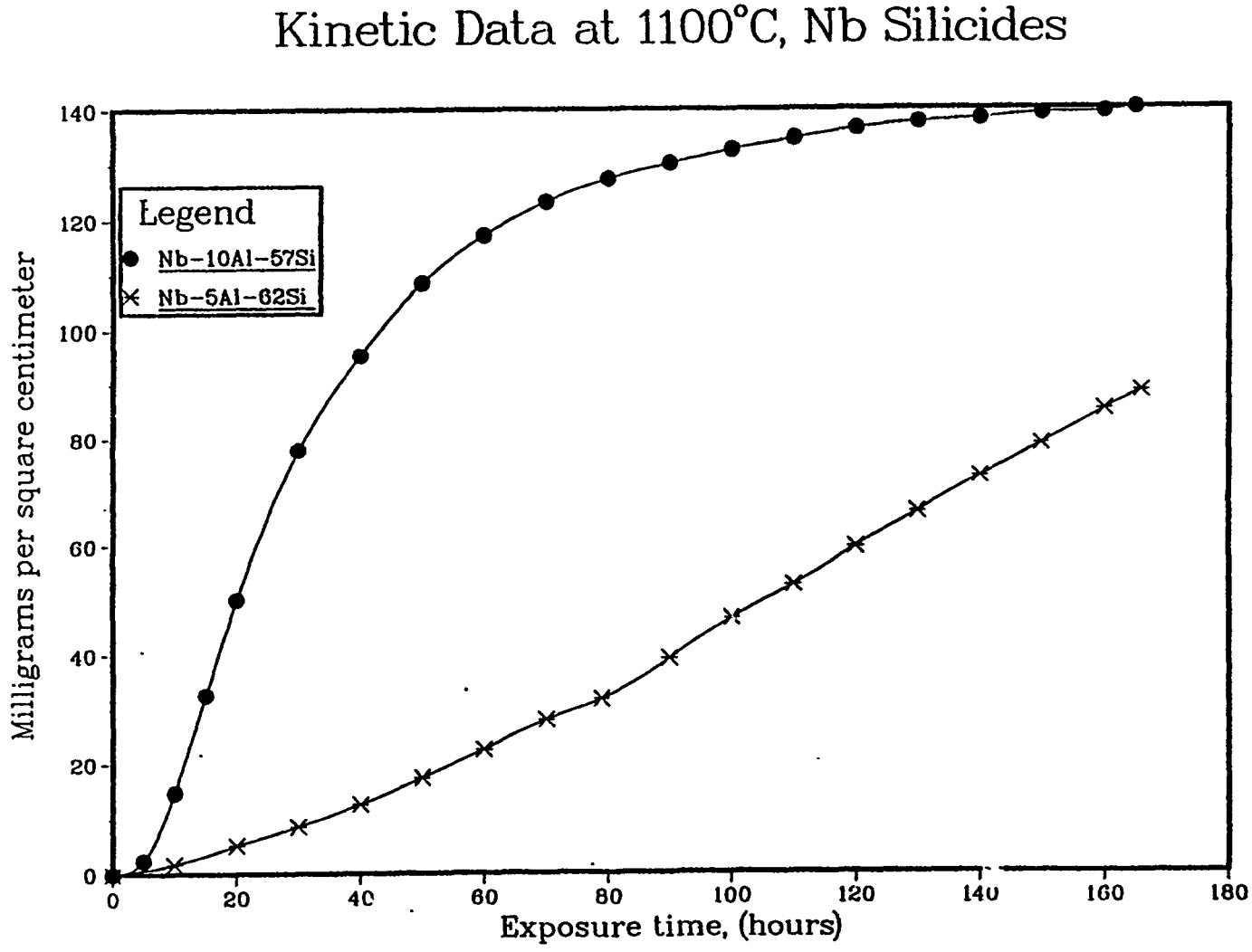

Figure 16. **Weight change versus time data for Al-modified $NbSi_2$ oxidized in oxygen at 1100°C.**

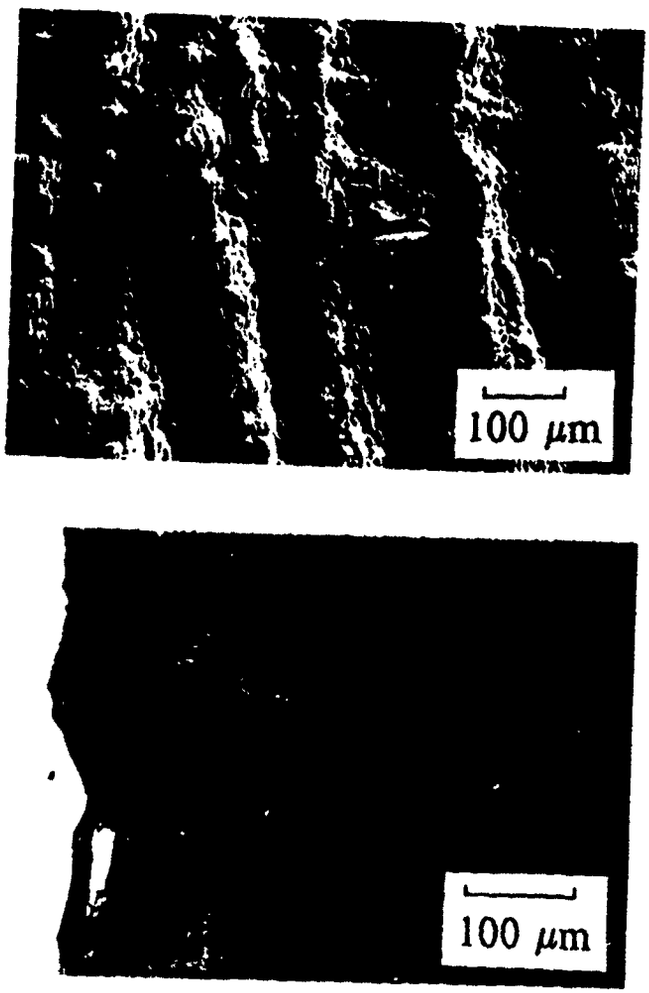

Figure 17. Surface and cross-section micrographs of Nb-5Al-62Si oxidized in oxygen at 1100°C.

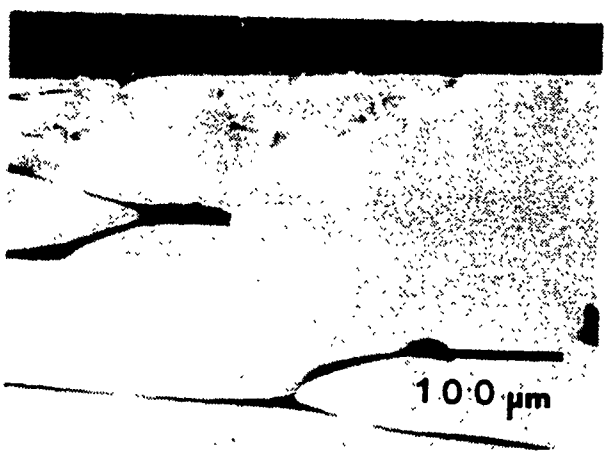

Figure 18. Initial microstructure of $TaSi_2$ (dark phase is elemental Si).

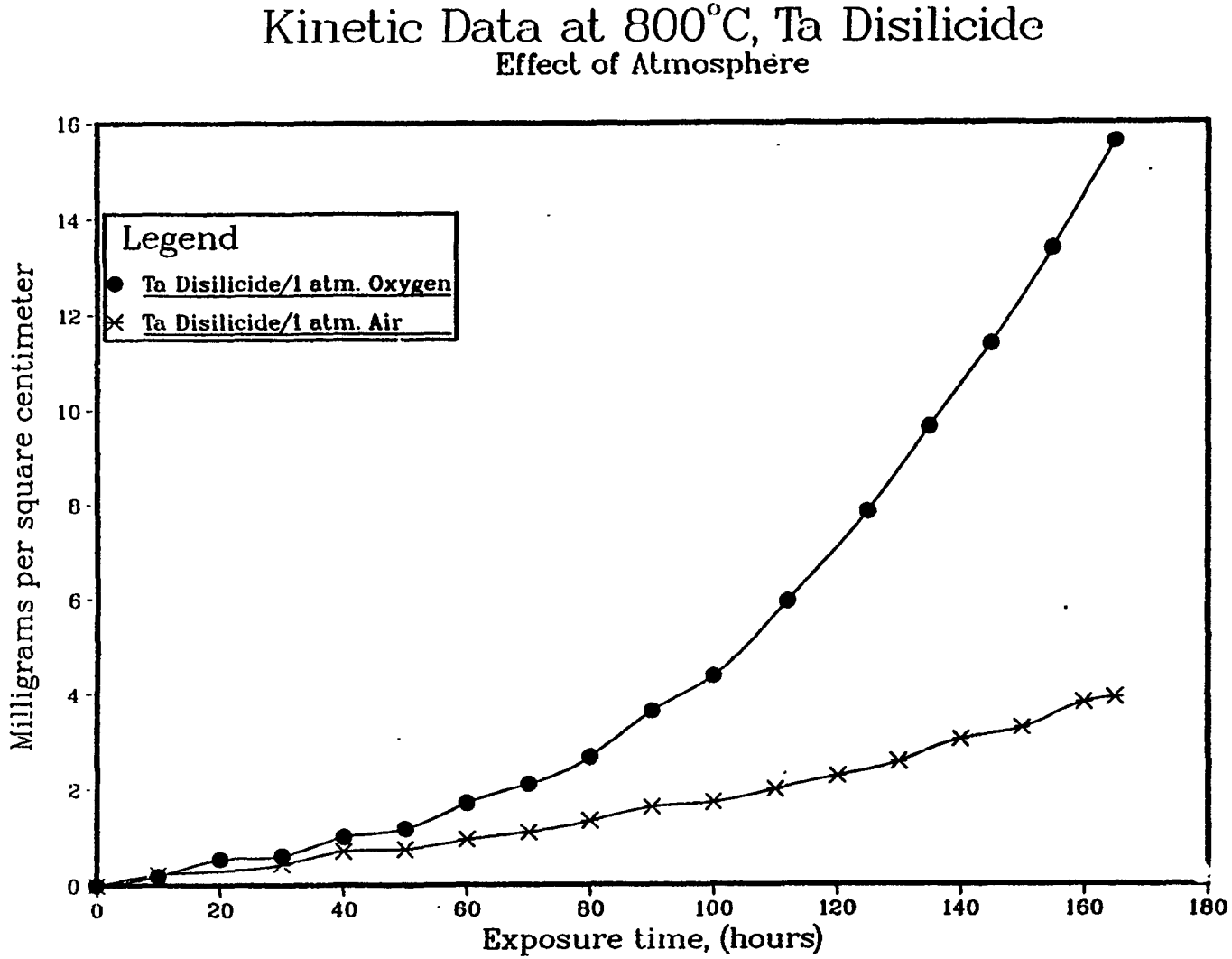

Figure 19. **Weight change versus time data for $TaSi_2$ oxidized in air and oxygen at 800°C.**

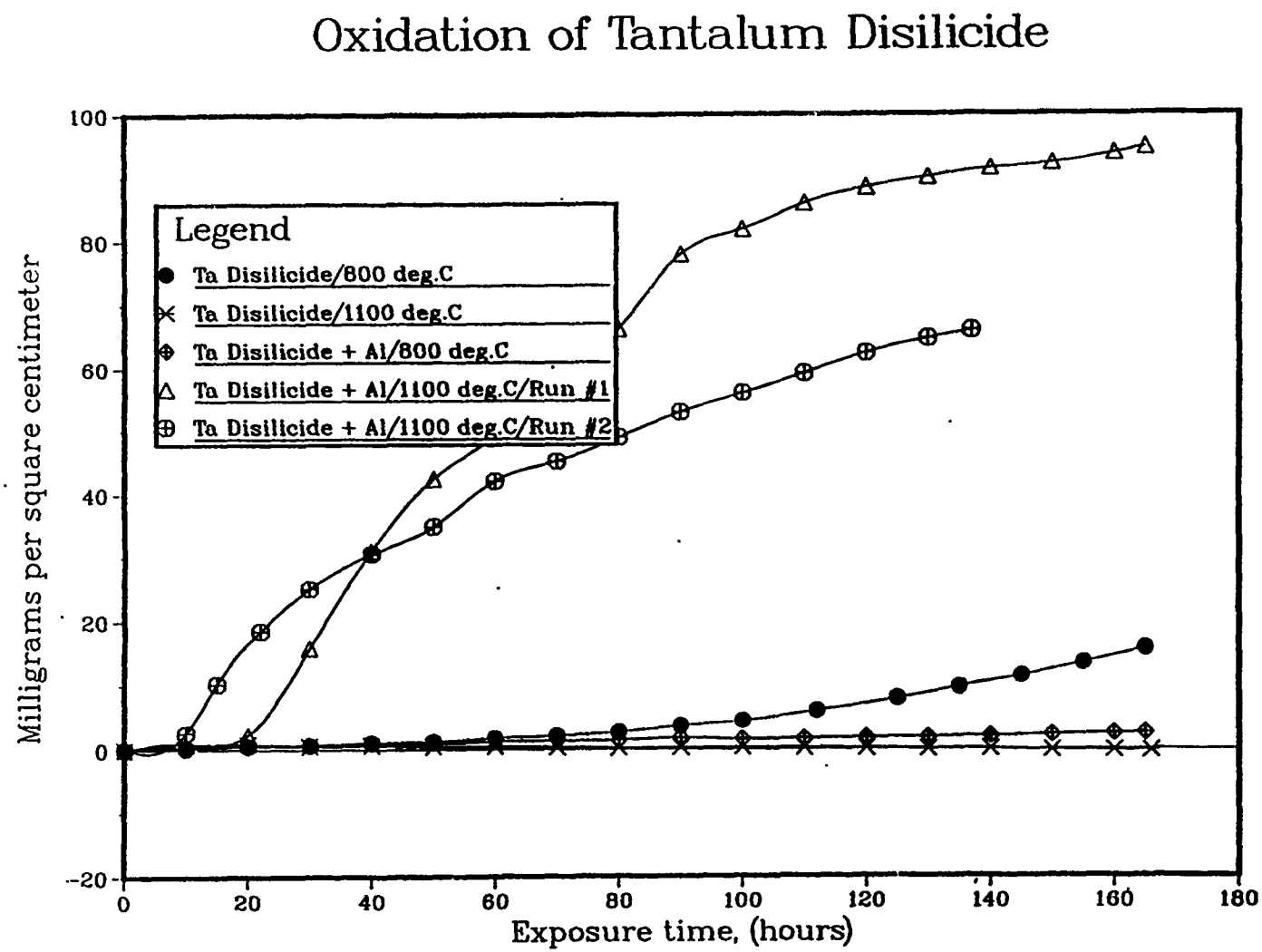

Figure 20. **Weight change versus time data for $TaSi_2$ and Al-modified $TaSi_2$ oxidized in oxygen at 800 and 1100°C.**

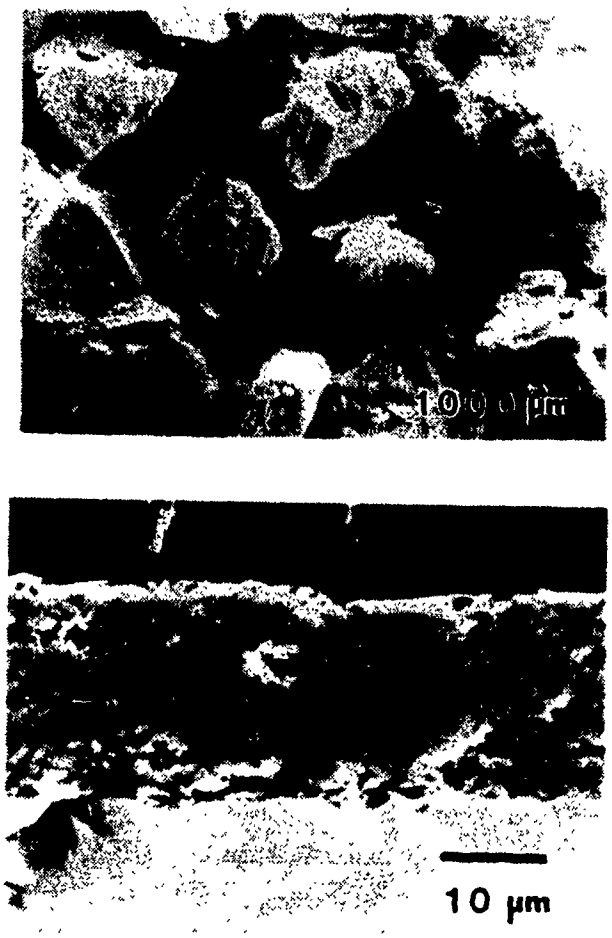

Figure 21. Surface (top) and cross-section (bottom) of $TaSi_2$ after 168 hrs oxidation at 800°C. The lighter phase is Ta_2O_5 and the dark phase is SiO_2.

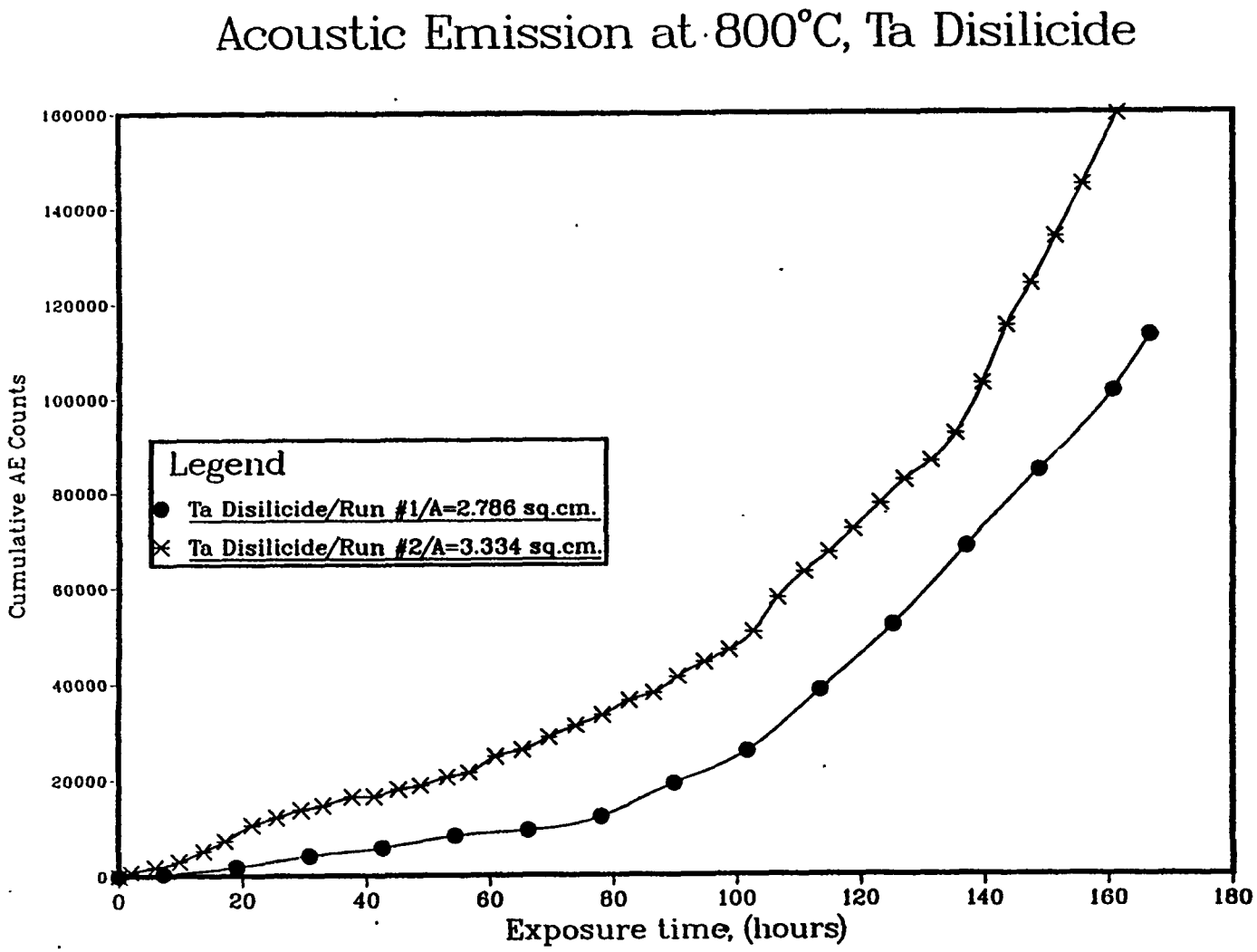

Figure 22: **Acoustic emission data obtained during the oxidation of $TaSi_2$ in air at 800°C.**

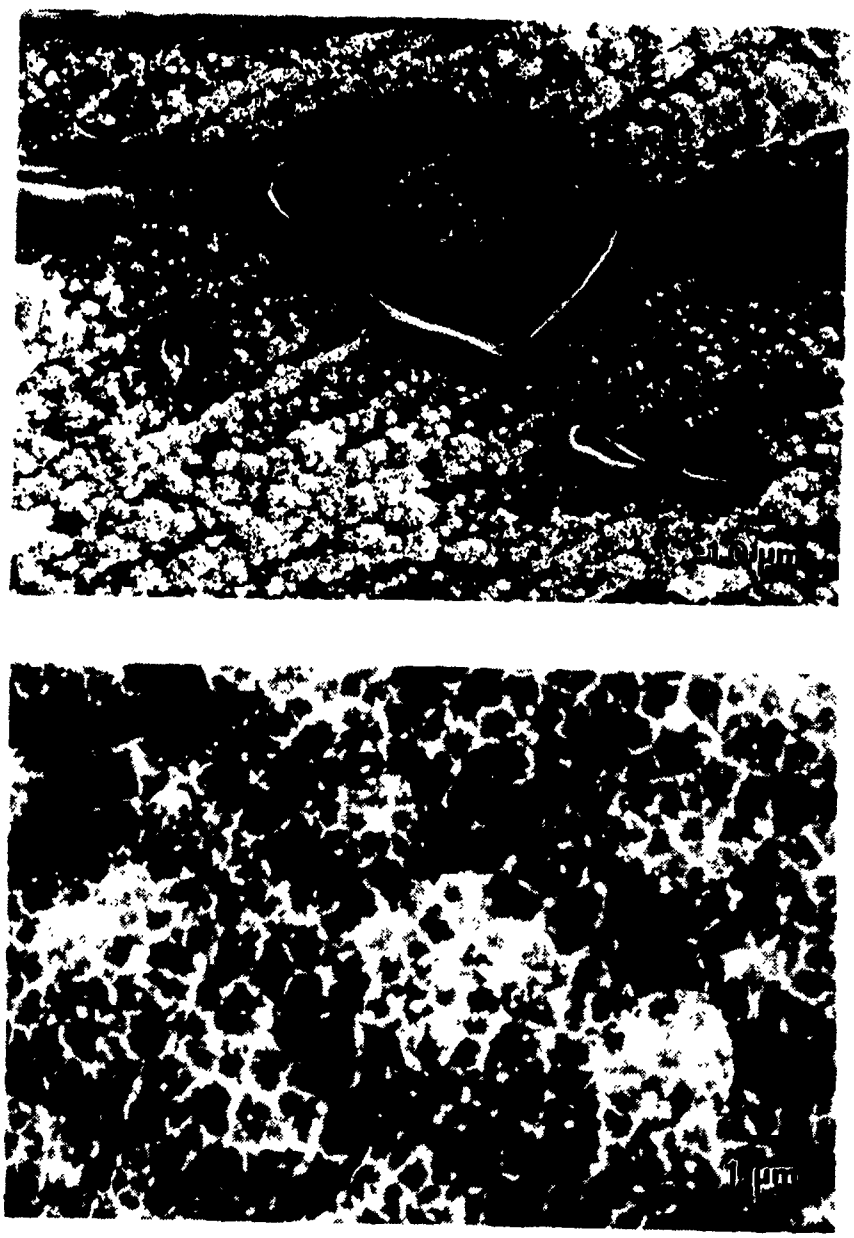

Figure 23. $TaSi_2$ oxidized at 1100°C for 168 hrs. in oxygen Top and bottom: Surface morphology consists of silica (dark) and Ta_2O_5 (light)

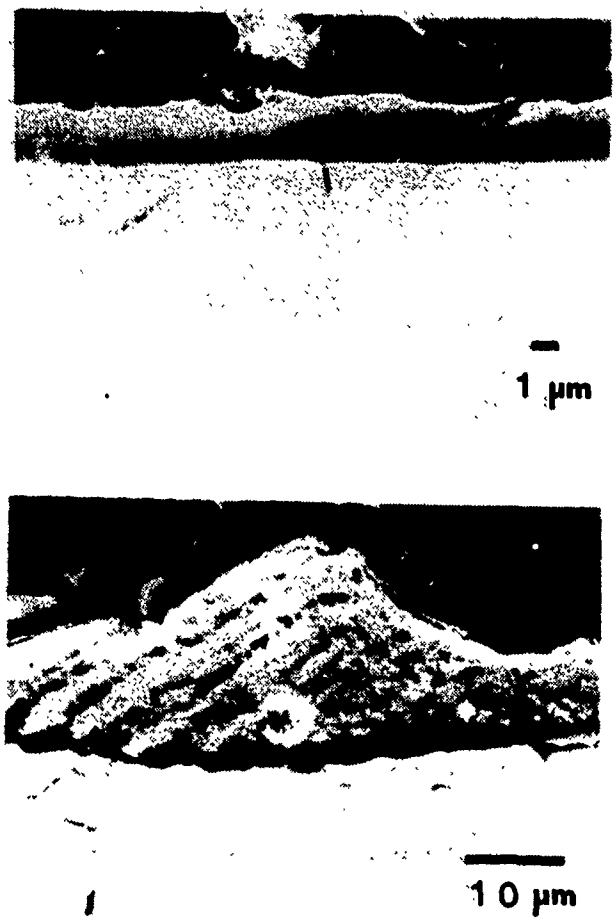

Figure 24. Cross-sections of $TaSi_2$ oxidized 168 hrs. at 1100°C showing exclusive formation of a silica film over some areas (top) and Ta-rich nodules over others (bottom).

Oxidation Behavior of γ-TiAl

by

G. H. Meier and F. S. Pettit
Materials Science and Engineering Department
University of Pittsburgh
Pittsburgh, PA 15261

Abstract

The oxidation behavior of γ-TiAl has been studied in the temperature range 750 to 1100°C for aluminum contents which essentially cover the homogeneity range of TiAl (50 to 56 at % Al). Exposures were carried out in pure oxygen and various oxygen-nitrogen mixtures. The oxidation behavior was found to depend on temperature, aluminum content, and the composition of the oxidizing gas. Protective alumina scales formed in pure oxygen up to a critical temperature above which scales consisting primarily of intermixed TiO_2 and Al_2O_3 were formed and oxidation rates accelerated dramatically. This critical temperature was found to increase with increasing aluminum content in the TiAl. Continuous alumina scales were not observed at any temperature when nitrogen was present in the oxidizing gas. The mechanism whereby nitrogen produces this effect was not completely defined but was shown to be associated with the initial development of the reaction product.

Introduction

Alloys in the Ti-Al system are of interest for high temperature systems such as aircraft engines because they have low density and, in the case of the ordered phases, substantial high temperature strengths. However, the resistance of these alloys to oxidation and interstitial embrittlement is a concern. Those alloys which form alumina scales have

excellent resistance while those which form titania-rich scales oxidize at rates which are unacceptably fast for most applications. The alloys based on γ-TiAl are generally regarded as having potentially better oxidation resistance than those based on α_2-Ti_3Al. The oxidation behavior of γ-TiAl is the subject of this paper.

Oxidation of γ-TiAl

Choudhury et al.[1] studied the oxidation of TiAl, having a nominal composition of Ti-36 w/o Al (50 at% Al), in oxygen and air over the temperature range 800 - 1200°C. Specimens were either cut from cast ingots or were obtained from the extrusion of pre-alloyed rotating-electrode-process powders. Results obtained for the cast specimens indicated a dependence on both surface preparation and the oxidizing atmosphere. Samples abraded through 120 grit SiC exhibited kp values in the range of 10^{-9} $g^2cm^{-4}hr^{-1}$ when oxidized in O_2 at 950°C. Polished samples, on the other hand, exhibited kp values of about 10^{-5} to 10^{-6} $g^2cm^{-4}hr^{-1}$ under the same conditions. XRD analysis of the oxides indicated Al_2O_3 as the major constituent and TiO_2 as a minor phase in the first case while TiO_2 was found to form an external scale with a subscale of mixed Al_2O_3-TiO_2 in the latter. In addition, a Ti_3Al layer was observed between the oxide and the alloy. Extruded samples, oxidized under similar conditions, displayed alumina forming kinetics regardless of surface preparation. Choudhury et al. explained the behavioral difference in terms of macroinhomogeneities in the cast structure which were absent in the extruded samples. Abrasion of the surface, in the case of the cast specimens, may assist in the interdiffusional process, thus eliminating the in-homogeneities more rapidly than is the case for the polished samples.

Oxidation behavior in air at 950°C was found to be independent of sample preparation for both the cast and extruded samples with titania-forming kinetics (kp about 10^{-5} - 10^{-6} $g^2cm^{-4}hr^{-1}$) observed in all cases. In addition, it was found that the oxide consisted of two layers; an outer layer, which tended to spall readily at low temperatures, and an adherent subscale. Further analysis of the oxide revealed a phase distribution similar to that for the cast and polished sample oxidized in O_2 at 950°C.

Oxidation kinetics for all alloys, regardless of surface preparation, at 1100 and 1200°C indicated TiO_2 formation, with mixed TiO_2-Al_2O_3 formation observed for oxidation at 800°C in air. The transition from titania to alumina forming kinetics as a function of decreasing temperature was determined to occur at a higher value when the tests were conducted in an oxygen atmosphere with internal oxidation noted at the two higher temperatures.

The influence of alloying elements on the oxidation behavior of the base alloy revealed that Nb and W aided in promoting the growth of Al_2O_3 while Y and Ga favored TiO_2 formation.

Choudhury et al. conducted experiments to determine the species responsible for the differing behavior of the samples as a function of oxidizing atmosphere. It was determined that CO, CO_2 and water-vapor impurities were not responsible. In addition, they eliminated the compositional differences in O_2 that exist between the two atmospheres. They concluded that N_2 was responsible for the increased rate of oxidation although no nitrogen containing phases were identified in the scale or substrate. Further experimentation revealed a time dependent increase in the oxidation rates for pre-oxidized samples subsequently oxidized in air at 950°C. The role of N_2 in this process was found to be related to the breakdown of the protective scale, thus allowing for the increased oxidation of the underlying phase, Ti_3Al.

Although the actual mechanism by which N_2 partakes in the oxidation process was not determined, several possible mechanisms were advanced including:

1) N_2 doping of an initial TiO_2 scale resulting in more rapid oxygen transport to the scale/Ti_3Al interface such that the egress of Al cannot compensate, resulting in the absence of continuous alumina formation.
2) The grain boundary diffusion of N_2 through the oxide to form AlN or possibly AlON at the scale/Ti_3Al interface. This depletion of Al at the interface likewise hinders alumina formation and leads to increased rates of oxidation due to titania formation. To date, no indication of AlN or AlON has been observed in the resulting oxides.
3) N_2 grain boundary diffusion through the scale to the scale/Ti_3Al interface with a subsequent stabilization of the Ti_3Al layer with the reduced Al activity at the interface promoting the growth of TiO_2. As the oxidation process continues, the growth of the Ti_3Al layer is controlled, on the one hand, by Ti_3Al oxidation at the scale/Ti_3Al interface and, on the other hand, by the rate determining flux of either Al diffusing from the Ti_3Al/alloy interface and undergoing oxidation at the scale/Ti_3Al interface or the N_2 flux arriving at the Ti_3Al/alloy interface.

Lee and Waldman[2] recently reported that a Ti-32.4wt%Al alloy formed a layered scale in air above 1000°C and internal oxidation above 1100°C. Mendiratta and Choudhury[3] reported that varying the Al-content of TiAl (36, 38.7, and 40 wt %;50, 53, and 54 at %) did not affect the oxidation behavior.

Experimental

A series of tungsten arc-melted Ti-Al alloys with Al contents from 36 to 42 wt%Al (50 to 56 at%Al) was studied. In some cases the alloys were exposed in the as-cast condition and in others they were annealed for 24 hours at 1150°C in Ar and furnace cooled. No effect of heat treatment was observed on the oxidation behavior. Therefore, the data will be presented without specifying heat treatment. All specimens were polished through 600 grit SiC. Oxidation experiments were carried out in pure O_2, air, tank argon containing oxygen impurities at $p_{O_2} \approx 10^{-4}$ atm, and various oxygen-nitrogen mixtures at temperatures

from 750 to 1100°C. The oxidation kinetics were studied using a Cahn Model 2000 microbalance and the oxidation morphologies were studied using x-ray diffraction (XRD), scanning electron microscopy, and energy-and wavelength dispersive x-ray analysis (EDS and WDS).

Results and Discussion

Thermodynamics

An important aspect of the oxidation of Ti-Al alloys is the relatively small difference in standard free energy of formation between alumina and the oxides of titanium which is accentuated by the negative deviation from ideal solution behavior in the Ti-Al system. This is illustrated in Figure 1 which plots estimated aluminum activities versus composition in titanium-aluminum alloys at 1100K. It is seen that the aluminum activity is much smaller than unity in the compounds of practical interest, Ti_3Al and TiAl. In fact, combining these activities with estimated titanium activities and standard free energy data for the oxides indicates that TiO is more stable in contact with the alloy than is Al_2O_3 for atom fractions of Al less than about 0.5. More detailed analyses of this situation are presented by Rahmel and Spencer[4] and Luthra[5]. The alloys in this study have Al concentrations high enough that Al_2O_3 should be stable in contact with the alloy at 1100K. However, the Al_2O_3 is only marginally more stable than TiO so any factor which lowers the activity of Al (such as depletion in forming a surface oxide) can make TiO become the oxide which is stable in contact with the alloy.

Effects of Temperature

Weight change data for Ti-40wt%Al (54 at %Al) are compared in Figure 2 for exposures in air and in oxygen at a number of temperatures. In both atmospheres the weight gains are low at lower temperatures and then increase drastically over a narrow range of temperatures. For exposure in air relatively large weight gains are evident at 800°C and above whereas in oxygen the large weight gains are only observed for exposure temperatures above 950°C. Such results indicate that this alloy is forming protective Al_2O_3 scales for those conditions where the small weight gains were evident. Examination of the surface morphologies of the specimens exposed in air, even at temperatures as low as 750°C, indicated continuous and protective scales of Al_2O_3 were not developed, Figure 3. Moreover at temperatures of 850°C and above relatively thick scales, containing substantial amounts of TiO_2, were apparent, Figure 4. In the case of exposure to oxygen, only an Al_2O_3 scale was evident below about 950°C, Figure 5. However, at temperatures above 950°C nodules of TiO_2 started to form on the surface with their area density increasing as oxidation temperature was increased, Figure 5, and by 1000°C these areas covered virtually the entire alloy surface. Cross-sections through these nodules, Figure 6, indicated the scale morphology was essentially the same as that formed in air.

In Figure 7 parabolic rate constants for the growth of Al_2O_3 and TiO_3 scales are presented as a function of reciprocal temperature. The rate constants for oxidation of Ti-40wt%Al are also included along with data from the literature for similar alloys. The data confirms that Ti-40Al is not an Al_2O_3-former above 950°C in oxygen. Furthermore, it may not be an Al_2O_3-former when exposed in air at any of the oxidation temperatures studied here. In the Ni-Al system a transition from nonprotective to protective alumina scales was

observed as temperature was increased[6]. Evidently, in that system, the relative diffusion rates of aluminum to the alloy surface and the diffusion of oxygen into the alloy can change with temperature such that protective Al_2O_3 is formed at higher temperatures. However, in the case of TiAl in oxygen the transition goes from protective to nonprotective behavior as temperature is increased. The differences between the two cases is that Al_2O_3 is much more stable than NiO. In the Ni-Al case the transition from protective to nonprotective behavior involves the formation of internal aluminum oxide particles, which is controlled by diffusion processes. The transition from protective to nonprotective behavior for TiAl involves the transition from an external alumina scale to an external mixed alumina + titania scale which is controlled by thermodynamic factors and, probably, the rate of transient oxidation. Table 1 indicates the values calculated by Rahmel and Spencer[8] for activities of Ti and Al at the $Ti_3Al/TiAl$ and $TiAl/TiAl_3$ phase boundaries over the temperature range 700° to 900°C along with the oxygen partial pressures for equilibria between the alloys and both TiO and Al_2O_3. It is seen that the calculated oxygen pressures indicate that TiO is more stable than Al_2O_3 in contact with TiAl at the low Al side of the phase field for all three temperatures. At the high Al side Al_2O_3 is more stable at 700 and 900°C while at 1100°C the p_{O_2}'s for TiO and Al_2O_3 formation are virtually the same. The reliability of the thermodynamic data used to calculate the activities in the various phases is open to question. In addition the high Al side of the TiAl field stands in equilibrium with $TiAl_2$ rather than $TiAl_3$ (Figure 1). Nevertheless these data indicate that, for a given Al concentration in TiAl, the stability of TiO, relative to Al_2O_3, increases as temperature increases. In addition the growth rate of the Ti-oxides increases with temperature so that, once nucleated, they can prevent continuous alumina from forming.

Effect of Al-Content

Figure 8 presents the parabolic rate constants versus reciprocal temperature for TiAl with three different Al concentrations 36, 39, and 42 wt% Al (50, 53, and 56 at %Al) which span the range of stoichiometry of TiAl[7]. The alloys formed continuous alumina in oxygen at 800°C with the Ti-56 at % alloy continuing this behavior up to 1000°C before undergoing the transition to rapidly growing, mixed oxide scales. As a result the rate constant for this alloy increases by six orders-of-magnitude between 1000° and 1100°C. The lower the Al content the lower is the temperature at which the transition to nonprotective scale formation occurs. This behavior is consistent with the discussion in the previous section regarding the relative thermodynamic stabilities of TiO and Al_2O_3.

Effects of Atmosphere

Figure 8 indicates that alloys with any Al content oxidize at the same rate in air (solid point). Figure 9 shows weight gain versus time data for Ti-52 at% Al exposed in various atmospheres at 900° C. The specimen exposed in oxygen forms a continuous alumina scale and exhibits a correspondingly slow oxidation rate. However, adding 10%N_2 to the oxygen results in an almost ten-fold increase in the oxidation rate. Larger additions of N_2 result in still more rapid oxidation kinetics. Figure 10 shows the cross-section of a specimen exposed in O_2-10%N_2. It is seen that the nitrogen has resulted in the formation of areas where the alumina is not continuous which leads to the formation of a rapidly growing mixed oxide scale. This rapid growth gives rise to the same type of nodules observed in pure oxygen at higher temperatures. The cross-section of the specimen exposed at air (O_2-80%N_2), Figure 11 shows that the area density of the nodules is increased by the higher nitrogen

concentration in the gas and in O_2-90%N_2, Figure 12, the surface is entirely covered with the mixed oxide scale. Therefore, it appears that increasing the nitrogen concentration in the oxidizing gas at a fixed temperature has the same effect on the oxidation mechanism as increasing the temperature does for oxidation in pure oxygen. The detailed mechanism of the effect of nitrogen is in need of further study. However, it appears that the effect involves the nucleation and initial growth of the scale since preoxidation in pure oxygen develops an alumina scale which remains protective during subsequent exposures in air, Figure 9. Kobayashi, et al.[6] have reported that preformed alumina scales formed on TiAl at reduced pressure remain protective during subsequent exposures in air, even under cyclic conditions. During the initial stages of oxidation there may be a depletion of oxygen from the gas adjacent to the surfaces of specimens and nitrides may be formed.

Summary

The oxidation behavior of γ-TiAl has been found to depend on temperature, aluminum content, and the composition of the oxidizing gas. Protective alumina scales are formed in pure oxygen up to a critical temperature which increases as the aluminum content of the TiAl is increased. Above this temperature a mixed TiO_2/Al_2O_3 scale forms which grows at rates which are orders-of-magnitude faster than that of alumina. This phenomenon is believed to result from the increase in growth rate of TiO_2 as temperature increases which, coupled with the closeness in stability of alumina and the titanium oxides, prevents the alumina from becoming continuous. Continuous alumina scales were not observed at any temperature when nitrogen was present in the oxidizing gas. The effect of the nitrogen

needs further investigation but has been shown to be involved with the initial development of the reaction products.

References

1. N.S. Choudhury, H.C. Graham, and J.W. Hinze, "Oxidation Behavior of Titanium Aluminides", in Properties of High Temperature Alloys, Z.A. Foroulis and F.S. Pettit eds., The Electrochemical Society, 1976, p. 668.

2. E.U. Lee and J. Waldman,Scripta Met., 22, 1389 (1988).

3. Mendiratta, M.G., and Choudhury, N.S., "Properties and Microstructure of High-Temperature Materials", AFML-TR-78-112, Contract No. F33615-75-C-1005, (Systems Research Laboratories, Inc., Ohio, August 1978).

4. A. Rahmel and P. J. Spencer, "Thermodynamic Aspects of TiAl and $TiSi_2$ Oxidation, The Al-Ti-O and Si-Ti-O Phase Diagrams", Oxidation of Metals, 35, 53 (1991).

5. K. L. Luthra, "A Comparison of the Mechanisms of Oxidation of Ti- and Ni-Base Alloys", to appear in the Proceedings of a TMS/ASM Symposium on Environmental Effects on Advanced Materials, Detroit, MI, Oct., 1990.

6. F. S. Pettit,Trans. AIME, 239,1296 (1967).

7. Appalonia, D.S., "The Oxidation of Gamma-Titanium Aluminides", Bachelor of Science Thesis, University of Pittsburgh, Pittsburgh, PA (1988).

8. E. Kobayashi, M. Yoshihara, and R. Tanaka, High Temp. Tech., 8, 179 (1990).

Table 1

Activities in the Ti-Al System and Metal/Oxide Equilibrium Pressures
(after Rahmel and Spencer)

Phases	T(°C)	a_{Al}	p_{O_2} (Al/Al_2O_3 bar	a_{Ti}	p_{O_2} (Ti/TiO) bar
Ti_3Al-TiAl	700	6.4×10^{-4}	1.8×10^{-43}	0.475	2.2×10^{-47}
	900	5.0×10^{-3}	3.5×10^{-36}	0.495	2.0×10^{-39}
	1100	1.4×10^{-27}	1.4×10^{-27}	0.545	2.2×10^{-32}
TiAl-$TiAl_3$	700	0.14	1.4×10^{-47}	0.002	2.5×10^{-45}
	900	0.29	1.5×10^{-38}	0.010	5.0×10^{-35}
	1100	0.48	1.9×10^{-29}	0.025	1.0×10^{-29}

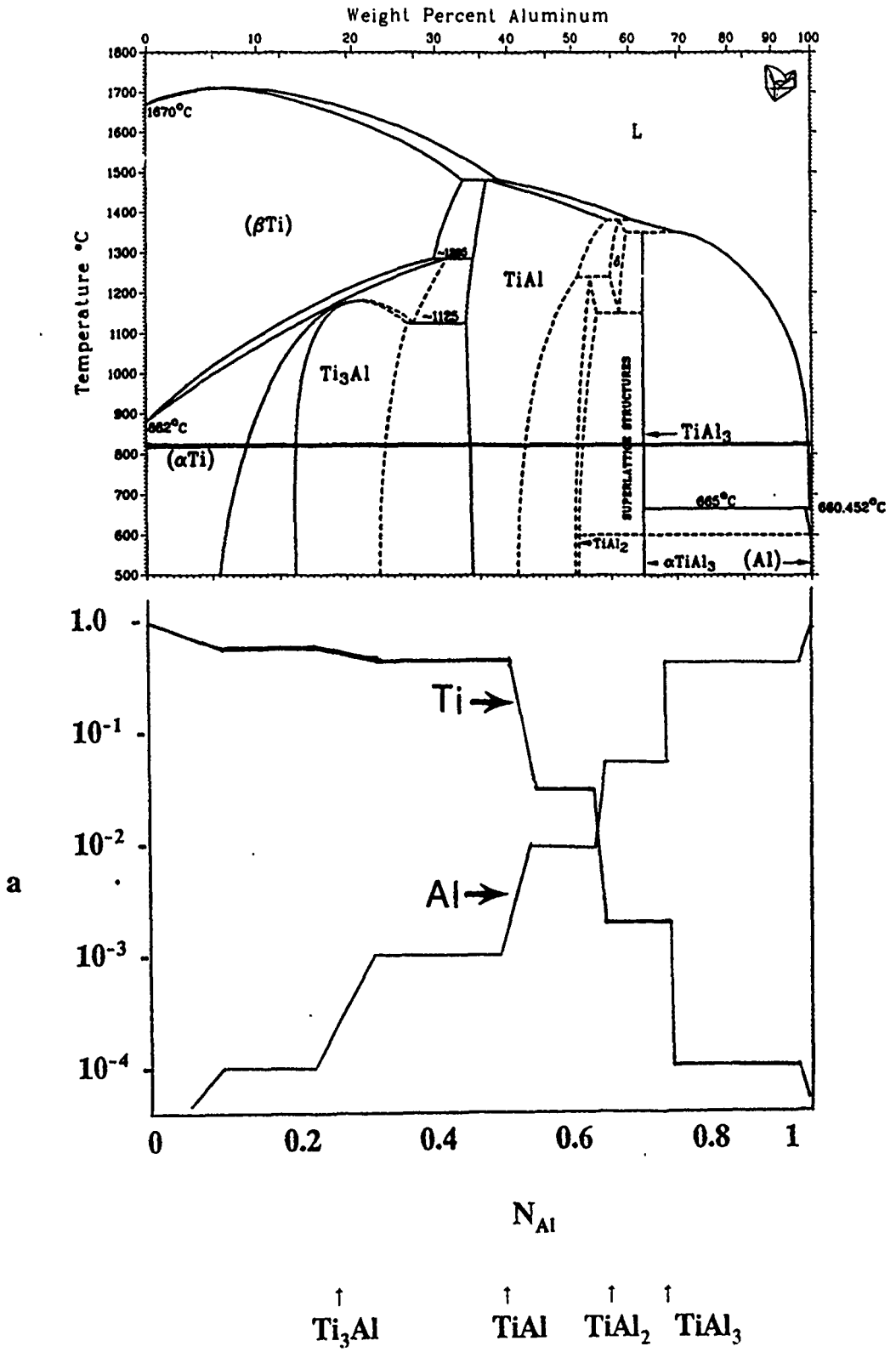

Figure 1. Published phase diagram for the Ti-Al system (top) and plot of calculated activities for Ti and Al versus atom fraction of Al at the indicated temperature (1100K).

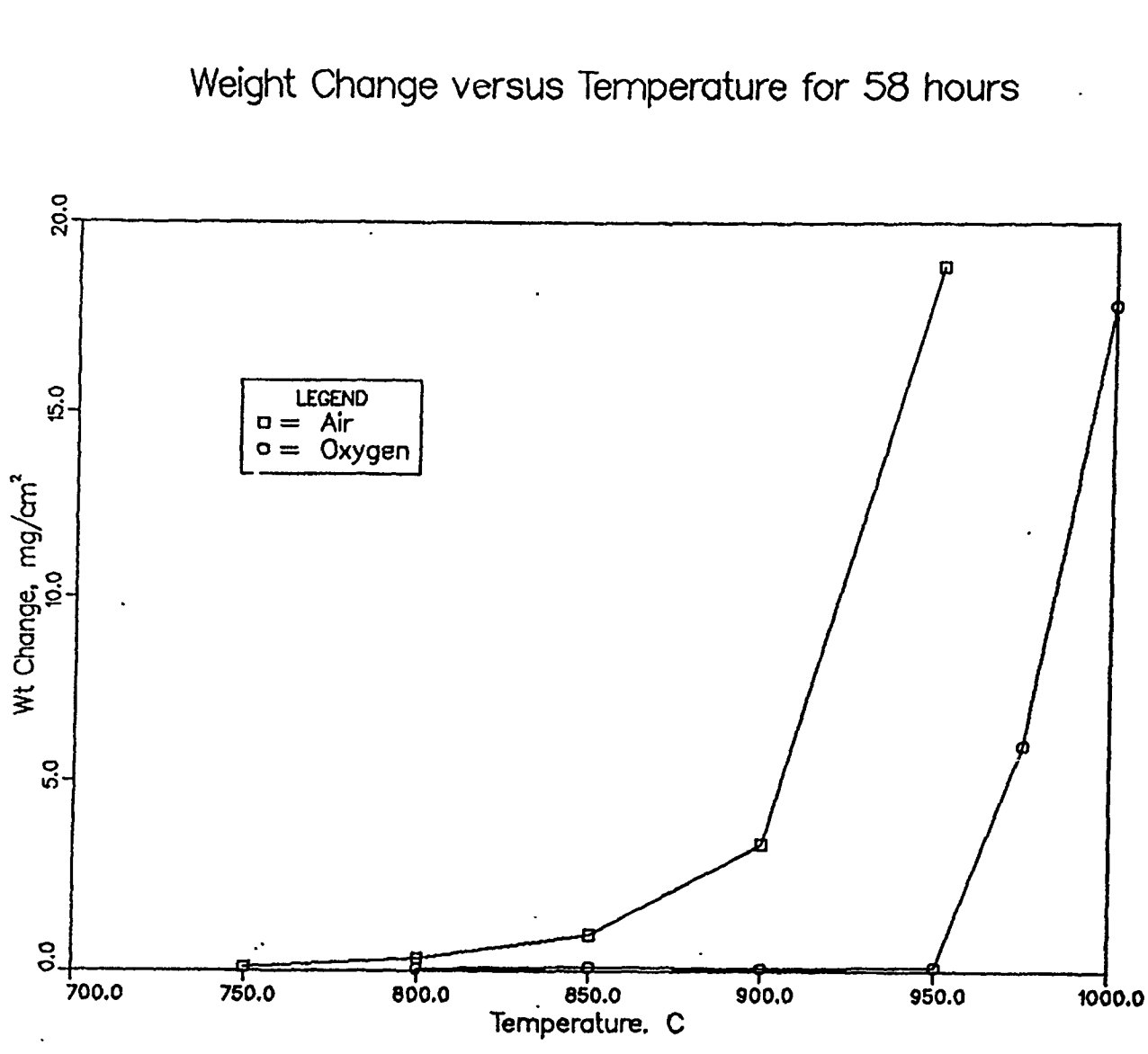

Figure 2. Weight change versus temperature for TiAl (54 at% Al) oxidized in air and oxygen for 58 hours.

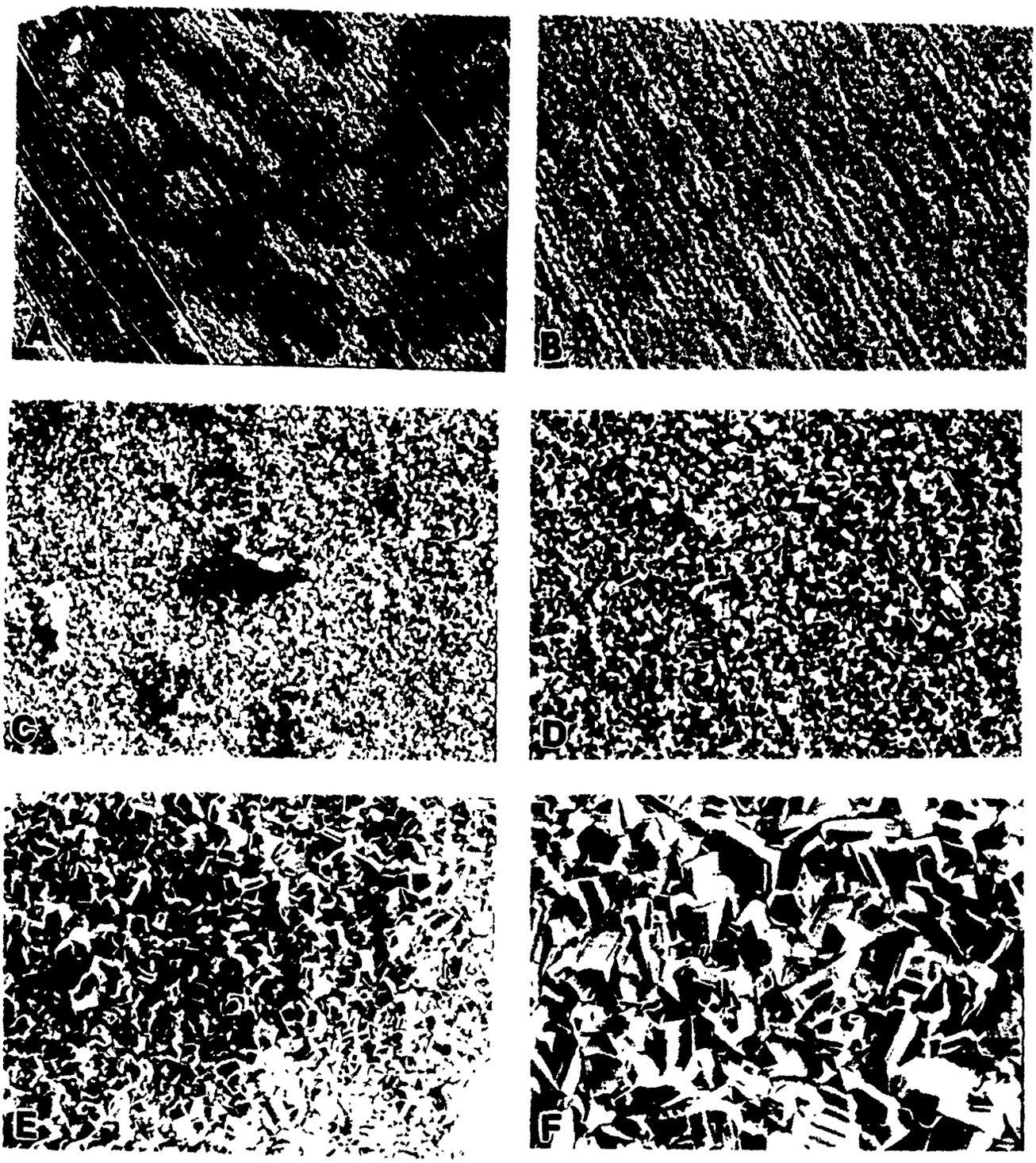

Figure 3. Surface morphologies of TiAl oxidized in air for 58 hrs. at (A) 750°C, (B) 775°C, (C) 800°C, (D) 850°C, (E) 900°C, and (F) 950°C.

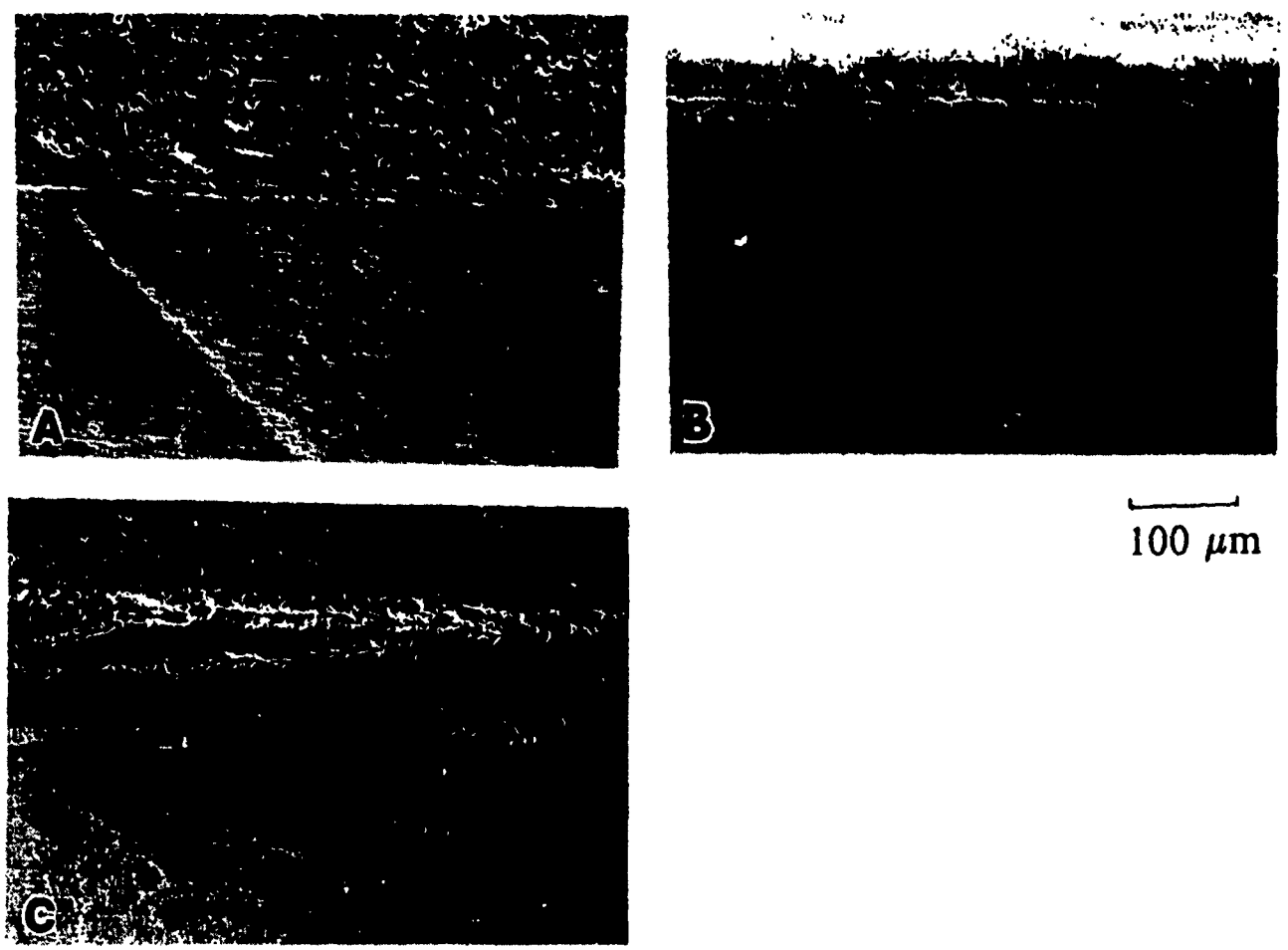

Figure 4. Cross-sections of TiAl oxidized for 58 hrs. in air at (A) 850°C, (B) 900°C, and (C) 950°C.

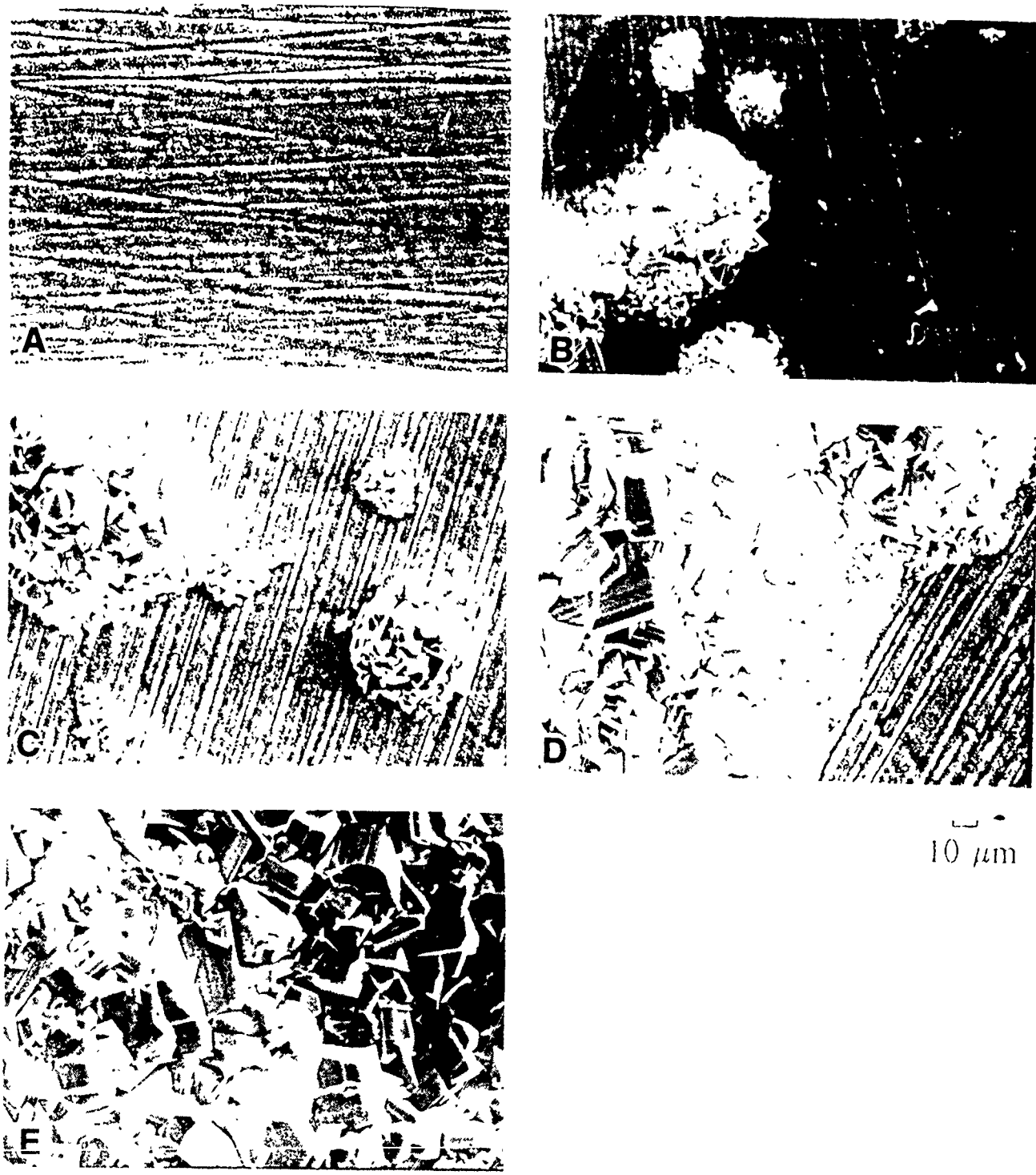

Figure 5. Surface morphologies of TiAl oxidized in oxygen for 24 hrs. at (A) 950 C, (B) 960 C, (C) 975 C, (D) 985 C, and 1000 C.

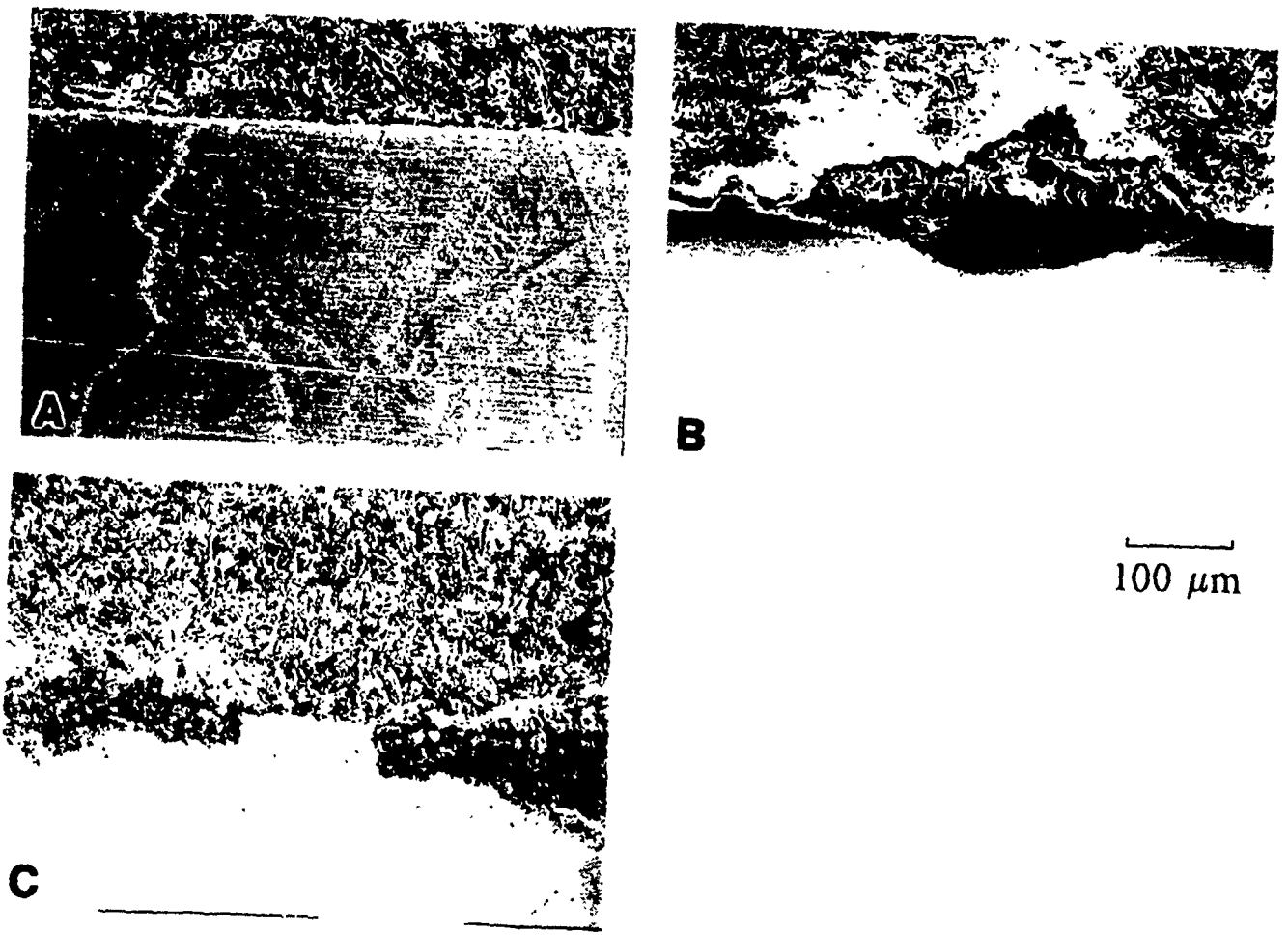

Figure 5. Cross-sections of TiAL oxidized for 58 hrs. in oxygen at (A) 950°C, (B) 975°C, and (C) 1000°C.

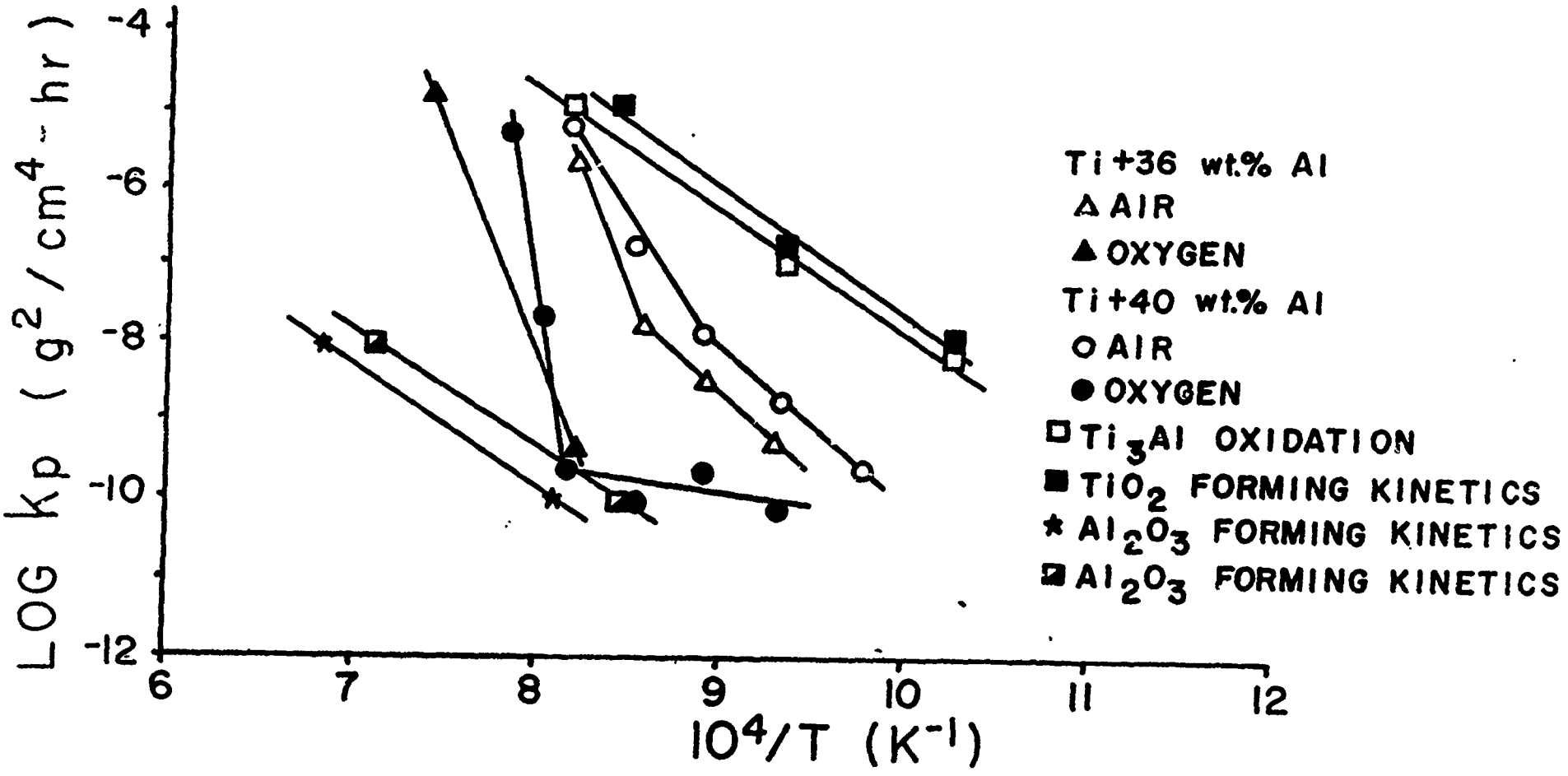

Figure 7. Arrhenius plot of the parabolic rate constants for various compositions of TiAl in both air and oxygen. The rate constants expected for growth of TiO_2 and Al_2O_3 are shown for comparison.

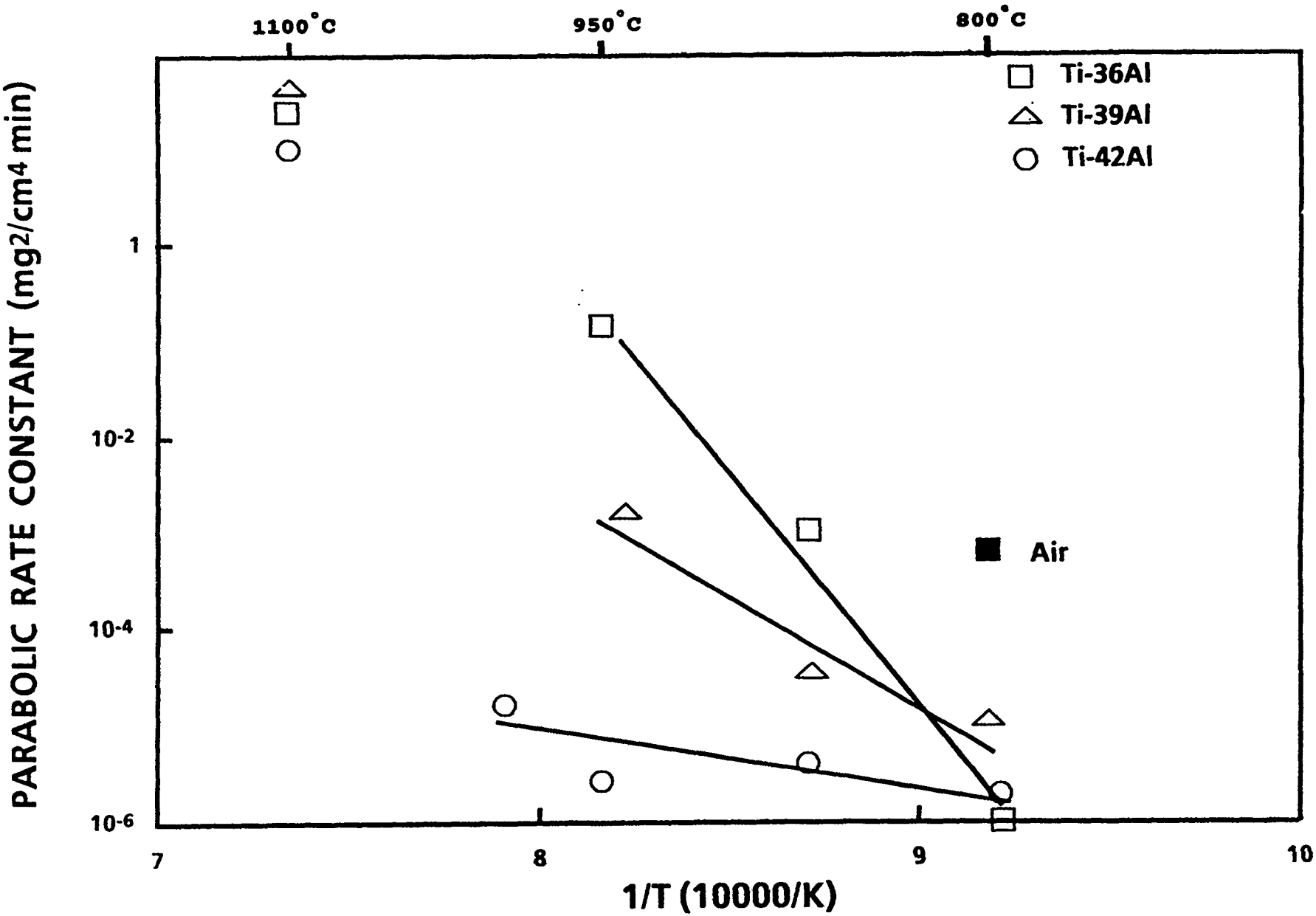

Figure 8. Arrhenius plot of the parabolic rate constants for the oxidation of TiAl with three different Al contents in oxygen (open symbols). The solid point represents the rate constants for all three alloys exposed in air at 800°C.

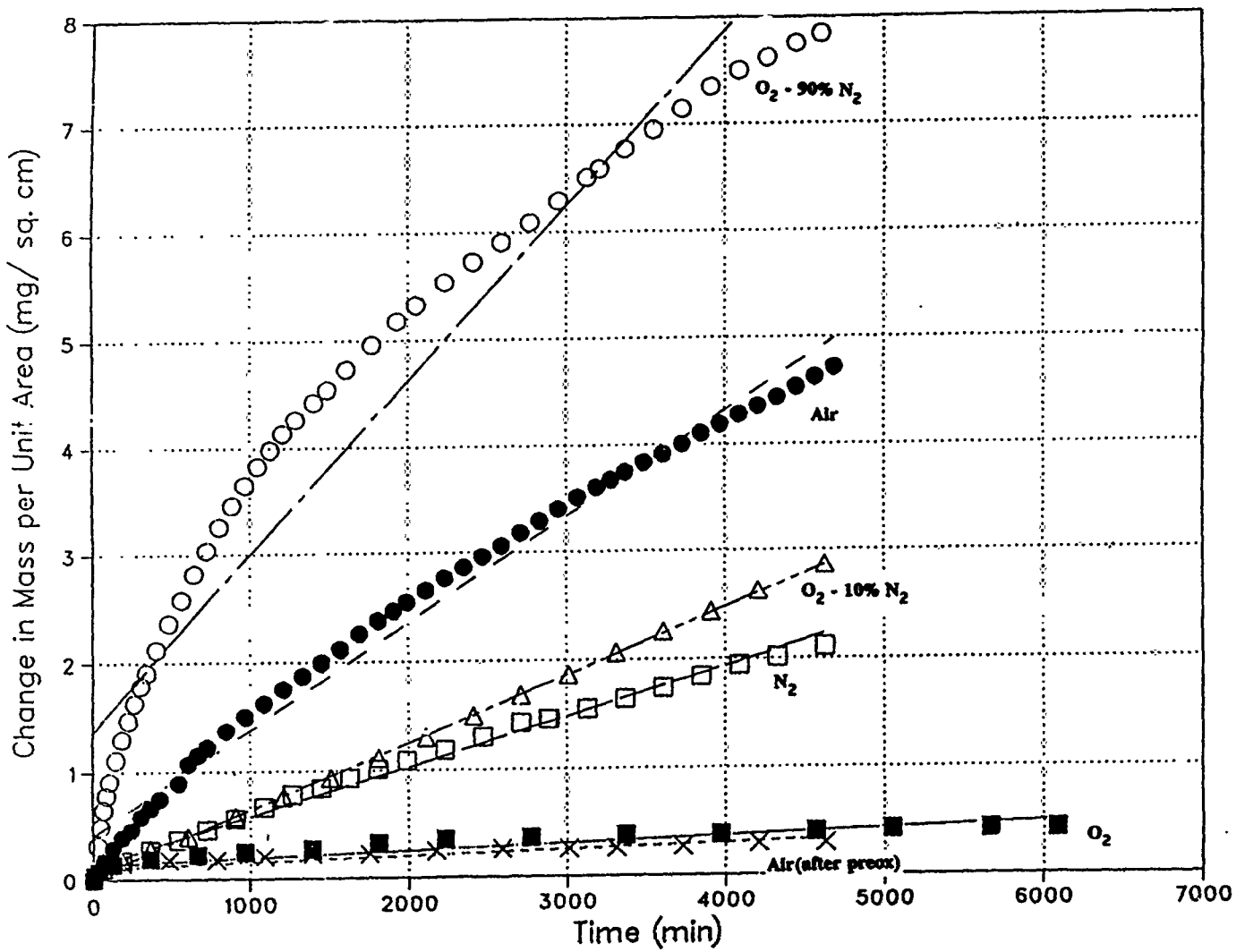

Figure 9. Weight change versus time data for TiAl (52 at% Al) oxidized at 900°C in various atmospheres.

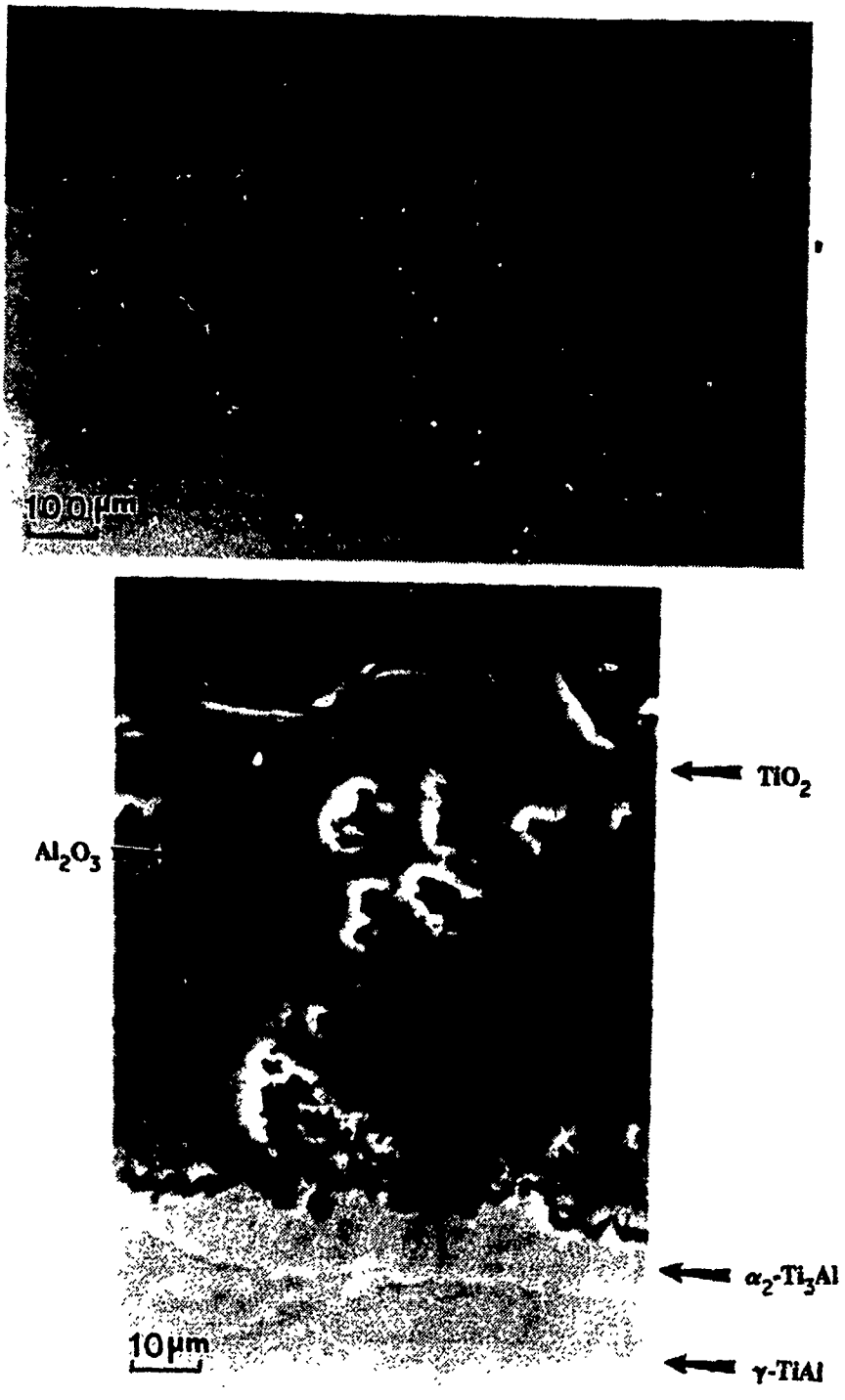

Figure 10. Cross-section of TiAl (52 at% Al) oxidized in 10% N_2 - 90% O_2 at 900°C for 80 hrs.

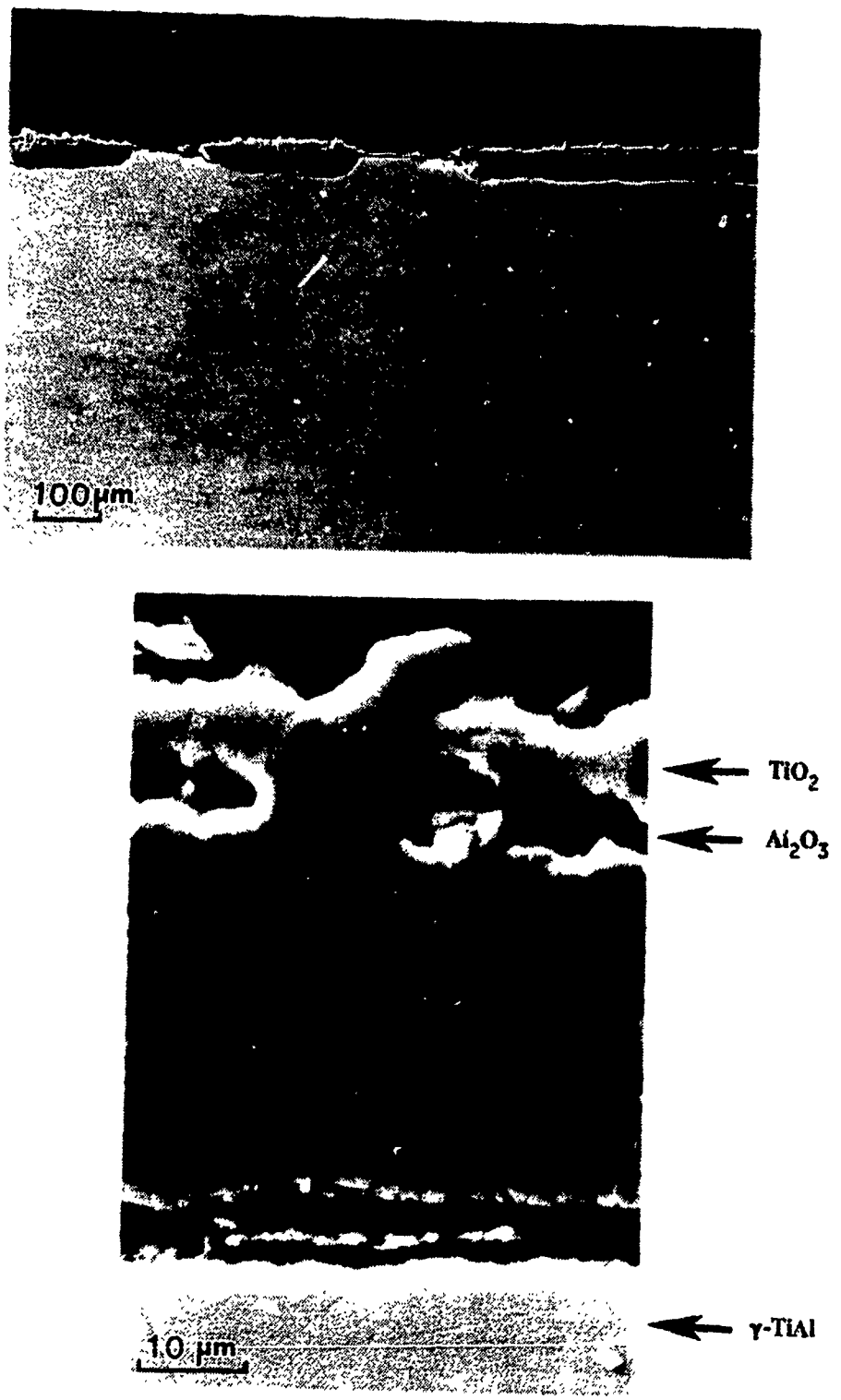

Figure 11. Cross-section of TiAl (52 at% Al) oxidized in at 900°C for 80 hrs.

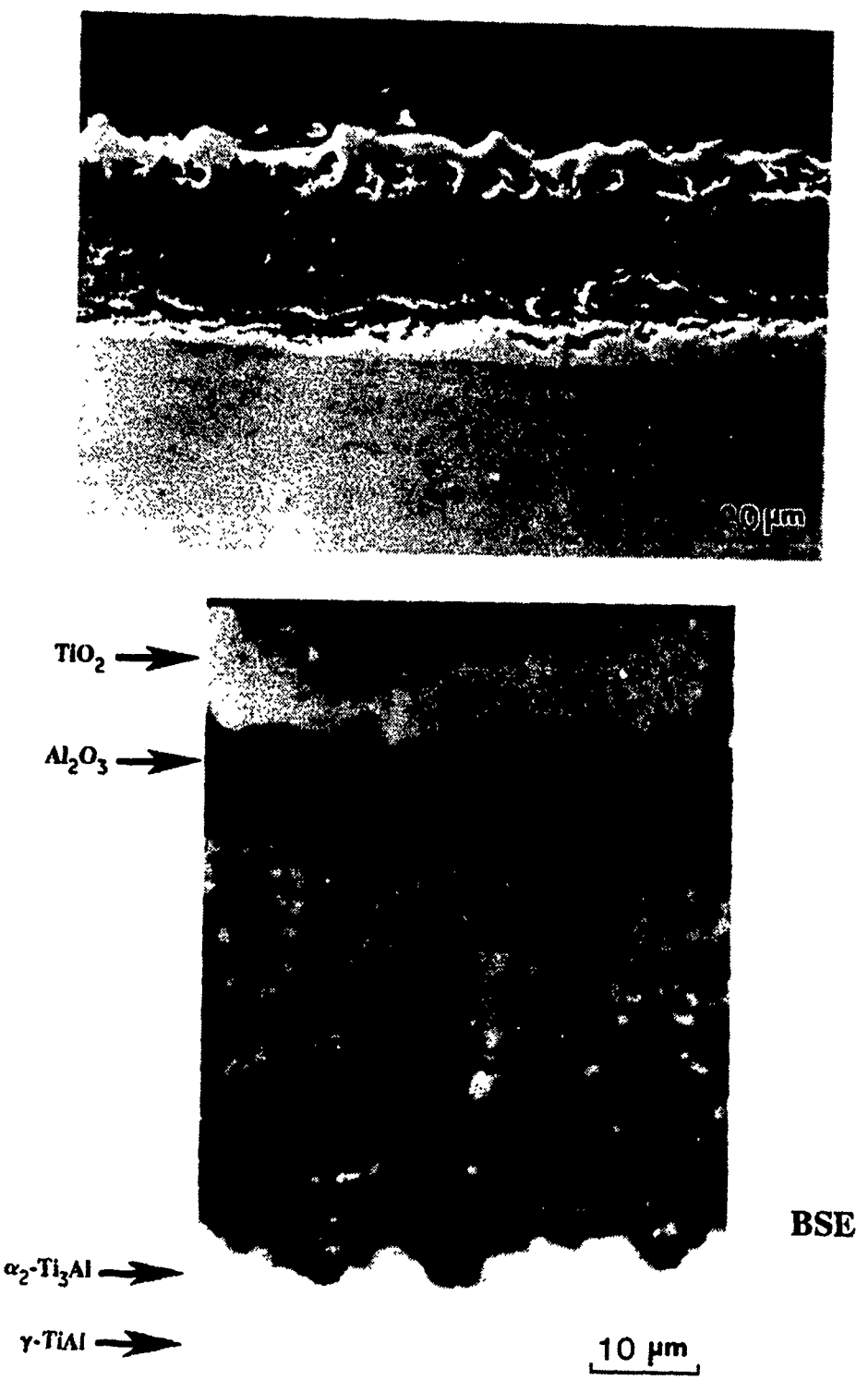

Figure 12. Cross-section of TiAl (52 at% Al) oxidized in 90% N_2 - 10% O_2 at 900°C for 80 hrs.

Oxidation Behavior of $MoSi_2$

by

D.A. Berztiss, F.S. Pettit and G.H. Meier
Materials Science and Engineering Department
University of Pittsburgh
Pittsburgh, PA 15261

Abstract

The oxidation behavior of $MoSi_2$ in two fabrication conditions (cast and HIPed) has been studied in oxygen and in air over the temperature range 500° to 1400°C. The cast material exhibited three regimes of behavior. Above 1000°C a continuous protective silica scale formed. Between 600° and 1000°C a silica scale formed, but formation of silica down grain boundaries, which are believed to be cracked, was observed. At temperatures near 500°C accelerated linear oxidation, involving the formation of both Mo- and Si-oxides was observed and the specimen fragmented into powder ("pested"). The HIPed material exhibited two regimes. Above 600°C a protective silica film formed. At temperatures around 500°C the HIPed material underwent accelerated oxidation but did not fragment. It was concluded, therefore, that accelerated oxidation is a necessary, but not sufficient, condition for pest to occur. The pesting of the cast material was concluded to occur by oxidation along pre-existing microcracks in the $MoSi_2$. Preoxidation at 1000°C was found to be only partially successful in limiting accelerated oxidation during subsequent exposure at 500°C.

Introduction

The intermetallic compound $MoSi_2$ exhibits excellent oxidation resistance at elevated temperatures (1000° - 1700°C). At such temperatures, a thin continuous protective oxide (SiO_2) layer forms, corresponding to small weight gains and little change of behavior over long periods of time (i.e. no spalling and/or cracking of protective scale). $MoSi_2$ has a high melting point (2020°C), relatively low density (6.24 g/cm^3), moderately good high temperature strength and ductility above 1000°C. In contrast to these favorable high temperature properties, at low to intermediate temperatures (400° - 550°C), accelerated oxidation and/or a "pest" mechanism proves problematic. Accelerated oxidation involves the formation of a thick, non-protective oxide layer, which does not prevent further degradation of the base material. The "pest" mechanism is a low temperature failure mechanism, whereby oxidation results in disintegration of the intermetallic to powder. For both, low temperature kinetics are linear with time, and orders of magnitude higher than one would anticipate by extrapolation from high temperature rates.

While this study deals with the oxidation behavior of $MoSi_2$ over a range of temperatures, the unresolved questions regarding the anomalous low-temperature behavior warrant special attention. A comparative study of the oxidation behavior of cast - vs. - HIPed $MoSi_2$ at 500°C is undertaken. The HIPed material is dense and crack-free, but contains second phases, whereas the single-phase cast material contains a large number of cracks. The oxidation sequence and morphology of reaction products as a function of time is carefully examined for both materials. Acoustic emission is further employed to characterize the differences in behavior. Finally, the effects of preoxidation at high temperatures on the subsequent low temperature oxidation is examined. While a detailed

mechanism of the oxidation of $MoSi_2$ at 500°C could not be determined, important features are described.

Background

Fitzer[1] first described the phenomenon of the disintegration of $MoSi_2$ to powder and named it "pest" in 1955. Prior to that, the excellent oxidation resistance at elevated temperatures had been well known. Since that time, many researchers have attempted to describe the behavior of $MoSi_2$ at lower temperatures and determine under what circumstances it occurs. It is difficult to interpret some of the results, as the starting material is often not characterized.

Berkowitz-Mattuck et al.[2,3] started with zone-refined material of less than 75% theoretical density, and determined, as had Fitzer[1], that "pesting" occurs in oxygen, but not nitrogen, carbon dioxide, carbon monoxide or argon, and that the rate of oxidation is very sensitive to the partial pressure of oxygen. Furthermore, as there are little or no lattice parameter changes when of $MoSi_2$ is equilibrated in oxygen, the solubility of oxygen in $MoSi_2$ is very low. They concluded that due to the high residual stresses introduced on cooling of the anisotropic material from the melt, a stress-enhanced oxidation could occur at the tips of Griffith flaws, eventually leading to brittle fracture. This "pesting" did not occur at T > 600°C as slip and/or plastic deformation of the matrix near the flaw accommodated the stresses. The crack density increased with exposure time at temperature, and the cracks were found to be mostly transcrystalline.

Westbrook et al[4] proposed that the catastrophic nature of the "pest" mechanism was due to preferential intergranular diffusion of a gaseous element (most likely oxygen or

nitrogen), coupled with a temperature dependent hardening reaction. At very low temperatures, the rate of diffusion of oxygen is very slow and the reactions are confined to the regions near the external surface. As temperature is increased, oxygen can diffuse rapidly through the sample along grain boundary paths, but volume diffusion of oxygen is still low. Therefore in this temperature range it is feasible that grain boundary embrittlement occurs. This leads to an increase in internal stresses, finally leading to cracking. The high temperature limit of this phenomenon is found as the temperature where grain boundary and bulk diffusion rates are comparable. As proof of their postulation, Westbrook et al. found that at the grain boundaries, there was an increase by 35% in the hardness compared to that at the bulk. There is a clear difference between the mechanisms proposed by Berkowitz et al. and Westwood et al.

Experimental

The oxidation data of cast and HIPed $MoSi_2$ was obtained by various experimental procedures. A Cahn 2000 microbalance continuously determined weight changes as a function of time in both air and oxygen. Test coupons with a surface area of about 1-3 cm^2 were polished through 600 grit SiC paper, ultrasonically cleaned in a 50% methanol - 50% acetone solution and placed in the balance. The cast material proved too brittle to drill holes for suspension, therefore those samples were placed on a small quartz platform or in a sapphire holder, which in turn was suspended by a platinum wire in the balance. EDM was used to produce holes in the HIPed samples, which were then directly suspended by a platinum wire. The surfaces and cross-sections of the oxidized samples were examined using XRD, EDX and SEM.

In order to observe the morphological aspects of the oxidation of both cast and HIPed samples as a function of time, polished samples were inscribed with an identifying mark using a diamond drill bit. These samples were placed in an alumina boat in the hot zone of a horizontal furnace. Exposure was in static air for 30 minutes to 958 hours for the HIPed material and 30 minutes to 43 hours for the cast material. After each exposure time, the samples were carbon coated and examined using SEM. A carbon coating was used since carbon quickly reacts with the atmosphere at elevated temperatures, and thus does not interfere with subsequent oxidation.

Acoustic emission was used to determine the effects of cracking on the oxidation behavior of $MoSi_2$. Cumulative counts were measured as a function of exposure time. Previous studies have shown that these counts correlate well with oxide scale cracking[5].

The acoustic emission monitoring system was the Dunegan/Endevco 3000 Series (Schematic in Figure 1). Ceramabond 569 paste (Aremco Products Inc.) was used to attach a 25" long by 0.25" diameter alumina waveguide to the sample. A platinum waveguide could not be used as it can react with Si in $MoSi_2$. A stainless steel cone was attached with Ceramabond 569 to the other end of the waveguide to allow the piezoelectric transducer to be attached. It is this high sensitivity transducer (Model S9204) that detects acoustic signals (elastic waves) from the surface of the specimen and has a frequency response over the range 100 - 400 KHz. The transducer signal is preamplified by a fixed gain of 40 dB (100 times) and passes through a 100 KHz high pass filter. The preamplified filter signal is then processed for count measurements for amplitude analysis. For count measurement, the signal is further amplified and fed to a threshold detector, which sends a digital pulse to a digital counter each time a signal exceeds the threshold voltage. The threshold voltage is

fixed at one volt so the signal has to be amplified such that the noise level is just below one volt to obtain the maximum sensitivity. The digital counter accumulates all the pulses and displays them on a LED window as AE counts. The digital signal is also converted into an analog signal to plot the counts on a recorder.

Finally, in order to make a closer observation of the scale formed on HIPed samples at 500°C, a sample was polished at a 12° angle from horizontal, thus increasing the observable scale by a factor of three. Figure 2 shows a schematic of this process.

Results

Three forms of $MoSi_2$ were studied: drop-cast, HIPed at 1540°C and 30 ksi for 5 hours and HIPed at 1650°C and 30 ksi for 4 hours. The first HIPed material was obtained from Pratt & Whitney in West Palm Beach, FL (designated 1540°C), while the latter was obtained from the same company in Connecticut (designated 1650°C). Both HIPed materials were made from Ceric powders and were composed of three phases: $MoSi_2$, Mo_5Si_3 and free SiO_2, the 1540°C material containing more Mo_5Si_3. Single phase drop cast $MoSi_2$ was made at the Westinghouse Electric Corp. by tungsten arc melting under an argon atmosphere and drop-casting into a copper mold. From semi-quantitative analysis (SSQ) on the SEM, nominal compositions for the three materials are as follows:

Cast:	37.3 at/o Mo	62.7 at/o Si
HIPed (1540°C):	36.6 at/o Mo	63.4 at/o Si
HIPed (1650°C):	38.8 at/o Mo	61.2 at/o Si

Both cast and HIPed materials were oxidized in air and in oxygen in the temperature range 500°C - 1400°C. Figure 3 shows weight change data as a function of time. Both cast

and HIPed materials fall into the ± 1 mg/cm^2 range for 600° - 1400°C in both air and oxygen. The cast material has many pre-existing cracks, therefore the weight change data are not extremely accurate, but serve well to exhibit trends. At 500°C, the cast material, showing the greatest weight gain, turns completely to powder. Optically, these powders are non-uniform in size and faceted in appearance. XRD determined the reaction products to be MoO_3 and amorphous SiO_2. HIPed material showed the same reaction products, but the scale (20 - 40 μm thick) remained intact. Weight changes at 500°C were greater for the 1540°C HIPed material (more Mo_5Si_3) and greater in oxygen than in air. Figure 4 illustrates the difference between HIPed and cast $MoSi_2$ behavior at 500°C

The cast material did not exhibit pesting (disintegration to powder) at T > 500°C, but internal oxides of SiO_2 did form at 600° to 1000°C. In this range, an oxide did form on the surface as the oxidized surfaces exhibited anywhere from a blue sheen to a dull gray finish. Figure 5 shows a SEM micrograph of a cast $MoSi_2$ cross-section at 800°C. The oxide appears to be going down grain boundaries, but it is also possible that the oxide is forming along pre-existing cracks. Figure 6 shows the same cast material at 1400°C. XRD indicates the scale is α-cristobalite. In some areas the scale was faceted (Figure 6b), while in other regions the surface scale appeared to have undergone devitrification. A contaminant of KCl of unknown origin was found near this region, therefore devitrification is a possibility. Cross-sections of the material show a silica layer about 3 - 7 μm thick was formed in air, while in oxygen a thinner scale of about 1 - 2 μm was formed. Table 1 provides a summary of the reaction products formed in air and in oxygen on cast and HIPed materials at different temperatures as determined by XRD.

Oxidation behavior of cast material was observed as a function of time and SEM surface sequence can be followed in Figure 7. The region on the as-received material showed cracks representative of the material as a whole. After 30 minutes, unidentifiable black spots had formed on the matrix. The white regions are MoO_3. At 17 hours, a bumpy morphology was first observed and can be seen at 25.5 hours. After 35 hours, flakes and rods, which are higher in Mo, were observed. After 38 hours, the bumps, becoming more profuse and growing outward, are found to be higher in Si than smoother regions. It is important to note that although the region chosen for observation exhibits a bumpy morphology, there are other smooth regions, which appear to be unaffected by oxidation. After 43 hours, some of the bumps on the surface appear to "burst" revealing MoO_3 rods. When the sample was removed from the SEM stage, it fractured. SEM micrographs of the fracture surface, showing signs of oxide build-up which appear to be a mixture of Si and Mo oxides, are shown in Figure 8. Throughout the experiment, certain regions of the sample showed widening of the pre-existing cracks with increased oxidation exposure.

Figures 9 through 11 show the results of sequential oxidation studies of HIPed material. In Figure 9a and 10, the as received structure shows three phases: $MoSi_2$ (matrix), Mo_5Si_3 (lighter region) and free SiO_2 (darker regions) along with minor porosity. Mo_5Si_3 and SiO_2 tend to form at grain boundaries. After 30 minutes, Mo_5Si_3 was found to preferentially oxidize to MoO_3 (Figures 9b, 9c). A fine unidentifiable oxide was observed on the $MoSi_2$ matrix, possibly a form of SiO_2. After 23 hours, reaction products on some grains became Si-rich (darker areas), while others became Mo-rich (lighter areas) (Figure 10). After 41 hours, protrusions began to form along what look like grain boundaries and the formation of MoO_3 rods was observed. With time these protrusions grew and cracks appeared at the

tops of the ridges. Figure 11b shows an enlargement of one protrusion, and the stratified lines indicate growth outward with accompanying stress. This sample was run to 958 hours. At that time, on removal from the furnace, a complete oxide layer spalled off, indicative of growth stresses developing at the edges of the sample. XRD of the exposed surface and spalled scale identified MoO_3 and amorphous silica.

Figure 12 is the oxidized surface of 1540°C HIPed material after one week in air at 500°C showing a similar surface morphology to that of the shorter times, indicating that the carbon coating did not affect oxidation behavior.

Figures 13 and 14 are SEM micrographs of cross-sections of HIPed $MoSi_2$ oxidized at 500°C, the latter being polished at a 12° angle. It is interesting to note the stratified layers in regions of Figure 13. The larger "voids" in Figure 14 may be remnants of these layers. Looking more closely at Figure 14, cracks perpendicular to the surface can be seen only at the topmost surface of the scale corresponding to cracks seen at the tops of ridges on the surface. Larger "voids" and extensive porosity are seen throughout the scale. In some regions, the oxide appears to penetrate further down grain boundaries than into the intermetallic matrix (note oxide/matrix interface). EDS shows similar Si/Mo ratios in the scale and matrix indicating simultaneous oxidation of both elements, but a slightly higher Si-content in the scale can be attributed to MoO_3 volatilization.

Pre-oxidation of HIPed samples at 1000°C was carried out to test if the protective scale would remain intact at 500°C. Figure 15 shows weight change as a function of time, indicating an incubation period prior to chipping or spalling of the oxide. These spalled regions show the same morphology as if the samples had been run at 500°C (i.e. not preoxidized).

Acoustic emission results at 500°C are found in Figure 16. The accelerated acoustic counts for the cast material are indicative of cracking during oxidation. More notable is the increase in counts on removal of the cast sample from the furnace, indicating that thermal shock has a much greater impact on cast than HIPed materials. This may be associated with thermal stresses generated at the tips of oxidized cracks because of the thermal expansion mismatch between the oxide and $MoSi_2$.

Discussion

The volatility of MoO_3 plays an important role in the oxidation behavior of $MoSi_2$ and a volatile species versus temperature diagram is given as Figure 17. MoO_3 is highly volatile with a melting point of 795°C and a high vapor pressure even at lower temperatures. At elevated temperatures (>1000°C), MoO_3 vaporizes and the diffusion of Si is rapid enough to form a continuous protective oxide scale to effectively seal the surface. At $T < 600$°C, mixed oxidation and volatilization of MoO_3 prevents continuous SiO_2 scale formation. However, inspection of Figure 17 shows that MoO_3 can still be retained on specimen surfaces up to 800°C. The experimental results indicate that continuous scales of silica may not have been formed on all specimens up to temperatures of 1000°C.

In the 600° - 1000°C range for cast $MoSi_2$, exhibiting a thin oxide layer on the surface (blue sheen to dull gray) and internal oxidation of SiO_2, a competition between SiO_2 formation in cracks and MoO_3 volatilization occurs, keeping the weight change data within ± 1 mg/cm^2. In the cracks, oxygen has a short-circuit path for diffusion, thus formation of SiO_2 can easily form within the cracks. At 500°C, MoO_3 can also form within the cracks, and at this temperature, little volatilization occurs. There is a large change in volume going from

Mo to MoO_3 (≈340%), along with the volume change of forming SiO_2 from Si (≈180%), which enhances the widening of the pre-existing cracks leading to "pesting" (i.e. turning to powder). Thus cracking of $MoSi_2$ as a result of oxide formation within pre-existing cracks is an integral part of the oxidation process and cool down for cast material, which is further shown in the acoustic emission data. These result support the oxidation of microcracks (Berkowitz mechanism) rather than the diffusion of oxygen down grain boundaries (Westbrook & Wood mechanism) as the major contributor to "pesting" of $MoSi_2$.

At T > 1000°C, silica scales, visible in cross-sections in the SEM, form. The change from internal to external oxidation occurs between 1000° and 1200°C and may in some way be associated with the brittle to ductile transition temperature (≈1000°C) and with the diffusion of Si and or O in this temperature range.

HIPed material at 500°C has no pre-existing cracks and it appears oxidation occurs at the alloy/scale interface, evidential of oxygen transport into the material. Simultaneous oxidation of both Si and Mo results, while some of the MoO_3 volatilizes leaving "voids". Little cracking of the material occurs during oxidation of this temperature as indicated by acoustic emission. Growth stresses at the edges of the square coupons finally lead to spalling of the scale. As no "short-circuit" paths exist in the material, there is no "internal oxidation".

At 1000°C, surface SEM showed some type of product had formed, but could not be detected by XRD, nor could any scale be found in cross-section. HIPed samples were not oxidized at higher temperatures, but it is presumed that at 1200° and 1400°C, the same sort of continuous silica layer would form.

Pre-oxidation at 1000°C proved to be a deterrent to accelerated oxidation at 500°C for a short time only. After some incubation period, spalling of the scale was observed, with

the subsequent growth of the dual MoO_3 and amorphous SiO_2 scale in the spalled regions. In fact, slight fragmentation of the $MoSi_2$ was also observed. It appears that the majority of the spalls occurred at the edges of the sample, where some prior matrix damage had been evident prior to oxidation. However, some of these greenish-gray regions of oxide were also found on the faces of the samples and could be explained by damage occurring to the scale on cool-down. It should be pointed out that this phenomenon was not observed when the HIPed specimens were exposed at 500°C without preoxidation. It is believed that thermal stresses generated during cooling from the preoxidation temperature nucleated microcracks at certain sites where the geometry was favorable, e.g. corners and edges, and that these areas were then susceptible to a form of degradation similar to that observed for the cast $MoSi_2$. This phenomenon raises a question about the application of $MoSi_2$ as a structural material in that thermal and applied stresses may be able to produce a microstructure which, if exposed at temperatures near 500°C, may be susceptible to pesting. Further work should be directed at characterizing this behavior more quantitatively.

Conclusions

The oxidation behavior of $MoSi_2$ is a function of fabrication condition i.e. microstructure. Cast material, which contained microcracks, underwent accelerated oxidation and fragmentation ("pesting") in a narrow temperature range near 500°C. HIPed material, without microcracks, underwent accelerated oxidation but did not fragment. The "pesting" phenomenon, in $MoSi_2$, is concluded to result from the formation of voluminous Mo-oxides in microcracks. The accelerated oxidation involves the simultaneous formation of MoO_3 and SiO_2 in essentially the amounts determined by the Mo and Si concentrations in the

intermetallic. At temperatures of 600°C and above both materials formed continuous silica scales and oxidized at very slow rates and no fragmentation was observed. It is concluded, therefore, that accelerated oxidation is a necessary, but not sufficient, condition for pesting. The cast material showed the additional feature of internal silica formation along grain boundaries, which may have been cracked, for oxidation temperatures between 600° and 1000°C. The HIPed material did not display this feature. Above 1000°C both materials formed only external silica scales. The ineffectiveness of preoxidation at 1000°C to completely suppress accelerated oxidation during subsequent exposures at 500°C, and the small amounts of fragmentation observed in these experiments, is a matter of concern for the application of $MoSi_2$ as a structural material.

References

1. E. Fitzer, Warmfest und Korrosionbestandige Sinterwerkstoffe, 2 Plansee Seminar, 19-23 June 1955, Reutte/Tirol, F. Benesovky, (Ed.), Vienna: Springer Verlag, 1956, p. 56.

2. J.B. Berkowitz-Mattuck, P.E. Blackburn and E.J. Felton, Trans AIME, 233, June 1965, p. 1093.

3. J.B. Berkowitz-Mattuck, M. Rosetti and D.W. Lee, Met. Trans., 1, Feb. 1970, p. 479.

4. J.H. Westbrook and D.L. Wood, J. Nucl. Mater., 12 1964, p. 208.

5 A. Ashary, G.H. Meier and F.S. Pettit, pp. 105-119, High Temperature Protective Coatings, S.C. Singhal, editor, The Metallurgical Society, Warrendale, PA, 1983. AIME, 239, 1296 (1967).

Temperature (°C)	Atmosphere	Cast	HIPed (1540°C)
As received		$MoSi_2$	$MoSi_2 + Mo_5Si_3$
500	Air	MoO_3 + amorphous SiO_2	$MoSi_2 + MoO_3$ + amorphous SiO_2
500	O_2		MoO_3 + amorphous SiO_2
600	Air	$MoSi_2$	
600	O_2	$MoSi_2$ + tridymite	
800	Air	$MoSi_2$ + tridymite	
800	O_2	$MoSi_2$ + tridymite	
1000	Air	$MoSi_2$ + tridymite	$MoSi_2$
1000	O_2	$MoSi_2$ + tridymite	$MoSi_2$
1200	Air	$MoSi_2$ + α-cristobalite	
1200	O_2	$MoSi_2$ + tridymite	
1400	Air	$MoSi_2$ + α-cristobalite	
1400	O_2	$MoSi_2$ + α–cristobalite	

Table 1. Summary of XRD results of oxidized cast and HIPed (1540°C) materials.

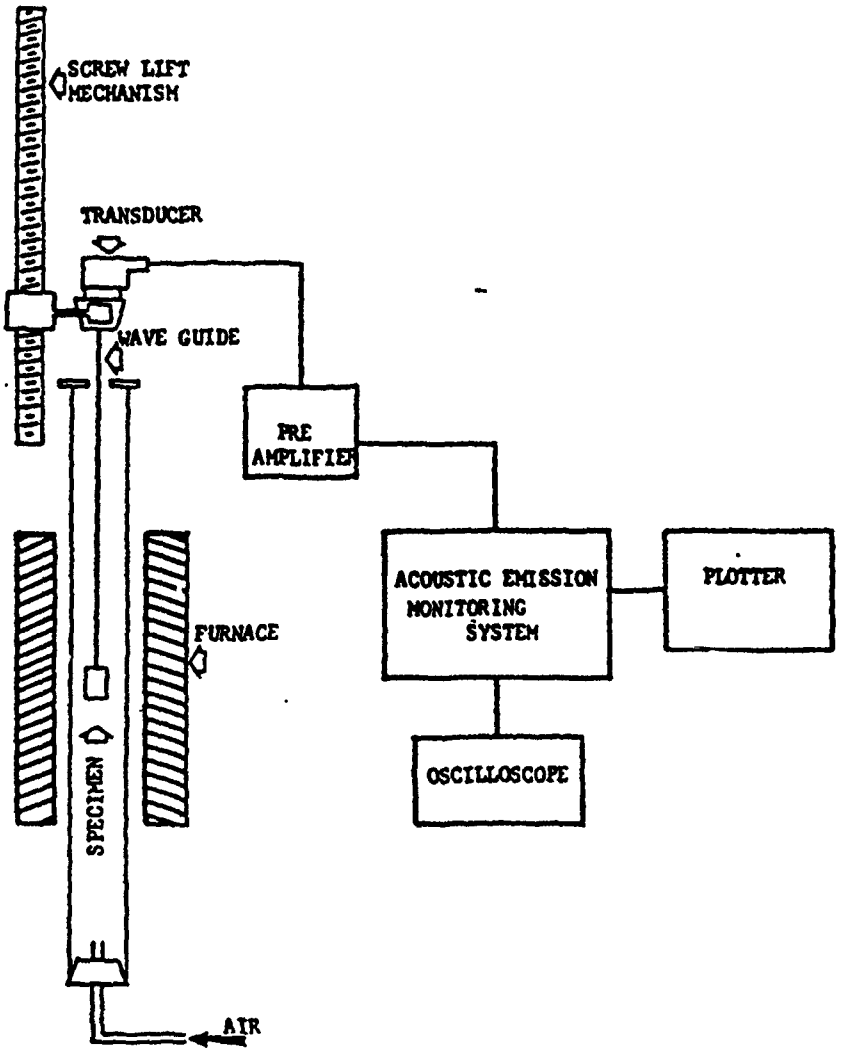

Figure 1. Experimental setup for acoustic emission study of oxide scale failure.

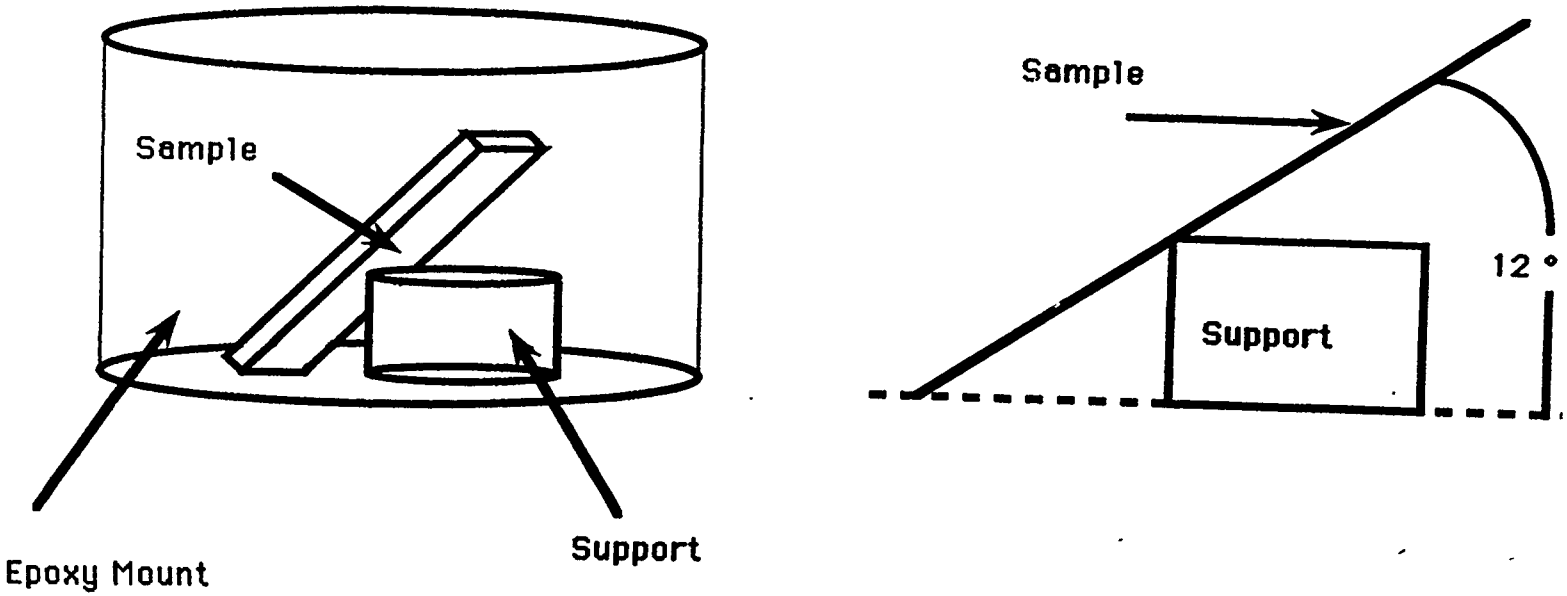

Figure 2. Schematic indicating how 12° polishing angle was achieved to perform detailed study of oxide scale.

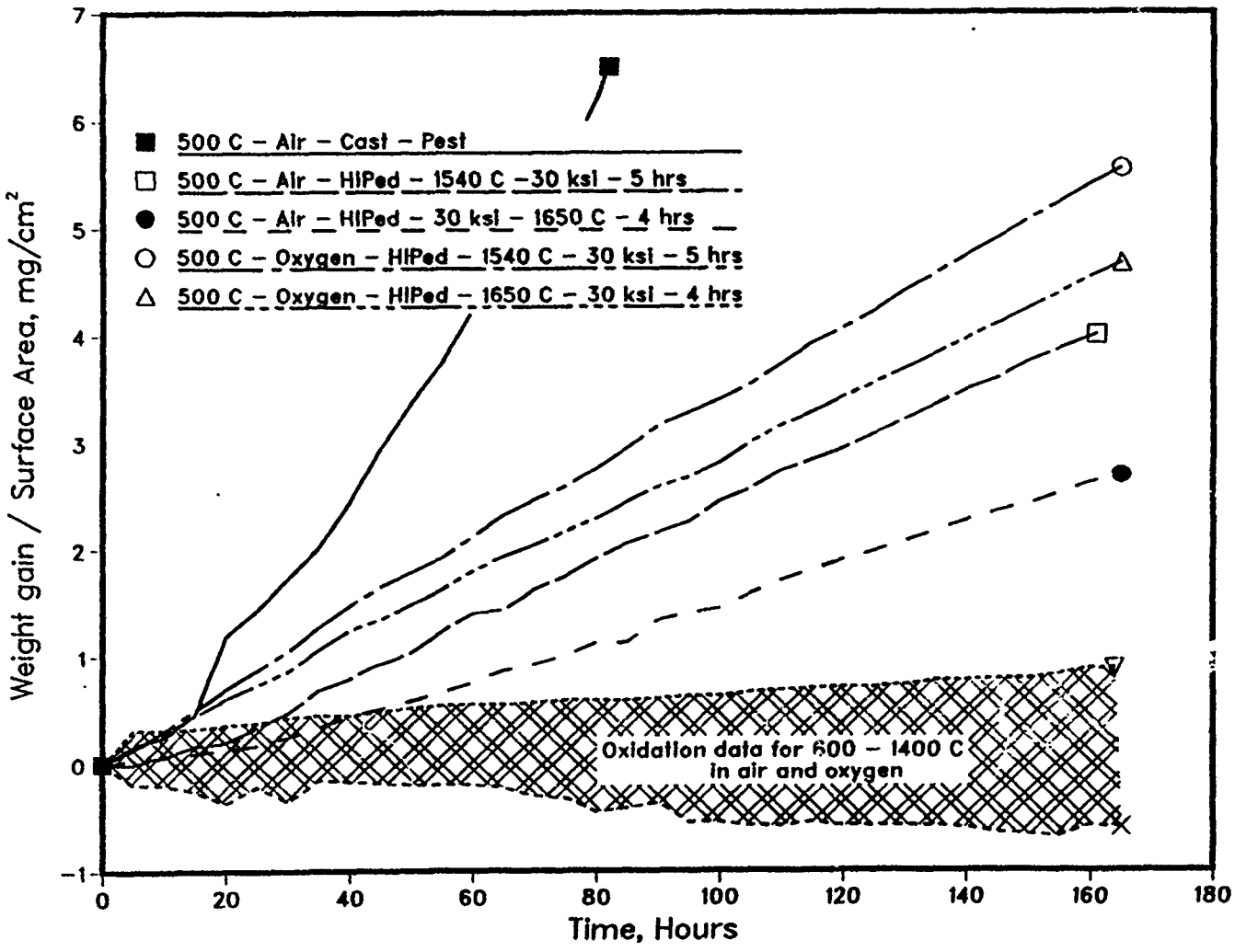

Figure 3. Isothermal oxidation results for 500 - 1400°C in air and oxygen; cross-hatched region is general behavior for 600 - 1400°C range, regardless of material processing.

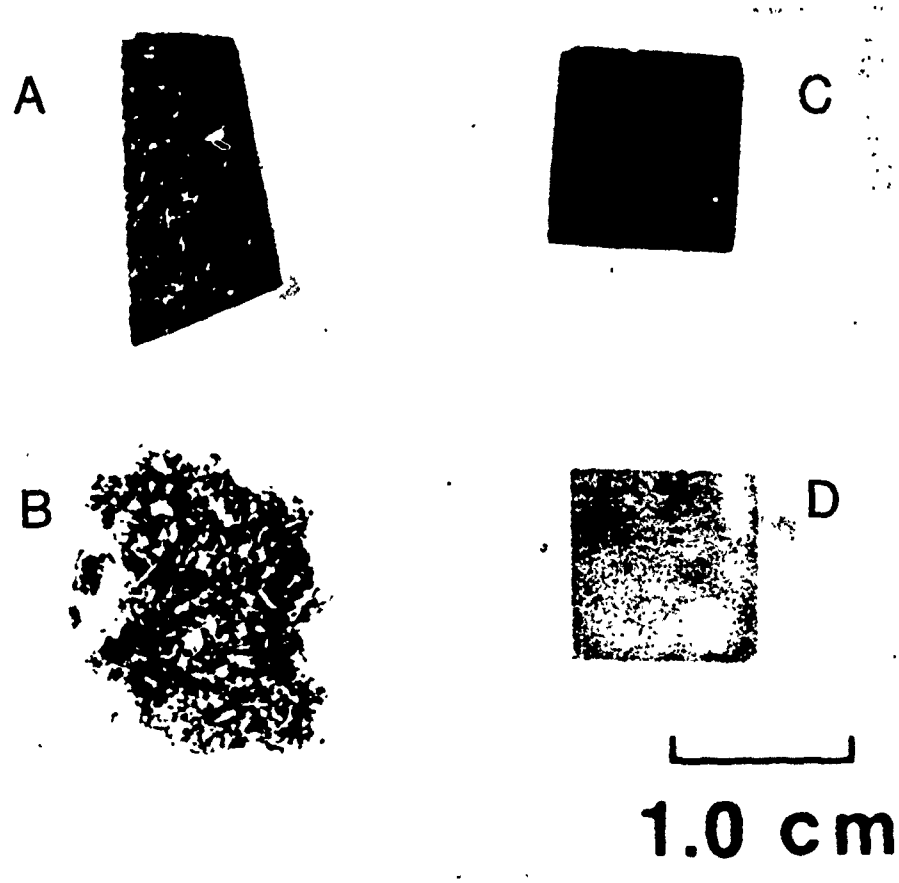

Figure 4. Effects of Initial Processing of Material
a. As-received drop-cast material
b. 500°C, 82 hrs., air — complete pesting
c. As-received HIPed (1540°C - 30 ksi - 5 hrs) material
d. 500°C, 165 hrs., air — accelerated oxidation

Figure 5. SEM cross-section micrograph of cast $MoSi_2$, oxidized in air at 800°C for one week.

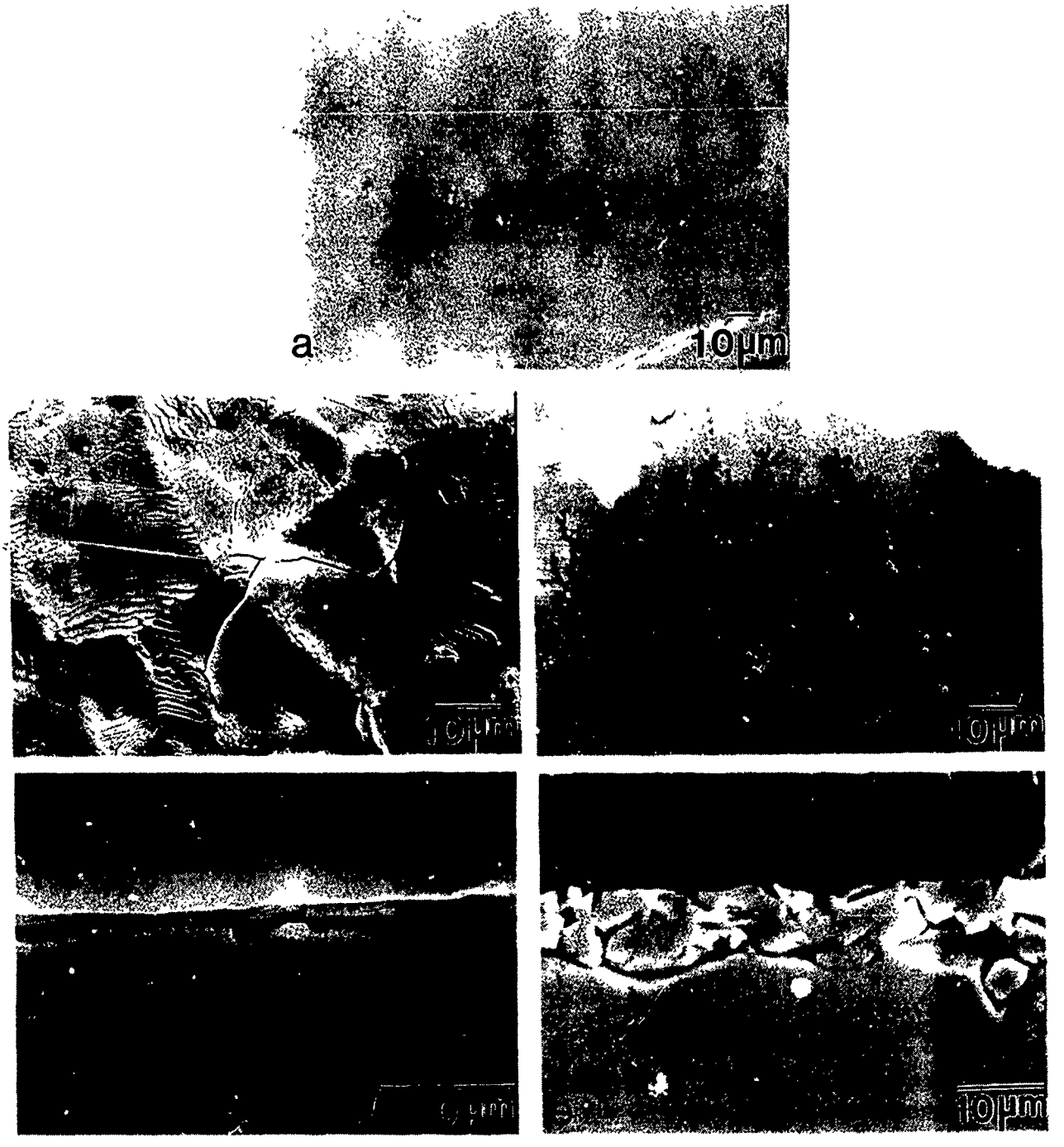

Figure 6. SEM micrographs of surfaces (a,b,c) and cross-sections (d,e) of cast $MoSi_2$ oxidized at 1400°C in air (a,c,e) and oxygen (b,d).

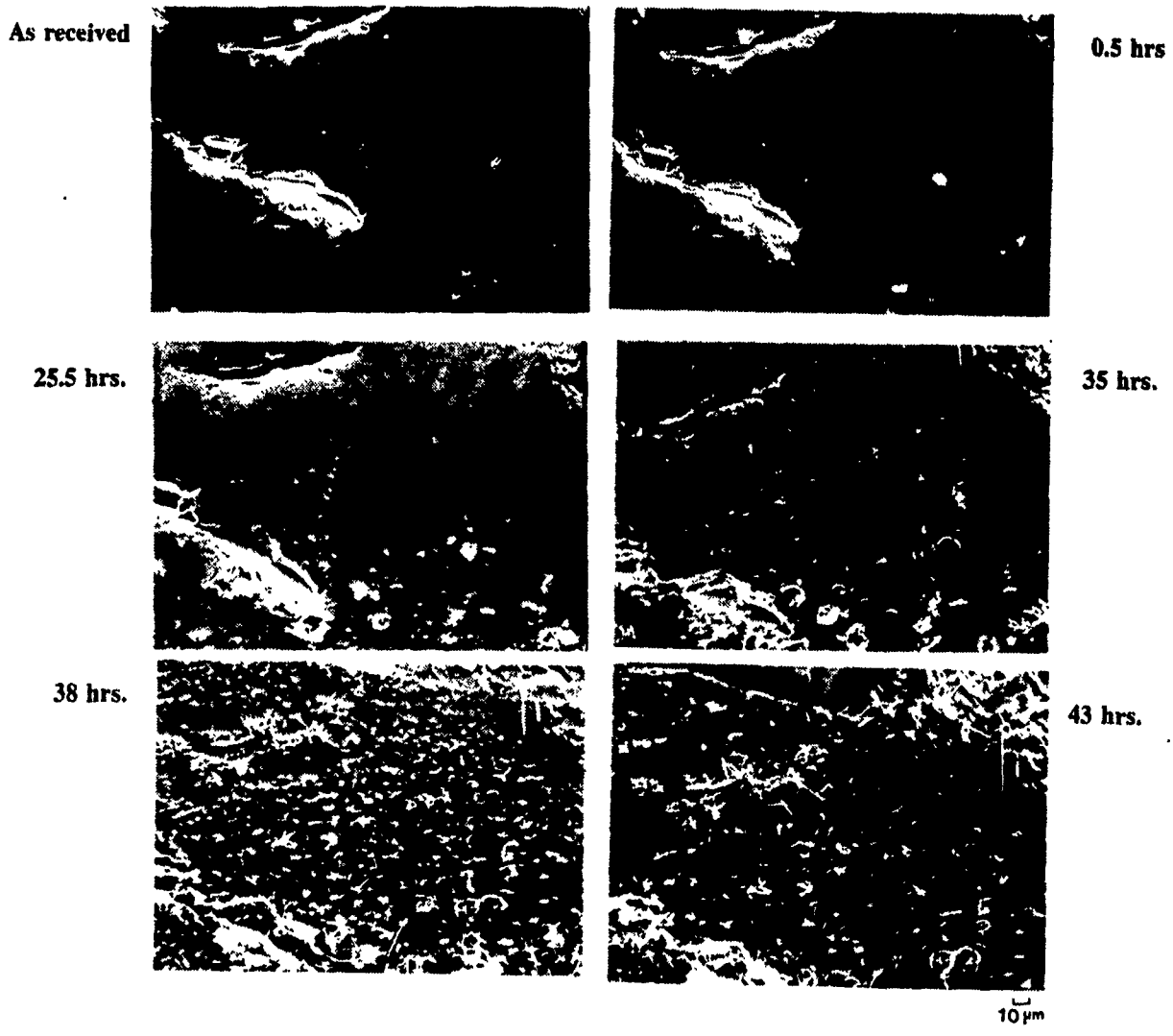

Figure 7. SEM surface micrograph sequence of cast $MoSi_2$ oxidized in static air at 500°C.

Fracture surface

43 hrs.

Surface

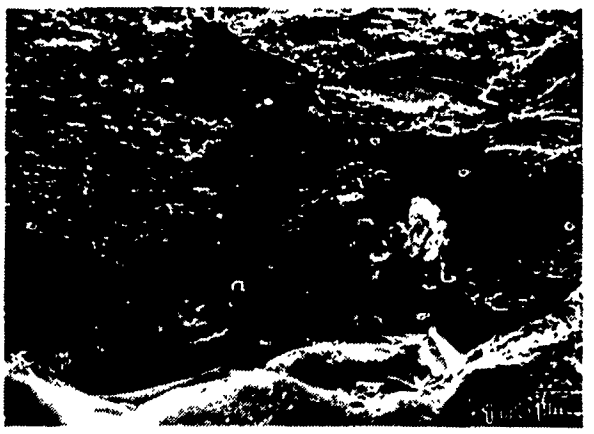

Figure 8. SEM fracture micrographs of cast $MoSi_2$ after 43 hours in static air at 500°C.

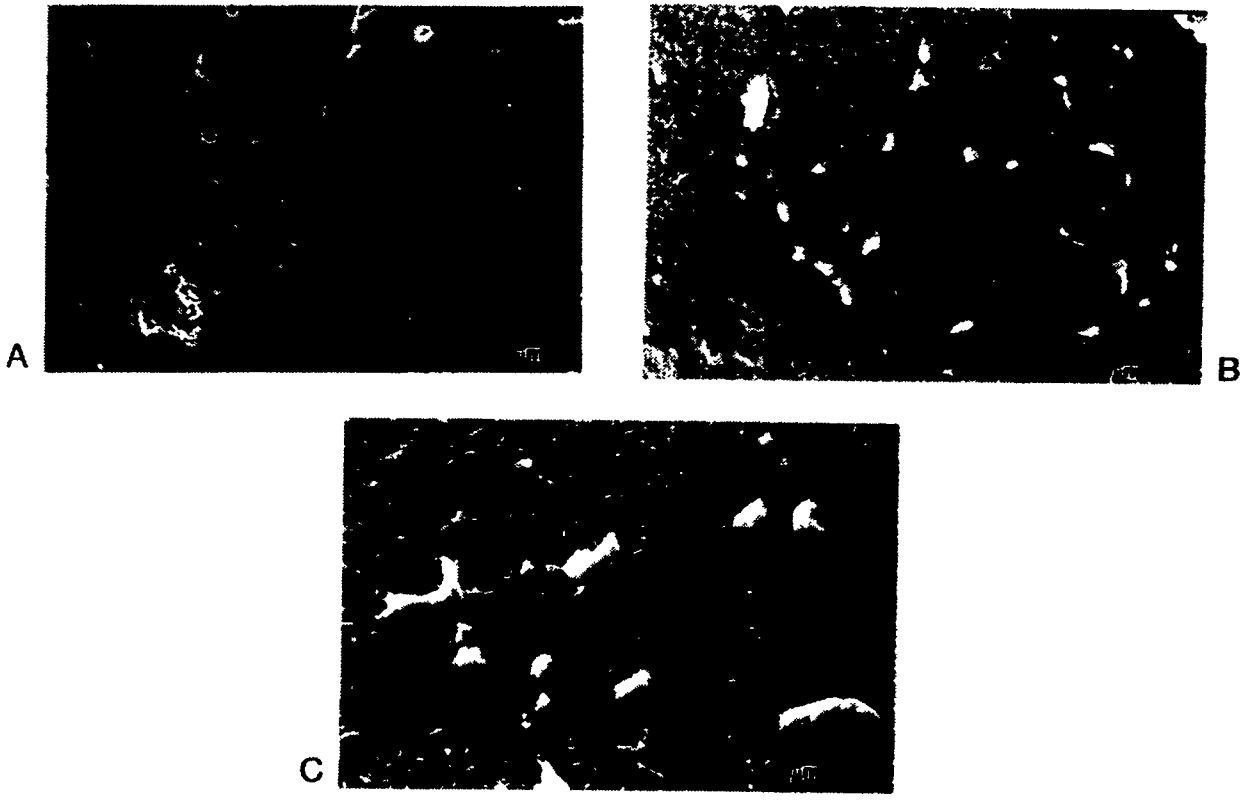

Figure 9. SEM surface micrographs of HIPed (1540°C) $MoSi_2$.

a. As received.
b. After 30 mins. of exposure in static air at 500°C
c. Same as b, but tilted 55°.

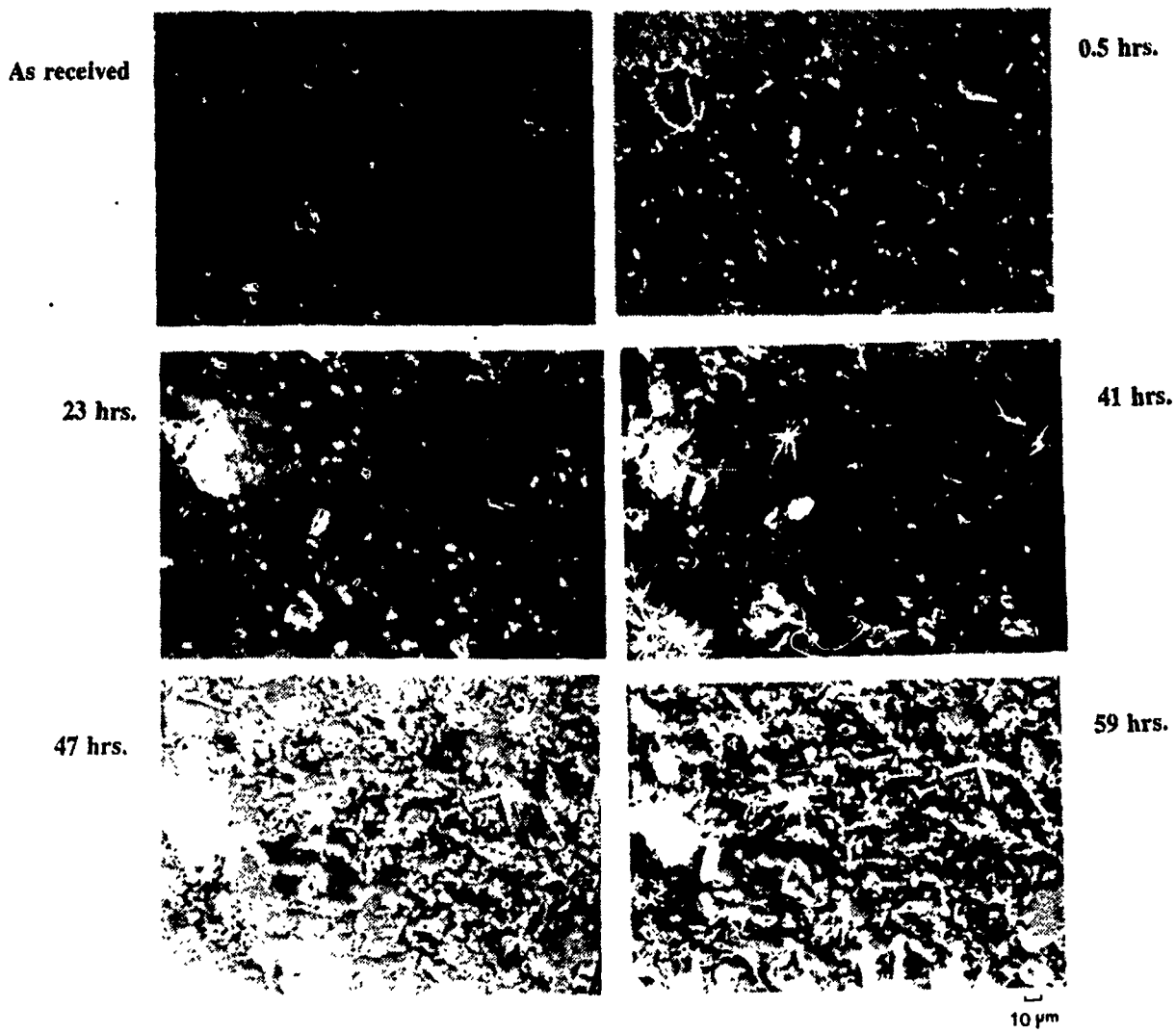

Figure 10. SEM surface micrograph sequence of HIPed (1540°C) $MoSi_2$ as a function of time at 500°C in static air.

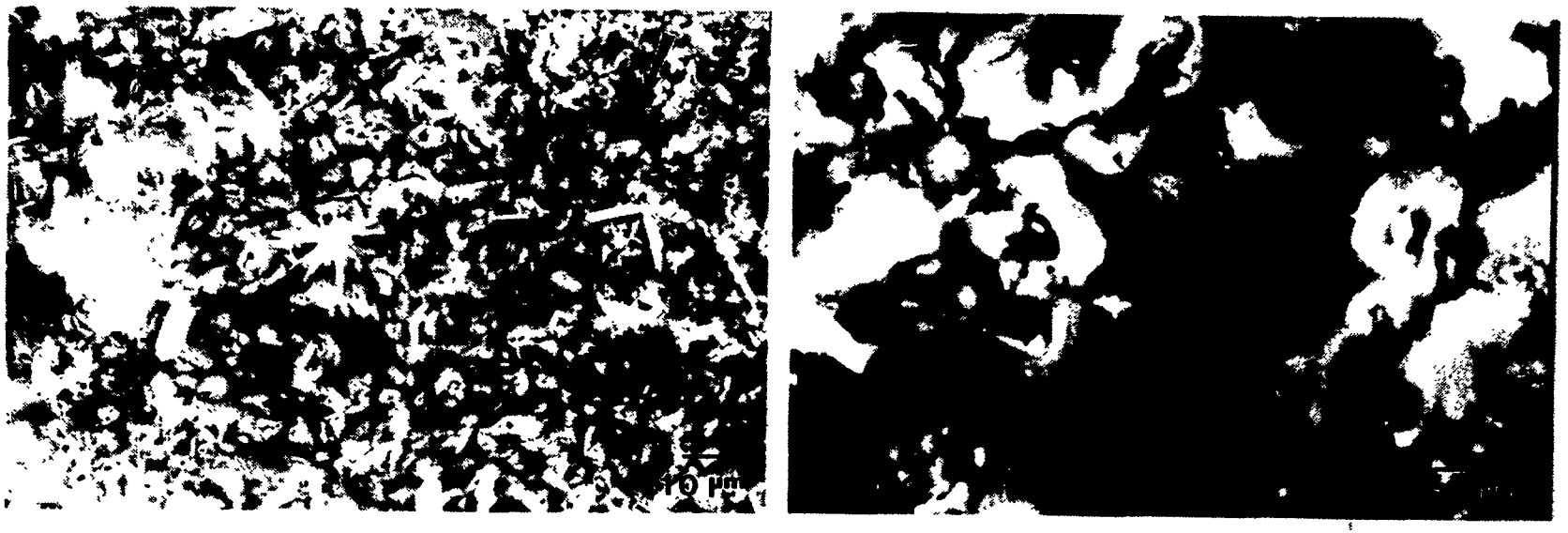

Figure 11. SEM surface micrographs of HIPed (1540°C) $MoSi_2$ after 62 hours in static air at 500°C showing growth of protrusions.

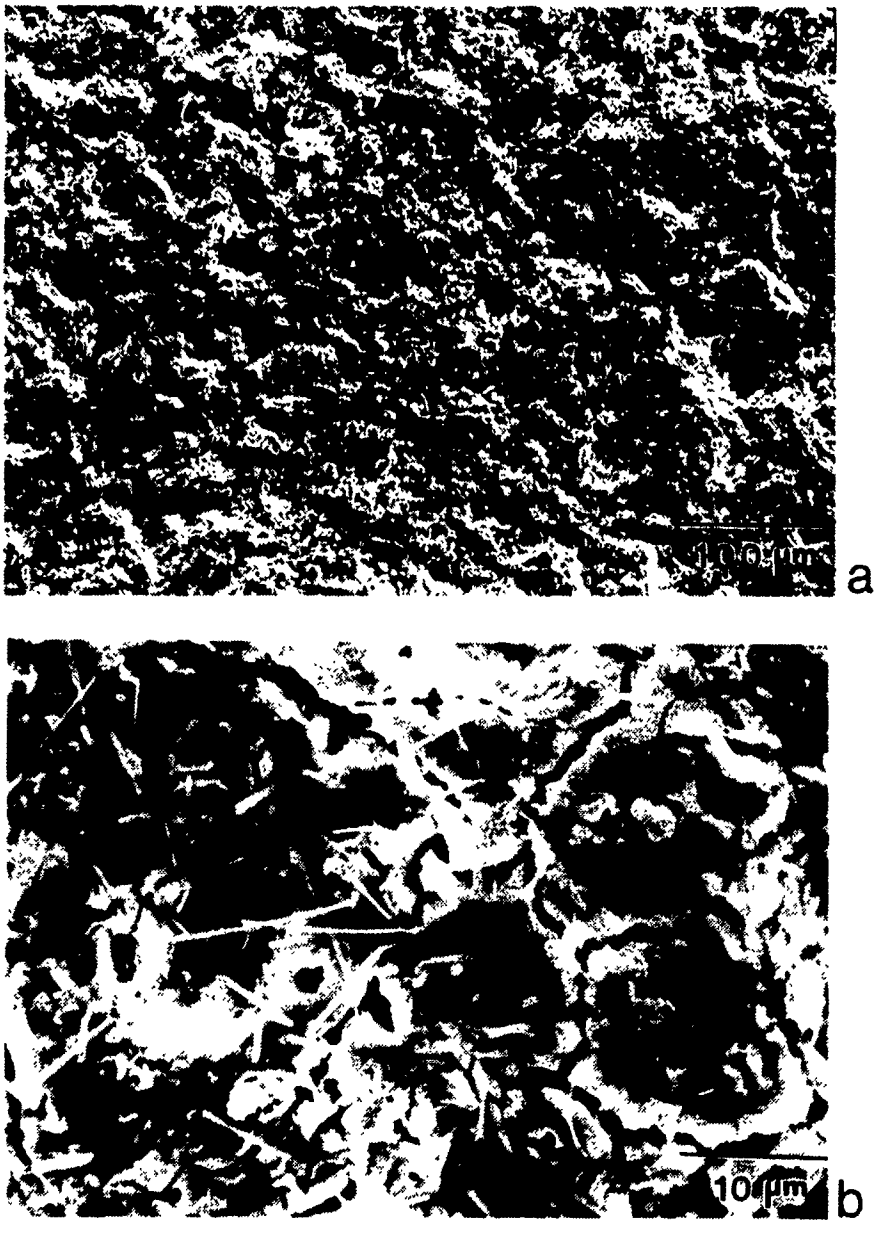

Figure 12. SEM surface micrographs of HIPed (1540°C) $MoSi_2$ after oxidation in air for one week at 500 °C.

Figure 13. SEM cross-section of HIPed (1540°C) $MoSi_2$ after one week exposure in oxygen at 500°C.

Figure 14. SEM cross-section montage of HIPed (1540°C) $MoSi_2$ at 500°C in O_2 polished at 12° angle.

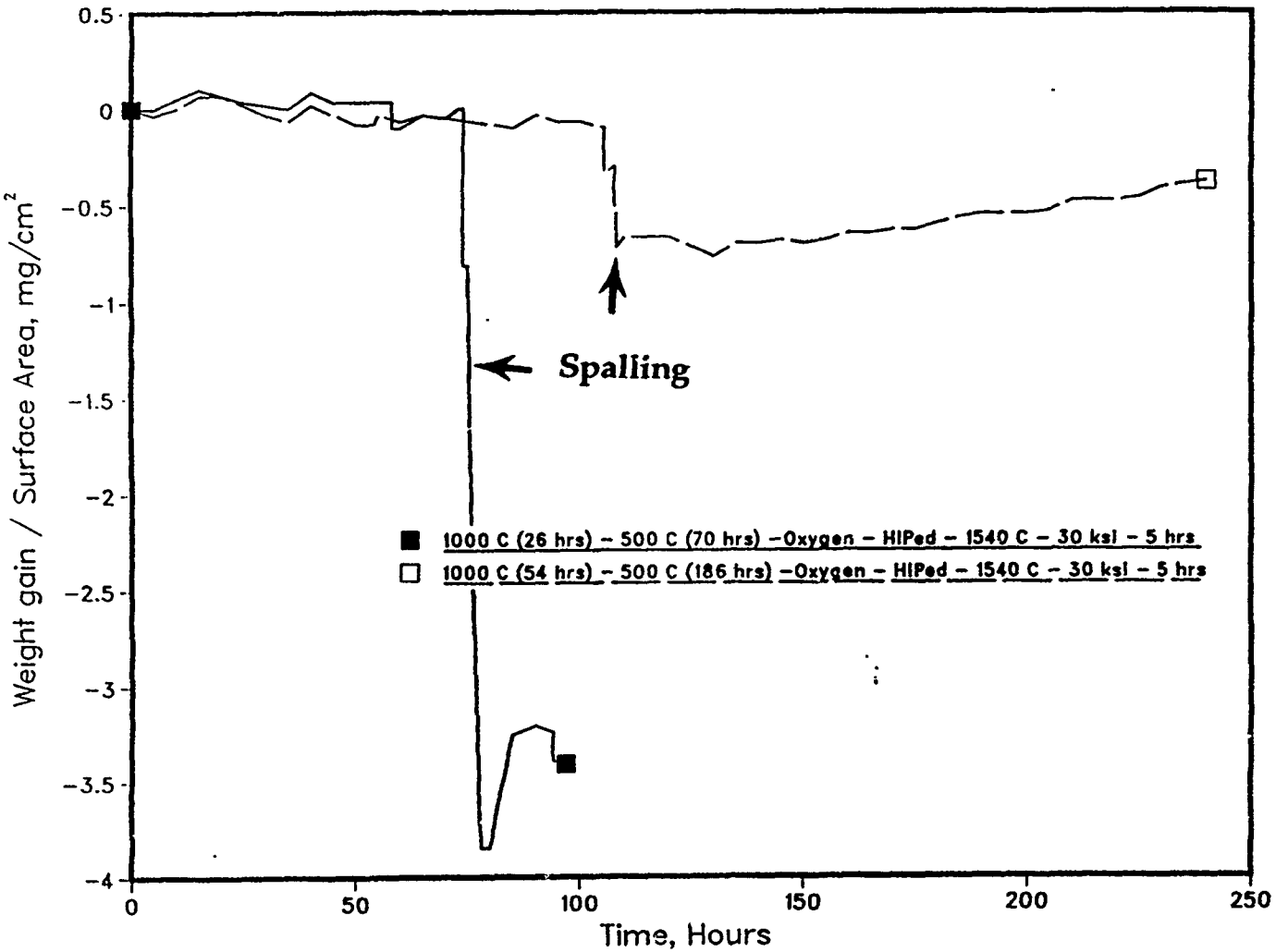

Figure 15. Results of pre-oxidation studies; pre-oxidation for 26 or 54 hrs at 1000°C, then at 500°C.

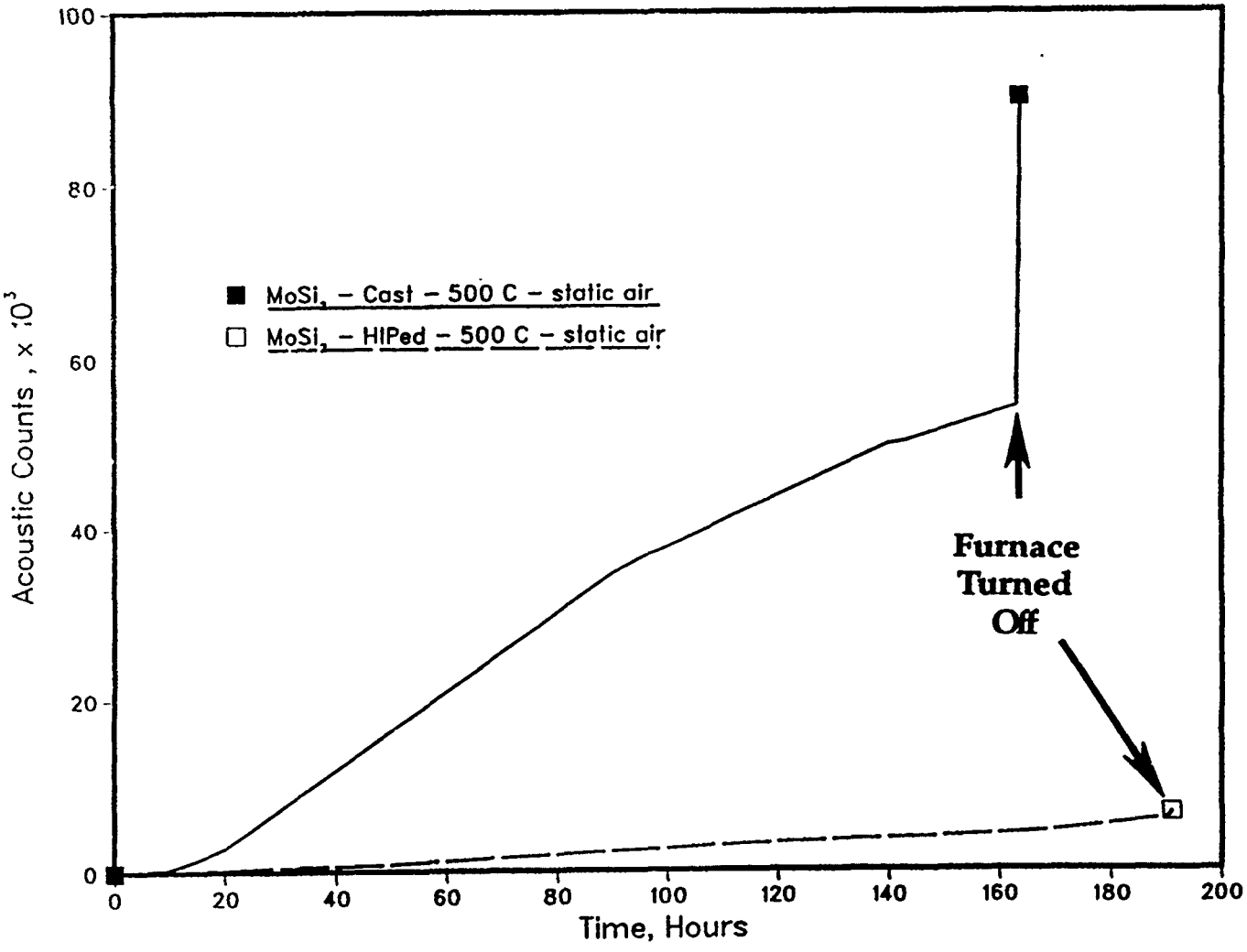

Figure 16. Acoustic emission results for drop-cast and HIPed (1540°C) materials at 500°C in air.

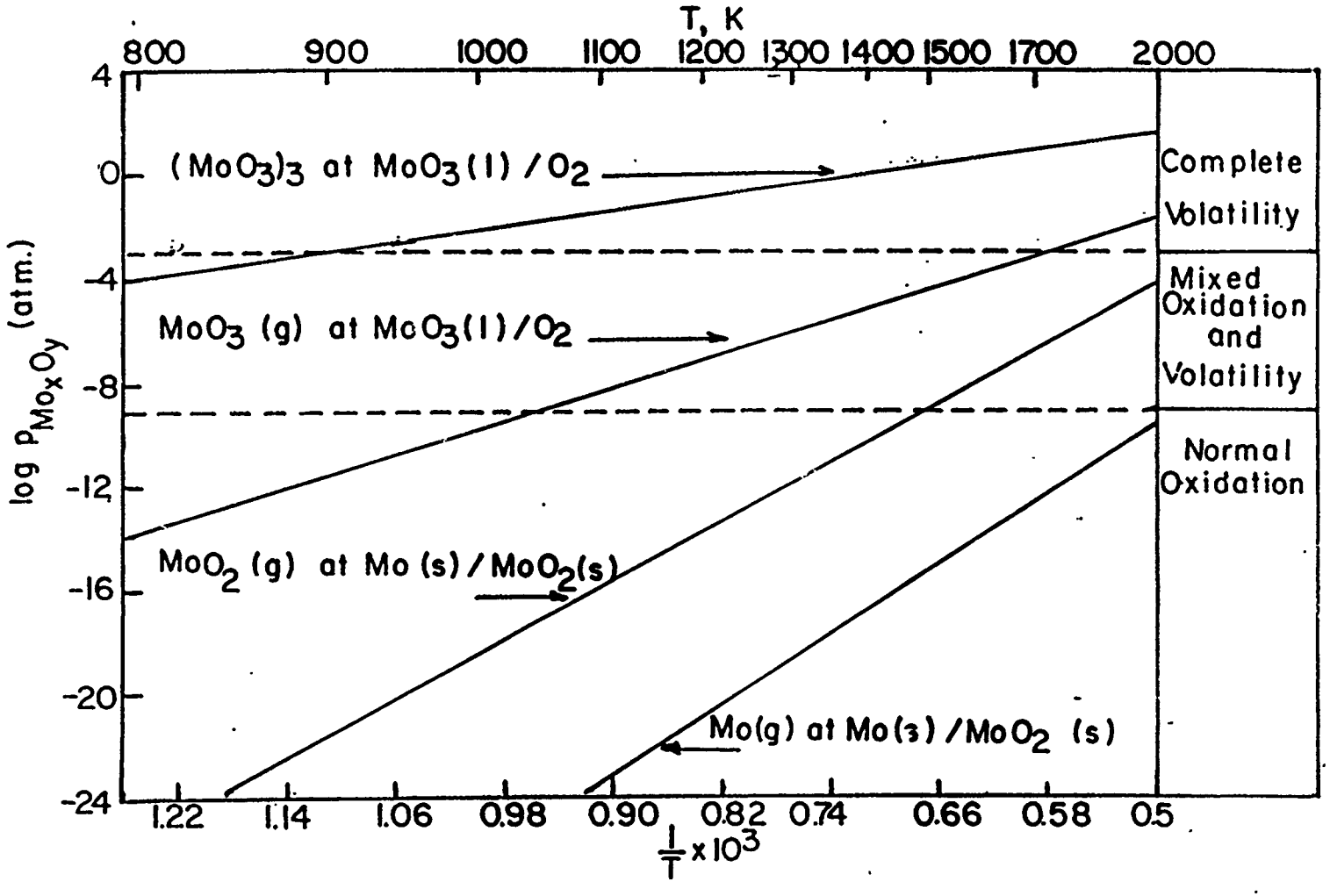

Figure 17. Mo - O System: Volatile Species vs. Temperature.

Part II

Hydrogen in Titanium Aluminides

Anthony W. Thompson, Principal Investigator
Carnegie Mellon University

Detailed descriptions of research progress in the Carnegie Mellon program on hydrogen in aluminide compounds have been presented in previous quarterly reports. Since much of that information has now been published or is in press, this final report takes the form of an overview summary, together with a list of program-sponsored publications and copies of key items among those publications.

A very extensive study has been performed to identify fundamentals of hydrogen effects in titanium aluminides, particularly in the alloy Ti-24 Al-11 Nb, but also including some work on TiAl. Although a few additional papers are still in preparation, the list of 13 papers sponsored under this program which is appended to this report identifies the principal papers, both general and detailed experimental reports of the work. A number of "firsts" were part of this work, as mentioned below.

Little understanding of hydrogen uptake in titanium aluminides was available at the start of this program, with reports ranging from no observed uptake at all, to amounts of several atomic per cent. Reported temperature-pressure-composition relations were sketchy and inconsistent with each other. Using a Sieverts apparatus and standard techniques for evaluation of gas-metal interaction, we conducted experiments to show that reversible, reproducible hydrogen uptake measurements could be made, using the α_2 alloy based on Ti_3Al, Ti-24 Al-11 Nb (in atomic per cent, called "Ti-24-11" below). These experiments, first reported at a NASP workshop [1] (reference numbers are to sponsored publications) and later submitted in complete form to a journal [11], determined not only the total uptake of hydrogen but also the solvus between hydrogen in α_2 solid solution, and hydrogen present as the hydride phase, as well as the thermodynamic parameters associated with hydrogen solution and hydride formation, such as the standard free energies, entropies and enthalpies, related as $\Delta G^\circ = \Delta H^\circ - T\Delta S^\circ$. The solvus is shown in the attached copy of ref. 11 as Fig. 4, and it clearly indicates the extensive hydrogen solubility at elevated temperature in this alloy.

As is implied by this solvus, the room temperature solubility of hydrogen in Ti-24-11 is very small. Calculation using thermodynamic parameters, or extrapolation to room temperature of the solvus using a spline fit, both suggest an estimated solubility of around 10 ppb at ambient temperature. All the remaining absorbed hydrogen precipitates as hydrides. Our report [1] of this hydride formation was among the earliest published, as has been reviewed [9]. In agreement with

other authors, we have found the hydride to have the same FCC fluorite structure as the binary Ti-H hydride, called "TiH_2" and readily determinable by X-ray or electron diffraction. At higher hydrogen content, the FCC structure becomes somewhat tetragonal [4,7,9,11], and is accordingly called FCT, although the conventional crystallographic convention is to call this structure BCT (the two are identical except for the size of the unit cell). The FCT notation avoids giving the impression that a fundamental structure change occurs, as might be inferred by a change from FCC to BCT.

Very extensive investigation of mechanical properties of hydride-containing Ti-24-11 material was carried out, ranging from simple tensile and compression tests, to notched bend and pre-cracked compact tension specimens, permitting determination of a number of fundamental mechanical parameters. Properties were determined as a function of both hydrogen (hydride) content and temperature, including yield and ultimate tensile strength, ductility, notched bend fracture stress and local true fracture stress, and valid fracture toughness K_{Ic}. Examples are given in the attached copy of ref. 9, and these results have been reported in complete form [1,2,4,7-9,12] well in advance of any other mechanical property publications for α_2 alloys containing hydrogen.

When experiments were begun to extend the foregoing results to other microstructures of Ti-24-11, inasmuch as the first suite of experiments had all been done on a single microstructure, it appeared convenient to conduct heat treatments in hydrogen, thus achieving hydrogen uptake and microstructural modification at the same time. It was of course recognized that hydrogen is a stabilizer of the beta phase in titanium alloys, and experience with conventional α alloys suggested that the β stabilization should itself be studied as a potentially significant effect. It was immediately observed that a profound degree of microstructural modification was achieved by the presence of hydrogen, in particular microstructural refinement of scale produced by β stabilization to lower temperatures and thus lower transformation temperatures of β to α_2. These refinement effects resulted in greatly enhanced strength *and* ductility, thus considerably increasing toughness [3,5], when the alloy was tested after removal of hydrogen but with the refined microstructure still present. These results are generally similar to, but somewhat larger than, what has been found for conventional α+β alloys with hydrogen as a temporary β stabilizer, as reviewed elsewhere [5].

Finally, the program on Ti-24-11 was extended to make measurements in the hydrogen environment [7], e.g. at temperatures such as 400°C, to examine behavior which may be affected by the kinetics of hydrogen uptake. Behavior, however, was not much different than for specimens which had been precharged with hydrogen, indicating, at least at 400°C, that transport of hydrogen is not a major influence on embrittlement. This in turn indicates either that the films of β phase, which are nearly continuous or continuous despite representing at most a few per cent of the microstructure we predominantly tested, are serving as short-circuit paths for hydrogen, or that hydrogen transport is associated with dislocations, as pipe diffusion paths or moving with the

dislocation in the form of hydrogen atmospheres. Examples of these results are shown in Figs. 7 and 8 of the attached copy of ref. 9.

Preliminary work on the TiAl stoichiometric alloy (49.9 atomic per cent Al) was undertaken to determine if the hydrogen uptake and mechanical property techniques would be equally effective for the TiAl or γ structure. For this alloy, not only were there few reports of hydrogen effects, but most such reports, for example at NASP workshops, were concluding that hydrogen had no adverse effects on TiAl. It is now clear that those results were obtained for specimens which absorbed little or no hydrogen. In our Sieverts system, large total hydrogen uptakes were observed [8-10,13], as shown in Fig. 10 of the attached copy of ref. 10, though at a given temperature the amounts are less than in Ti-24-11. Once again, the room temperature solubility is predicted to be very small, so that virtually all absorbed hydrogen is precipitated as hydrides. We again determined that these hydrides have the FCC or FCT structures familiar from binary Ti-H hydrides [10,13].

Mechanical properties were studied on various grain sizes, as a microstructural variation in the single-phase material. It was soon found [6] that the effect of grain size on yield strength was small, particularly when compared to published inferences, as shown in the attached copy of ref. 10, Fig. 6. Yield strength was also studied in the presence of hydrides [10,13], and although these results were only preliminary, the pattern (see attached ref. 10, Fig. 12) suggests rather less effect on strength than in the case of the Ti-24-11.

Publications sponsored under this program

1. A.W. Thompson, W.-Y. Chu and J.C. Williams, "Hydrogen in Titanium Aluminides", in *Summary Proceedings of the 2nd Workshop on Hydrogen-Materials Interaction*, H.G. Nelson, ed., NASP Joint Program Office Workshop Pub. 1004, NASA-Ames, Moffett Field, CA, Nov. 1988, pp. 133-135.

2. A.W. Thompson and W.-Y. Chu, "Mechanical Behavior of the Titanium Aluminide Alloy Ti-24-11," in *Summary Proceedings of the 3rd Workshop on Hydrogen-Materials Interaction*, H.G. Nelson, ed., NASP Joint Program Office Workshop Pub. 1007, NASA-Ames, Moffett Field, CA, Aug. 1990, pp. 125-130.

3. W.-Y. Chu and A.W. Thompson, "The Effect of Microstructure and Hydrogen as a Temporary Beta Stabilizer on Cleavage Fracture Behavior in Titanium Aluminide," in *Hydrogen Effects on Material Behavior*, N.R. Moody and A.W. Thompson, eds., TMS-AIME, Warrendale, PA (1990), 285-296.

4. W.-Y. Chu, A.W. Thompson, and J.C. Williams, "Brittle Fracture Behavior and Influence of Hydride in Titanium Aluminide," in *Hydrogen Effects on Material Behavior*, N.R. Moody and A.W. Thompson, eds., TMS-AIME, Warrendale, PA (1990), 543-553.

5. W.-Y. Chu and A.W. Thompson, "Effect of Hydrogen as a Temporary β Stabilizer on Microstructure and Brittle Fracture Behavior in a Titanium Aluminide Alloy," *Metall. Trans. A*, 22A (1991) 71-81.

6. W.-Y. Chu and A.W. Thompson, "Effects of Grain Size on Yield Strength in TiAl," *Scripta Metall. Mater.*, 25 (1991) 641-644.

7. W.-Y. Chu and A.W. Thompson, "Hydrogen Induced Cracking and Microstructure Effect in Titanium Aluminide," in *High Performance Composites for the 1990's*, S.K. Das, C.P. Ballard and F. Marikar, eds., TMS-AIME, Warrendale, PA, in press.

8. A.W. Thompson and W.-Y. Chu, "Hydrogen Effects in Titanium Aluminides," in *Summary Proceedings of the 4th Workshop on Hydrogen-Materials Interaction*, H.G. Nelson, ed., NASP Joint Program Office Workshop Pub., NASA-Ames, Moffett Field, CA, in press.

9. A.W. Thompson, "Environmental Effects in Titanium Aluminide Alloys," in *Environmental Effects on Advanced Materials*, R.E. Ricker and R.H. Jones, eds., TMS-AIME, Warrendale, PA, in press.

10. A.W. Thompson and W.-Y. Chu, "Effect of Grain Size and Hydrides on Mechanical Behavior of TiAl," in *Microstructure/Property Relationships in Titanium Alloys and Titanium Aluminides*, R.R. Boyer and J.A. Hall, eds., TMS-AIME, Warrendale, PA, in press.

11. W.-Y. Chu, A.W. Thompson and J.C. Williams, "Hydrogen Solubility in a Titanium Aluminide Alloy", *Acta Metall. Mater.*, submitted.

12. W.-Y. Chu, A.W. Thompson, and J.C. Williams, "Brittle Fracture Behavior and Influence of Hydride in Titanium Aluminide," *Metall. Trans. A*, submitted.

13. W.-Y. Chu and A.W. Thompson, "Effect of Microstructure and Hydrides on Fracture in TiAl," *Scripta Metall. Mater.*, submitted.

Appendix II

Effect of Hydrogen as a Temporary β Stabilizer on Microstructure and Brittle Fracture Behavior in a Titanium Aluminide Alloy

REF. 5

WU-YANG CHU and ANTHONY W. THOMPSON

Microstructures of Ti-24Al-11Nb were solution treated in either the $\alpha_2 + \beta$ or β phase field under vacuum or hydrogen gas, followed by air (AC), furnace (FC), or controlled cooling (CC), and then aged or outgassed at 800 °C. All mechanical tests were on hydrogen-free specimens. If 1147 °C β solution treatment (ST) was followed by AC, hydrogen as a temporary β stabilizer clearly decreased the size of the α_2 phase and increased greatly the retained or transformed β phase content. As a result, room-temperature tensile strength, fracture strength (σ_F), ductility (ε_f), and fracture toughness (K_{Ic}) resulting from 1147 °C solution treating in hydrogen increased by 120, 100, 60, and 42 pct, respectively, as compared with that under vacuum. If β ST was followed by FC, hydrogen as a β stabilizer increased only the β phase content but did not decrease the size of α_2 phase or colony; and made ultimate tensile strength (UTS), σ_F, ε_f, and K_{Ic} increase only moderately. Cooling from the $\alpha_2 + \beta$ phase field (1000 °C or 1075 °C), hydrogen as a β stabilizer changed the size of transformed α_2 phase and UTS, σ_F, ε_f, and K_{Ic} increased slightly. Properties were also a function of crosshead speed. For all microstructures, α_2/β boundaries appeared to be effective barriers to slip and crack initiation.

I. INTRODUCTION

TITANIUM aluminide materials based on Ti_3Al with additions of Nb are relatively brittle and fracture by a cleavage-like mechanism at or near room temperature. The effects of the strain rate and hydride content on the brittle fracture behavior, apparent cleavage fracture strength, and fracture toughness have been investigated.[1] Because the mechanical properties and the fracture behavior of conventional $\alpha + \beta$ titanium alloys have been shown to be strongly dependent on microstructure,[2,3,4] the same could be expected to be true for titanium aluminide. Recently, the effect of microstructure on the mechanical properties and creep have been studied in some $\alpha_2 + \beta$ titanium aluminides.[5-8] However, there have been no detailed investigations of the influence of microstructure on cleavage fracture behavior in titanium aluminide. Theretore, one of the purposes of this work was to investigate the effect of microstructure on the mechanical properties, fracture strength, σ_F, and fracture toughness, K_{Ic}.

The solubility of hydrogen in α_2 titanium aluminide is very high at high temperature, but the terminal solubility of hydrogen at room temperature is very low, so that almost all hydrogen is precipitated as hydride.[9] The high solubility of hydrogen at high temperature in conventional titanium alloys has led to the utilization of hydrogen as a temporary alloying element.[10,11] As a β stabilizer, hydrogen was found to affect the phase transformation in the conventional $\alpha + \beta$ titanium alloy Ti-6Al-4V, which resulted in a unique, fine microstructure.[11] The same might be true for the titanium aluminide. Therefore, the other purpose of this paper was to investigate the effect of hydrogen as a temporary alloying element on microstructure and on the mechanical properties, particularly fracture properties, of hydrogen-free material.

II. EXPERIMENTAL PROCEDURE

The material used for this investigation was Ti-24Al-11Nb (at. pct), called Ti-24-11 below, in the form of a forged cylinder of 140-mm diameter. The chemical composition was analyzed to be, in atomic percent, 25.3Al, 10.8Nb, $0.25O_2$, 0.033Fe, 0.017N, and balance Ti.

The specimens tested included a flat tensile with a gage section of 17 × 0.4 mm; a three-point bend bar of 2.5-mm thickness and 5-mm width containing a Charpy-type notch[12] of 1.67-mm depth, a 45-deg flank angle, and a root radius of 0.25 mm; and a modified wedge-opening loading (WOL) specimen[13] with a thickness of 10 mm. All specimens were oriented such that the gross fracture plane was parallel to the forging direction.

Microstructures were controlled by solution treating in either the $\alpha_2 + \beta$ or the β phase field under vacuum or one atmosphere hydrogen gas, respectively. The two kinds of solution treatment (ST) are referred to below as VST (vacuum) or HST (hydrogen). The β transus temperature for the Ti-24-11 alloy with low oxygen has been reported to be in the range of 1079 °C to 1095 °C.[5,6] Transformed β microstructures were produced by a 1.5-h/β ST at 1147 °C under vacuum or hydrogen gas, respectively, followed by air cooling (AC) in a quartz tube (average cooling rate of 180 °C/min from 1147 °C to 800 °C), furnace cooling (FC, 5 °C/min) and controlled cooling (CC, 0.8 °C/min); and 1225 °C VST or HST followed by AC $\alpha_2 + \beta$ solution treatments were done at 1000 °C and 1075 °C VST or HST, followed by AC.

WU-YANG CHU, formerly Visiting Professor, Carnegie Mellon University, is Professor, Department of Materials Physics, Beijing University of Science and Technology, Beijing 100083, People's Republic of China. ANTHONY W. THOMPSON, Professor, is with the Department of Metallurgical Engineering and Materials Science, Carnegie Mellon University, Pittsburgh, PA 15213.

Manuscript submitted September 8, 1989

The furnace with specimens was kept in high vacuum or filled with one atmosphere hydrogen, respectively, after the vacuum reached 0.67 mPa (5×10^{-6} torr) or less, then heated to the solutionizing temperatures. After cooling to room temperature, the specimens were aged or dehydrogenated, respectively, in vacuum at 800 °C for 3 hours. The furnace with hydrogenated specimens was pumped down to 0.67 mPa or less, then heated to and maintained at 800 °C until the chamber pressure again reached 0.67 mPa or less, which took about 2 hours. The hydrogen contents of specimens were determined by weighing specimens on a microbalance[11] before and after hydrogenation or dehydrogenation. Sometimes there was a net weight gain (<300 wppm) after dehydrogenation in the WOL specimens, which was attributed to oxygen pickup during the cycle.[11] However, all specimens tested were nominally free of hydrogen.

The tensile and bending tests were conducted on an Instron machine with crosshead speeds varying from 5×10^{2} mm/min to 5×10^{-2} mm/min. The three-point notched bend specimen was used to measure the nominal fracture stress $\sigma_{nom} = 6M/bh^2$, where M is the maximum bending moment, h is the specimen depth below the notch, and b is the thickness.[12,13,14] The true local fracture strength, σ_F, *i.e.*, the maximum local tensile stress under the notch at fracture, was calculated in the established fashion[12-15] based on σ_{nom}, the YS at the same crosshead speed, and the plastic stress concentration factor σ_{max}/YS obtained by Griffiths and Owen.[12,14] At the highest crosshead speed (500 mm/min), σ_{nom}/UTS was generally less than 0 5, and an elastic stress concentration factor $\sigma_{max}/\sigma_{nom} = 2.78$ was used to get σ_F.[1]

The modified WOL specimen was used to measure the resistance (R) curve[13] to brittle crack propagation and the fracture toughness, K_{Ic}, which is the critical stress intensity factor corresponding to crack propagation of 2 pct.[1,13]

The fracture surface of each tested specimen was examined by scanning electron microscopy (SEM) to determine both gross fracture appearance and also fracture process details.

III. EXPERIMENTAL RESULTS

A. *Microstructural Development and the Effect of Hydrogen*

The temporary hydrogen contents after hydrogenation at the solutionizing temperatures were 5 to 7 at. pct in the WOL specimens (B = 10 mm) and 10 to 13 at. pct in the tensile (B = 0.4 mm) and bend (B = 2.5 mm) specimens, respectively, as shown in Table I. Although this size dependence suggests a surface effect, other experiments have not confirmed such an effect.

Figures 1(a) and (b) illustrates the microstructures resulting from 1147 °C VST and HST, respectively, followed by AC. The significant variables in these microstructures were the size and morphology of α_2 phase and the amount of retained or transformed β phase. Hydrogen as a temporary β stabilizer evidently affects the kinetics of the phase transformation following treatment in the β field, which results in unique and fine α_2 and a large amount of retained or transformed β phase.

Increasing the temperature of ST in the β phase field under vacuum slightly increased the amount of the retained or transformed β phase, comparing Figure 1(c) with Figure 1(a). In this case, adding 5 to 7 at. pct hydrogen also decreased the size of the α_2 phase and increased the amount of the retained β phase, as shown in Figures 1(c) and (d).

The microstructures resulting from $\alpha_2 + \beta$ ST followed by AC are shown in Figure 2. The $\alpha_2 + \beta$ process under vacuum produced large and elongated primary α_2 in a transformed β matrix. Adding 5 to 7 at. pct hydrogen decreased the size of the transformed α_2 phase and increased the amount of the retained β phase rather than changing the size and morphology of the primary α_2 phase.

Furnace cooling (5 °C/min) and controlled cooling (0.8 °C/min) after 1147 °C β VST produced moderate-sized colonies of similarly aligned plates, as shown in Figure 3(a). Adding 5 to 7 at. pct hydrogen as a temporary β stabilizer increased the amount of the retained β even though it did not change the size of the α_2 platelets and colonies, comparing Figure 3(b) with Figure 3(a).

B. *Room-Temperature Tensile Properties*

The variations in tensile properties of hydrogen-free material with solutionizing temperature for both VST and HST are shown in Figure 4. The strength, both 0.2 pct YS and UTS, and the fracture strain (ε_f), resulting from 1147 °C β HST were 120 and 60 pct, respectively, higher than that for VST because hydrogen as a temporary β stabilizer evidently increased the retained or transformed β phase content and decreased significantly the size of α_2 phase (Figure 1).

Increasing the temperature of β solution treating under vacuum from 1147 °C to 1225 °C made the strength, *i.e.*, YS and UTS, increase by 20 pct. On the other hand, the strength and ε_f resulting from 1225 °C HST increased by 57 and 36 pct, respectively, as compared with that for VST (Figure 4).

The YS, UTS, and ε_f resulting from 1000 °C $\alpha_2 + \beta$ HST all increased by about 30 pct, as compared with

Table I. Temporary Hydrogen Content (Atomic Percent)

	Temperature (°C)				
	$\alpha_2 + \beta$ Field		β Phase Field		
Sample	1000/AC	1075/AC	1147/AC	1147/FC	1225/AC
WOL	4.9 to 5.4	6.1 to 7.5	5 0 to 5.7	5.0 to 6.7	5.4 to 7.7
Tensile, bend	10.8	11.5	12 6	10.2	13 0

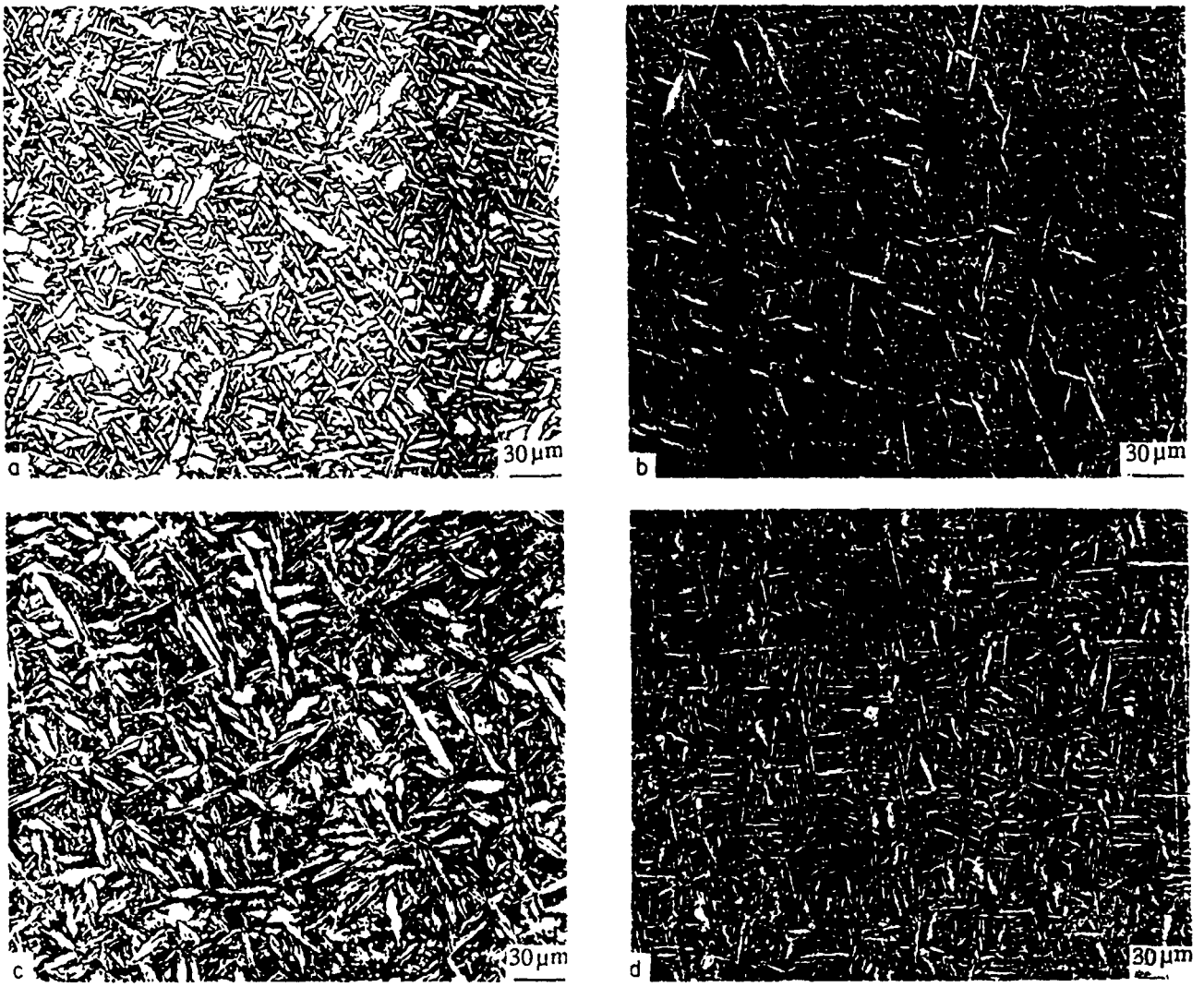

Fig 1—Microstructures resulting from β ST in vacuum (VST) or in hydrogen (HST), followed by AC and aging or outgassing at 800 °C. Light microscopy of samples taken from center of WOL specimens (*a*) VST at 1147 °C, (*b*) HST at 1147 °C, (*c*) VST at 1225 °C, and (*d*) HST at 1225 °C

that for VST If the temperature of the $\alpha_2 + \beta$ solution treating under hydrogen was 1075 °C, the strength and ε_f increased by 20 and 5 pct, respectively.

In the microstructures resulting from 1147 °C β VST and HST, both strength and ductility decreased as cooling rate decreased from 180 °C/min (AC) to 5 °C/min (FC), as shown in Figure 5.

Furnace cooling and controlled cooling resulted in similar microstructures and in comparable values of strength and ductility. Slow cooling, resulting in moderate-sized colonies, produced low strength and ductility, which was consistent with Blackburn *et al* 's result.[5] On the other hand, the efficacy with which hydrogen as a temporary β stabilizer increased both strength and ductility through microstructural refinement evidently decreased as cooling rate decreased For example, in the furnace-cooled condition, hydrogen as a temporary β stabilizer made the strength and ductility (ε_f) increase 10 and 20 pct instead of 120 and 58 pct in the air-cooled condition

When the tensile properties are considered as a function of strain rate, it can be seen that UTS decreased rapidly at the highest strain rate, 0.5/s, corresponding to a crosshead speed of 500 mm/min, but attained a constant value for strain rates lower than 5×10^{-3}/s, corresponding to 5 mm/min, independent of microstructure, as shown in Figure 6. At the highest strain rate, the effects of microstructure and hydrogen as a temporary β stabilizer on the strength and ductility were negligible, as in previous work.[1]

C. *Nominal Fracture Stress and Brittle Fracture Strength*

The nominal fracture stress measured by a three-point notched bend bar is characterized as a function of crosshead speed with the above-mentioned microstructures in Figure 7(a), which indicates that at crosshead speeds less than 50 mm/min, the nominal fracture stress, σ_{nom}, resulting from 1147 °C HST followed by AC has gone up 120 pct over that for VST + AC, but at the highest

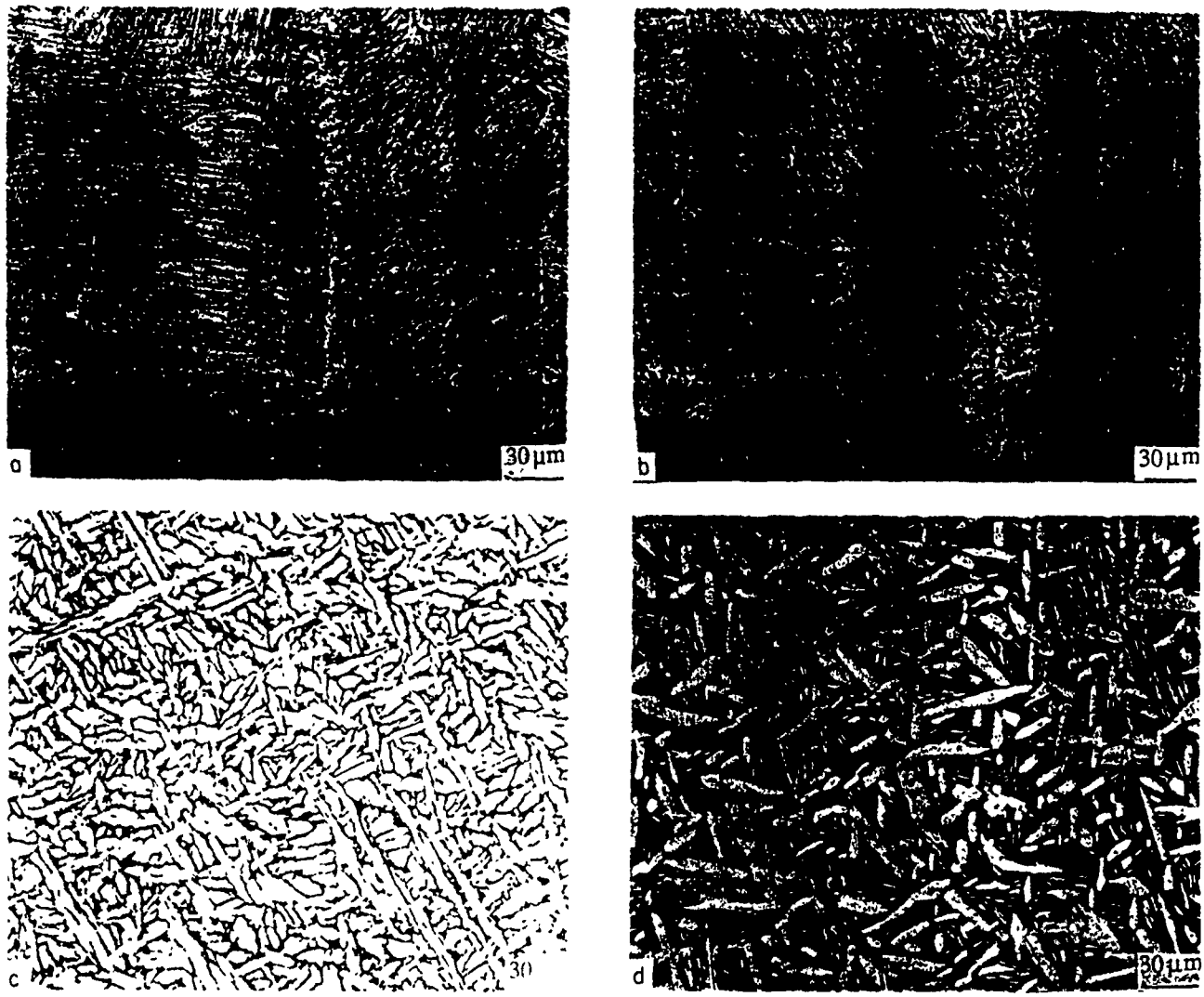

Fig 2—Microstructures resulting from ST in the $\alpha_2 + \beta$ phase field in vacuum (VST) or hydrogen (HST), followed by AC and aging or outgassing at 800 °C Light microscopy of samples taken from center of WOL specimens: (*a*) VST at 1000 °C, (*b*) HST at 1000 °C, (*c*) VST at 1075 °C; and (*d*) HST at 1075 °C.

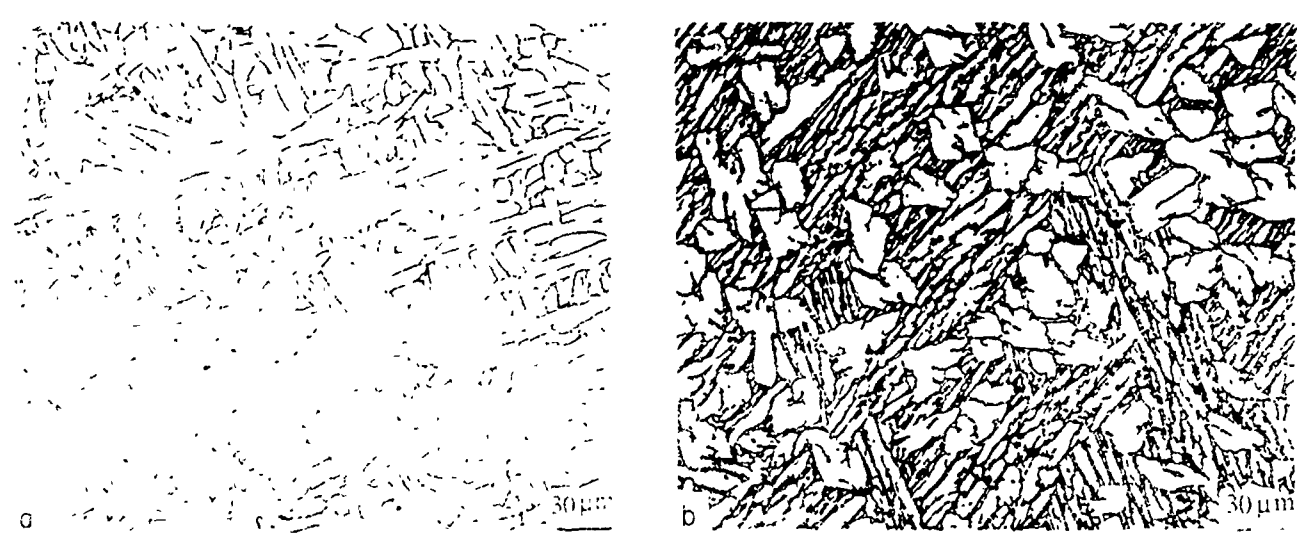

Fig 3—Microstructures resulting from the treatment of Figs 1(a) and (b), namely VST or HST at 1147 °C, but followed by FC (*a*) VST and (*b*) HST

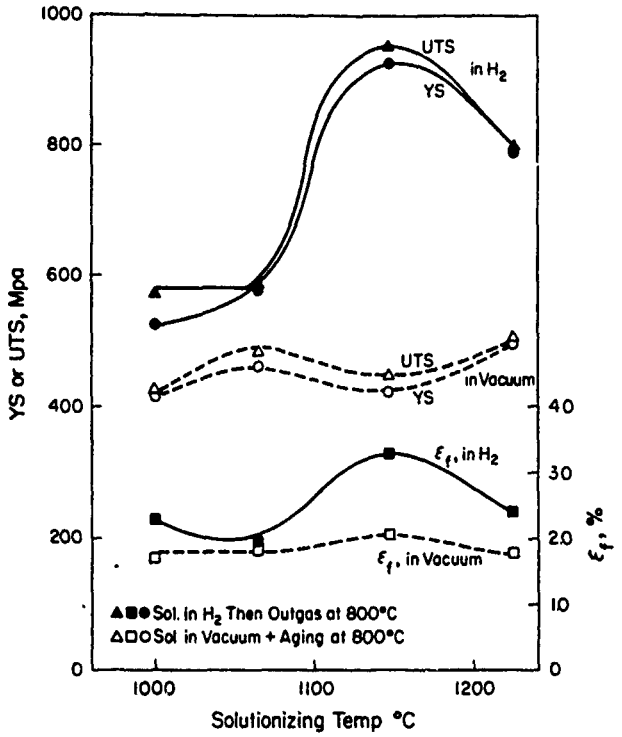

Fig. 4—Dependence of tensile properties on solutionizing temperature, comparing VST and HST materials which were air cooled. Properties shown are YS, UTS, and ε_f. Each value shown is the average of 5 to 6 tests.

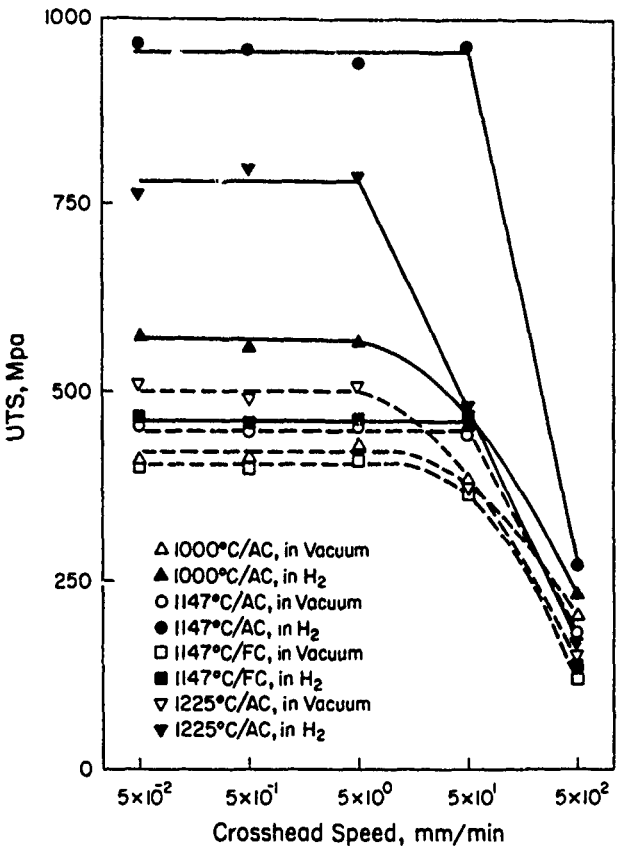

Fig. 6—Effect of strain rate, expressed as crosshead speed, on UTS or fracture stress, for various VST and HST microstructures. All values are averages of 3 to 6 tests.

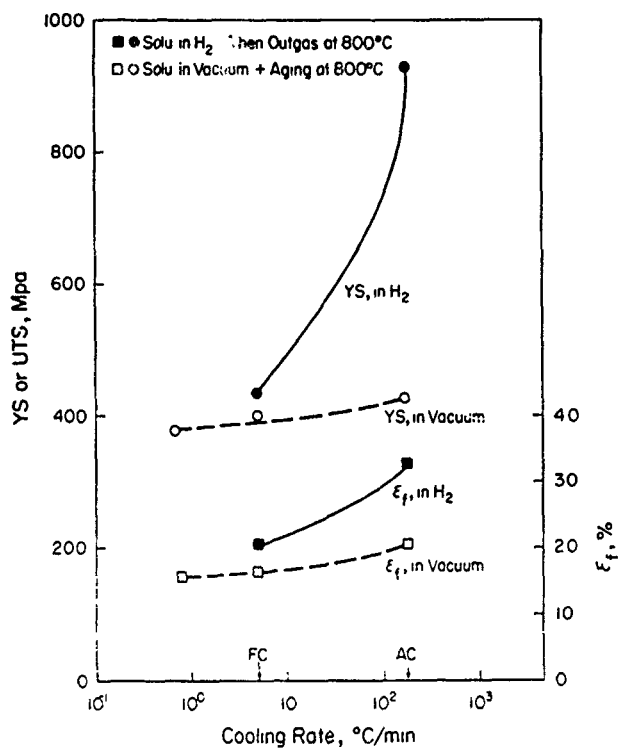

Fig. 5—Dependence of tensile properties, as in Fig. 4, on cooling rate from a ST temperature of 1147 °C, comparing VST and HST material. All values are averages of 5 to 6 tests.

crosshead speed, *i.e.*, 500 mm/min, there is little difference between VST and HST. In the furnace-cooled condition, σ_{nom} values resulting from 1147 °C were identical with those for VST at any crosshead speed studied. Figure 7(a) also shows that σ_{nom} results from 1000 °C HST followed by AC have the same values with those for VST, independent of crosshead speed.

The brittle fracture strength, σ_F, with aforesaid microstructures, which is calculated from σ_{nom}, YS, and the plastic stress concentration factor,[12,13,14] as a function of crosshead speed is indicated in Figure 7(b), which is very similar to the UTS and σ_{nom} curves (Figures 6 and 7(a)).

The brittle fracture strength, σ_F, *vs* solutionizing temperature for both VST and HST is shown in Figure 8, which is similar to the dependence of YS on solutionizing temperature (Figure 4). Figure 9 is the variation in the σ_F with cooling rate after both 1147 °C VST and HST, which is also similar to that in the YS (Figure 5).

To summarize, when the β ST was followed by AC and the crosshead speed was less than 500 mm/min, adding about 13 at. pct hydrogen as a temporary β stabilizer increased σ_F by 100 pct (1147 °C) and 57 pct (1225 °C ST), respectively; but in the furnace-cooled condition, the σ_F resulting from 1147 °C HST increased only by 4 pct. In other words, cooling rate from β solution temperature, and the attendant microstructural change, is decisive in this hydrogen effect. On the other hand, the σ_f resulting from $\alpha_2 - \beta$ HST increased 15 pct

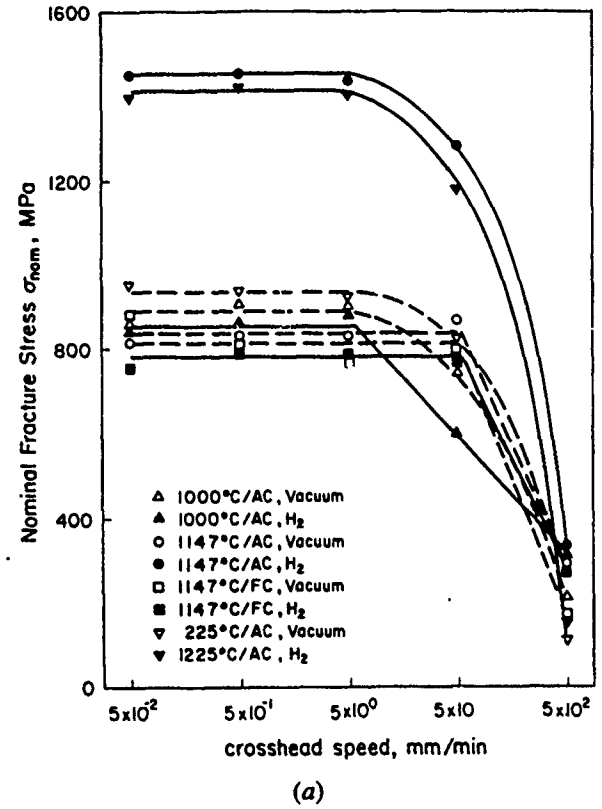

(*a*)

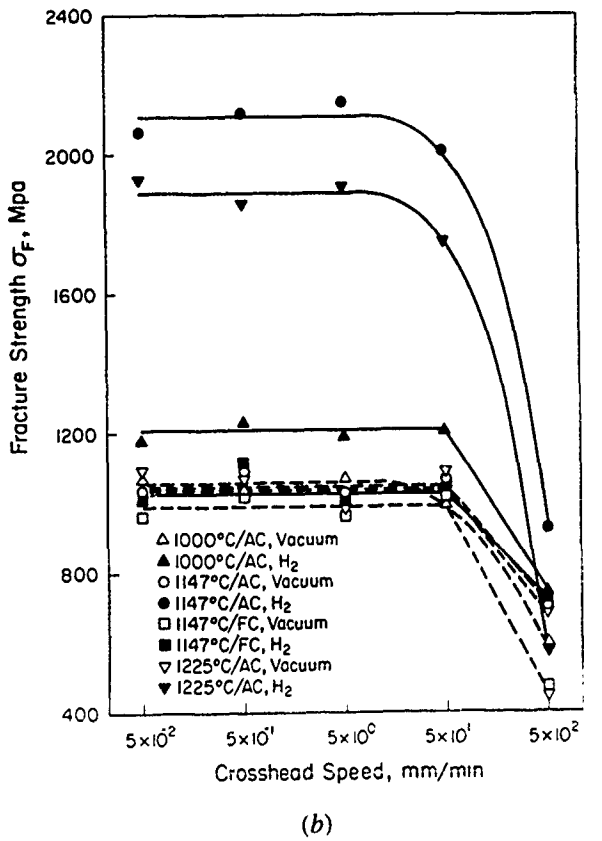

(*b*)

Fig. 7—Effect of strain rate, expressed as crosshead speed, on fracture properties in bend bar tests of VST and HST microstructures (averages of 2 to 4 tests) (*a*) nominal fracture stress and (*b*) true local fracture stress for brittle or cleavage fracture

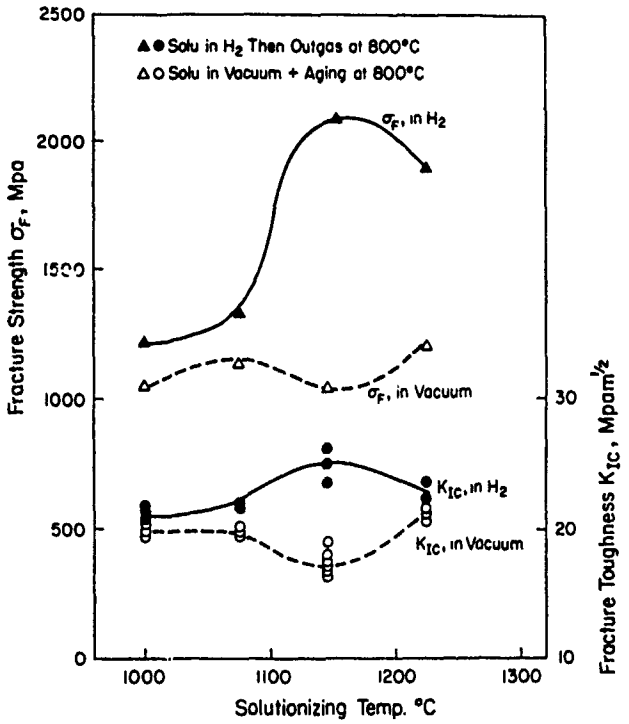

Fig. 8—Dependence of true local fracture stress, σ_f, and fracture toughness, K_{Ic}, on ST temperature for VST and HST material for air-cooled specimens.

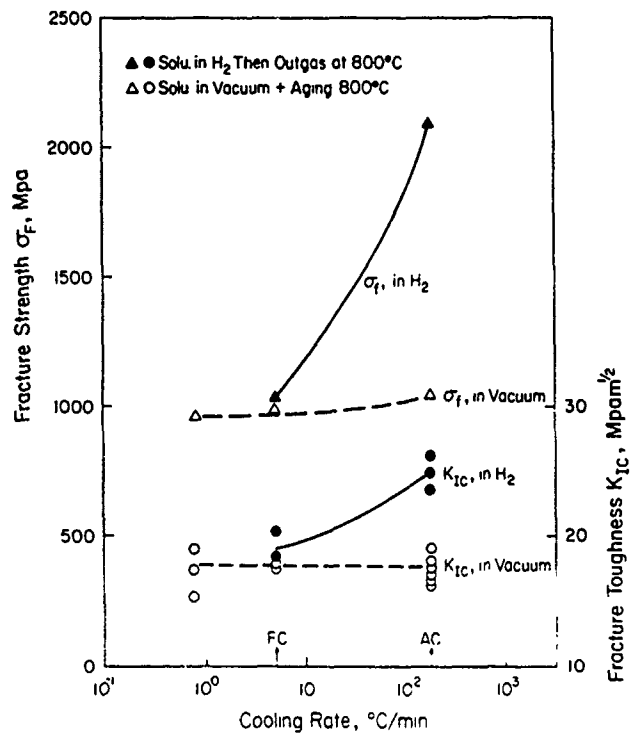

Fig. 9—Dependence of true local fracture stress, σ_f, and fracture toughness, K_{Ic}, on cooling rate from a ST temperature of 1147 °C for VST and HST material

(1000 °C) or 17 pct (1075 °C), compared with those for VST. At the highest crosshead speed, there were negligible effects of the microstructure and hydrogen as a temporary β stabilizer.

D. *Resistance Curve and Fracture Toughness K_{Ic}*

The average propagation speed of the brittle crack in the titanium aluminide was low, so a resistance or R curve for crack propagation could be measured using a modified WOL specimen.[1,13] The typical resistance curves with aforementioned microstructures are shown in Figure 10. The fracture toughness K_{Ic}, which is the critical stress intensity factor corresponding to $\Delta a/a = 2$ pct, can be obtained based on the resistance curves and has also been plotted in Figures 8 and 9. Figures 8 and 9 show that the variation in K_{Ic} with the solutionizing temperature and cooling rate has the same tendency as does σ_F. However, the increase in K_{Ic} by addition of hydrogen as a temporary alloying element was less than the increase in σ_F, particularly for β HST followed by AC. For example, comparing 1147 °C HST followed by AC with VST + AC σ_F increased by 100 pct but K_{Ic} only 42 pct, and after 1225 °C HST, σ_F and K_{Ic} increased 60 and 10 pct, respectively. This may be partially due to the different content of hydrogen as a temporary β stabilizer in the WOL specimens compared to the bend specimens (Table I), although all the mechanical tests were done on hydrogen-free specimens.

E. *Deformation and Cracking*

For $\alpha_2 + \beta$ titanium aluminide, even though the Burgers relationship is expected to exist between α_2 and ordered or disordered retained β phase,[8,16–18] the α_2/β boundaries appear to be effective barriers to slip and act to confine active dislocations to individual α_2 platelets.[1,8,19] Our light microscopy observations are consistent with this view, as shown in Figure 11. When WOL specimens with 1075 °C HST were loaded to K_I = 16.6 MPa $m^{1/2}$, some single slip bands occurred in a primary α_2 platelet at site b (Figure 11(b)). Increasing K_I to 18 MPa $m^{1/2}$, the slip bands were observed in the other primary α_2 platelets at a, c, and d locations, and the secondary slip system was activated in the primary α_2 platelets at a and b sites (Figure 11(c)). In general, the slip was limited to the individual α_2 platelets, particularly for low K_I values. When the plastic deformation developed to a critical extent, the discontinuous brittle cracks, *e.g.*, g in Figure 11(e), initiated preferentially in the α_2 platelets.

Figure 12(a) shows that when the WOL specimen with 1147 °C VST followed by CC was loaded to K_I = 13.9 MPa $m^{1/2}$, the discontinuous crack arrested at an interphase boundary at the b site; and with increasing K_I, the new discontinuous cracks initiated in the individual α_2 phase at b, c, and d locations rather than passing through the α_2/β boundary at the b site. The abovementioned situations are applicable for all microstructures. For example, Figure 12(b) indicates that the brittle cracks in the specimen with 1147 °C VST + AC initiated discontinuously in the individual α_2 platelets.

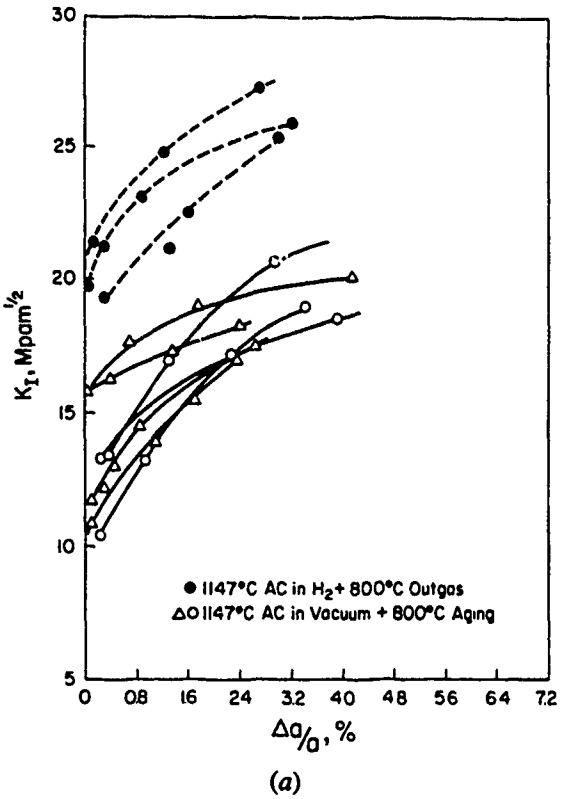

(*a*)

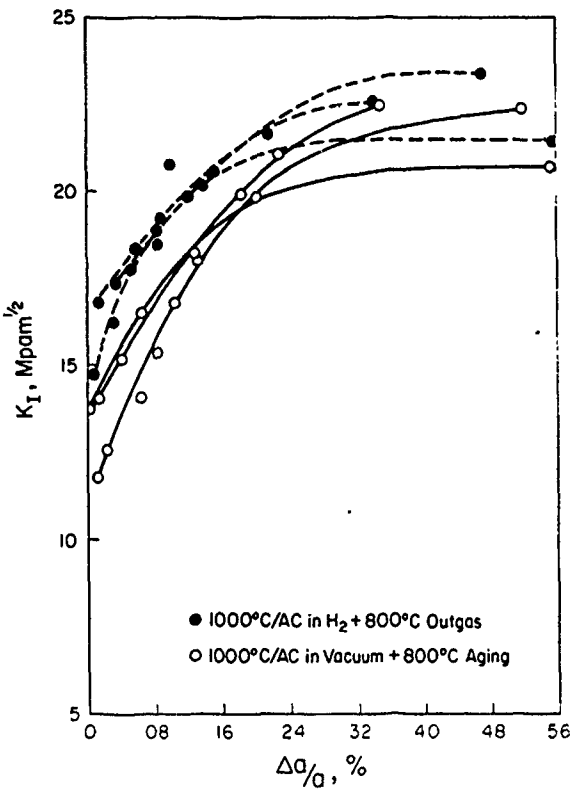

(*b*)

Fig 10—Crack growth resistance or R curves for brittle cracking, showing applied K_I as a function of $\Delta a/a$ (a = crack length), comparing VST and HST material: (*a*) VST and HST at 1147 °C, followed by AC, and (*b*) VST and HST at 1000 °C.

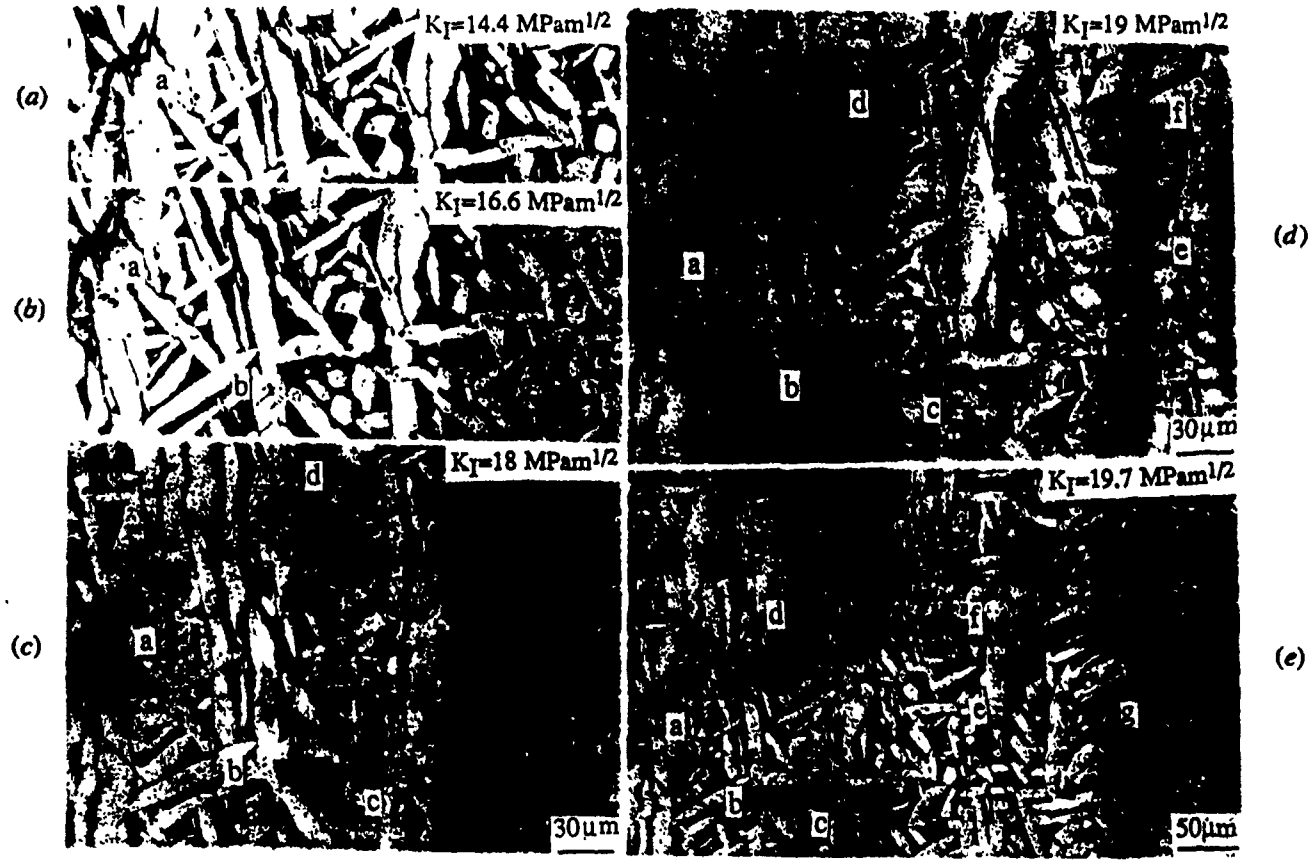

Fig. 11—(*a*) through (*e*) Appearance of deformation and crack initiation and growth with increasing applied K_I for a WOL specimen which received 1075 °C HST, AC, and 800 °C outgassing. Sites (*a*) through (*g*) identified in the light micrographs are discussed in Section III–E.

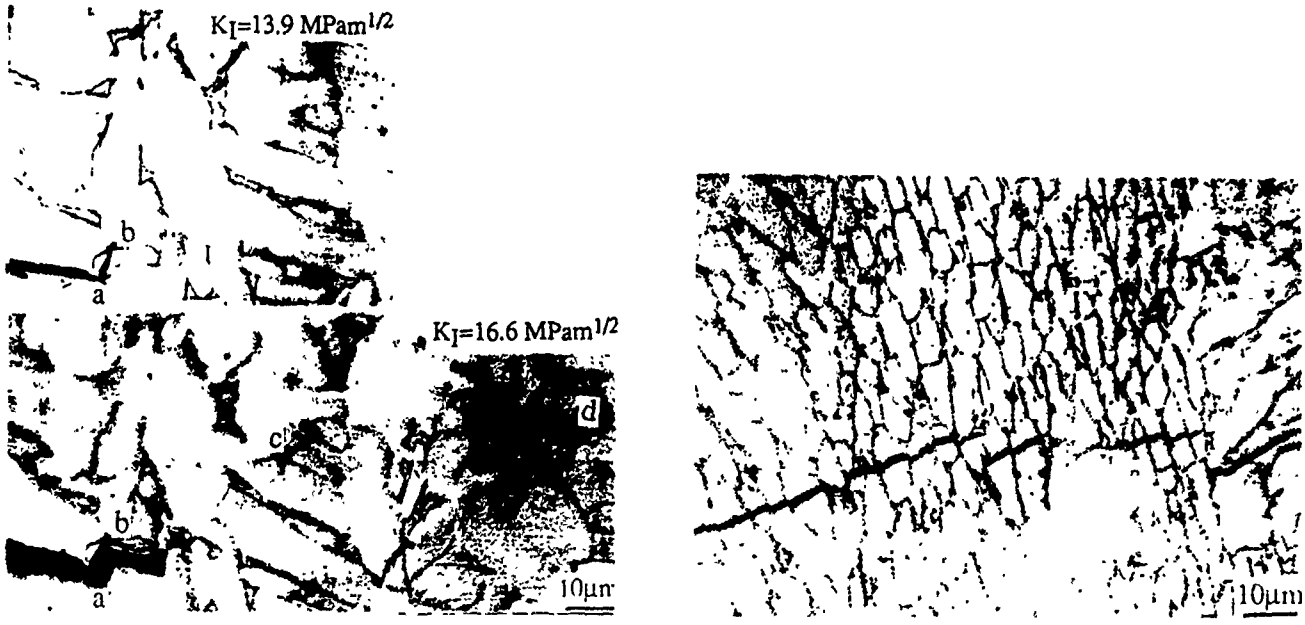

(*a*) (*b*)

Fig 12—Interactions of brittle cracks with microstructural features Light microscopy of WOL specimens. (*a*) Initiation and propagation of cracks within individual α_2 platelets at the K_I levels shown for a specimen given 1147 °C VST and CC. (*b*) Discontinuous brittle cracks apparently arrested at α_2/β interfaces in a microstructure produced by 1147 °C VST and AC

and the interphase boundaries are effective barriers to crack initiation and propagation.

F. *Fractography*

The fracture surface resulting from β HST followed by AC, which consists of small brittle fracture regions with a cleavage-like appearance, surrounded by very small areas of ductile tearing, is evidently different from that for VST, which consists of predominantly larger brittle fracture regions, comparing Figure 13(b) with Figure 13(a). This is consistent with the microstructures shown in Figure 1, because one would expect that cleavage fracture would occur first in the individual α_2 platelets and then join together through ductile tearing of the retained or transformed β phase. That is consistent with Figure 14, which is a fractograph corresponding to the microstructure resulting from 1147 °C HST followed by AC. Note that the fracture units correspond in scale and morphology to the adjacent microstructure in this plateau-etched[20] specimen.

In the furnace-cooled condition, however, the fracture surface resulting from HST seems similar to that under vacuum, as shown in Figures 15(a) and (b). Both fracture surfaces consist of predominantly cleavage-like fracture, and the colonies behave as a unit during this brittle fracture.

Fig. 14—Comparison of fracture surface with microstructural scale and morphology in an 1147 °C HST air-cooled specimen which has been plateau-etched.[20]

Comparing the fracture surface resulting from $\alpha_2 + \beta$ solution treating followed by AC with that under vacuum, there is some difference, because HST can decrease the size of transformed α_2 phase and increase the retained β phase content, as shown in Figures 15(c) and (d).

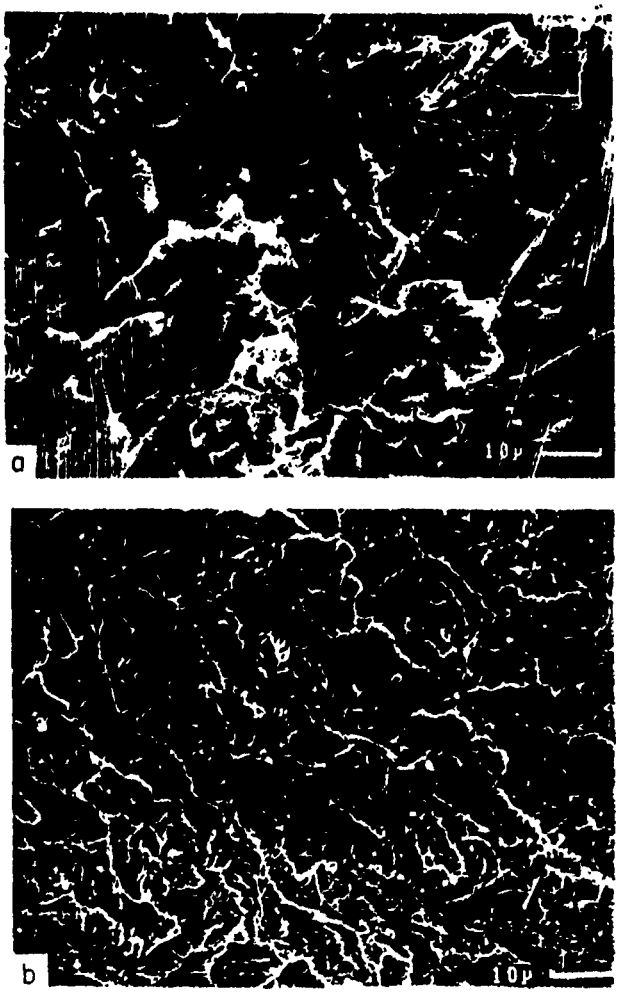

Fig. 13—Fracture surfaces of notched bend bars which were solution treated at 1147 °C and air cooled observed by SEM (*a*) VST and (*b*) HST

IV. DISCUSSION

Addition of Nb, which is a β stabilizer, to Ti_3Al resulted in significant increases not only in ductility but also in strength.[5,6,21] Figure 4 shows that hydrogen as a temporary β stabilizer clearly increased strength if ST was within the β phase field and was followed by AC. There are several possible strengthening contributions[7,22] in the $\alpha_2 + \beta$ titanium aluminide. Included are long-range order strengthening of the α_2 phase, solution strengthening of the individual phases, grain boundary and interphase boundary strengthening, slip length effects, and possibly some texture strengthening.[7] For the titanium aluminide, β grain size was about 2 to 3 mm and was not under the influence of the above-mentioned heat treatments, including solution treating under hydrogen. Hydrogen, as a *temporary* alloying element, will influence neither long-range order strengthening nor solution strengthening of the final material. Therefore, an additional strengthening resulting from hydrogen should be due to increases in the interphase boundary strengthening, reduction in slip length, or some texture strengthening, any of which could result from the microstructure change induced by solution treating under hydrogen gas.

The transfer of slip across an interphase boundary requires some readjustment locally so that the Burgers vector of the slip dislocation in the first phase is conserved between the two structures. On the other hand, elastic

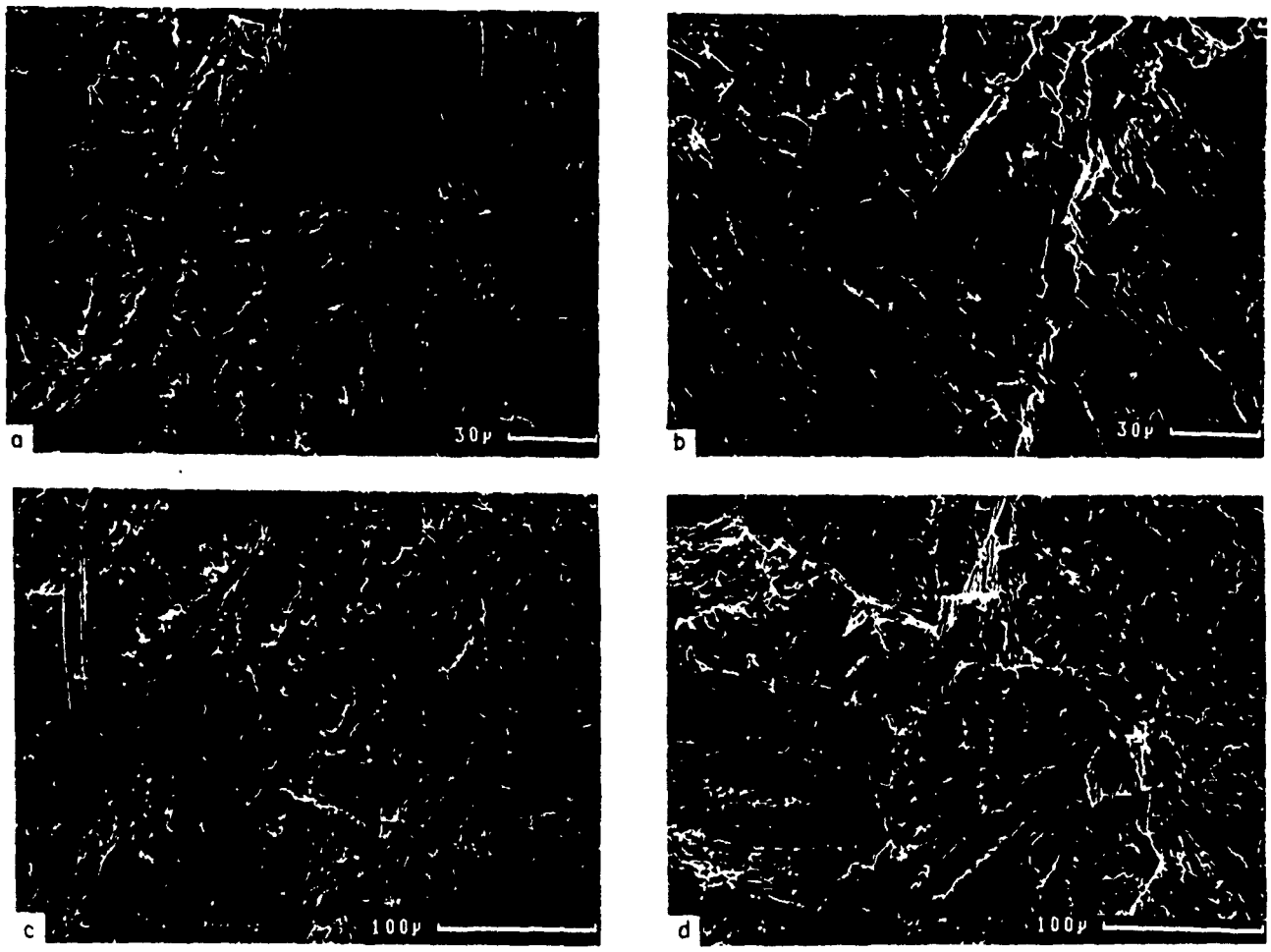

Fig 15—Fractography by SEM of bend bar specimens, showing details of the brittle, cleavage-like fracture. (*a*) 1147 °C VST which was furnace cooled, (*b*) 1147 °C HST which was furnace cooled, (*c*) 1000 °C VST plus AC, and (*d*) 1000 °C HST plus AC.

constraint also increases the local flow stress and provides a substantial additional increment in strength. Therefore, the unique, fine α_2 phase surrounded by fine retained or transformed β phase, which is just the microstructure resulting from β HST followed by AC, will result in the largest strengthening effect. In addition, slip is limited in the individual α_2 platelets, particularly in the earlier period of plastic deformation (Figure 11); thus, the narrower the α_2 platelet, the smaller the slip length, which results in the larger strengthening effect.

Furnace cooling resulted in a moderate size of the α_2 colony and produced low strength. Besides, FC after β HST resulted in only a little increase in strength compared with that under vacuum, because the sizes of the colony and the α_2 were not under the influence of hydrogen as a temporary β stabilizer.

Because the brittle cracks were found to initiate discontinuously within the individual α_2 platelets and the α_2/β interphase boundary is an effective barrier to initiation and propagation of these cracks, the greater the retained or transformed β content and the finer the α_2 platelets surrounded by the β phase, the larger the resistance to brittle crack propagation and the larger the fracture toughness K_{Ic}. K_{Ic} has the same dependence on microstructure as do the fracture strength, σ_f, and the tensile strength. Previous work indicated that the K_{Ic} *vs* hydride content curve was almost parallel to the σ_F *vs* hydride content curve. Therefore, K_{Ic} can be measured against σ_F for this titanium aluminide alloy.

V. CONCLUSIONS

1. For 1147 °C β solution treating followed by AC, hydrogen as a temporary β stabilizer clearly decreased the size of the α_2 phase and increased greatly the retained or transformed β phase content. Consequently, strength, ductility, fracture strength (σ_F), and fracture toughness (K_{Ic}) increased by 120, 60, 100, and 42 pct, respectively, in specimens for which hydrogen was present during $\beta \rightarrow \alpha_2$ transformation but was removed before mechanical tests.
2. Slow cooling, resulting in moderate-sized α_2 colonies produced low values of properties like strength, ductility, σ_f, and K_{Ic}. The solution treating under hydrogen followed by FC did not decrease the size of the α_2 phase and colony but only increased the retained or transformed β content and resulted in only a little increase in various properties. Thus, increases in the retained or transformed β content only were not effective in improving properties.
3. In the $\alpha_2 + \beta$ phase field, hydrogen as a temporary β stabilizer changed the size of transformed α_2 phase

and retained β content, rather than the size and morphology of primary α_2 phase, and resulted in some increases in various properties.

4. Strength, ductility, and σ_F decreased rapidly at crosshead speeds of 50 to 500 mm/min but attained constant values for crosshead speeds less than 50 mm/min, independent of microstructure. At the crosshead speed of 500 mm/min, the effects of microstructure and hydrogen as a temporary alloying element on properties were negligible.
5. For all microstructures, α_2/β boundaries appeared to be effective barriers to slip and to brittle crack initiation and propagation.

ACKNOWLEDGMENTS

We appreciate helpful discussions with J.C. Williams and C.G. Rhodes. This work was sponsored by the Defense Advanced Research Projects Agency, under DARPA Order No. 6155, and monitored by the Air Force Office of Scientific Research under Contract No. F49620-88-C-0013.

REFERENCES

1. W.-Y. Chu, A.W. Thompson, and J.C. Williams: *Metall. Trans. A*, unpublished research, 1990.
2. J.E. Coyne: in *The Science, Technology and Application of Titanium*, Proc. 1st Int. Conf. on Ti, R.I. Jaffee and N. Promisel, eds., Pergamon, New York, NY, 1970, pp. 97-110.
3. D.H. Rogers: in *Titanium Science and Technology*, Proc. 2nd Int. Conf. on Ti, R.I. Jaffee and H.M. Burte, eds., Plenum Press, New York, NY, 1973, vol. 3, pp. 1719-30.
4. J.C. Williams, A.W. Thompson, C.G. Rhodes, and J.C. Chesnutt: in *Titanium and Titanium Alloys*, Proc. 3rd Int. Conf. on Ti, J.C. Williams and A.F. Belov, eds., Plenum Press, New York, NY, 1982, vol. 1, pp. 467-96
5. M.J. Blackburn, D.L. Ruckle, and C.E. Bevan: Technical Report, AFML-TR-78-18, Air Force Materials Laboratory, Wright-Patterson AFB, OH, 1978.
6. M.J. Blackburn and M.P. Smith: Technical Report, AFML-TR-80-4175, Air Force Materials Laboratory, Wright-Patterson AFB, OH, 1980.
7. C.H. Ward, J.C. Williams, A.W. Thompson, D.G. Rosenthal, and F.H. Froes: in *Titanium Science, Technology and Applications*, Proc. 6th World Conf. on Ti, P. Lacombe, R. Tricot, and G. Beranger, eds., Les Editions de Physique, Paris, 1989, pp. 1103-08.
8. W. Cho, A.W. Thompson, and J.C. Williams: *Metall. Trans. A*, 1990, vol. 21A, pp. 641-51.
9. A.W. Thompson, W.-Y. Chu, and J.C. Williams: in *Proc. 2nd Workshop on Hydrogen-Materials Interaction*, H.G. Nelson, ed., NASP Joint Program Office Workshop Pub. 1004, NASA-Ames, Moffett Field, CA, Nov. 1988, pp. 133-35.
10. N. Birla and V. Depierre: Technical Report, AFML-TR-75-171, Air Force Materials Laboratory, Wright-Patterson AFB, OH, 1975.
11. W.R. Kerr: *Metall. Trans. A*, 1985, vol. 16A, pp. 1077-87.
12. J.R. Griffiths and D.R.J. Owen: *J. Mech. Phys. Solids*, 1971, vol. 19, pp. 419-31.
13. J.F. Knott: *Fundamentals of Fracture Mechanics*, Butterworth's, London, 1973.
14. D.J. Alexander, J.J. Lewandowski, W.J. Sisak, and A.W. Thompson: *J. Mech. Phys. Solids*, 1986, vol. 34, pp. 433-54.
15. J.J. Lewandowski and A.W. Thompson: *Acta Metall.*, 1987, vol. 35, pp. 1453-62.
16. J.C. Williams: in *Titanium Science and Technology*, Proc. 2nd Int. Conf. on Ti, R.I. Jaffee and H.M. Burte, eds., Plenum Press, New York, NY, 1973, vol. 3, pp. 1433-94.
17. D. Banerjee, T. Nandi, and A.K. Gogia: *Scripta Metall.*, 1987, vol. 21, pp. 597-601.
18. R. Strychor, J.C. Williams, and W.A. Soffa: *Metall. Trans. A*, 1988, vol. 19A, pp. 225-34.
19. B.J. Marquardt, G.K. Scarr, J.C. Chesnutt, C.G. Rhodes, and H.L. Fraser: in *Titanium, Science, Technology, and Applications*, Proc. 6th World Conf. on Ti, P. Lacombe, R. Tricot, and G. Beranger, eds., Les Editions de Physique, Paris, 1989, vol. 2, pp. 955-63.
20. J.C. Chesnutt and R.A. Spurling: *Metall. Trans. A*, 1977, vol. 8A, pp. 216-18.
21. C.G. Rhodes, C.H. Hamilton, and N.E. Paton: Technical Report, AFML-TR-78-130, Air Force Materials Laboratory, Wright-Patterson AFB, OH, 1978.
22. J.C. Williams and A.W. Thompson: in *Metallurgical Treatises*, J.K. Tien and J.F. Elliott, eds., TMS-AIME, Warrendale, PA, 1981, pp. 487-504.

Scripta METALLURGICA et MATERIALIA
Vol. 25, pp. 641-644, 1991
Printed in the U.S.A.

REF. 6

EFFECTS OF GRAIN SIZE ON YIELD STRENGTH IN TiAl

Wu-Yang Chu* and Anthony W. Thompson
Dept. of Metallurgical Eng. and Materials Science
Carnegie Mellon University
Pittsburgh, PA 15213

*Now at: Dept. of Materials Physics
University of Science and Technology
Beijing 100083, China

(Received December 4, 1990)
(Revised December 27, 1990)

Introduction

The Hall-Petch equation, in which yield strength σ_y is related to grain size d through the relation $\sigma_y = \sigma_0 + k_y d^{1/2}$, where σ_0 and k_y are constants, describes the behavior of many materials (1-5). Vasudevan, *et al.* (6) found that the yield strength in TiAl, an intermetallic compound which has enjoyed considerable recent attention (7), apparently obeyed the Hall-Petch relationship, and they obtained a relatively large value for the constant k_y. However, each of the five data (6,8,9) comprising their Hall-Petch plot was obtained from a separate material which had different composition, microstructure, or both. For example, the Ti-48 at.%Al alloy (9) had a $\gamma+\alpha_2$ structure, while both Ti-52 at.% Al (9) and Ti-54 at.% Al (8) were single-phase γ, and Ti-50 Al-0.4 Er (6) contained a second phase, Er_2O_3, which increased the yield strength (γ is the TiAl phase, α_2 is based on Ti_3Al). In fact, it should not be necessary to infer the grain size dependence of yielding from such a disparate data set, since the size of equiaxed grains of single-phase γ in the TiAl alloys can be readily changed through heat treatments at different temperatures. Therefore, the effect of grain size of single-phase γ on the yield strength can be investigated without changing composition and microstructure. Such measurements were one goal of this work.

For the Ti-50 at.%Al alloy, either equiaxed grains of single-phase γ, or a lamellar structure of intimately mixed γ and α_2, was obtained through heat treatments at different temperatures. In addition to the goal of grain-size investigation, we wished to assess the effect of the lamellar microstructure on the mechanical properties.

Experimental Procedure

Our starting material was a cast and homogenized ingot of TiAl, with composition as follows (in atomic %): Al = 49.9, Fe = 0.16, O = 0.12, N = 0.005, H = 0.14. The specimens were rough-cut from the ingot, heat treated, and finish-machined and polished. The tensile specimens had a rectangular gage section of 8 mm x 0.4 mm; compression parallelopipeds had dimensions of 2.5 mm x 3.5 mm x 5.5 mm. All specimens were sealed in evacuated tubes and heat treated at 1135°C to 1425°C for 0.5 to 65 hours to get various grain sizes and (above 1300°C) to produce lamellar microstructures. They were then air cooled, and subsequently annealed at 900°C for 2 hours to stabilize the microstructure. Grain size was measured as the mean linear intercept diameter. Three to five tests were conducted for each grain size, in both tension and compression.

Results and Discussion

Equiaxed grains of single-phase γ were obtained if the Ti-50 Al alloy was heat treated between 1135°C and 1300°C, as shown in Fig. 1(a). Specimens for test had grain sizes of 19, 22.4, 39, 63 and 123 μm. After heat treatment at 1425°C, a lamellar structure with a mixture of γ and α_2 was formed. This two-phase microstructure may have resulted either from

0036-9748/91 $3.00 + .00

entering the $\gamma+\alpha$ phase field at higher temperature (10), with α ordering to α_2 on cooling, or from aluminum loss during high temperature heat treatment (10). There should, however, be no aluminum loss for the *equiaxed* grains of this study (10), since none were heat-treated above 1300°C. In the lamellar structure, the volume fraction of α_2 was about 0.3; the average width of the individual lamellae was about 5-10 μm, as shown in Fig. 1(b). A mixed structure with various volume fractions of the lamellar constituent, mixed with γ grains, was obtained after heat treatment at 1320°C to 1400°C. X-ray diffraction analysis of the bulk samples confirmed that the equiaxed grains were single-phase γ but that the lamellar structure consisted of two-phase $\gamma+\alpha_2$, as has been presented elsewhere (11).

The dependence of the average yield strength (tensile and compression tests) on grain size is shown in Fig. 2. For the equiaxed grains of single-phase γ, the yield strength measured by either tensile or compression tests obeyed the Hall-Petch relationship, i.e.

$$\sigma_y = 173 \text{ MPa} + 0.130 \text{ MPam}^{1/2}\, d^{-1/2} \text{ (tension)}$$
$$\sigma_y = 235 \text{ MPa} + 0.124 \text{ MPam}^{1/2}\, d^{-1/2} \text{ (compression)}$$

The fracture strain in tension increased a little when the size of the equiaxed grains was decreased. The yield strength of the lamellar structure, however, was larger than that of the equiaxed grains, e.g., 236 MPa (tensile) or 278 MPa (compression), respectively, as shown in Fig. 2. For the fully lamellar structure obtained by heat treatment at 1425°C, the value of σ_y was larger than would be predicted from the prior γ grain size (which is the dimension d for which the lamellar data point is plotted in Fig. 2). It would of course be expected that the lamellar boundaries in the $\gamma+\alpha_2$ structure might act as slip barriers, making the lamellar width a more appropriate value of d for Fig. 2 than the prior γ grain size. Extrapolation of the plotted line for compressive test results, by the equation above, to the measured yield strength for the lamellar structure provides an estimate of the effective slip distance, or d, in that structure. That estimate is 8 μm, in reasonable accord with the measured width of the lamellae, 5-10 μm. This does not necessarily prove that the lamellar width is the primary slip unit in this microstructure, only that there is a quantitative agreement between the estimated and measured values for this parameter. There are many other factors which potentially affect the strengthening of microstructures with two phases, both of which are ductile (12,13), including the roles of heterophase boundaries and the individual flow stresses and textures of each phase. Thus more work would be needed to assess accurately the strengthening contributions in this microstructure.

The value of the Hall-Petch slope, k_y, in Fig. 2 is given in the equations above. The slope values in tension and compression are quite similar, and are more than an order of magnitude smaller than the value estimated by Vasudevan, *et al.* (6), which was $k_y = 1.37 \text{ MPam}^{1/2}$. The present data are inserted in the previous figure (6) in Fig. 3. Although it is difficult to be sure of the basis for such a large difference in results, there are some possible explanations. One is impurity content. Oxygen and other interstitial impurities are expected to be potent strengtheners in TiAl, and published reports on TiAl do not always give interstitial content. Our oxygen plus nitrogen content was 1250 at. ppm, while that of both Lipsitt, *et al.* (8) and Huang (9) was about 2900 at. ppm. One estimate (9) is that 3000 at. ppm interstitials in TiAl could increase the yield strength by as much as 200 MPa at room temperature. Another possible variable is the starting dislocation density, which should depend on processing history. But since both these variables increase strength as their value is raised, it could be concluded that results with lower yield strength should represent more nearly intrinsic behavior. The one variable which could either raise or lower strength is crystallographic texture (14). Neither we nor any of the accounts in the literature have presented texture results, so this is at present a moot point; however, our diffractometer intensities are in good agreement with the powder data file, and Laue results indicate no strong texture in our material. In light of all these factors, we suggest that our data are a more reliable measure of k_y than the prior value (6).

In light of the foregoing, it may be appropriate to observe that the single-phase Ti-50 Al data point (6) in Fig. 3 appears to agree well with the trend of the present data. The higher strengths of the 52 and 54 at.% materials may reflect high interstitial content, solution strengthening by aluminum, or other effects. The 48 at.% and Ti + Er, which were not single-phase structures, are still stronger but probably are inappropriate for inclusion in the same figure with the single-phase γ data. It may also be noted that the values of σ_0 in our results, shown above, are in reasonable agreement with the TiAl single crystal results of Kawabata, *et al.* (15), who found for various orientations an average yield strength of about 200 MPa. This average includes the multiple-slip orientations appropriate (4) for comparison to polycrystal data.

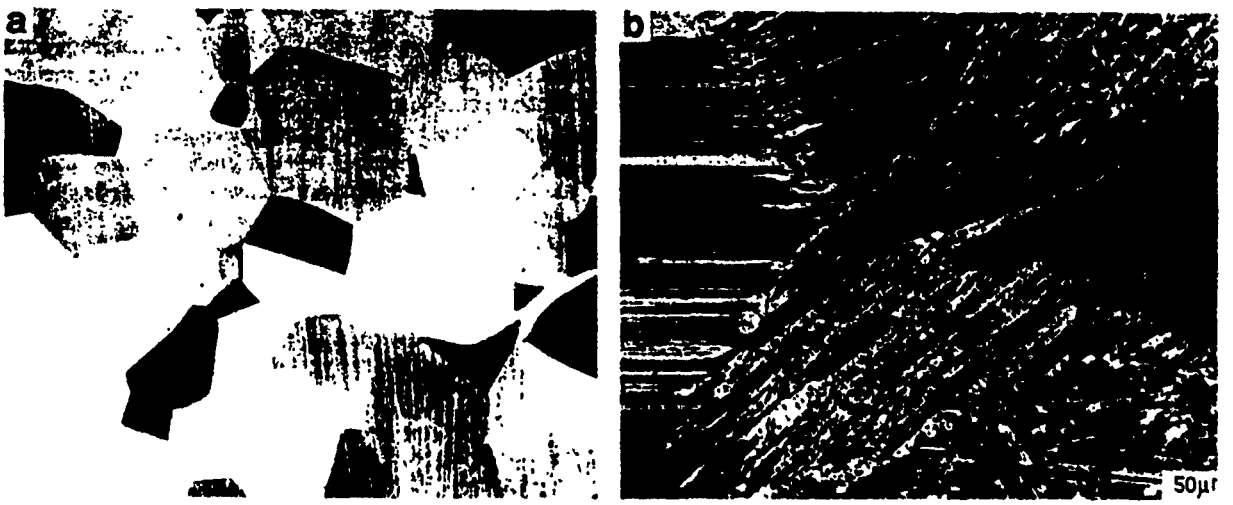

Fig. 1. Microstructures of TiAl, both at same magnification. (a) Equiaxed grains of single-phase γ produced by heat treatment at 1250°C, 2 hrs. (b) Lamellar structure after heat treatment at 1425°C.

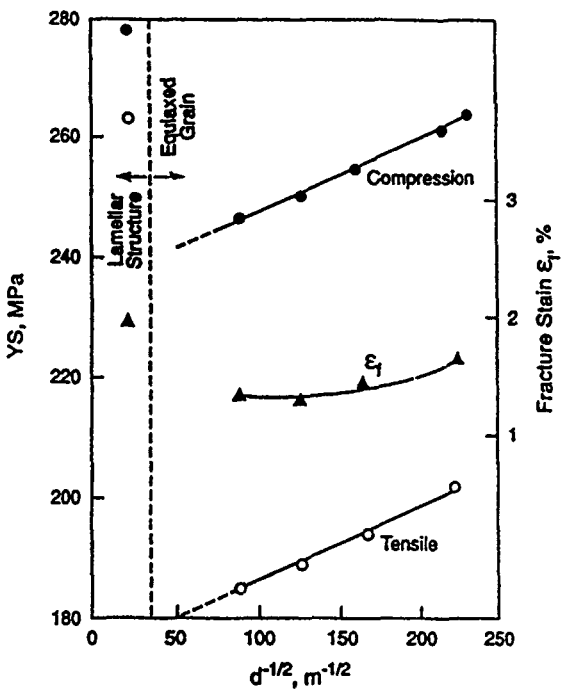

Fig. 2. The variation of the yield strength (average value of 3 to 5 data) and the fracture strain with grain size at room temperature. The symbols to the left of the dashed line denote the lamellar structure.

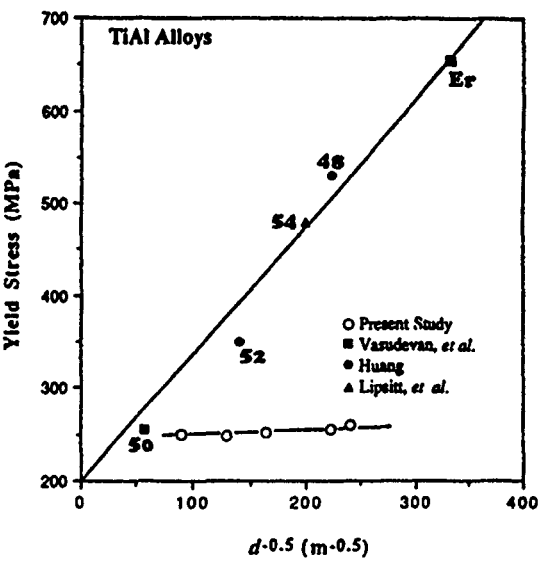

Fig. 3. The Hall-Petch plot of Vasudevan, *et al.* (6), with the compression data of the present study added and the atomic per cent aluminum noted by each point from earlier work (6,8,9). The uppermost point, denoted "Er," represents the Ti-50 Al alloy with erbia particles.

We do not know the reason for the tension-compression asymmetry or strength differential in Fig. 2. The data shown are the result of multiple tests, results of which were quite consistent, so scatter in the data is not the answer. We have particular confidence in the compression tests, because compression specimens could be strained to considerably greater strains with no evidence of cracking, whereas cracks could be observed in some of the tensile specimen gage lengths, away from the location of fracture, after failure. We found no indication, in sectioning experiments, that this tensile cracking occurred at strains near the yield strain. Nevertheless, the absence of any cracking in compression specimens, at strains larger than the failure strain in tension, probably rules out any cracking effect on the compression data. If the asymmetry in Fig. 2 is real, as we believe it is, it should be noted that it has the same sign as does the strength differential in steels, though of a somewhat greater magnitude (16-19). The conventional explanation for the effect in steels, based on dislocation density (19), would not appear to apply to the γ microstructures of the present work. Further work is needed on this topic, as on numerous other problems in mechanical behavior of titanium aluminides (7,11,20).

Acknowledgements

We appreciate the sponsorship of the Defense Advanced Research Projects Agency through DARPA Order 6155, monitored by the Air Force Office of Scientific Research under Contract F49620-88-C-0013. This is a joint contract of the University of Pittsburgh and Carnegie Mellon University.

References

1. E.O. Hall, Proc. Phys. Soc., B64 (1951), 747-753.
2. N.J. Petch, J. Iron Steel Inst., 173 (1953), 25-28.
3. J.P. Hirth, Metall. Trans., 3 (1972), 3047-3067.
4. A.W. Thompson, in Work Hardening in Tension and Fatigue, pp. 89-126, TMS-AIME, New York (1976).
5. N. Hansen, Metall. Trans. A, 16A (1985), 2167-2190.
6. V.K. Vasudevan, S.A. Court, P. Kurath and H.L. Fraser, Scripta Metall., 23 (1989), 467-469.
7. R.L. Fleischer, D.M. Dimiduk and H.A. Lipsitt, Ann. Rev. Mater. Sci., 19 (1989), 231-263.
8. H.A. Lipsitt, D. Schechtman and R.E. Schafrik, Metall. Trans. A, 6A (1975), 1991-1996.
9. S.C. Huang, Scripta Metall., 22 (1988), 1885-1888.
10. C. McCollough, J.J. Valencia, H. Mateos, C.G. Levi, R. Mehrabian and K.A. Rhyne, Scripta Metall., 22 (1988), 1131-1136.
11. A.W. Thompson and W.-Y. Chu, in Microstructure/Property Relationships in Titanium Alloys and Titanium Aluminides, R.R. Boyer and J.A. Hall, eds., TMS-AIME, Warrendale, PA, in press.
12. S.M. Copley and J.C. Williams, in Alloy and Microstructural Design, J.K. Tien and G. Ansell, eds., pp. 3-63, Academic Press, New York (1976).
13. J.C. Williams and A.W. Thompson, in Metallurgical Treatises, J.K. Tien and J.F. Elliott, eds., pp. 487-504, TMS-AIME, Warrendale, PA (1981).
14. D. Juul Jensen, A.W. Thompson and N. Hansen, Metall. Trans. A, 20A (1989), 2803-2810.
15. T. Kawabata, T. Kanai and O. Izumi, Acta Metall., 33 (1985), 1355-66.
16. W.C. Leslie and R.J. Sober, Trans. ASM, 60 (1967), 459-84.
17. G.C. Rauch and W.C. Leslie, Metall. Trans., 3 (1972), 373-85.
18. R. Chait, Metall. Trans., 3 (1972), 365-71.
19. W.C. Leslie, The Physical Metallurgy of Steels, pp. 223-226, McGraw-Hill, New York (1981).
20. W.-Y. Chu and A. W. Thompson, in Hydrogen Effects on Material Behavior (4th Int. Conf. on Hydrogen), N.R. Moody and A.W. Thompson, eds., pp. 543-553, TMS-AIME, Warrendale, PA (1990).

REF. 9

ENVIRONMENTAL EFFECTS IN TITANIUM ALUMINIDE ALLOYS

Anthony W. Thompson

Dept. of Metallurgical Engineering and Materials Science
Carnegie Mellon University
Pittsburgh, PA 15213

Abstract

Environmental effects on titanium aluminide alloys are potentially of great importance for engineering applications of these materials, although little has been published to date on such effects. The primary emphasis in this paper is on hydrogen effects, with a brief reference to oxygen effects. Hydrogen is readily absorbed at elevated temperature into all the titanium aluminide compositions studied to date, in amounts as large as 10 at. %, and on cooling virtually all this hydrogen is precipitated as a hydride phase or phases. The presence of these precipitated hydride plates affects mechanical properties in ways similar to what is observed in other hydride-forming materials, although effects per unit volume of hydride are not particularly severe in the titanium aluminides. Microstructure, and thus thermal and mechanical history, plays a major role in controlling the severity of hydrogen effects.

Introduction

Titanium aluminide alloys have enjoyed considerable recent attention, with both a specific development goal as potentially useful aerospace materials for future generations of both jet engines and airframes, and also with a general goal as a new generation of titanium alloys [1,2]. One particular property of interest for aerospace usage, particularly in the National Aerospace Plane (NASP) project [3], is compatibility with hydrogen. Among the earliest titanium aluminide alloys developed [4,5] was one based on Ti_3Al, Ti-24-11 (24% Al, 11%Nb in atomic per cent). Initial work on hydrogen effects was focused on this alloy, because of its availability, metallurgical knowledge (recently reviewed [6]), and technical interest for near-term aerospace applications. In addition, it can be prepared with very small amounts of beta phase in many accessible microstructures, when composition is on the lean side of the specification, making it either a single-phase aluminide alloy with the α_2 structure or an $\alpha_2 + \beta$ alloy.

Extensive knowledge of hydrogen embrittlement phenomena provides a complete set of analytical and experimental tools to evaluate performance of an alloy like Ti-24-11. A variety of mechanical tests, described below, have been performed and the results interpreted in terms of conventional procedures and models. These are compared in this work to mechanical properties of uncharged material, with the goal of understanding both types of properties.

Experiments

The composition and thermomechanical history of the starting materials have been described in previous publications[7,8]. Most of the work was conducted on the α_2 phase (Ti_3Al) alloy, Ti-24-11, with some additional testing on one γ alloy, Ti-50 Al. Both these alloys were close to their nominal compositions. For the Ti-24-11, most work was conducted on a microstructure prepared by β solution treatment at 1150°C, air cooling, and stabilization aging at 700 or 800°C. Microstructural variations were achieved by solution treating in either the $\alpha_2+\beta$ or β phase fields. The β transus is about 1100°C in this material, so treatments at 1000 and 1075°C were sub-transus, while the 1150 and 1225°C treatments are in the all-β field. Treatments were carried out in vacuum. After solution treatment, specimens were subjected to three cooling rates: air cooling (most rapid), furnace cooling, and controlled cooling (slowest). Upon reaching room temperature, all specimens were then given a final treatment of 800°C for 3 hours in vacuum.

Mechanical tests included tensile, bend bar, and both wedge-opening load (WOL) and compact tension specimens with a thickness of 9 mm, tested at a variety of temperatures and strain rates. Other specimen dimensions have been presented elsewhere [7-9]. The bend bars were chosen to match the dimensions analyzed by Griffiths and Owen [10] to facilitate mapping of local stress and strain below the notch root [10-12]. The WOL specimens were used both for conventional fracture toughness testing, i.e., determination of K_{Ic} under ASTM validity conditions, together with the compact tension specimens, and also for sustained-load testing with bolt loading, in order to determine the threshold stress for initiation of cracking with hydrogen, K_{IH}, under falling-load conditions [13]. Crack propagation tests were also performed with the WOL specimens.

These alloys absorb considerable hydrogen from the gas phase at 1 atm pressure, at temperatures above 500°C. Electrolytic and gas-phase methods for introducing hydrogen were developed, although most testing was conducted with gas-phase charged hydrogen. Gas-phase charging with a Sieverts apparatus [14,15] was found to be fully reversible, an important point not only for solvus measurements, but also for the separation of intrinsic hydrogen effects from damage caused during charging [11]. In the present experiments, charging of several atomic per cent of hydrogen made the verification of uptake simple through weighing of samples on a microbalance. Removal of hydrogen by repeating the aging heat treatment in vacuum was also verified by return of the sample to its original weight. For solvus measurements, 10-g specimens were used, and when weighed on a balance with a 10 μg sensitivity, the precision of measurement was within 10 wppm. Samples typically returned to the original weight within 25 μg after hydrogen removal.

Results

Hydrogen Dissolution

A hydrogen solvus has been measured for Ti-24-11 [16,17], as illustrated in Figure 1. The solvus measurements, heats of solution and partial molar free energies for hydrogen, and other related observations have been collected elsewhere [16]. Measurements were also made of the equilibrium solvi for various overpressures of hydrogen, over the temperature range 400 to 675°C. These solvi provide a tool for charging to chosen levels of hydrogen, using low hydrogen gas pressures *circa* 1 atm. It may also be noted that extrapolation of the solvus in Figure 1 to room temperature, using a spline fit, gives an estimate of the room temperature solubility of about 10 ppb. This is, of course, a crude estimate, but does suggest that virtually all charged hydrogen precipitates as hydride upon cooling.

The hydride phase forms as elongated plates in the α_2 phase. X-ray diffraction was used to determine that the hydride typically has the same structure as does the γ hydride in the Ti-H system, sometimes called TiH_2, though since the γ structure extends to either side of "TiH" and barely, if at all, reaches to TiH_2, TiH would probably be a more appropriate term. For low charged amounts of hydrogen, the hydride c/a ratio was sometimes observed to be unity, i.e., f.c.c. γ, but in other cases the structure was f.c.t. For large charged amounts of hydrogen, we consistently found the f.c.t. hydride structure. Others have reported that they did not observe this hydride structure in Ti-24-11 using electron diffraction [18], but we have made numerous observations of the γ hydride structure by X-ray in this investigation. We do not know the stoichiometry of the hydride in Ti-24-11, neither its metal-to-hydrogen ratio nor the identity of the metal element(s). Since Nb substitutes for Ti in the α_2 lattice, it would seem likely that Nb also participates in the hydride, i.e. that the nominal composition is (Ti,Nb)H. Moreover, it is at least possible [18] that Al also participates as (Ti,Nb,Al)H. These suggestions are supported by the observation that the Ti-24-11 hydride has a larger lattice parameter than the γ hydride in the Ti-H system.

Hydrogen is a potent stabilizer of the beta phase in titanium alloys, and particularly when amounts of the order of 10 at. % are charged, acts as a significant alloying element. This alloying element is then readily removed by low-temperature heat treatment in vacuum. These circumstances raise the possibility that in Ti-24-11, as in conventional titanium alloys[19], significant modification to microstructure would be achievable through use of hydrogen as a temporary alloying element. This expectation has been explored in some detail, and results are reported elsewhere [8].

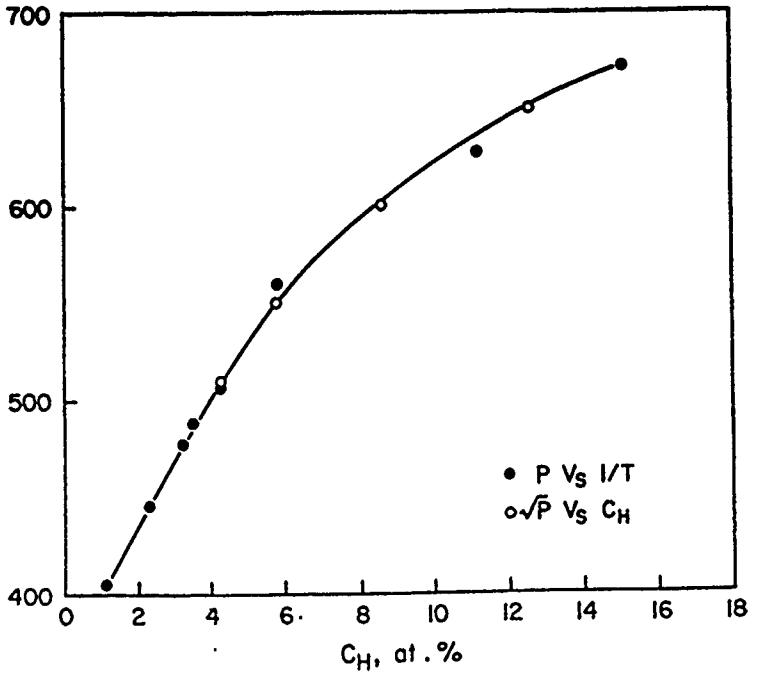

Figure 1. Solvus for hydrogen in Ti-24-11, measured by two methods (cf. [16]), dividing hydrogen in solid solution in the α_2 phase (at left) from the two-phase equilibrium between α_2 and hydride. (Figure from ref. 17).

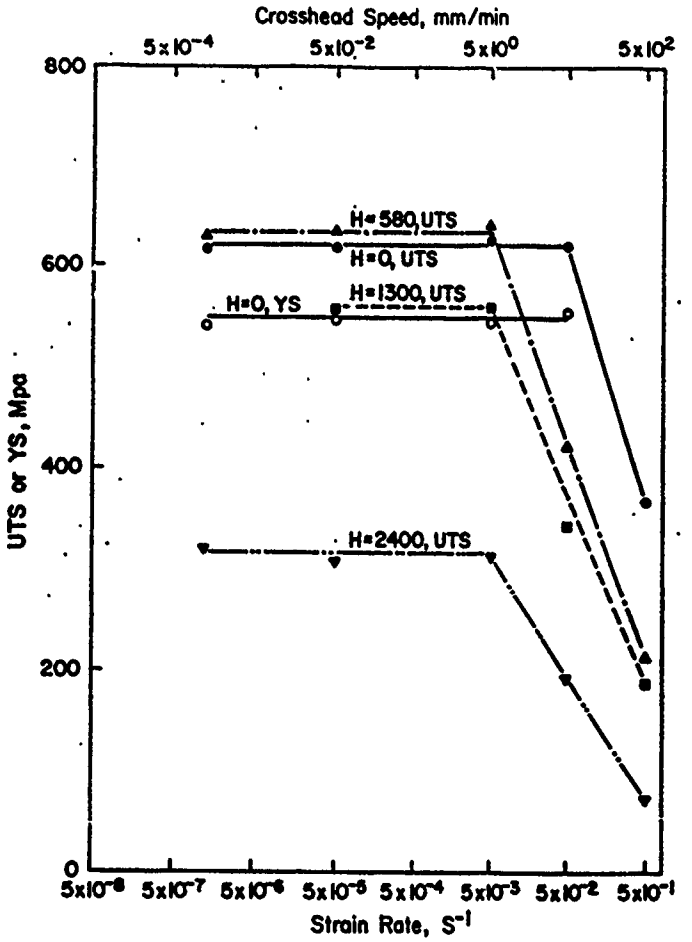

Figure 2. Dependence of tensile yield or ultimate strength on applied strain rate. When fracture was coincident with or preceded yield, the stress was designated "UTS" for simplicity. Hydrogen content shown as ppm by weight. (From ref. 9).

Mechanical Properties

Mechanical properties of the Ti-24-11 alloy have been studied using the specimen types described above. The first part of the mechanical investigation comprised tensile tests using a range of strain rates, performed at several temperatures in the range -200°C to 400°C. Uncharged specimens as well as specimens thermally charged to hydrogen contents between 500 and 2500 ppm by weight (2.5 -12.5 at. %) were tested under the conditions mentioned. Among the results were observation of a range in tensile ductilities, from 0.5 to 2.5%, and a pronounced strain rate effect, with an extremely steep fall in ductility for tests at rates above about 0.01 s^{-1}. This was true both with and without hydrogen, Figure 2, although the introduction of hydrogen lowered the critical rate somewhat, in addition to decreasing the stress and strain associated with fracture. This rate effect essentially represents the intervention of fracture in the stress-strain curve prior to yield, since no such rate effect could be detected when compression tests were conducted under otherwise identical conditions [20].

The dependence of tensile properties [9] on temperature and hydrogen content, respectively, is shown in Figures 3 and 4. In Figure 3, a strongly increasing ductility and a moderate increase in work hardening capacity are evident as temperature rises from the essentially nil ductility behavior at liquid nitrogen temperature, where tensile yield and fracture are essentially coincident. Figure 4 shows that for hydrogen contents exceeding 1000 wppm (essentially all in the form of precipitated hydrides), fracture precedes yield in tension. Yet even in this apparently brittle circumstance, some necking and consequent fracture strain are still observed.

To facilitate study of the brittle fracture process in Ti-24-11, notched bend bar specimens were also tested, under parallel conditions to those mentioned for the tensile tests. Generally, very similar phenomena were observed, including the pronounced strain rate effect [7,9]. Using established analysis methods [10-12,21], it was possible from these tests to calculate the true, intrinsic fracture strength σ_F for brittle fracture (having the appearance of cleavage) in these specimens. This strength was found to be independent of temperature, in agreement with the

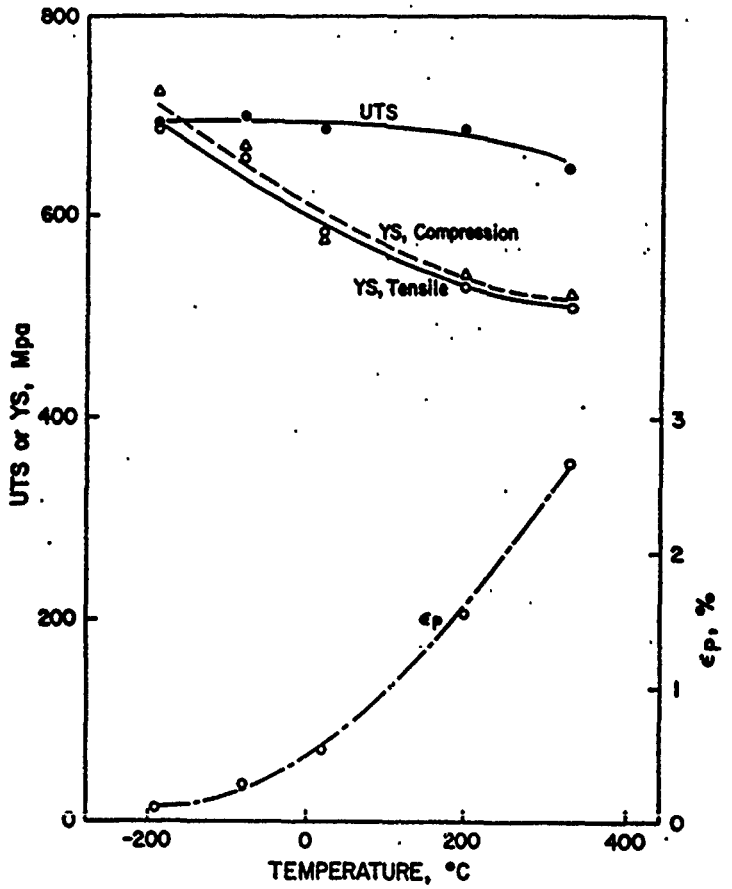

Figure 3. Dependence of tensile properties on temperature. Both tensile and compressive yield behavior are shown to illustrate similarity. The ε_p data are uniform true strain.

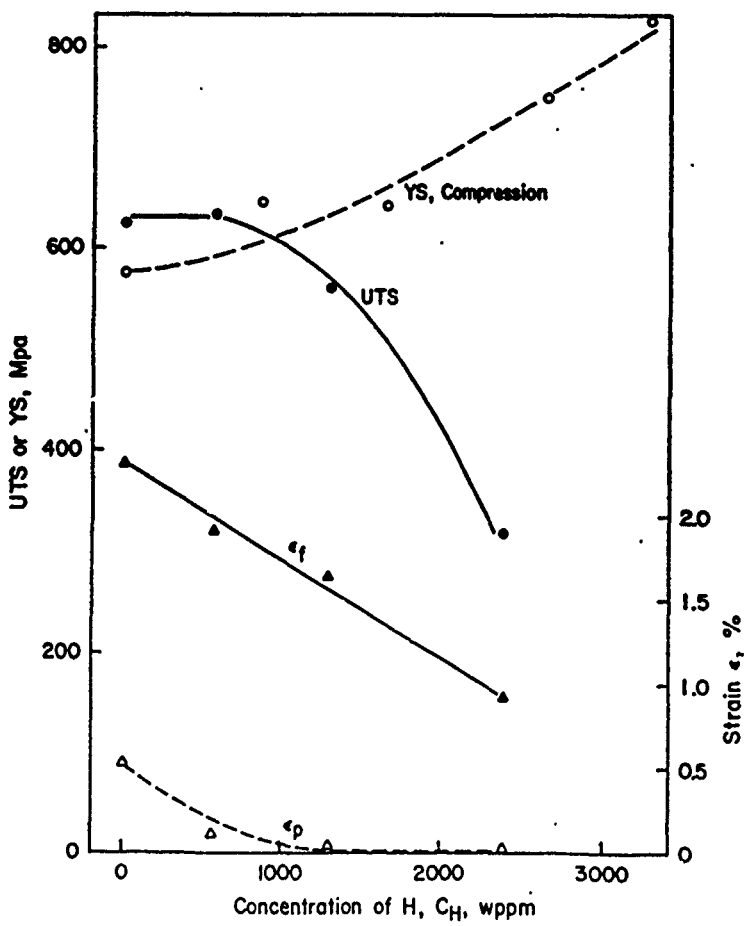

Figure 4. Tensile properties as a function of hydrogen content at room temperature. "UTS" means fracture stress when fracture preceded yield. Fracture strain is ε_f. (From ref. 9).

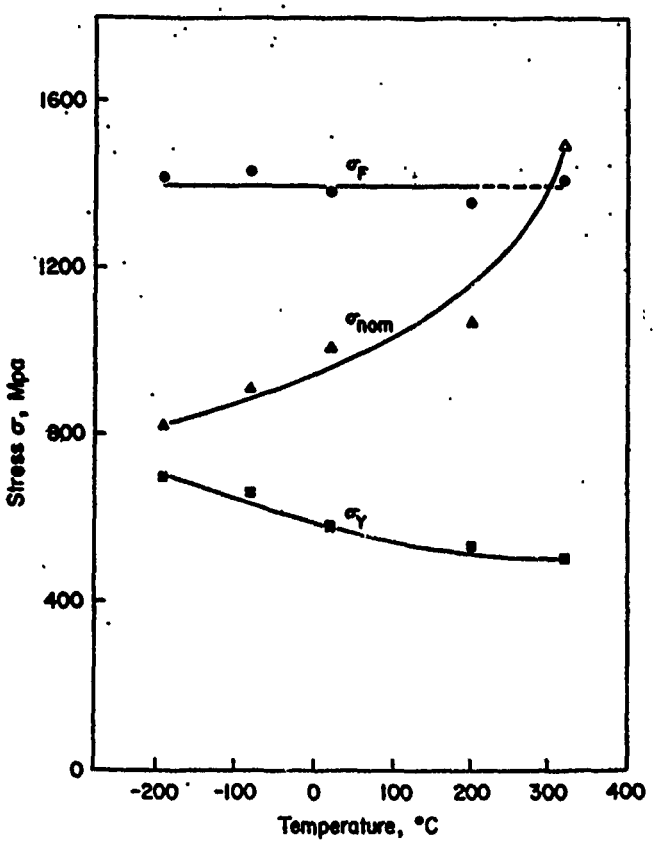

Figure 5. Results of bend-bar tests on Ti-24-11, comparing yield strength (cf. Figure 3) with nominal stress and true local fracture stress measured in bend bars as a function of temperature.

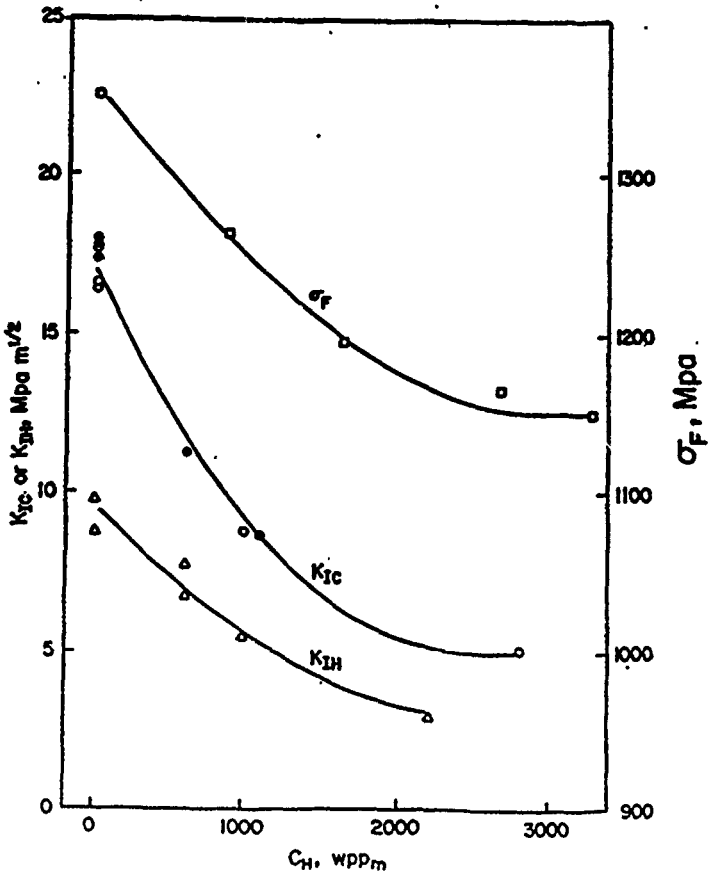

Figure 6. Plane strain fracture toughness K_{Ic}, sustained-load cracking threshold K_{IH}, and true, local fracture strength in bend bars σ_F, as functions of precharged hydrogen content in Ti-24-11.

classical expectation [21], Figure 5. It should be pointed out, however, that this observation does not necessarily imply that fracture occurs by cleavage, only that it is a stress-controlled brittle fracture [21].

The bend-bar experiments showed that propagation of brittle cracks appeared to take place in a stable manner during slow loading, and resistance to this slow propagation was dependent on crosshead speed and hydrogen content. Accordingly, additional tests were conducted with pre-cracked WOL specimens to permit measurement of crack resistance or R curves [9] and conventional toughness properties as well as crack initiation resistance. Toughness, as measured by K_{Ic}, and the threshold stress to initiate cracking in hydrogen, K_{IH}, were both found to decrease smoothly with increasing hydrogen content in tests using fracture mechanics specimens (both in compact tension and WOL configurations). These data, together with the fracture strength measured in bend bars, are collected in Figure 6. Although the toughness does decrease considerably with charged hydrogen (as do tensile properties in Figure 4), it should be noted that the hydrogen contents are very large, compared to damaging amounts in a number of other materials, including steels and nickel-base alloys [22]. Thus Figures 4 and 6 could be interpreted as showing that Ti-24-11 actually is a relatively hydrogen-tolerant alloy.

The possibility that the reduced toughness and crack initiation resistance observed in hydrogen-charged Ti-24-11 could lead to sustained-load crack propagation was also investigated. This was done in two different experiments. One involved sustained-load testing of a conventional pre-cracked WOL specimen which was precharged with hydrogen, then tested at room temperature. A second test examined environmental effects by inserting a precracked WOL specimen into hydrogen gas at 400°C, under 1 atm. pressure. The results showed that although hydrogen-induced cracking did initiate at RT in the pre-charged specimen, only a small distance of crack propagation ensued. At 400°C, however, more extensive crack growth occurred, and it was possible to measure the increase of crack length, a, with time, da/dt. The threshold for cracking, K_{IH}, could be measured as cracking began. Crack initiation appeared to begin at the specimen surface within the plastic zone, in a discontinuous fashion, when the level of plastic deformation in the zone reached a critical value. This pattern of behavior was similar to what was seen with brittle crack initiation during monotonic loading in the earlier results.

The variation of toughness and ductility with temperature is shown in Figure 7. The effect of hydride in a precracked specimen, as a function of microstructure, has been tested at 400°C, and both the toughness and the hydrogen threshold K_{IH} were found to decrease with increasing hydride content at 400°C, Figure 8. This is similar to the general pattern of results at room temperature, and shows that the increased ductility and work-hardening capacity observed at 400°C in Figure 3 does not result in greater resistance to hydrogen effects at the same temperature.

Metallography and Fractography

For all microstructures, slip was observed to occur discontinuously in the individual plates of α_2 phase [8,9,23]. With increasing stress intensity levels in precracked specimens, discontinuous cracks nucleated in individual α_2 plates ahead of the main crack and then joined up to accomplish crack extension. Thus it appears that the α_2/β interphase boundaries are effective barriers to both slip and crack propagation. Slip lines were readily evident on prepolished specimen surfaces, making the extent of plasticity at notch roots or crack tips observable in the scanning electron microscope (SEM) or by polarized light in the light microscope.

Fractographic examination revealed that fracture in tension or bend bars took place by a cleavage-like process in small facet-like features. The size and shape of these features corresponded accurately to the plates of α_2 in the microstructure, Figure 9. One means of demonstrating this was by "plateau etching" [24] of fracture surfaces, as shown in Figure 10. Here the direct correspondence between microstructural and fractographic features is evident.

Since it has not been determined that this fracture is crystallographic in α_2 nor that it occurs on a low-index plane of the α_2, it would be inappropriate to designate it as "cleavage," although the fractographic appearance is consistent with micro-fracture in a cleavage mode. The fracture process thus appears to be one of tearing in the "matrix" of transformed beta around the primary

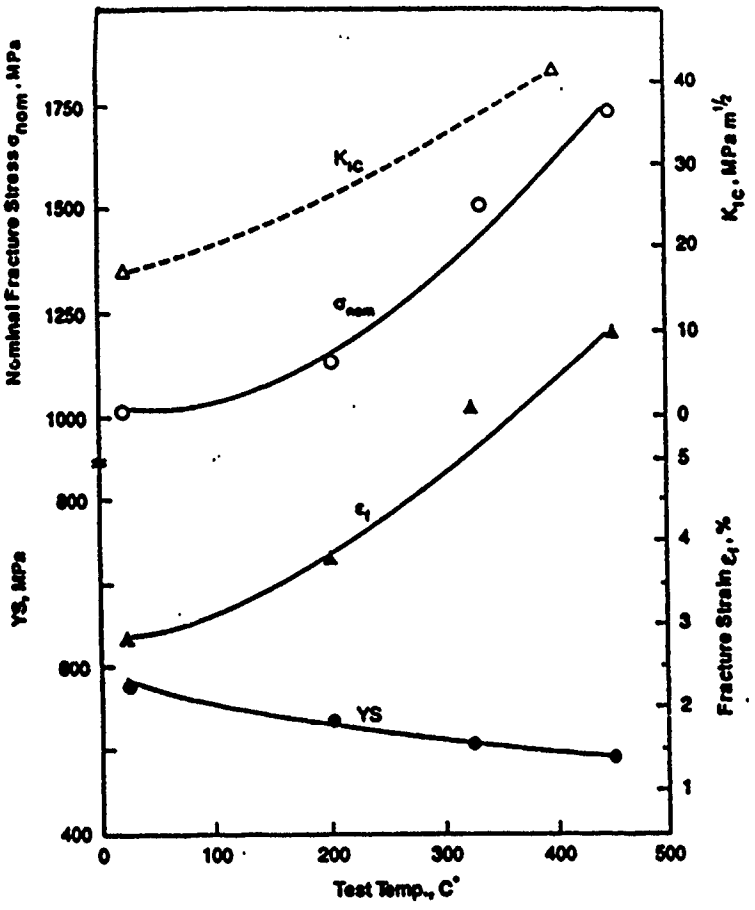

Figure 7. Dependence of yield strength, fracture strain, nominal fracture stress in bend bars, and toughness K_{Ic} as a function of test temperature.

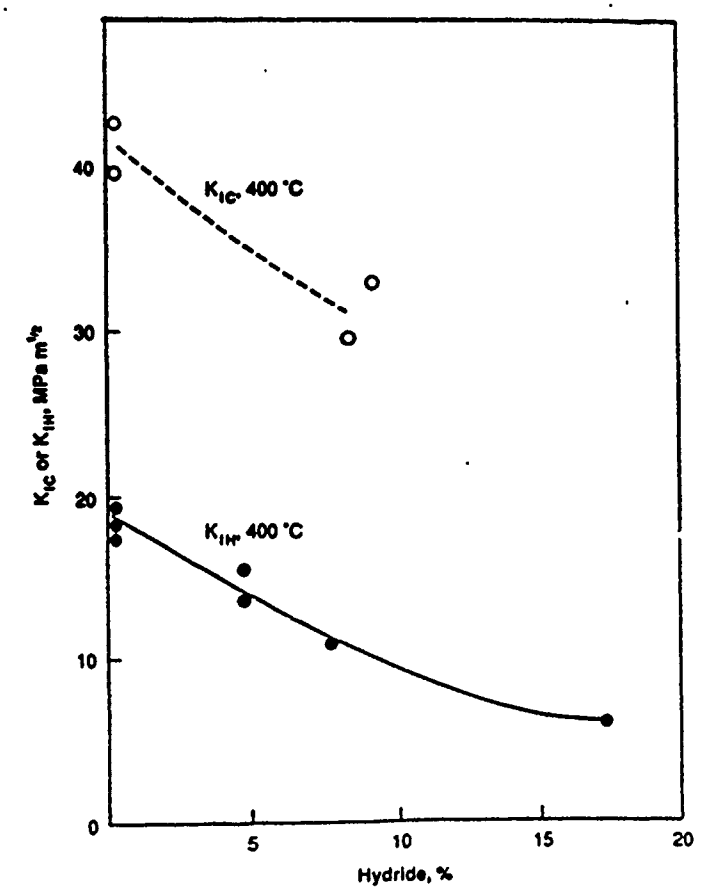

Figure 8. Variation of fracture toughness K_{Ic} and threshold for hydrogen cracking K_{IH} as a function of hydrogen content, expressed as volume fraction of hydride phase, for tests at 400°C.

α_2 plates, and a brittle fracture of cleavage-like appearance in the plates themselves. Similar observations have been made in other titanium alloys and in certain microstructures of titanium aluminides [25,26].

Fracture surfaces of the hydrogen-induced cracking in hydrogen gas at 400°C was closely related to the microstructure, as in room temperature tests conducted earlier, such as Figure 10. A brittle fracture appearance, cleavage-like in character, was found for all microstructures, and appeared to be somewhat more brittle than was observed for uncharged specimens tested at 400°C.

TiAl Results

We have begun work on TiAl alloys of mixed α_2 and γ microstructure, primarily in the binary alloys Ti-50 Al and Ti-46Al. The first step was to establish the hydrogen solvus for the Ti-50 Al material, since no solvus appears to have been determined to date for any γ or near-γ alloy. Our result is shown in Figure 11, with which our Ti-24-11 solvus shown in Figure 1 can be compared. Although substantial amounts of hydrogen can be charged into this alloy above 800°C, the levels of solubility at each temperature are distinctly lower than for Ti-24-11. This presumably reflects a lower solubility in the γ phase. Below 1300°C, our Ti-50 Al material was all γ. As solution treatment temperatures were increased above 1300°C, the alloy contained increasing amounts of α_2, to as much as one-third, resulting either from entering the $\alpha + \gamma$ phase field (α orders to α_2 on cooling), or possibly due to aluminum loss during heat treatment [27].

Examination of the charged and cooled γ phase material reveals very extensive hydride formation, as in the case of Ti-24-11, and again, the hydride in Ti-50 Al has the structure of TiH, the f.c.t. γ hydride in the Ti-H system, for hydrogen contents below about 1000 wppm. At higher hydrogen contents, it appears from our X-ray observations that one or two additional hydride crystal structures are also present. Work on mechanical behavior of hydride-containing Ti-50 Al has necessitated care with cooling rates from hydrogen charging temperatures, for hydrogen levels above 2000 wppm. At such hydrogen levels, cracking can result on cooling unless slow cooling rates are maintained. At very high hydrogen levels, 6000 wppm and above, powdering of the alloy was encountered even at moderate cooling rates, a convenient result for X-ray analysis but one effectively precluding mechanical tests.

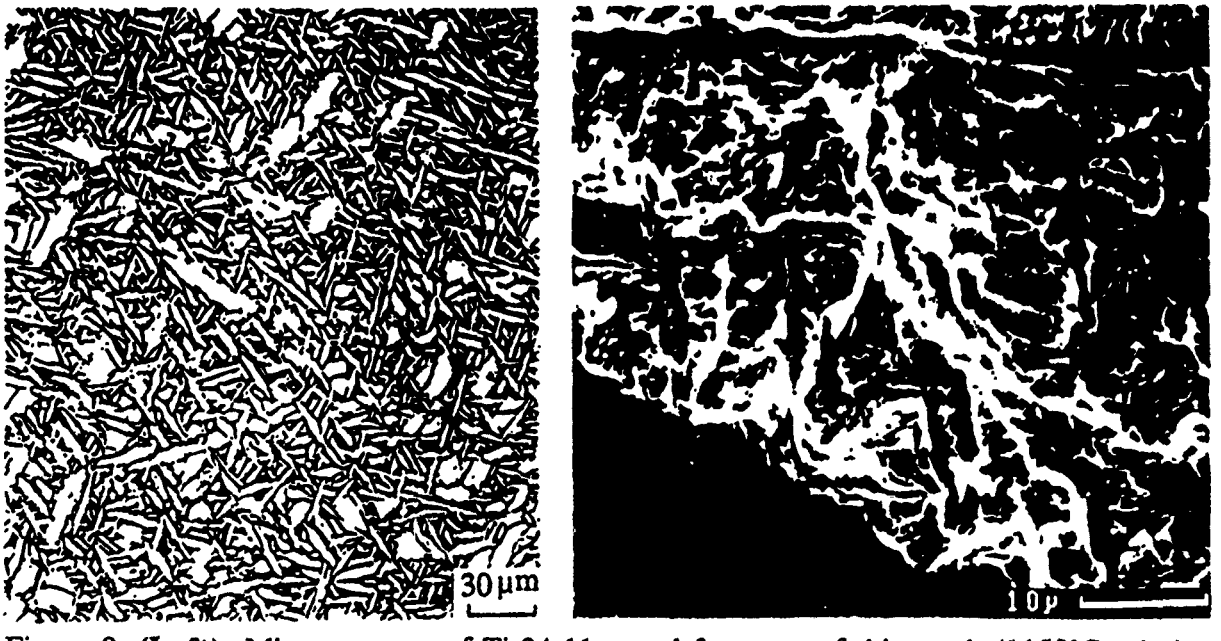

Figure 9. (**Left**) Microstructure of Ti-24-11 tested for most of this work (1150°C solution treatment, air cooled, and aged 3 h at 800°C. Figure 10 (**Right**) Fracture surface of microstructure in Figure 9, plateau etched [24]. Lower left corner is polished and etched, rest of photograph is fracture surface, with scanning electron microscopy.

Preliminary mechanical tests have been conducted on all-γ material, with hydrogen contents up to 5000 wppm. To minimize complications from premature fracture, these tests were conducted in compression. Results are shown in Figure 12. As in Ti-24-11, the hydride phase strengthens the material, but compared to Figure 3, the magnitude of the effect in Figure 12 is quite modest. In Ti-50 Al, the higher charging temperatures used for higher hydrogen contents also coarsened the grain size. Thus the modest strengthening shown in Figure 12 is understated if a correction for grain size strengthening is considered. It is interesting that the strengthening "saturates" above about 1500 wppm hydrogen. If the strengthening is due to reduction of slip length by increasing subdivision of the γ grains by hydride plates, the effect would be expected to saturate as the volume increasingly fills with hydride, leaving little matrix to subdivide further.

Oxidation

As a brief summary, oxidation tests on both Ti_3Al and TiAl have shown that protective oxides tend not to be formed in air. For Ti_3Al there is evidence that titania is the oxide formed, and is poorly protective, with relatively large weight gains observed. For TiAl, oxidation is more rapid in air than in oxygen, with a rapid increase in oxidation rate above 850°C in air and above 950°C in oxgyen. This evidently represents the formation of a relatively protective scale, probably Al_2O_3, at the lower temperatures, with increasing amounts of titania at the higher temperatures. The nucleation of oxide islands suggests that even at relatively low temperatures, the oxide formed may not be entirely protective. These preliminary results [28] have stimulated additional work to examine the behavior of both alloys as a function of gas composition and temperature. Particularly for TiAl, there appears to be a selective oxidation process involved.

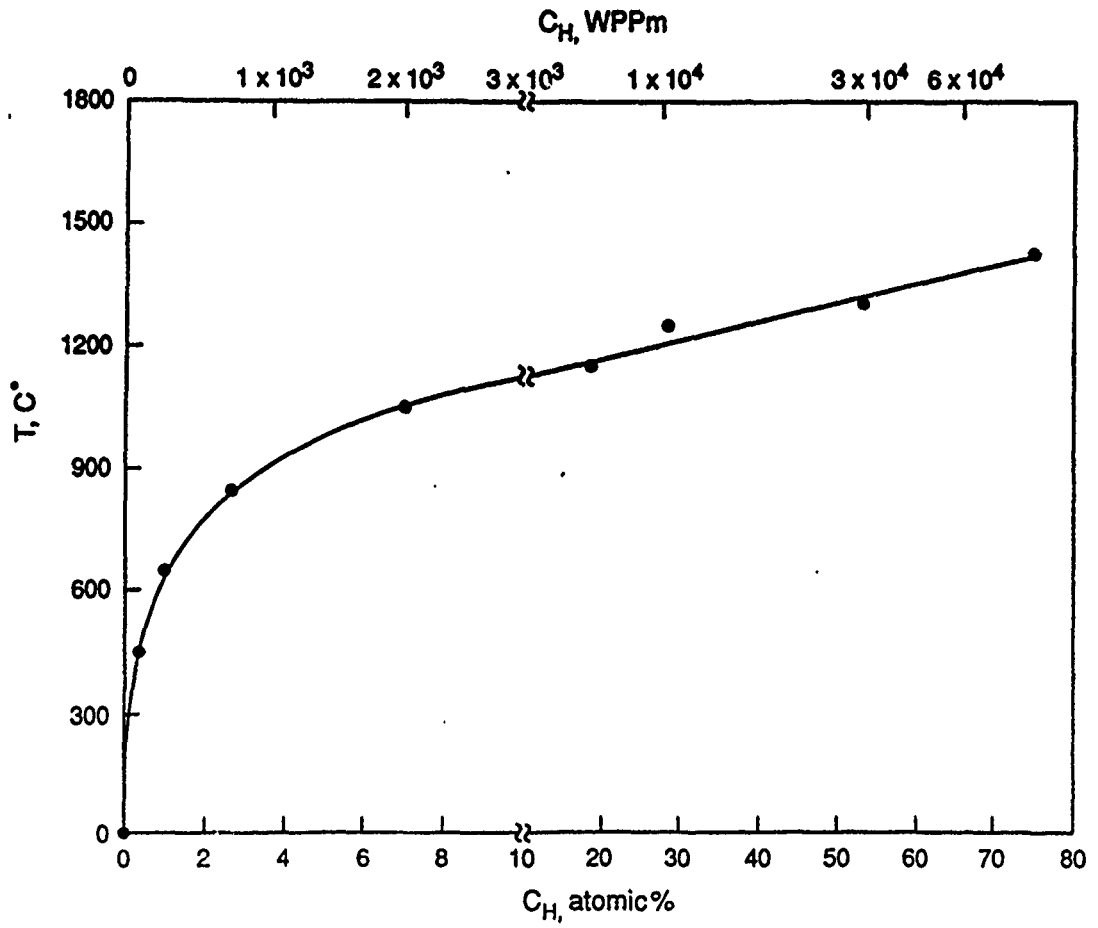

Figure 11. Apparent hydrogen solvus for Ti-50 Al, in all-γ microstructure, in equilibrium with hydride phase(s), determined by P (pressure) vs. 1/T method. Note break in scale of hydrogen concentration in order to display full range of data clearly.

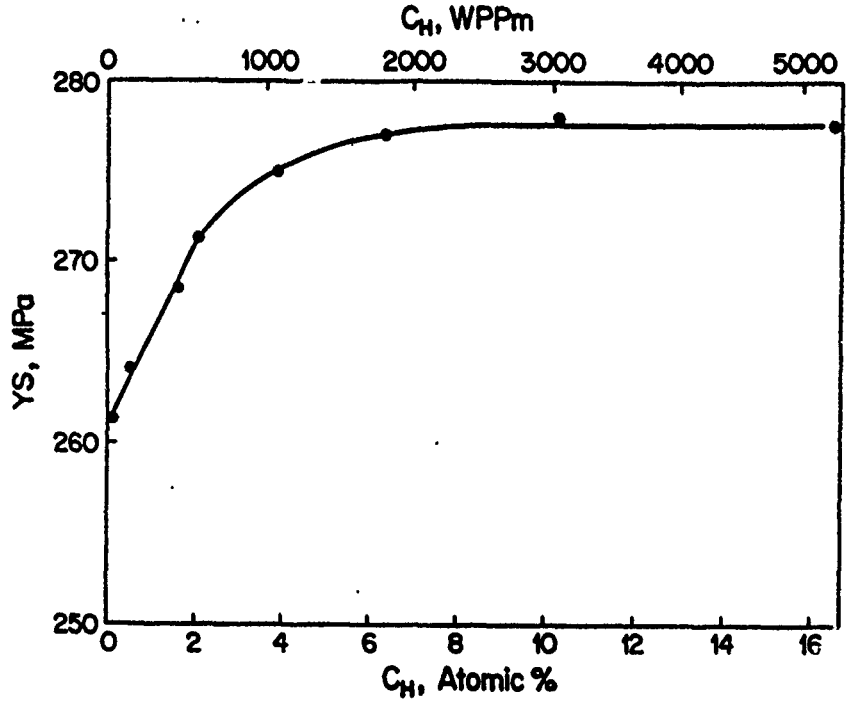

Figure 12. Yield strength as a function of hydrogen concentration (present as hydride) at room temperature, in Ti-50 Al. All charging conducted below 1000°C, so material was all γ.

Concluding Remarks

Major features of the experimental results have received comment as presented above. It remains to discuss the larger issues raised by these data. Most of the results obtained here are generally similar to literature results. Deformation observations in particular agree in all respects with published results [e.g. refs. 23,29,30]. The hydride results shown here are substantially more complete than any in print, though some significant questions remain. The stoichiometry and in some instances the crystal structure of the hydride(s) in these alloys needs investigation.

The fracture process, although cleavage-like in appearance, may not be classical cleavage in character. Expectations of basal plan cleavage [30] have not been borne out in any fracture determinations to date, and in the present work, microcracking has been observed parallel to, not perpendicular to [30] slip traces. Of greater significance is the tearing process observed in the regions of transformed beta surrounding the α_2 constituent. Wheither this reflects the dominant role of retained β, or is caused by microstructural units being too small for cracks to nucleate by a cleavage process [21], is not known. It has been shown, at least, that brittle fracture in Ti-24-11 is not a classical stress-controlled fracture, but has a critical strain component to cracking [9]. Additional work on microstructural variation and micromechanisms of fracture would be most welcome.

Acknowledgements

I am grateful to Prof. Wu-Yang Chu for extensive experimental work and many technical discussions, and to Profs. I.M. Bernstein and D.A. Koss for helpful discussions on this research. This work was sponsored by the Defense Advanced Research Projects Agency through DARPA Order 6155, monitored by the Air Force Office of Scientific Research under Contract F49620-88-C-0013. This is a joint contract of the University of Pittsburgh and Carnegie Mellon University.

References

1. H. A. Lipsitt, in *High-Temperature Ordered Intermetallic Compounds* (MRS Symp. 39), ed. C.C. Koch, *et al.* (Pittsburgh: Materials Research Society, 1985) 351-364.

2. R. L. Fleischer, D.M. Dimiduk and H.A. Lipsitt, *Ann. Rev. Mater. Sci.*, vol. 19 (1989), 231-263.

3. T. M. Ronald, in *Summary Proceedings of the 2nd Workshop on Hydrogen-Materials Interaction*, NASP Joint Program Office Workshop Pub. 1004, ed. H.G. Nelson (Moffett Field, CA: NASA-Ames, Nov. 1988), 3-17.

4. M.J. Blackburn, D.L. Ruckle and C.E. Bevan, Technical Report No. AFML-TR-78-18, Wright-Patterson AFB, OH, 1978.

5. M.J. Blackburn and M.P. Smith, Technical Report No. AFML-TR-81-4046, Wright-Patterson AFB, OH, 1981.

6. R.G. Rowe, "Recent Developments in Ti-Al-Nb Titanium Aluminide Alloys," in *High Temperature Aluminides and Intermetallics* (Warrendale, PA: TMS-AIME), in press.

7. W.-Y. Chu, A.W. Thompson, and J.C. Williams, in *Hydrogen Effects on Material Behavior*, eds. N.R. Moody and A.W. Thompson (Warrendale, PA: TMS-AIME,1990), in press.

8. W.-Y. Chu and A.W. Thompson, "Effect of Hydrogen as a Temporary β Stabilizer on Microstructure and Brittle Fracture Behavior in a Titanium Aluminide Alloy," *Metall. Trans. A*, in press.

9. W.-Y. Chu, A.W. Thompson, and J.C. Williams, "Brittle Fracture Behavior and Influence of Hydride in Titanium Aluminide," *Metall. Trans. A.*, submitted.

10. J. R. Griffiths and D.R.J. Owen, *J. Mechanics and Physics of Solids*, vol. 19 (1971), 419-431.

11. A.W. Thompson, *Materials Science and Technology*, vol. 1 (1985), 711-718.

12. D. J. Alexander, J.J. Lewandowski, W.J. Sisak, and A.W. Thompson, *J. Mechanics and Physics of Solids*, vol. 34 (1986), 433-454.

13. A.W. Thompson, in *Transmission and Storage*, Vol. II of *Hydrogen: Its Technology and Implications*, eds. K.E. Cox and K.D. Williamson (Cleveland: CRC Press, 1977), 85-124.

14. A. Sieverts, *Z. f. Metallkunde*, vol. 21 (1929), 37-44.

15. C.J. Smithells, *Gases and Metals* (London: Chapman and Hall, 1937), 140-159.

16. W.-Y. Chu and A.W. Thompson, "Hydrogen Solubility in Ti-24 Al-11 Nb," submitted.

17. A.W. Thompson, W.-Y. Chu and J.C. Williams, in *Summary Proceedings of the 2nd Workshop on Hydrogen-Materials Interaction*, NASP Joint Program Office Workshop Pub. 1004, ed. H.G. Nelson (Moffett Field, CA: NASA-Ames, Nov. 1988), 133-135.

18. D.S. Shih, G.K. Scarr and G.E. Wasielewski, *Scripta Metall.*, vol. 23 (1989), 973-978.

19. W.R. Kerr, *Metall. Trans. A*, vol. 16A (1985), 1077-1087.

20. A.W. Thompson and W.-Y. Chu, in *Summary Proceedings of the 3rd Workshop on Hydrogen-Materials Interaction*, NASP Joint Program Office Workshop Pub. 1007, ed. H.G. Nelson (Moffett Field, CA: NASA-Ames, Aug. 1990), 125-130.

21. J.F. Knott, *Fundamentals of Fracture Mechanics*, esp. Ch. 7, Butterworths, London, 1973.

22. A.W. Thompson and I.M. Bernstein, *Advances in Corrosion Science and Technology*, Vol. 7, ed. M.G. Fontana and R.W. Staehle (New York: Plenum, 1980), 53-175.

23. B.J. Marquardt, G.K. Scarr, J.C. Chesnutt, C.G. Rhodes and H.L. Fraser, in *Titanium Science, Technology and Applications* (Proc. 6th World Conf. on Ti), ed. P. Lacombe, R. Tricot and G. Beranger (Paris: Les Editions de Physique, 1989), Vol. 2, 955-963.

24. J. C. Chesnutt and R.A. Spurling, *Metall. Trans. A*, vol. 8A (1977), 216-218.

25. J. C. Williams, A. W. Thompson, C. G. Rhodes, and J. C. Chesnutt, in *Titanium and Titanium Alloys* (Proc. 3rd Int. Conf. on Titanium), eds. J. C. Williams and A. F. Belov (New York: Plenum, 1982), Vol. 1, 467-496.

26. C.H. Ward, J.C. Williams, A.W. Thompson, D.G. Rosenthal, and F.H. Froes, in *Titanium Science, Technology and Applications* (Proc. 6th World Conf. on Ti), eds. P. Lacombe, R. Tricot and G. Beranger (Paris: Les Editions de Physique, 1989), 1103-1108.

27. C. McCollough, J.J. Valencia, H. Mateos, C.G. Levi, R. Mehrabian and K.A. Rhyne, *Scripta Metall.*, vol. 22 (1988), 1131-1136.

28. G.H. Meier and F.S. Pettit, University of Pittsburgh, personal communication, 1989.

29. S.J. Gittis and D.A. Koss, in *High-Temperature Ordered Intermetallic Alloys* (MRS Symp. 133), ed. C.T. Liu, *et al.* (Pittsburgh: Materials Research Society, 1989), 323-328.

30. D.A. Koss, D. Banerjee, D.A. Lukasak and A.K. Gogia, in *High Temperature Aluminides and Intermetallics* (Warrendale, PA: TMS-AIME), in press.

REF. 10

EFFECT OF GRAIN SIZE AND HYDRIDES ON MECHANICAL BEHAVIOR OF TiAl

Anthony W. Thompson and Wu-Yang Chu*

Dept. of Metallurgical Engineering and Materials Science
Carnegie Mellon University
Pittsburgh, PA 15213

*now at: Dept. of Materials Physics
University of Science and Technology
Beijing 100083, CHINA

Abstract

Equiaxed grains of varying size were produced in a single-phase γ microstructure of TiAl of equiatomic composition by heat treatment between 1135°C and 1300°C. The yield strength measured in compression for these microstructures obeyed a Hall-Petch relation,

$$\sigma_y = 235 \text{ MPa} + 0.124 \text{ MPam}^{-1/2}\, d^{-1/2},$$

which includes a Hall-Petch slope more than ten times smaller than recently reported in the literature. The discrepancy may have arisen from impurity or other material effects. Heat treatment above 1300°C produced a $\gamma + \alpha_2$ microstructure of lamellar morphology. After heat treatment at 1425°C, the lamellar constituent formed 100% of the microstructure and contained about one-third α_2 phase. Yield and fracture strengths of this mixed microstructure were higher than for the single-phase γ material. Results on hydrogen effects are also included. Hydrogen is readily absorbed at elevated temperature into the γ titanium aluminide, in amounts as large as 50 at. %, and on cooling virtually all this hydrogen is precipitated as a hydride phase or phases. The presence of these precipitated hydrides affects mechanical properties in ways similar to what is observed in other hydride-forming materials. Strengthening produced by the hydride phase appeared to "saturate" at about 6 at.% hydrogen.

Introduction

There has been extensive interest expressed in recent years in titanium aluminide alloys. In addition to their potential as a new generation of titanium alloys [1,2], they also have been identified as candidate aerospace materials for future generations of both jet engines and airframes, particularly for the National Aerospace Plane (NASP) project [3]. Among the earliest titanium aluminide alloys developed [4,5] was one based on Ti_3Al, Ti-24-11 (24% Al, 11%Nb in atomic per cent), with a family of related alloys emerging since that time [6]. More recently, interest has also been drawn to TiAl alloys [2], either with a single-phase γ aluminide structure or as a $\gamma + \alpha_2$ structure.

This paper is a brief description of our recent experiments on yield strength and hydride effects on mechanical behavior in a single-phase γ alloy, Ti-50 Al. The interest in yield strength arose from the publication of Vasudevan, *et al.* [7], reporting determination of Hall-Petch parameters for TiAl. For the subject of hydrogen effects, we draw upon a broad background of knowledge about hydrogen embrittlement phenomena [8,9], including recent work on hydrogen in Ti-24-11 [10-12] and in TiAl [13], to address hydrogen performance of this γ alloy.

Experimental Procedure

The starting TiAl material had the following composition (in atomic %): Al = 49.9, Fe = 0.16, O = 0.12, N = 0.005, H = 0.14. It was in the form of a cast and homogenized ingot Specimens were rough-cut from the ingot, heat treated, and finish machined. The specimens included a flat tensile with a gage section 8 mm x 0.4 mm; compression cubes with dimensions of 2.5 mm x 3.5 mm x 5.5 mm; and single-edge notched bend bars containing a Charpy-type notch of depth 1.67 mm and root radius 0.25 mm (following the Griffiths and Owen [14] design). All samples were sealed in evacuated tubes and heat treated at 1135°C to 1425°C for selected times to obtain various grain sizes, cooled to room temperature, and then annealed at 900°C for 2 hours to stabilize the microstructure.

Separate specimens were used for investigation of hydrogen dissolution in TiAl. Thin sections with dimensions of 0.5 mm x 12 mm x 12 mm were sealed in quartz tubes backfilled with 300 to 400 torr hydrogen (40-50 kPa) to achieve the desired pressure at the heat treatment temperature, and times ranged from 0.5 to 65 hours to accomplish equilibration under the chosen conditions. Results were used to determine the variation of maximum hydrogen concentration with charging temperature. The weight gain, determined by an analytic balance with a sensitivity of 10 μg, was used to calculate the hydrogen concentration in the specimens. The total weight of the charging specimens was about 3 grams, so that the error in calculated hydrogen concentration was less than 10 wppm.

After heat treatment at 1150°C for 2h, air cooling, and 900°C, 2h/AC, some compression specimens were precharged with hydrogen at different temperature using a Sieverts apparatus [15-18], in order to investigate the variation of the yield strength with the amount of hydride. This γ alloy absorbs considerable hydrogen from the gas phase at 1 atm pressure, at temperatures above 700°C. Gas-phase charging with the Sieverts apparatus was found previously [19,20] to be fully reversible, an important point not only for solvus measurements, but also for the separation of intrinsic hydrogen effects from damage caused during charging [8]. Reversibility was demonstrated, for example, through removal of hydrogen by repeating the aging heat treatment in vacuum, which resulted in a return of the sample to its original weight. Samples typically returned to the original weight within 25 μg after hydrogen removal.

Results

Microstructures

For Ti-50 at.%Al alloy, equiaxed grains of single-phase γ, or a lamellar structure, or mixed structures with various volume fractions of the lamellar structure, were obtained through heat treatment at the temperatures already described. Equiaxed grains of single-phase γ with the sizes of 19 μm, 22.4 μm, 39.1 μm, 63 μm and 123 μm were obtained when the Ti-50 Al alloy was heat treated between 1135°C and 1300°C, as shown in Fig. 1. After heat treatment at 1425°C, a

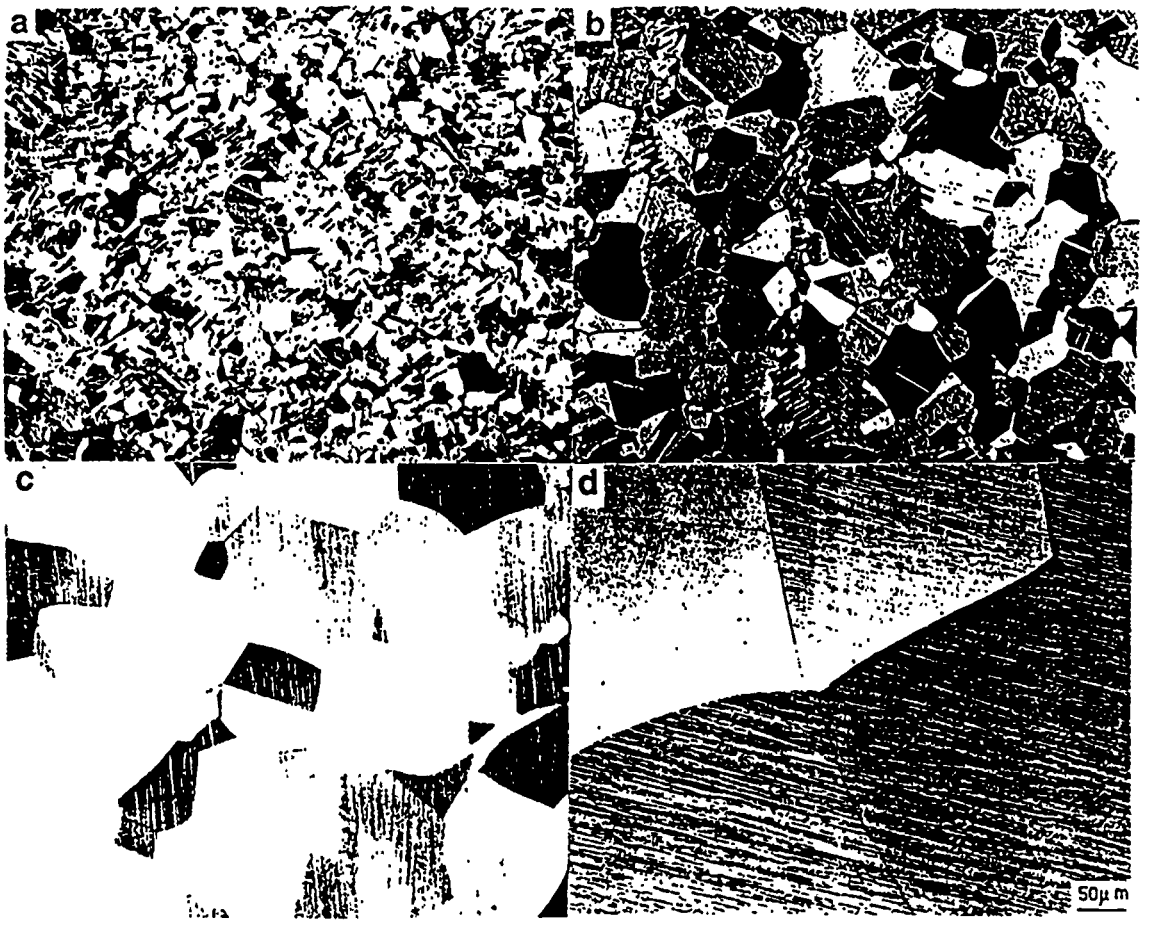

Figure 1. Examples of equiaxed grains of single-phase gamma. (a) 1135°C, 0.5 hr.; (b) 1150°C, 2 hrs.; (c) 1250°C, 2 hrs.; (d) 1300°C, 2 hrs. All at same magnification.

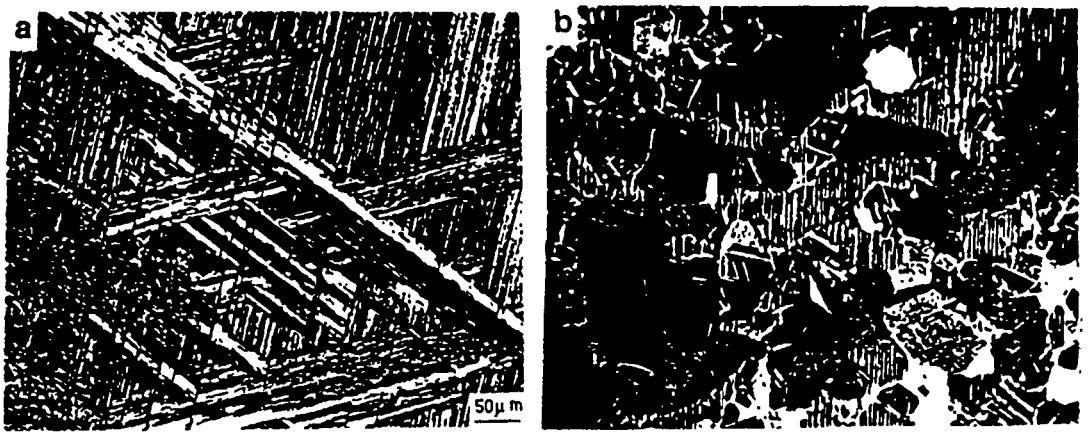

Figure 2. Lamellar structures, all at same magnification. (a) Fully lamellar structure developed at 1425°C. (b) About 20% lamellar structure, heat treated at 1320°C.

lamellar structure with an average width of the individual α_2 lamellae of about 5-10 μm was observed, as shown in Fig. 2(a). A mixed structure with various volume fraction of the lamellar structure were observed after heat treated at 1320°C to 1400°C, as shown in Fig. 2(b). As solution treatment temperatures were increased above 1300°C, the alloy contained increasing amounts of lamellar α_2, to as much as one-third, resulting either from entering the $\alpha + \gamma$ phase field (α orders to α_2 on cooling), Fig. 3, or possibly due to aluminum loss during heat treatment [21]. X-ray diffraction analysis of the bulk samples revealed that the equiaxed grains were single-phase gamma but the lamellar structure consisted of two-phase $\gamma + \alpha_2$. Examples of X-ray results, for comparison to hydride diffraction results, are shown in Fig. 4.

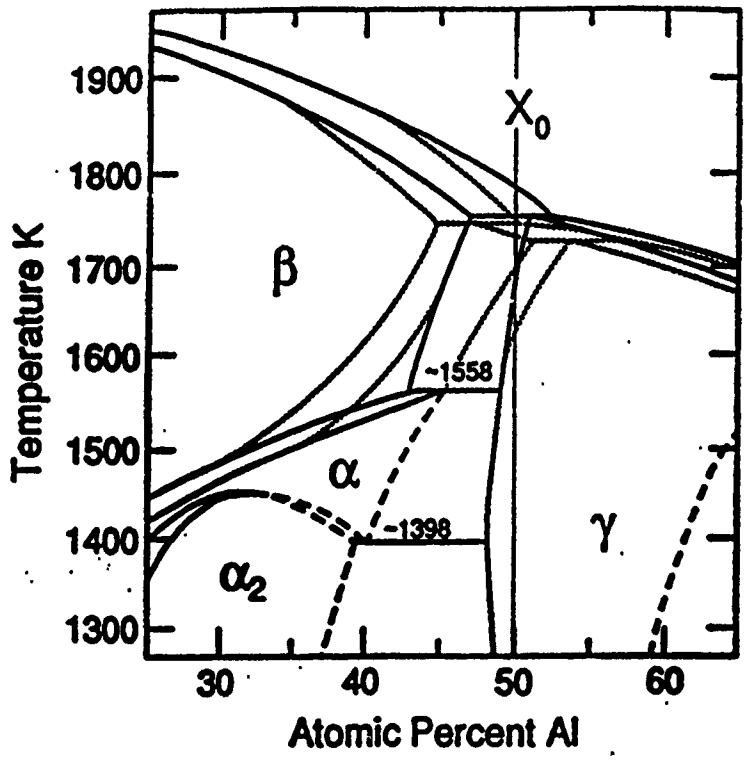

Figure 3. Ti-Al phase diagram from McCollough, *et al.* [21]; "X_0" designates the TiAl composition.

Yield Strength

The Hall-Petch equation, in which yield strength σ_y is given as $\sigma_y = \sigma_0 + k_y d^{-1/2}$, where d is grain size and σ_0 and k_y are constants, describes behavior of many materials [22-24]. Vasudevan *et al.* [7] found that the yield strength in TiAl apparently obeyed the Hall-Petch relationship, and they obtained a relatively large number for the constant k_y. However, each of their five data were from a separate material which had different composition and microstructure. For example, the Ti-48 at.% Al alloy had $\gamma + \alpha_2$ structure but Ti-52 at.% Al and Ti-54 at% Al were single-phase γ and Ti-50 Al-0.4 Er contained a second phase, Er_2O_3, which increased the yield strength (γ is the TiAl phase, α_2 is based on Ti_3Al). But since the size of equiaxed grains of single-phase γ in TiAl can be readily changed through heat treatment at different temperature, the effect of grain size of single-phase γ on the yield strength can be investigated without changing composition and microstructure. Such measurements were one goal of this work.

The variation of the average yield strength (tensile and compression tests) and the fracture strain with grain size is shown in Fig. 5. For the equiaxed grains of single-phase γ, the yield strength measured by either tension or compression obeyed the Hall-Petch relationship, i.e.

$$\sigma_y = 173\ \text{MPa} + 0.130\ \text{MPam}^{-1/2}\, d^{-1/2}\ \text{(tension)}$$
$$\sigma_y = 235\ \text{MPa} + 0.124\ \text{MPam}^{-1/2}\, d^{-1/2}\ \text{(compression)}$$

These k_y values may be compared to the k_y of Vasudevan, *et al.* [7], namely 1.4 $\text{MPam}^{-1/2}$. The present values are more than ten times smaller than the published value [7], as is clearly shown in plotting our results on the same plot as that of Vasudevan, *et al.* [7], Fig. 6. Since the published results [7] include, as mentioned, different compositions and microstructures, it would appear that the present values, all for equiaxed grains of the same composition, are to be preferred. It should also be mentioned that some of the previous results cited by Vasudevan, *et al.* [7] do not report the oxygen or other interstitial content of their material, raising the possibility that impurity effects may have greatly affected the prior determination of k_y [7]. Incidentally, the data point for single-phase Ti-50 Al measured by Vasudevan, *et al.*, themselves, at the lower left of Fig. 6, is in reasonable agreement with our data.

The yield strength of the lamellar structure, however, was much higher than that of the equiaxed grains, e.g., 236 MPa (tensile) or 278 MPa (compression), respectively, as shown in Fig. 5. Extrapolation of the equiaxed-grain compressive data to the yield strength of the lamellar

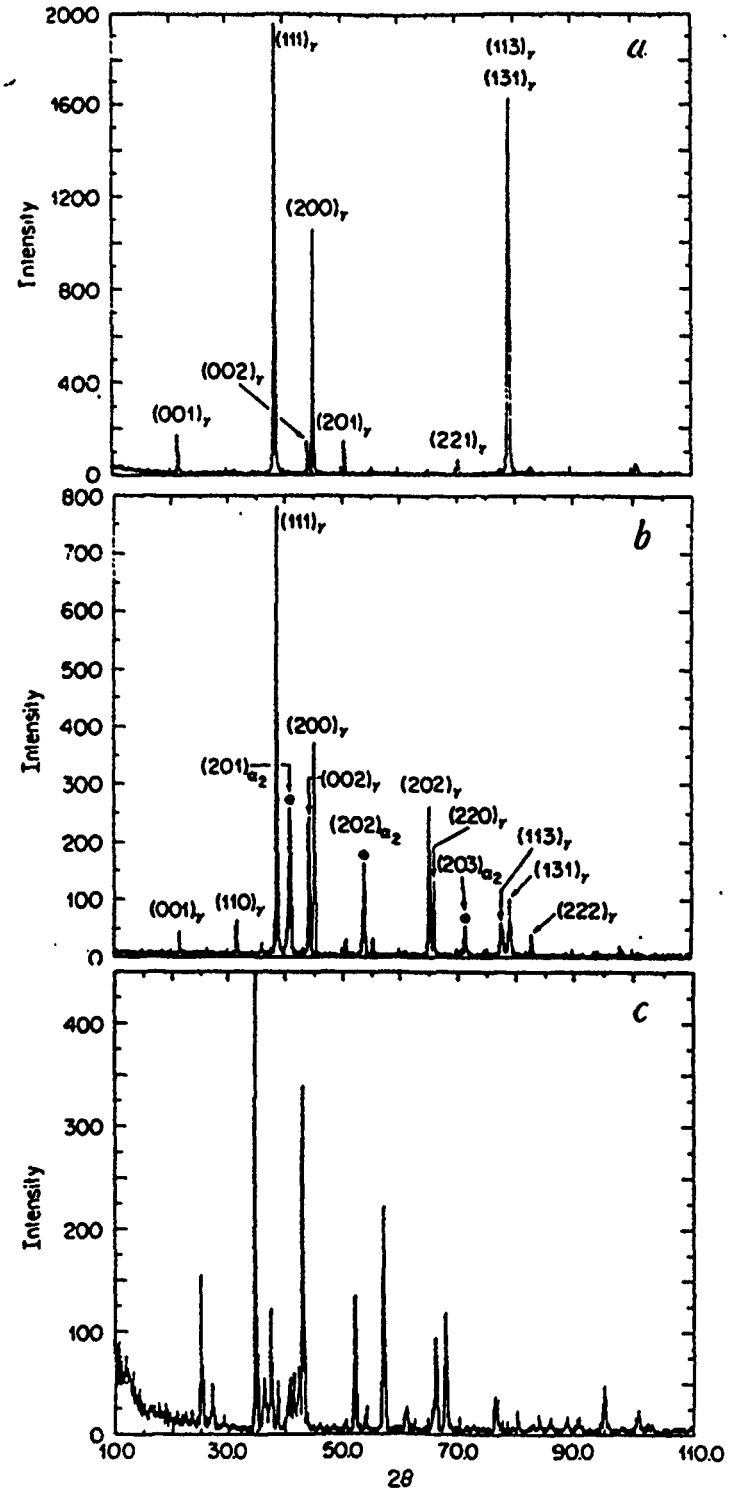

Figure 4. X-ray diffraction patterns of TiAl microstructures. (a) single-phase γ, heat treated at 1320°C; (b) γ + α_2 structure, heat treated at 1425°C; (c) hydride-containing material with about 50 at.% hydrogen.

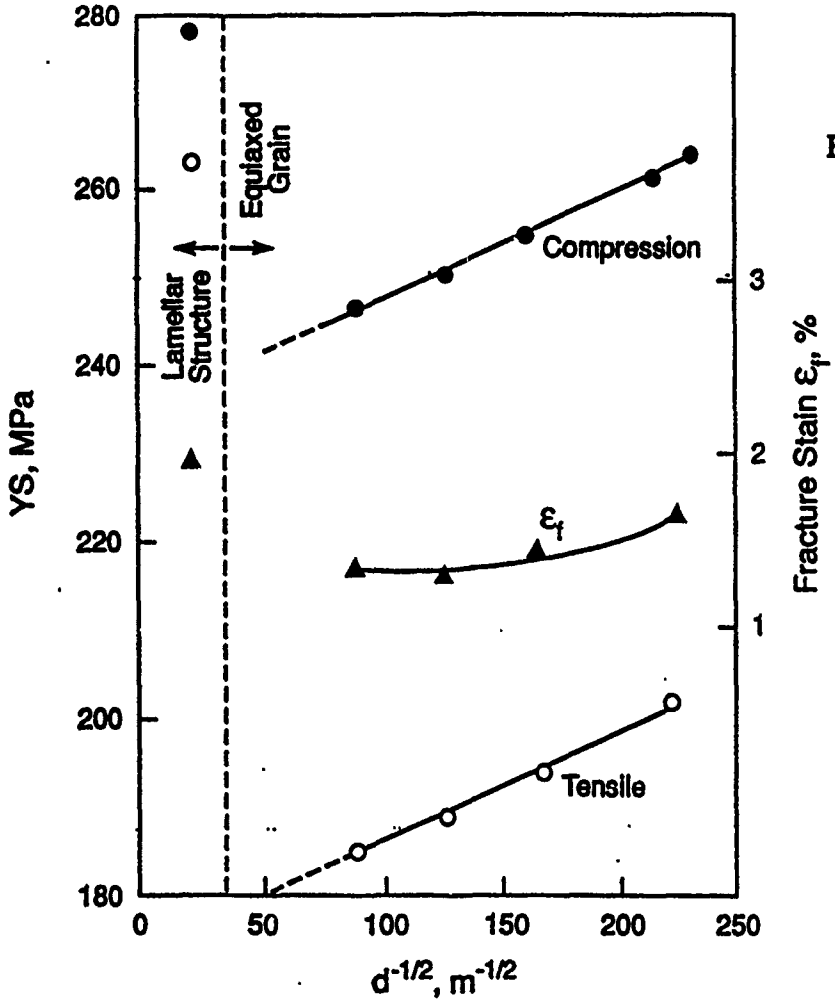

Figure 5. The variation of the yield strength (average value of 3 to 5 data) and the fracture strain with grain size. Data for the lamellar structure shown at left, plotted with prior γ grain size.

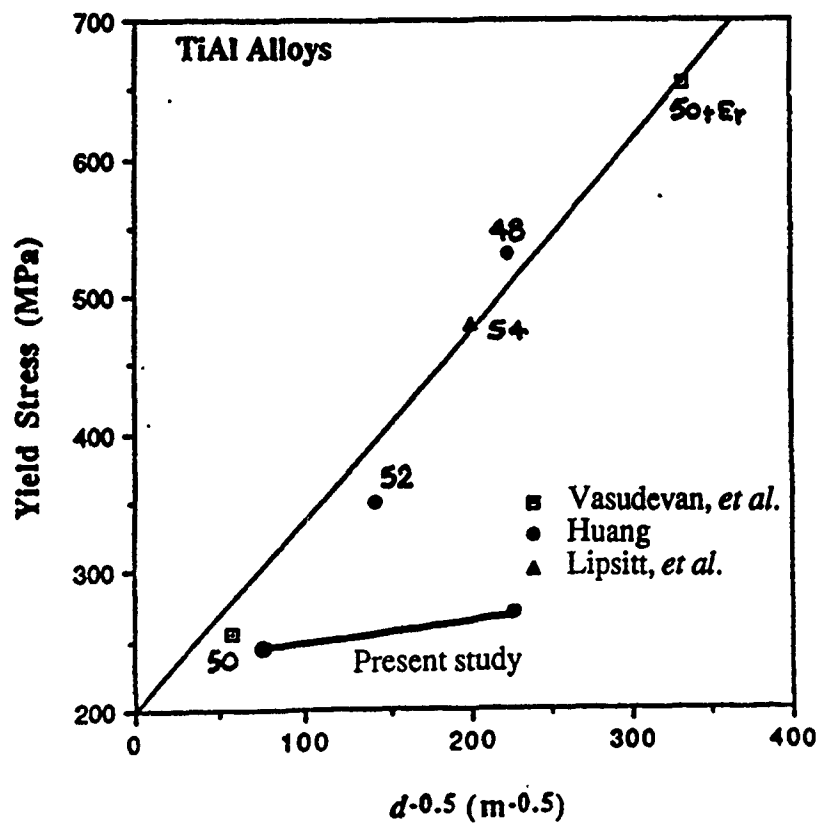

Figure 6. Hall-Petch plot of Vasudevan, *et al.* [7], with data trend of present work added. Of the two ref. 7 data shown, one is for an Er-containing alloy. The at.% Al is shown for all other points. Huang data from *Scripta Metall.*, vol. 22 (1988), 1885-88;Lipsitt, *et al.* data from *Metall. Trans. A*, vol. 6A (1975), 1991-96.

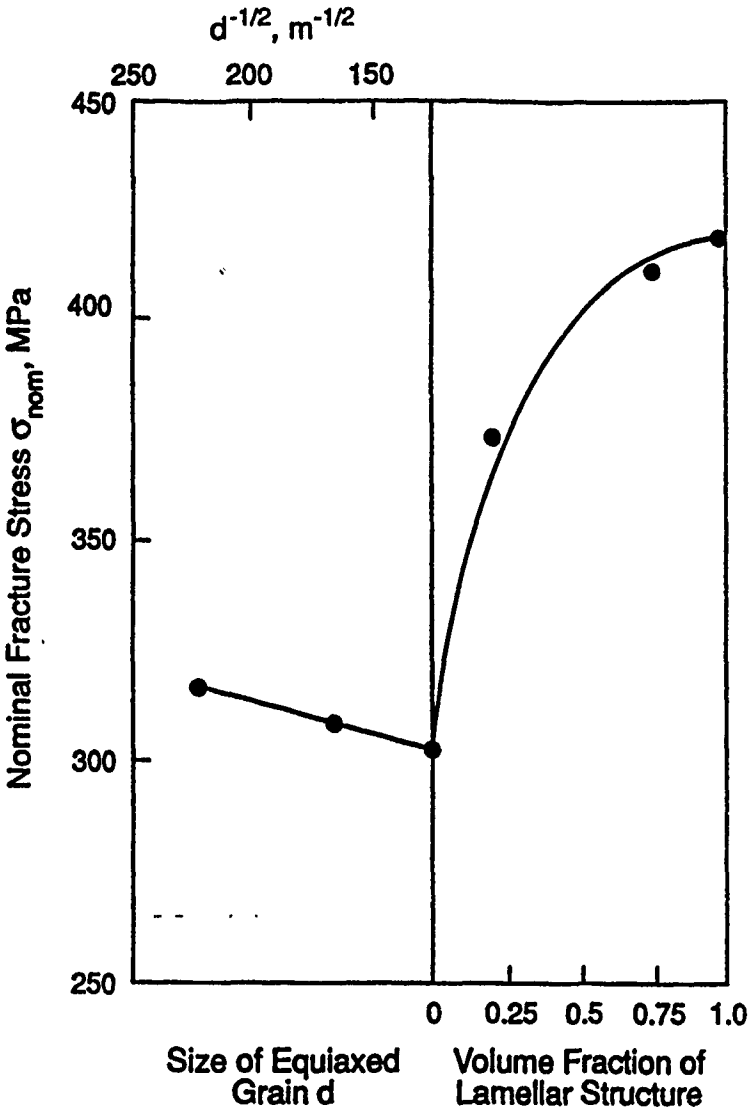

Figure 7. The nominal fracture stress in bend bars vs grain size of the equiaxed grains (left) and the volume fraction of the lamellar structure (right). See also Table I.

structure gives an implied value for "effective grain size" of 8 μm, comparable to the 5-10 μm observed widths of the lamellae in this structure. This apparent agreement suggests that the α_2 lamella width may be an effective slip distance in the lamellar microstructures.

Fracture Behavior

The fracture strain in tension was only weakly dependent on grain size, as shown in Fig. 5, for the equiaxed grain microstructures. For the equiaxed grains, the nominal fracture stress of the notched bend specimens, σ_{nom}, only increased from 302 MPa to 317 MPa while the grain size decreased from 63 μm to 23 μm, as shown in Fig. 7. If there was some lamellar structure mixed with the equiaxed grain, however, σ_{nom} increased substantially, even if the mixed structure had the same prior γ grain size as the equiaxed grain. The σ_{nom} value increased with increasing volume fraction of the lamellar structure, as shown in Fig. 7 and Table I.

Table I. Nominal fracture stress vs. the volume fraction of the lamellar structure:

volume fraction of the lamellar structure	γ grain size, μm	σ_{nom}, MPa*
0	63	302
20	55	375
75	70	412
100	740	420

*Computed with standard methods [25-27]

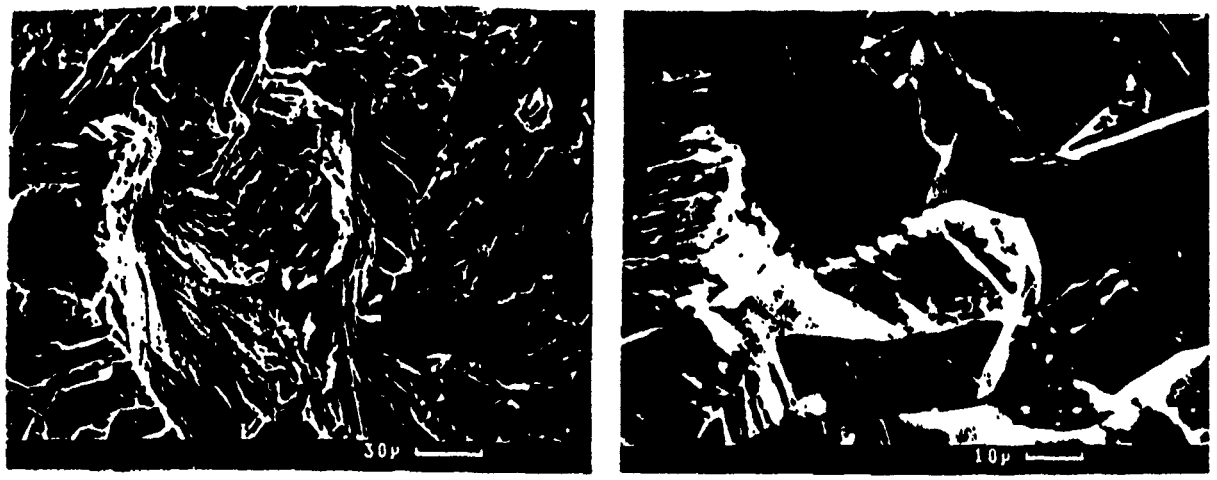

Figure 8. Fracture surfaces of notched bend specimens for the equiaxed grains.

All fractured specimens were examined by scanning electron microscopy (SEM). For the equiaxed grains, the fracture surfaces were very brittle-looking and consisted of predominantly cleavage-like and blocky fracture areas, with occasional intergranular fracture, as shown in Fig. 8. The cleavage-like regions did not generally appear to correspond to entire grains. Instead, it appeared that part of a grain fractured transgranularly by the cleavage-like process, while the remainder, typically nearer grain edges, exhibited the blocky appearance. Intergranular-appearing areas were less than 10% of the surface, and were entirely absent from some areas which were many tens of micrometers in extent.

Since it has not been determined that this fracture is crystallographic in γ nor that it occurs on a low-index plane of the γ, it would be inappropriate to designate it as "cleavage," although the fractographic appearance is often consistent with micro-fracture in a cleavage mode. In many areas, however, the cleavage-like fracture is not planar but appears curved or conchoidal in character. More work will be necessary to clarify the micromechanism of this fracture process.

For the mixed structures with various volume fractions of the lamellar structure, there were many areas of stepped appearance which suggested a lamellar fracture, as shown in Fig. 9. In these microstructures, the occasional intergranular fracture seen in equiaxed grains was not observed, and the cleavage-like appearance was much less prevalent, consistent with the reduced volume fraction of γ grains. The stepped or lamellar fracture appears to be brittle across the lamellae but to include some tearing or secondary fracture between lamellae.

Figure 9. Fracture surfaces for notched bend specimens for the mixed structure with 80% lamellar structure.

Hydrogen Effects

To carry out hydrogen studies, it was necessary to estimate the hydrogen solvus for the Ti-50 Al material, since no solvus appears to have been determined to date for any γ or near-γ alloy. Our result for hydrogen uptake is shown in Figure 10. It may also be noted that extrapolation of the curve in Figure 10 to room temperature, using a spline fit, gives an estimate of the room temperature solubility of less than 10 ppb. This is, of course, a crude estimate, but does suggest that virtually all charged hydrogen precipitates as hydride upon cooling. Although substantial amounts of hydrogen can be charged into this alloy above 800°C, the levels of aparent solubility at each temperature are distinctly lower than for Ti-24-11 [10,19,28]. This presumably reflects a lower solubility in the γ phase, compared to what has been observed in α_2. Below 1300°C, our Ti-50 Al material was all γ, but above that temperature, as mentioned above, the microstructure comprised a lamellar mixture of γ and α_2. Thus Fig. 10 depicts the solubility of mixed microstructures above 1300°C.

Examination of the charged and cooled γ phase material revealed very extensive hydride formation, as in α_2 materials [11,12,20,29], as shown in Fig. 11. X-ray diffraction was used to determine that the hydride typically has the same structure as does the γ hydride in the Ti-H system, sometimes called TiH_2. We have not determined the stoichiometry of the hydride in Ti-50 Al. As in the case of Ti-24-11 and other alloys, this hydride in Ti-50 Al has the f.c.t. γ structure, for hydrogen contents below about 1000 wppm. At higher hydrogen contents, it appears from our X-ray observations that one or two additional hydride crystal structures are also present, as suggested in Fig. 4(c). Work on mechanical behavior of hydride-containing Ti-50 Al has necessitated care with cooling rates from hydrogen charging temperatures, for hydrogen levels above 2000 wppm. At such hydrogen levels, cracking can result on cooling unless slow cooling rates are maintained. At very high hydrogen levels, 6000 wppm and above, powdering of the alloy was encountered even at moderate cooling rates. Such a result is convenient for X-ray analysis but effectively precludes mechanical testing.

Preliminary mechanical tests have been conducted on all-γ material, with hydrogen contents up to 5000 wppm. To minimize complications from premature fracture, these tests were

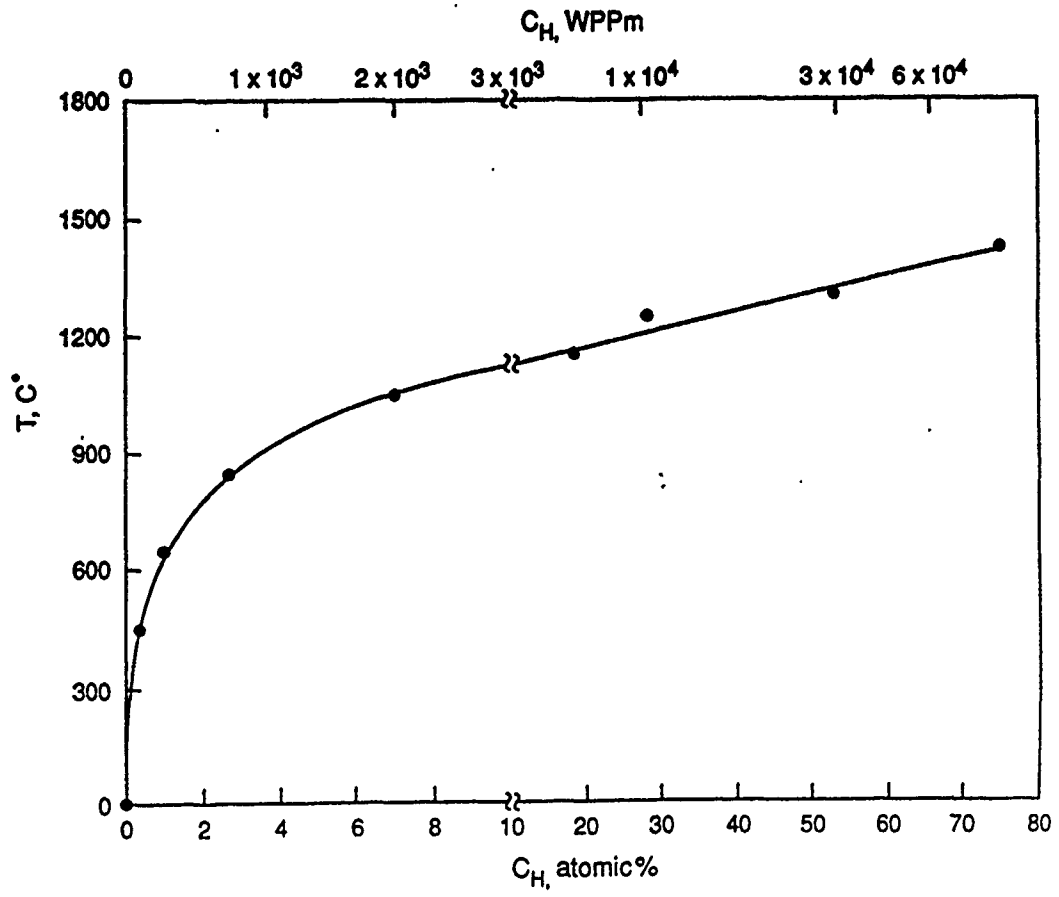

Figure 10. The maximum hydrogen concentration vs charging temperature for Ti-50 Al.

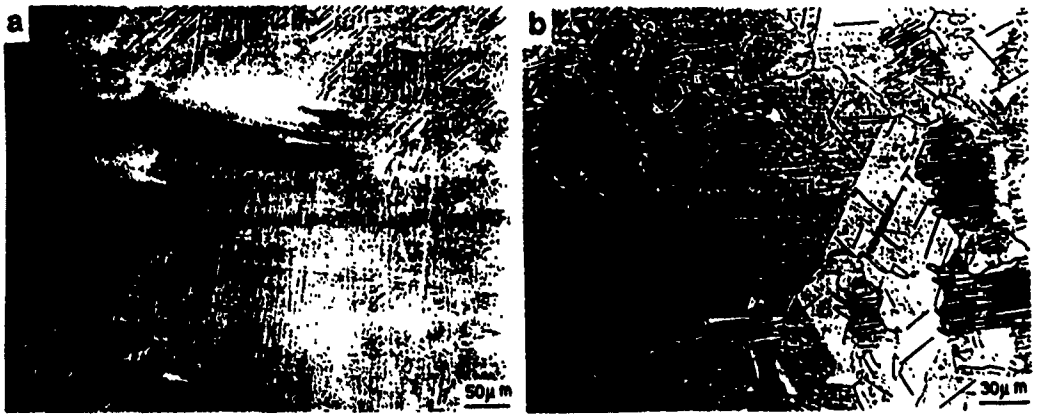

Figure 11. Hydride appearance. (a) No etching, polarized light. (b) Etching with HNO_3 (5 parts)+HF (2 parts)+Lactic acid (20 parts).

conducted in compression. Results are shown in Figure 12. As in Ti-24-11, the hydride phase strengthens the material, but the magnitude of the effect in Figure 12 is quite modest compared to Ti-24-11 [20,28,30]. In Ti-50 Al, the higher charging temperatures used for higher hydrogen contents also coarsened the grain size. Thus the modest strengthening shown in Figure 12 is understated if a correction for grain size strengthening is considered. It is interesting that the strengthening "saturates" above about 1500 wppm hydrogen, or about 6 at.% H. If the strengthening is due to reduction of slip length by increasing subdivision of the γ grains by hydride plates, as in Fig. 11(b), the effect would be expected to saturate as the volume increasingly fills with hydride, leaving little matrix to subdivide further.

Concluding Remarks

The preceding presention of results has included comment on major features of the experimental results. It remains to discuss the larger issues raised by these data. Most of the

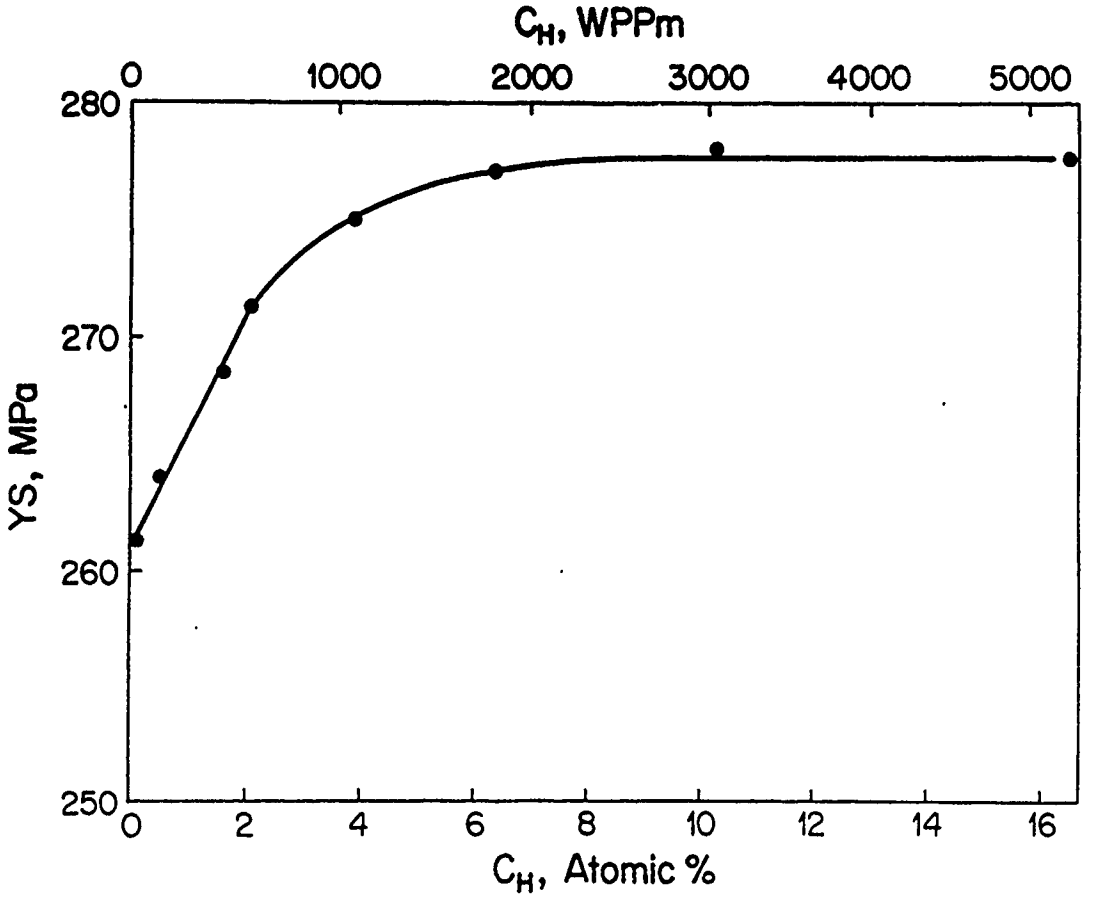

Figure 12. Yield strength as a function of hydrogen concentration (present as hydride) at room temperature, in Ti-50 Al. All charging conducted below 1200°C, so material was all γ.

results obtained here are generally similar to literature results. It is important to note that our data on single-phase, equiaxed grain structures of Ti-50 Al have a Hall-Petch slope which is more than an order of magnitude smaller than that estimated by Vasudevan, *et al.* [7]. Most of the reasons for discrepancies in Hall-Petch data, such as impurity content or starting dislocation density, tend to increase yield strength, suggesting that our lower values are more reliable. The possible role of crystallographic texture cannot be assessed since none of the published reports have included texture characterization; diffractometer intensities as well as Laue results for our material suggest that a strong texture is not present, though we cannot estimate the strength of whatever texture may be present.

The deformation and fracture behavior of either the single-phase γ, or of the mixed $\gamma + \alpha_2$ microstructures, probably cannot be interpreted in parallel with that of α_2 alloys based on Ti_3Al [2,6,12,28,31-35]. The absence of the relatively ductile β phase significantly alters the fracture process in particular. The fracture process in Ti-50 Al, although cleavage-like in appearance, may not be classical cleavage in character. It has been shown that brittle fracture in Ti-24-11, at least, is not a classical stress-controlled fracture, but has a critical strain component to cracking [20,30]. Additional work on microstructural variation and micromechanisms of fracture would be most welcome. The hydride results shown here raise some significant questions. The stoichiometry and in some instances the crystal structure of the hydride(s) in these alloys needs investigation, as do the modes of formation and dissolution of the phase(s). More extensive mechanical property measurements would also be welcome for detailed interpretation of the behavior of the TiAl alloys.

Acknowledgements

We are grateful to Profs. I.M. Bernstein and J.C. Williams for many helpful discussions on this research. This work was sponsored by the Defense Advanced Research Projects Agency through DARPA Order 6155, monitored by the Air Force Office of Scientific Research under Contract F49620-88-C-0013. This is a joint contract of the University of Pittsburgh and Carnegie Mellon University.

References

1. H. A. Lipsitt, in *High-Temperature Ordered Intermetallic Compounds* (MRS Symp. 39), ed. C.C. Koch, *et al.* (Pittsburgh: Materials Research Society, 1985) 351-364.

2. R. L. Fleischer, D.M. Dimiduk and H.A. Lipsitt, *Ann. Rev. Mater. Sci.*, vol. 19 (1989), 231-263.

3. T. M. Ronald, in *Summary Proceedings of the 2nd Workshop on Hydrogen-Materials Interaction*, NASP Joint Program Office Workshop Pub. 1004, ed. H.G. Nelson (Moffett Field, CA: NASA-Ames, Nov. 1988), 3-17.

4. M.J. Blackburn, D.L. Ruckle and C.E. Bevan, Technical Report No. AFML-TR-78-18, Wright-Patterson AFB, OH, 1978.

5. M.J. Blackburn and M.P. Smith, Technical Report No. AFML-TR-81-4046, Wright-Patterson AFB, OH, 1981.

6. R.G. Rowe, "Recent Developments in Ti-Al-Nb Titanium Aluminide Alloys," in *High Temperature Aluminides and Intermetallics* (Warrendale, PA: TMS-AIME), in press.

7. V.K. Vasudevan, S.A. Court, P. Kurath and H.L. Fraser, *Scripta Metall.*, vol. 23 (1989), 467-469.

8. A.W. Thompson and I.M. Bernstein, *Advances in Corrosion Science and Technology*, Vol. 7, ed. M.G. Fontana and R.W. Staehle (New York: Plenum, 1980), 53-175.

9. A.W. Thompson, *Materials Science and Technology*, vol. 1 (1985), 711-718.

10. A.W. Thompson, W.-Y. Chu and J.C. Williams, in *Summary Proceedings of the 2nd Workshop on Hydrogen-Materials Interaction*, NASP Joint Program Office Workshop Pub. 1004, ed. H.G. Nelson (Moffett Field, CA: NASA-Ames, Nov. 1988), 133-135.

11. D.S. Shih, G.K. Scarr and G.E. Wasielewski, *Scripta Metall.*, vol. 23 (1989), 973-978.

12. W.-Y. Chu, A.W. Thompson, and J.C. Williams, in *Hydrogen Effects on Material Behavior*, eds. N.R. Moody and A.W. Thompson (Warrendale, PA: TMS-AIME, 1990), 543-554.

13. S.M.L. Sastry, W.O Soboyejo and R.J. Lederich, in *Summary Proceedings of the 3rd Workshop on Hydrogen-Materials Interaction*, NASP Joint Program Office Workshop Pub. 1007, ed. H.G. Nelson (Moffett Field, CA: NASA-Ames, Aug. 1990), 191-200.

14. J. R. Griffiths and D.R.J. Owen, *J. Mechanics and Physics of Solids*, vol. 19 (1971), 419-431.

15. A. Sieverts, *Z. f. Metallkunde*, vol. 21 (1929), 37-44.

16. C.J. Smithells, *Gases and Metals* (London: Chapman and Hall, 1937), 140-159.

17. W.M. Mueller, J.P. Blackledge and G.G. Libowitz, *Metal Hydrides* (Academic Press: New York, 1968), 151.

18. B. Bandyopadhyay, A. Ghoshray and N. Chatterjee, *Bull. Mater. Sci.*, vol. 9 (1987), 305-308.

19. W.-Y. Chu and A.W. Thompson, "Hydrogen Solubility in Ti-24 Al-11 Nb," submitted.

20. A.W. Thompson, "Environmental Effects in Titanium Aluminide Alloys," in *Environmental Effects on Advanced Materials*, ed. R.H. Jones and R.E. Ricker (Warrendale, PA: TMS-AIME), in press.

21. C. McCollough, J.J. Valencia, H. Mateos, C.G. Levi, R. Mehrabian and K.A. Rhyne, *Scripta Metall.*, vol. 22 (1988), 1131-1136.

22. E.O. Hall, *Proc. Phys. Soc.*, vol. B64 (1951), 747-753.

23. N.J. Petch, *J. Iron Steel Inst.*, vol. 173 (1953), 25-28.

24. N. Hansen, *Metall. Trana. A*, vol. 16A (1985), 2167-2190.

25. J.F. Knott, *Fundamentals of Fracture Mechanics*, esp. Ch. 7, Butterworths, London, 1973.

26. D.J. Alexander, J.J. Lewandowski, W.J. Sisak, and A.W. Thompson, *J. Mechanics and Physics of Solids*, vol. 34 (1986), 433-454.

27. J.J. Lewandowski and A.W. Thompson, *Acta Metall.*, vol. 35 (1987), 1453-1462.

28. A.W. Thompson and W.-Y. Chu, in *Summary Proceedings of the 3rd Workshop on Hydrogen-Materials Interaction*, NASP Joint Program Office Workshop Pub. 1007, ed. H.G. Nelson (Moffett Field, CA: NASA-Ames, Aug. 1990), 125-130.

29. P.S. Rudman, J.J. Reilly and R.H. Wiswall, *J. Less-Common Metals*, vol. 58 (1978), 231-240.

30. W.-Y. Chu, A.W. Thompson, and J.C. Williams, "Brittle Fracture Behavior and Influence of Hydride in Titanium Aluminide," *Metall. Trans. A.*, submitted.

31. B.J. Marquardt, G.K. Scarr, J.C. Chesnutt, C.G. Rhodes and H.L. Fraser, in *Titanium Science, Technology and Applications* (Proc. 6th World Conf. on Ti), ed. P. Lacombe, R. Tricot and G. Beranger (Paris: Les Editions de Physique, 1989), Vol. 2, 955-963.

32. C.H. Ward, J.C. Williams, A.W. Thompson, D.G. Rosenthal, and F.H. Froes, in *Titanium Science, Technology and Applications* (Proc. 6th World Conf. on Ti), eds. P. Lacombe, R. Tricot and G. Beranger (Paris: Les Editions de Physique, 1989), 1103-1108.

33. S.J. Gittis and D.A. Koss, in *High-Temperature Ordered Intermetallic Alloys* (MRS Symp. 133), ed. C.T. Liu, *et al.* (Pittsburgh: Materials Research Society, 1989), 323-328.

34. D.A. Koss, D. Banerjee, D.A. Lukasak and A.K. Gogia, in *High Temperature Aluminides and Intermetallics* (Warrendale, PA: TMS-AIME), in press.

35. K.S. Chan, *Metall. Trans. A*, vol. 21A (1990) 2687-2699.

Acta Met., submitted REF. 11

Hydrogen Solubility in a Titanium Aluminide Alloy

Wu-Yang Chu,* Anthony W. Thompson, and James C. Williams**

Dept. of Metallurgical Engineering and Materials Science
Carnegie Mellon University
Pittsburgh, PA 15213

*Now at: Dept. of Materials Physics
University of Science and Technology
Beijing 100083, China

**Now at: Engineering Materials Technology Laboratory
General Electric Aircraft Engines
Evendale, OH 45215

ABSTRACT

The dissolution of hydrogen in a titanium aluminide alloy based on Ti_3Al, Ti-24 Al-11 Nb, has been measured as a function of temperature and hydrogen pressure. Both the terminal solubility and the overall solubility, or total uptake of hydrogen, were determined. The terminal solubility of hydrogen in the α_2 matrix phase increases with temperature, while the overall solubility decreases with increasing temperature in the high-temperature region. The partial molar heat of solution in the α_2 phase was determined to be - (5250 ± 350) cal/mol [H], while the partial molar heat of formation of the hydride phase was -(16,800 ± 560) cal/mol [H]. The standard partial molar free energy of hydrogen in the α_2 phase in equilibrium with the hydride was - (17,700 ± 480) + (21 ± 0.5) T cal/mol [H].

INTRODUCTION

Alloys based on the compound Ti_3Al have received sufficient attention to show that they may be legitimate candidate materials of construction for aerospace systems [1-3]. Of particular interest are both the engines and the airframe of a hydrogen-burning propulsion system [3,4]. Since such alloys contain Ti, with its well-known propensity to interact with hydrogen, it is important to have a clear picture of the effects of hydrogen on the properties and microstructure of these aluminide alloys. Yet since the original interest in this material has been for high performance aircraft engines which typically operate under oxidizing conditions, there has been little effort expended in studying the effects of hydrogen.

On the basis of pioneering studies [5-7], it is now well established [8-10] that the low temperature phase of pure titanium, α-Ti, has a relatively low solubility for hydrogen and precipitates a hydride when the solubility limit is reached. This hydride, the γ phase in the Ti-H system, was originally designated TiH_2 but in more recent literature [11,12] has been designated as TiH, a better description of its typical stoichiometry, although the limiting composition of the γ phase stoichiometry is indeed TiH_2. In the case of the Ti_3Al compound, which is designated α_2 in the titanium-aluminum system, hydrides are also reported to form [13], and the same is true for alloys based on Ti_3Al [14-19]. However, the quantitative description of hydride formation conditions is still largely an open question, and no data on the solubility of hydrogen in this compound are available, other than a preliminary report [14].

For some metals, like Ti and Zr, the maximum amount of hydrogen absorbed increases with pressure and decreases with temperature within a high temperature region [8,20]. Due to this temperature behavior, they were classed as exothermic occluders. However, some workers have shown that the terminal solubility of α-Zr in equilibrium with the hydride phase increased as the temperature rose [21,22].

Among the first alloys based on Ti_3Al was Ti-24 Al-11 Nb (at %), developed by Blackburn and co-workers [23,24]. Our preliminary experiments [14,18] showed that hydride could form in this alloy, designated "Ti-24-11" below, after either cathodic charging in H_2SO_4 solution with recombination poisons, or after thermal charging in hydrogen gas, and the maximum amount of hydrogen absorbed decreased with increasing temperature within a high temperature region (e.g. $T \geq 550°C$). Therefore, it was the purpose of this paper to investigate the formation of hydride in this alloy, and measure the overall solubility of hydrogen in the alloy as well as the terminal solubility of hydrogen in the α_2 phase in equilibrium with the hydride phase. We define "overall solubility" as total equilibrium hydrogen uptake, combining hydrogen in solution with that contained in hydrides, at a given temperature, while "terminal solubility" refers to the maximum amount of hydrogen in solution at that temperature.

EXPERIMENTS

Analytical Basis for Experiments

According to Sieverts' law [20,25-27], the overall solubility of hydrogen in either the α_2 phase or the hydride (γ-phase in the Ti-H system) is proportional to the square root of the hydrogen gas pressure in contact with the phase, $\sqrt{P_{H_2}}$, according to

(1a) $C_H = W\sqrt{P_{H2}}$, with

(1b) $W = e^{-\Delta G/RT} = e^{-\Delta H/RT}\, e^{\Delta S/R}$,

since $\Delta G = \Delta H - T\Delta S$. Here C_H, ΔG, ΔH and ΔS are, respectively, the hydrogen content, partial molar free energy, partial molar enthalpy of solution, and partial molar entropy of solution in the phase under consideration, e.g. α_2, and R is the gas constant. Note that all the relevant thermodynamic quantities can be obtained from measurements varying any two of C_H, P_{H2}, and T, while keeping the third constant, as discussed in more detail below, since [20,27] ΔG can be obtained from $\frac{1}{2} RT \ln P_{H2}$.

The dissolution of hydrogen in metals has been treated using statistical mechanics [22,28]. It can be assumed that the number and position of N_H hydrogen atoms arranged randomly on N_S intersititial sites are related to the partial molar entropy ΔS as

(2a) $$\Delta S = -R \frac{N_H}{N_S - N_H} \text{ and } \Delta G = RT \ln \frac{N_H}{N_S - N_H},$$

and the overall solubility should be

(2b) $$\frac{N_H}{N_S - N_H} = \sqrt{P_{H2}}\, e^{-\Delta G/RT}.$$

Although it has not been established directly, it can be assumed [11-13] that the hydrogen atoms occupy tetrahedral sites on the hexagonal symmetry (DO_{19}) Ti_3Al parent lattice. There are four sites of tetrahedral co-ordination per unit cell in the Ti_3Al structure, therefore

(2c) $$\frac{N_H}{N_S - N_H} = \frac{C_A}{2 - C_A}, \text{ so that}$$

(3) $$\frac{C_A}{2 - C_A} = \sqrt{P_{H2}}\, e^{-\Delta H/RT}\, e^{\Delta S/R},$$

where $C_A = N_H / N_{Ti3Al}$ is the atom ratio. Thus Eq. 3 is the statistical mechanics or "crystallographic" concentration, while Eq. 1 represents the thermodynamic concentration. Since Eq. 3 depends on assumptions about site occupancy, it is potentially less reliable than Eq. 1.

To obtain the terminal solubility of hydrogen in the α_2 structure in equilibrium with the hydride, the condition of equilibrium is that the partial molar free energy of hydrogen is equal in the α_2 phase and the γ phase. Then from Eq. 1, the H concentration ratio is

$$(4) \qquad \frac{C_{H(\alpha_2)}}{C_{H(\gamma)}} = \exp\left[(\Delta S(\alpha_2) - \Delta S(\gamma))/R\right] \exp -\left[(\Delta H(\alpha_2) - \Delta H(\gamma))/RT\right]$$

where the phase is referenced for each parameter. Eq. 4 then describes the terminal solubility.

The terminal solubility could be measured in two ways, which are called the $\sqrt{P}$ vs. C method and the P vs 1/T method. Their basis is as follows, from Eq. 1. The square root of the decomposition (or equilibrium) pressure, $\sqrt{P_{H_2}}$, at a fixed temperature should change linearly with increase of hydrogen concentration C_H, in a single-phase region. However, due to Gibbs' phase rule, in a two-phase region the decomposition pressure would not change with the hydrogen concentration. Thus, the intercept of the straight-line C_H-$\sqrt{P_{H_2}}$ relation and the constant-pressure plateaus give the terminal solubility.

It may also be seen from Eq. 1 that a plot of the decomposition pressure on a logarithmic scale against 1/T is a straight line, for a fixed hydrogen content. Note from Eq. 1 that ΔH can be calculated from the slope of this line. But when a single-phase region goes over into a two-phase region or vice versa, the slope of the straight line will change (e.g. refs. 13, 29). (Observation of a straight line in the two-phase region, incidentally, indicates [20] that only the volume fractions of the two phases, and not the composition of either the solid solution or the hydride, are changing appreciably with temperature; or that the compositions of the two phases are changing in exactly the same way with temperature.) The intersection of two such ln P_{H_2} vs 1/T straight line segments gives the temperature at which the given hydrogen concentration represents the terminal solubility.

Experimental Procedure

All the present experiments were conducted on the titanium aluminide alloy Ti-24-11, which was obtained in bar form from Reactive Metals (RMI). The chemical compositions of the Ti-24-11 were provided by RMI as follows (wt.%): Al = 13.09-13.34, Nb = 20.57-20.64, Fe = 0.14, O =0.09-0.1, N = 0.011-0.016. Blanks with dimensions of 20 mm x 20 mm x 40 mm were machined, cleaned, and solution treated in an argon atmosphere at 1149°C (2100°F) for 2 hrs. and air cooled, then aged at 705°C (1300°F) for 2 hrs. and air cooled. The microstructure after this heat treatment was essentially all α_2 phase. The bcc β phase could not be detected by X-ray, while examination by transmission electron microscopy indicated 0.1 to 1% of the β phase, present only as isolated, discontinuous β regions.

Specimens for hydrogen measurement with dimensions of 20 mm x 20 mm x 1 mm., were sectioned from the bulk samples. The specimens were precharged at different temperature for different times. The weight gain, determined by an analytic balance with a sensitivity of 10^{-5} g was used to calculate the hydrogen concentration in the specimens, which were in the range of 230 wppm (1.1 at.%) to 3720 wppm (15.1 at.%). The total weight of the specimens for each time of charging was about 10 g; therefore, the error calculating the hydrogen concentration was less than 10 wppm.

A Sieverts apparatus [20,25,26,29,30] was used to measure the decomposition pressure in this work. During an experimental run, the specimen tube and the operative pressure devices were isolated from the remainder of the system by means of vacuum valves. The whole apparatus was capable of being evacuated initially to a pressure of about 10 μPa (1×10^{-7} torr). The decomposition pressures over the samples were read on two mercury manometers. One of them was a McLeod gage with a range of 125 Pa (1 torr), and the other had a range of 2 kPa (15 torr). For each composition, the number of the samples was changed to keep the total amount of hydrogen about constant, e.g. 3.3 mg to 4.6 mg of H_2 for each constant temperature. Temperature was controlled within ± 1°C.

The decomposition pressure was measured many times until a stable pressure was obtained. To assure that the equilibrium pressures were actually determined, measurements were made on both the decomposition (heating cycle) and absorption (cooling cycle) for some samples. Fully reversible behavior was always observed in such runs. Reversibility was also checked by repeating some measurements on the same sample. After measurement, a sample would be heated in the evacuated Sieverts apparatus to remove all hydrogen (it was verified that sample weight would return to the precharging value within 10 μg), re-charged with hydrogen, and additional measurements made. Reproducibility of results in such repetitions was excellent.

RESULTS

Terminal solubility of hydrogen in α_2, in equilibrium with hydride, was determined by the methods described above. Fig. 1 shows a typical log decomposition pressure ($\sqrt{P_{H_2}}$) vs 1/T graph obtained for the hydrogen concentration of 2.3 at. % (490 wppm) hydrogen. Table 1 summarizes the experimental data for eight hydrogen concentrations.

In Fig. 1 the slope change at the phase boundary is clearly evident. Fig. 1 indicates the α_2 to be the stable phase over the section BC of the graph, while a mixture of the α_2 phase and the hydride

phase are stable over the section AB. The point B gave the temperature at which the concentration of 2.3 at. % represented the terminal solubility, which was 447°C. The slope of BC gave a partial molar heat of solution as $\Delta H_{\alpha 2}$ = -5010 cal/mol [H] for the α_2 phase, while the slope of AB gave a value of ΔH_γ = -17,900 cal/mol [H] for the hydride phase. This calculation assumes the composition of the hydride phase was invariant with temperature, as is implied by the reasonably straight AB lines in Figs. 1 and 2.

The partial molar heats of solution $\Delta H_{\alpha 2}$, ΔH_γ and the partial molar entropies of solution $\Delta S_{\alpha 2}$, ΔS_γ were calculated using the data listed in Table 1 and are tabulated in Table 2. From these data, 95% confidence limits on the mean values of the thermodynamic parameters were calculated, using *t* statistics. The data in Table 2 show that neither $\Delta H_{\alpha 2}$ nor ΔH_γ were dependent on the hydrogen concentration. The hydrogen content at the phase boundary of the γ-hydride in Ti [8,31], which was $C_{H\gamma}$ = 60 at.% or $N_{H(\gamma)}/N_{Ti}$ = 1.45, was used to calculate ΔS_γ.

Fig. 2 shows a plot of all decomposition pressure data for the determination of the terminal solubilities. The line AB on the figure represent the average data of all hydrogen concentrations in the two-phase region. The intersection of the decomposition pressure curve for the α_2 phase with the line AB gave the temperature at which the given composition represented the terminal solubility. These values are listed in Table 3.

Fig. 3 shows a plot of the square root of the decomposition pressure as a function of the hydrogen concentrations. In the α_2-phase region, a set of straight lines passing through the zero point were obtained, and the constant-pressure plateaus corresponded to the region where the two phases, hydrogen-saturated α_2 phase and hydride, co-existed. The intersection of each straight line with its constant-pressure plateau gave the terminal solubility, which is the concentration at which the hydride precipitates. The results are included in Table 3. A plot of $\sqrt{P_{H2}}$ vs C_A / 2-C_A (following Eq. 3) was similar to that of $\sqrt{P_{H2}}$ vs C_H (at%), shown in Fig. 3, although some of the straight lines did not exactly pass through the zero point, suggesting that Eq. 1 may be a more suitable description for these data. The terminal solubilities determined from Eq. 3 are listed in Table 3.

The variation of the terminal solubility (C_H) with temperature, i.e. the hydride solvus, is shown in Fig. 4, using the Eq. 1 results. It indicates that the terminal solubility of hydrogen in the α_2 in equilibrium with the hydride increases with increasing temperature. The equation of the terminal solubility as function of temperature, at 1 atm pressure, is

(5a) $$C_H \text{ (at. \%)} = 6.8 \times 10^3 \, e^{-5750/T} \text{ and}$$

(5b) $$\frac{C_A}{2 - C_A} = 57\, e^{-6200/T},$$

where C_A is the atomic ratio and T is in K. Insertion of room temperature into Eq. 5 predicts a solubility of hydrogen of about 0.2 ppm (atomic); a spline fit to Fig. 4 and extrapolation to room temperature gives a value of about 0.05 ppm. Though these are only estimates, they do indicate that equilibrium room temperature solubility is probably very small, and virtually all charged hydrogen is precipitated as hydride on cooling to ambient.

Overall Solubility

The slopes of $C_H = W\sqrt{P_{H2}}$ (or $C_A / 2 - C_A = W\sqrt{P_{H2}}$) straight lines of Fig. 3 under constant temperature were calculated and are presented in Table 4. From these data, we obtain the equation of overall solubility or total uptake of hydrogen in the α_2 phase., i.e.

(6) $$C_H \text{ (at. \%)} = 2.67\sqrt{P_{H2}}\, e^{2650/T} \text{ and}$$

where T is in K, and the unit of P is Pa.

Figure 5 shows a plot of the overall solubility of hydrogen in the α_2 phase as a function of temperature above 400°C. This figure indicates that the overall solubility of hydrogen in the α_2 phase decreases with increasing temperature when $T \geq 500$°C. In this sense, the α_2 phase is an exothermic occluder [20]. This conclusion has been verified by the thermal charging under high temperature. For the higher pressure, shown in Fig. 5, the hydrogen pressure was adjusted with time to keep hydrogen pressure at 1 atm.

Identification of the Hydride

Although description of the hydride phase itself was not a primary goal of this study, a few observations may be of interest in view of apparent disagreements in the literature [15,16,19] about hydrides in the α_2 phase. The hydrides appeared as fine markings or lines on the polished surface of the sample without etching after cathodic charging in H_2SO_4 + 0.5 g/l $NaAsO_2$ solution, as shown in Fig. 6. In the situation of thermal charging in hydrogen gas, the hydrides precipated into well-develop platelets, visible as "upsets" on the polished surface without etching, as shown in Fig. 7. It is interesting to note that the distribution of the hydrides is uniform throughout the surface of the sample, but locally the hydride platelets were arranged along certain preferential orientations, as shown in Fig. 7.

X-ray diffraction patterns were obtained on a diffractometer using Cu Kα radiation. The diffraction data are listed in Table 5. For "TiH_2" hydride in the Ti-H system, the three strong diffraction lines were, respectively [8,31], (111) $2\theta = 35.9°$, $I/I_0 = 50$, (200) $2\theta = 41°$, $I/I_0 = 100$, and (311) $2\theta = 70.8°$, $I/I_0 = 35$, which was in good agreement with our observations in Table 5 for the present α_2 -H system. Other lines also matched the literature data. Therefore, the hydride we have observed in the α_2 phase of Ti-24-11 has the fluorite structure of γ TiH.

DISCUSSION

Thermodynamic properties

It was shown in Fig. 2 that all data of the two-phase region formed a straight line, thus, the partial molar heat and entropy of formation for the hydride phase could be calculated from Eq. 1 and 3. As the calculations were more consistent with Eq. 1, those results are emphasized here; results from Eq. 3 have been collected in Table 2. The mean values showed ΔH_γ = -16,800 cal/mol [H] or -33,600 cal/mol H_2, with ΔS_γ = -11.9 cal/K/mol [H]. The partial molar enthalpy for the hydride is in good agreement with the corresponding value in the Ti-H system [8,29], which was from -29,900 cal/mol H_2 to -34,000 cal/mol H_2.

The mean partial molar heat and entropy of solution in the α_2 phase were $\Delta H_{\alpha 2} = 5250 \pm 350$ cal/mol [H] , and $\Delta S_{\alpha 2} = -2.45 \pm 0.43$ cal/K/mol [H], with 95% confidence intervals. These data are believed to represent adequately the α_2 phase, although a minor amount of β phase was present. The straight-line appearance of Figs. 1 to 3, and the general similarities to behavior both of α titanium [8,28] and of binary Ti_3Al [13], indicate that the behavior we observed was essentially that of the α_2 phase. The very small and discontinuous content of β does not seem to have had a major effect on the results. That conclusion is also consistent with the relatively small differences in thermodynamic parameters for the α_2 and β phases [8,13].

The standard partial molar free energies of solution for the α_2 phase and the hydride phase, therefore, are, from Eq. 1 with 95% confidence intervals:.

(7a) $\Delta G^\circ_{\alpha 2} = \Delta H^\circ_{\alpha 2} - T\Delta S^\circ_{\alpha 2} = -(5250 \pm 350) + (2.45 \pm 0.43)T$ cal/mol [H];

(7b) $\Delta G^\circ_\gamma = \Delta H^\circ_\gamma - T\Delta S^\circ_\gamma = -(16{,}800 \pm 560) + (11.9 \pm 0.8)\,T$ cal/mol [H].

Substituting the equation of the terminal solubility, Eq. 5, and the partial molar free energy of solution for the α_2 phase, i.e., Eq. 7, into Eq. 1, the standard partial molar free energy of hydrogen in the α_2 phase in equilibrium with the hydride phase can be obtained, i.e.

(8a) $\Delta G^{\circ}_{\alpha 2} = -(17{,}700 \pm 480) + (21 \pm 0.5)\ T$ cal/mol [H],

and for hydrogen in the hydride phase, using Eq. 3 and the values of $N_{H(\gamma)}/N_{Ti} = 1.45$ and $N_S / N_{Ti} = 2$, we obtain

(8b) $\Delta G^{\circ}_{\gamma} = -16{,}800 + 20.2\ T$ cal/mol [H].

As would be expected, the ΔG° value for hydrogen in the α_2 phase in equilibrium with the hydride phase, Eq. 8a, is in very good agreement with the value for the hydride phase, Eq. 8b. The result in Eq. 8a is derived from Eq. 1 and has better statistical support, and thus is preferred.

Overall Solubility and Terminal Solubility

Comparing the values of Eq. 7 for α_2 and γ phases shows that the difference in partial molar heats of formation of the α_2 and γ is 11,550 cal/mol [H], i.e. greater than zero, therefore, based on Eq. 5, the terminal solubility of hydrogen in the α_2 phase in equilibrium with hydride should increase with increasing temperature. However, Eq. 7a indicates $\Delta H_{\alpha 2} = -5250$ cal/mol [H], or less than zero, so according to Eq. 1 or Eq. 3, the overall solubility of hydrogen in the α_2 phase should decrease with increasing temperature. Therefore, it can be explained why the terminal solubility can show an endothermic behavior while the overall solubility is exothermic in nature.

Since Eq. 7 contains the thermodynamic parameters for hydrogen in the α_2 phase in equilibrium with the hydride phase, we can get the terminal solubility equation for 1 atm pressure from Eq. 1, for which the result is

(9) $$C_H \text{ (at. \%)} = 60\, e^{9.5 \pm 0.5/R}\, e^{-11500 \pm 300/RT}$$
$$= (5.4 - 8.9) \times 10^3\, e^{-5750 \pm 150/T}\ .$$

Comparing this equation to the experimental results in Eq. 5, it is obvious that the terminal solubility equation calculated from Sieverts' Law is in very good agreement with the experimental results. Almost equally good agreement with Eq. 5 is obtained with the statistical treatment, Eq. 3.

Substituting the parameters of Eq. 8a into Eq. 1, we obtain the equation of overall solubility of hydrogen in the α_2 phase, with P in Pa, i.e.

(10) $$C_H \text{ (at. \%)} = (3.35 \pm 0.81)\ \sqrt{P_{H_2}}\ e^{2650 \pm 150/T}$$

The results are in agreement with Eq. 6. A similar calculation for Eq. 3 should be used in the situation of large hydrogen concentration, since that equation is more appropriate for the condition of high hydrogen pressure.

However, if we extend Eq. 10 (from either Eq. 1 or Eq. 3) to 1 atm pressure, the calculated hydrogen concentration is higher than that measured under thermal charging in hydrogen gas of 1 atm. Since the reaction chamber used in the present work is large (57 mm diameter x 460 mm length), the cooling rate of the samples after charging and removing from the furnace is not very high. This may be one of the reasons why the observed hydrogen concentrations after thermal charging at 1 atm pressure are lower than those inferred from thermodynamic parameters measured at sub-atmospheric pressure.

Hydrides

We have determined that the hydride phase observed had the fluorite structure of γ TiH, although we have not determined to what extent the present hydrides incorporate Nb or Al [13-16,32-34]. For binary Ti_3Al, i.e. no Nb, there is evidence [13] that at the temperatures of Fig. 4, the hydride is the binary Ti-H compound. We also have not determined the value of the atom ratio of Ti to H, though presumably [6-8,13,22,29] it is a function of hydrogen content; variations in stoichiometry are accommodated in the γ structure by hydrogen vacancies [35,36]. The degree of tetragonality of γ also varies with hydrogen content [8,13,35,37]. The literature on Ti and Ti alloy hydrides consistently refers to the tetragonal structure as fct, to avoid confusion as the fcc symmetry of the γ becames tetragonal, but of course the fct structure is equivalent to bct and has occasionally been reported as bct [19,31]. The possible roles of Al and Nb in these effects, by analogy [9,38] with α–Ti, are not known. More work is clearly needed on the hydride phase.

CONCLUSIONS

1. For the α_2-H system, the terminal solubility of hydrogen in the α_2 phase in equilibrium with the hydride phase increases with increasing temperature, while the overall solubility decreases with increasing temperature in the high temperature region.

2. The experimental equations of the terminal and overall solubility in the α_2-H system are, respectively,

$$C_H \text{ (at. \%)} = 6.8 \times 10^3 \, e^{-5750/T} \quad \text{and}$$
$$C_H \text{ (at. \%)} = 2.67 \sqrt{P_{H_2}} \, e^{2650/T} \, ,$$

where T is in K, and the unit of P is Pa.

3. The standard partial molar heats and free energies of solution for the α_2, and the hydride phase are respectively as follows, with 95% confidence limits:

$$\Delta H^{\circ}_{\alpha 2} = -(5250 \pm 350) \text{ cal/mol [H]}, \quad \Delta H^{\circ}_{\gamma} = -(16{,}800 \pm 560) \text{ cal/mol [H]; and}$$
$$\Delta G^{\circ}_{\alpha 2} = -(5250 \pm 350) + (2.45 \pm 0.43)T \text{ cal/mol [H]};$$
$$\Delta G^{\circ}_{\gamma} = -(16{,}800 \pm 560) + (11.9 \pm 0.8)\,T \text{ cal/mol [H]}.$$

The ΔG° values for hydrogen in the α_2 phase in equilibrium with the hydride phase are

$$\Delta G^{\circ}_{\alpha 2} = \Delta G^{\circ}_{\gamma} = -(17{,}700 \pm 480) + (21 \pm 0.5)T \text{ cal/mol [H]}.$$

4. The hydride phase at room temperature represents nearly all the hydrogen content of the material, and precipitates with the γ fluorite structure of titanium hydride.

ACKNOWLEDGEMENTS

We appreciate helpful discussions with I.M. Bernstein and R.J. Fruehan, and are grateful for the sponsorship of the Defense Advanced Research Projects Agency through DARPA Order 6155, monitored by the Air Force Office of Scientific Research under Contract F49620-88-C-0013. This is a joint contract of the University of Pittsburgh and Carnegie Mellon University.

REFERENCES

1. H. A. Lipsitt, in *High-Temperature Ordered Intermetallic Alloys* (MRS Symp. 39), ed. C.C. Koch, *et al.*, Materials Research Society, Pittsburgh, 1985, pp. 351-364.
2. R. L. Fleischer, D.M. Dimiduk and H.A. Lipsitt, *Ann. Rev. Mater. Sci.*, 1989, vol. 19, pp. 231-263.
3. H.G. Nelson, *SAMPE Quarterly*, 1988, vol. 20, no. 1, pp. 20-23.
4. T. M. Ronald, in *Summary Proceedings of the 2nd Workshop on Hydrogen-Materials Interaction*, NASP Joint Program Office Workshop Pub. 1004, H.G. Nelson, ed., NASA-Ames, Moffett Field, CA, Nov. 1988, pp. 3-17.
5. L. Kirschfeld and A. Sieverts, *Zeits. f. Phys. Chem.*, 1929, vol. 145A, pp. 227-240.

6. A.D. McQuillan, *Proc. Roy. Soc. (London), Ser. A*, 1950, vol. 204, pp. 309-322.

7. G.A. Lenning, C.M. Craighead and R.I. Jaffee, *Trans. AIME*, 1954, vol. 200, pp. 367-376.

8. W.M. Mueller, in *Metal Hydrides*, W.M. Mueller, J.P. Blackledge and G.G. Libowitz, eds., Academic Press, NY, 1968, pp. 337-383.

9. N.E. Paton and J.C. Williams, in *Hydrogen in Metals*, I.M. Bernstein and A.W. Thompson, eds., Amer. Soc. Metals, Metals Park, OH, 1974, pp. 409-431.

10. J.C. Williams, in *Effect of Hydrogen on Behavior of Materials*, A.W. Thompson and I.M. Bernstein, eds., AIME, NY, 1976, p. 367-375.

11. H. Numakura and M. Koiwa, *Acta Metall.*, 1984, vol. 32, pp. 1799-1807.

12. O.T. Woo, G.C. Weatherly, C.E. Coleman and R.W. Gilbert, *Acta Metall.*, 1985, vol. 33, pp. 1897-1906.

13. P.S. Rudman, J.J. Reilly and R.H. Wiswall, *J. Less-Common Metals*, 1978, vol. 58, pp. 231-240.

14. A.W. Thompson, W.-Y. Chu and J.C. Williams, in *Summary Proceedings of the 2nd Workshop on Hydrogen-Materials Interaction*, NASP Joint Program Office Workshop Pub. 1004, H.G. Nelson, ed., NASA-Ames, Moffett Field, CA, Nov. 1988, pp. 133-135.

15. D.S. Shih, G.K. Scarr and G.E. Wasielewski, *Scripta Metall.*, 1989, vol. 23, pp. 973-978.

16. E. Manor and D. Eliezer, *Scripta Metall.*, 1989, vol. 23, pp. 1313-1318.

17. D. Eliezer, E. Manor and F.H. Froes, in *Hydrogen Effects on Material Behavior*, N.R. Moody and A.W. Thompson, eds., TMS-AIME, Warrendale, PA, 1990, pp. 523-532.

18. W.-Y. Chu, A.W. Thompson, and J.C. Williams, in *Hydrogen Effects on Material Behavior*, N.R. Moody and A.W. Thompson, eds., TMS-AIME, Warrendale, PA, 1990, pp. 543-553.

19. M. Gao, J.B. Boodey and R.P. Wei, *Scripta Metall. Mater.*, 1990, vol. 24, pp. 2135-2138.

20. R. Speiser, in *Metal Hydrides*, W.M. Mueller, J.P. Blackledge and G.G. Libowitz, eds., Academic Press, NY, 1968, pp. 69-89.

21. C.M. Schwartz and M.W. Mallett, *Trans. ASM*, 1954, vol. 46, pp. 640-651.

22. E.A. Guibransen and K.F. Andrew, *Trans. AIME*, 1955, vol. 203, pp. 136-144.

23. M.J. Blackburn, D.L. Ruckle and C.E. Bevan, Technical Report No. AFML-TR-78-18, Wright-Patterson AFB, OH, 1978.

24. M.J. Blackburn and M.P. Smith, Technical Report No. AFML-TR-81-4046, Wright-Patterson AFB, OH, 1981.

25. A. Sieverts, *Zeits. f. Metallkunde*, 1929, vol. 21, pp. 37-44.

26. C.J. Smithells, *Gases and Metals*, Chapman and Hall, London, 1937, pp. 140-159.

27. C.H.P. Lupis, *Chemical Thermodynamics of Materials*, North-Holland, New York, 1983.

28. A.L.G. Rees, *Trans. Faraday Soc.*, 1954, vol. 50, pp. 335-342.

29. R.M. Haag and F.J. Shipko, *J. Amer. Chem. Soc.*, 1956, vol. 78, pp. 5155-5159.

30. J.P. Blackiedge, in *Metal Hydrides*, W.M. Mueller, J.P. Blackledge and G.G. Libowitz, eds., Academic Press, NY, 1968, pp. 151-156.

31. L.D. Jaffe, *Trans. AIME*, 1956, vol. 206, p. 861.

32. A.W. Thompson, "Environmental Effects in Titanium Aluminide Alloys", in *Environmental Effects in Advanced Materials*, R.E. Ricker and R.H. Jones, eds., TMS-AIME, Warrendale, PA, in press.

33. W.-Y. Chu, A.W. Thompson, and J.C. Williams, "Brittle Fracture Behavior and Influence of Hydride in Titanium Aluminide," *Metall. Trans. A.*, submitted.

34. W.-Y. Chu and A.W. Thompson, "Effect of Hydrogen as a Temporary β Stabilizer on Microstructure and Brittle Fracture Behavior in a Titanium Aluminide Alloy," *Metall. Trans. A*, in press.

35. G.G. Libowitz, *Adv. Chem. Ser.*, 1963, vol. 39, pp. 74-87.

36. P.E. Irving and C.J. Beevers, *Metall. Trans.*, 1971, vol. 2, pp. 613-615.

37. G.G. Libowitz, *J. Nucl. Mater.*, 1960, vol. 2, pp. 1-22.

38. N.E. Paton, B.S. Hickman and D.H. Leslie, *Metall. Trans.*, 1971, vol. 2, pp. 2791-2796.

TABLE 1: Decomposition Pressure of α_2 - H System

Composition		Pressure at Temperature °C, Pa									
wppm	at.%	350	400	450	500	550	600	650	675	700	725
230	1.1	0.13	0.93	2.0	2.9	4.1	5.5	8.3		12	
490	2.3	0.11	1.2	5.6	9.3	13	19	27		33	
680	3.2	0.13	1.1	6.0	16	24	33	47		61	
750	3.5	0.13	0.93	6.0	20	32	43	63		80	
930	4.3	0.20	0.93	6.4	28	43	64	83		109	
1290	5.8	0.13	1.2	5.3	24	100	136	180	253	293	
2620	11.2	0.11	1.3	6.7	27	93	293	640	800	947	1040
3720	15.1	0.13	1.1	7.3	25	113	266	613	1290	1470	1670

TABLE 2: ΔH and ΔS of Hydrogen in the α_2 Phase and Hydride Phase

Hydrogen Concentration		In α_2 Phase			In Hydride Phase		
		ΔH_{α_2}	ΔS_{α_2} Cal/C/Mol[H]		ΔH_{γ}	ΔS_{γ} cal/C/mol[H]	
at.%	$\frac{100C_A}{2-C_A}$	Cal/mol[H]	Eq. 1	Eq. 3	Cal/mol[H]	Eq. 1	Eq. 3
1.1	0.55	-5070	-2.54	-13.14	-16400	-11.1	-17.4
2.3	1.16	-5010	-2.12	-12.70	-17900	-13.5	-19.8
3.2	1.65	-5050	-2.08	-12.62	-17200	-12.5	-18.7
3.5	1.83	-5190	-2.33	-12.84	-17100	-12.4	-18.6
4.3	2.25	-5110	-2.15	-12.66	-15600	-10.2	-16.4
5.8	3.20	-5770	-3.16	-13.56	-16700	-11.8	-18.0
11.2	6.67	-6030	-3.30	-13.55	-16900	-12.0	-18.2
15.1	9.77	-4800	-1.90	-11.97	-16600	-11.6	-17.9

TABLE 3: Terminal Solubility of Hydrogen in α_2

Method		InP vs 1/T								$\sqrt{P}$ vs C			
Temperature, ° C		403	447	478	489	506	560	638	671	500	550	600	650
Terminal	at.%	1.1	2.3	3.2	3.5	4.3	5.8	11.2	15.1	4.3	5.8	8.6	(12.6)*
Solubilities	$\frac{100C_A}{2-C_A}$	0.55	1.15	1.65	1.83	2.25	3.2	6.67	9.77	2.25	2.9	4.74	(8.3)*

*Not exact value

TABLE 4: $C/\sqrt{P}$ Under Different Temperature

T, ° C	500	550	600	650
$C/\sqrt{P}$	9.37	6.98	5.90	5.11
$100\frac{C_A}{2 - C_A}/\sqrt{P}$	5.48	3.85	3.28	3.13

TABLE 5: X-ray Diffraction Data

Uncharged deg 2θ	35.5	36.5	38.6	40.6	41.3		78	80.3	116.3	144.5
I/I_o	15	15	15	35	20		100	20	20	30
Charged deg 2θ	35.9		39	40.9		71.4	77.7			
(C_H=13.3 at%) I/I_o	75		20	100		48	20			

FIGURE CAPTIONS

Fig. 1. An example of decomposition pressure in α_2-H system vs 1/T, 2.3 at % hydrogen, measured both on heating and on cooling.

Fig. 2. Summary plot of log P_{H_2} vs 1/T. AB line is for α_2 and hydride phases, and the other lines represent atomic percent hydrogen concentration in the α_2 phase. Different symbols represent different hydrogen concentrations.

Fig. 3. Square root of the decomposition pressure in the α_2-H system vs hydrogen concentration (atomic percent) at different temperatures.

Fig. 4. Terminal solubility of hydrogen in the α_2 phase in equilibrium with the hydride phase, i.e. solvus for hydride in α_2, for Ti-24-11.

Fig. 5. Overall solubility (total uptake) of hydrogen in the α_2 phase vs 1/T, for two pressures shown on the curves in units of atm (or 130 Pa and 0.1 MPa).

Fig. 6. Hydride marking on the polished surface of the sample after cathodic charging in 1N H_2SO_4 + 0.5 g/l $NaAsO_2$ solution with an applied current density of 0.2 A/cm^2.

Fig. 7. Hydride platelets precipitated during thermal charging in hydrogen gas; unetched surface viewed with polarized light. (a) C_H = 5.8 at %. (b) C_H = 11.2 at %.

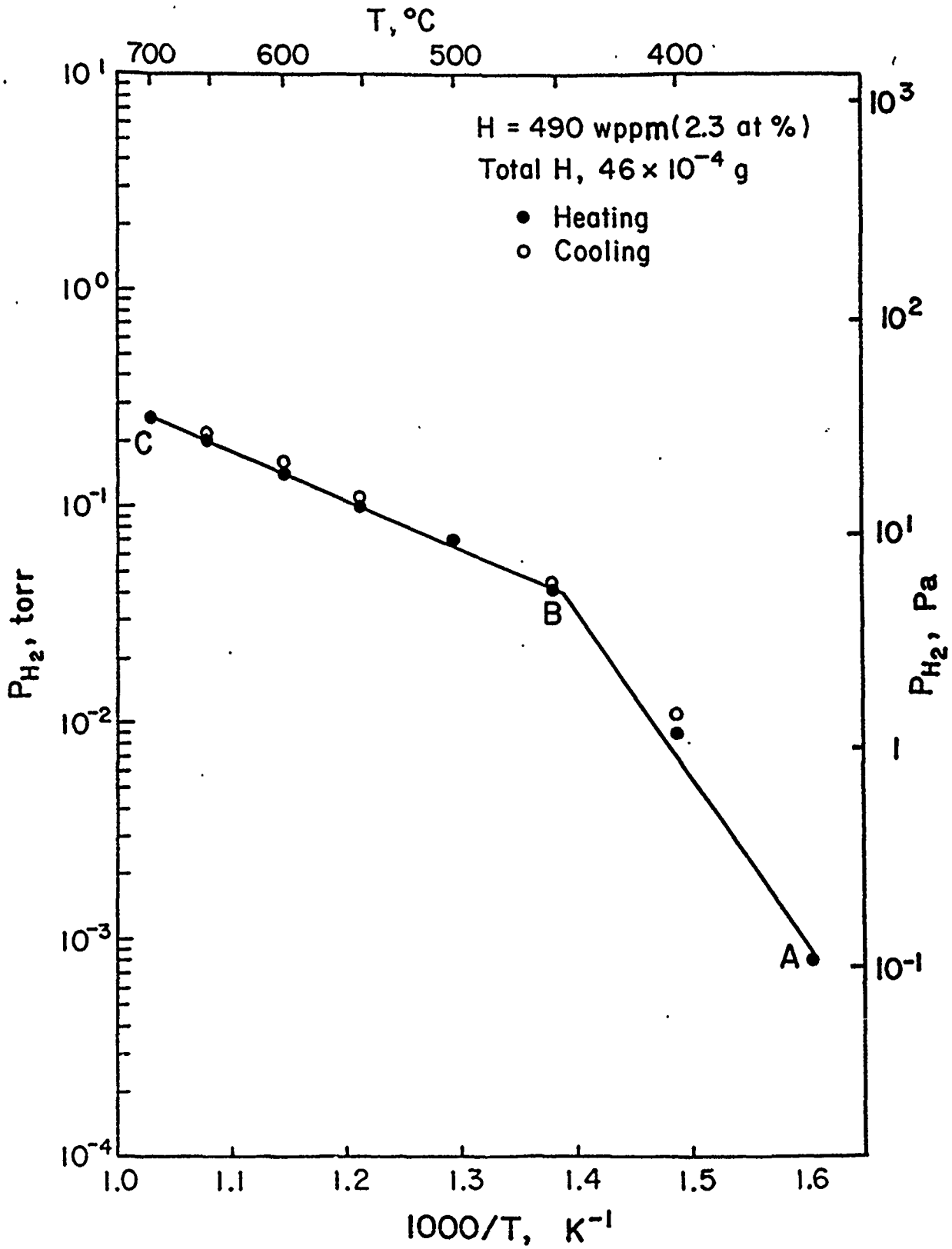

Fig. 1. An example of decomposition pressure in α_2-H system vs 1/T, 2.3 at % hydrogen, measured both on heating and on cooling.

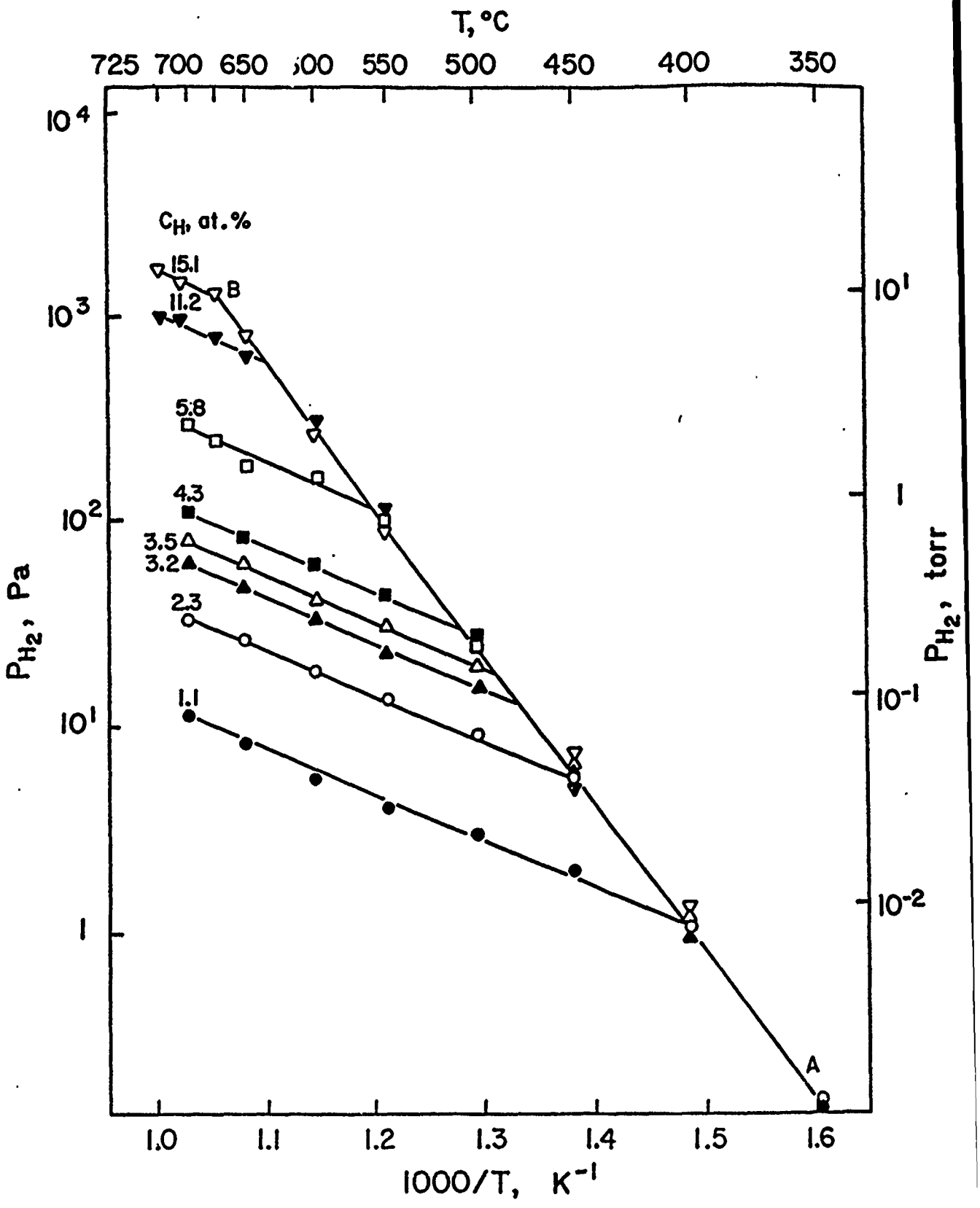

Fig. 2. Summary plot of log P_{H2} vs 1/T. AB line is for α_2 and hydride phases, and the other lines represent atomic percent hydrogen concentration in the α_2 phase. Different symbols represent different hydrogen concentrations.

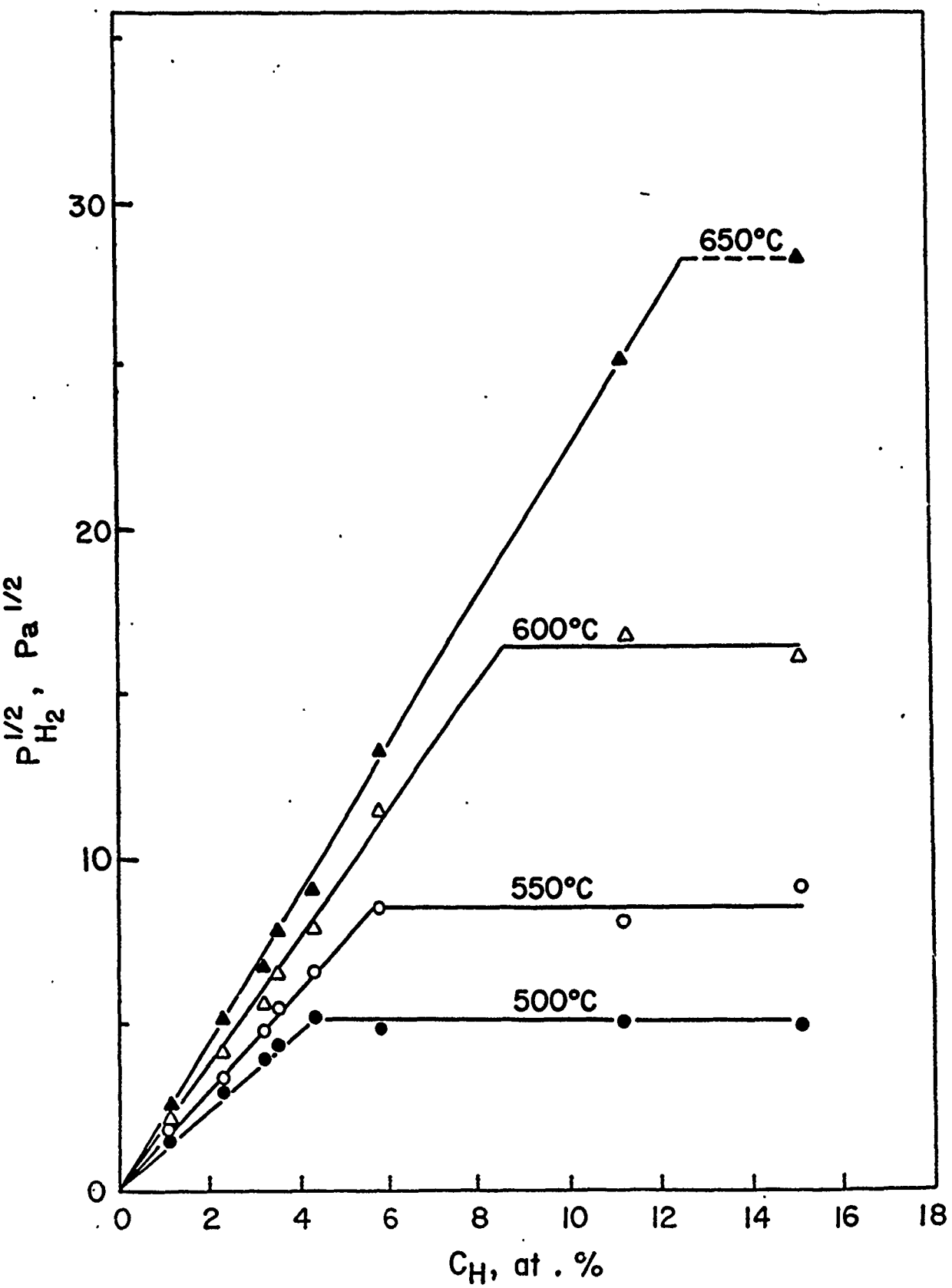

Fig. 3. Square root of the decomposition pressure in α_2-H system vs hydrogen concentration (atomic percent) at different temperatures.

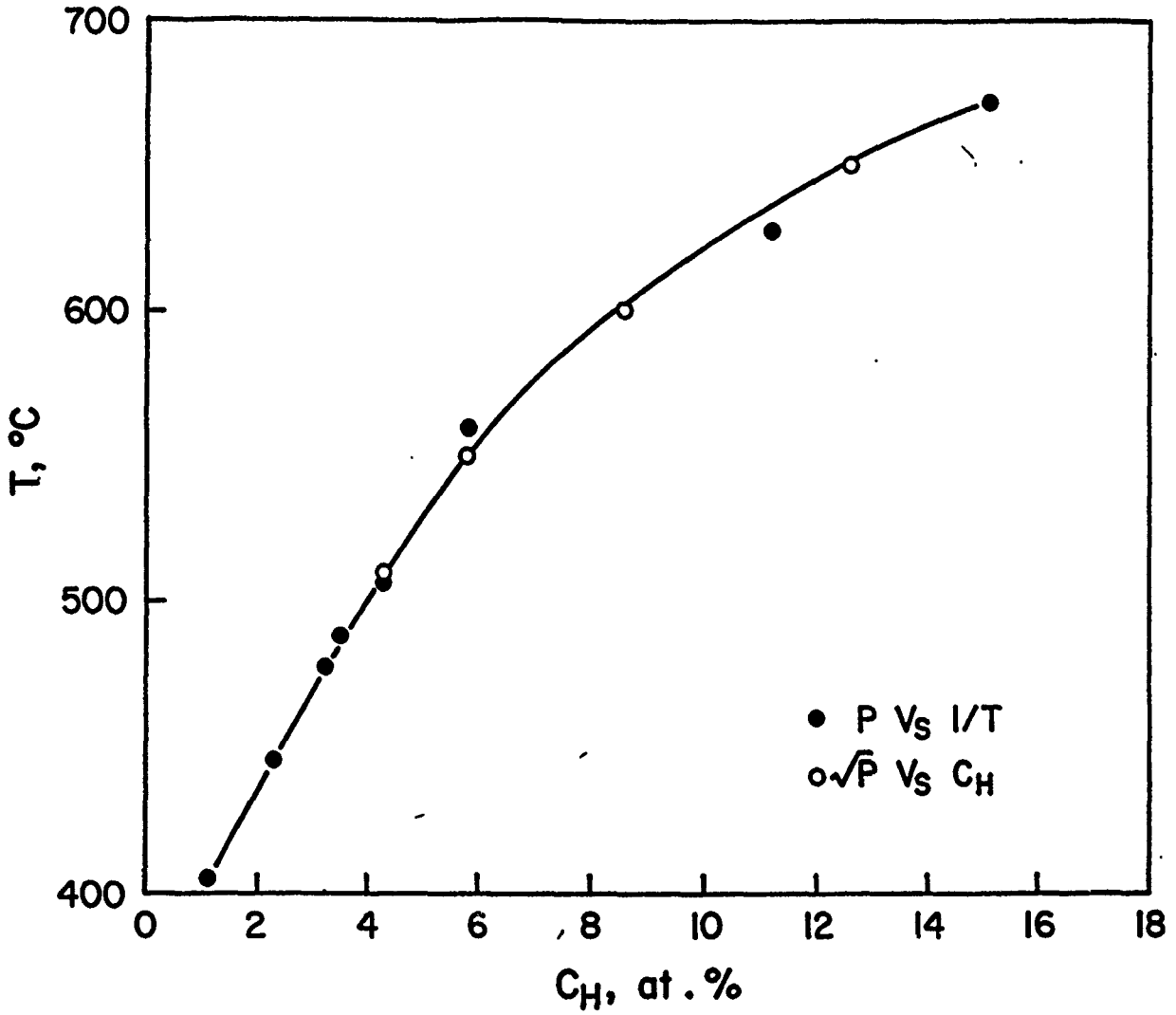

Fig. 4. Terminal solubility of hydrogen in the α_2 phase in equilibrium with the hydride phase, i.e. solvus for hydride in α_2, for Ti-24-11.

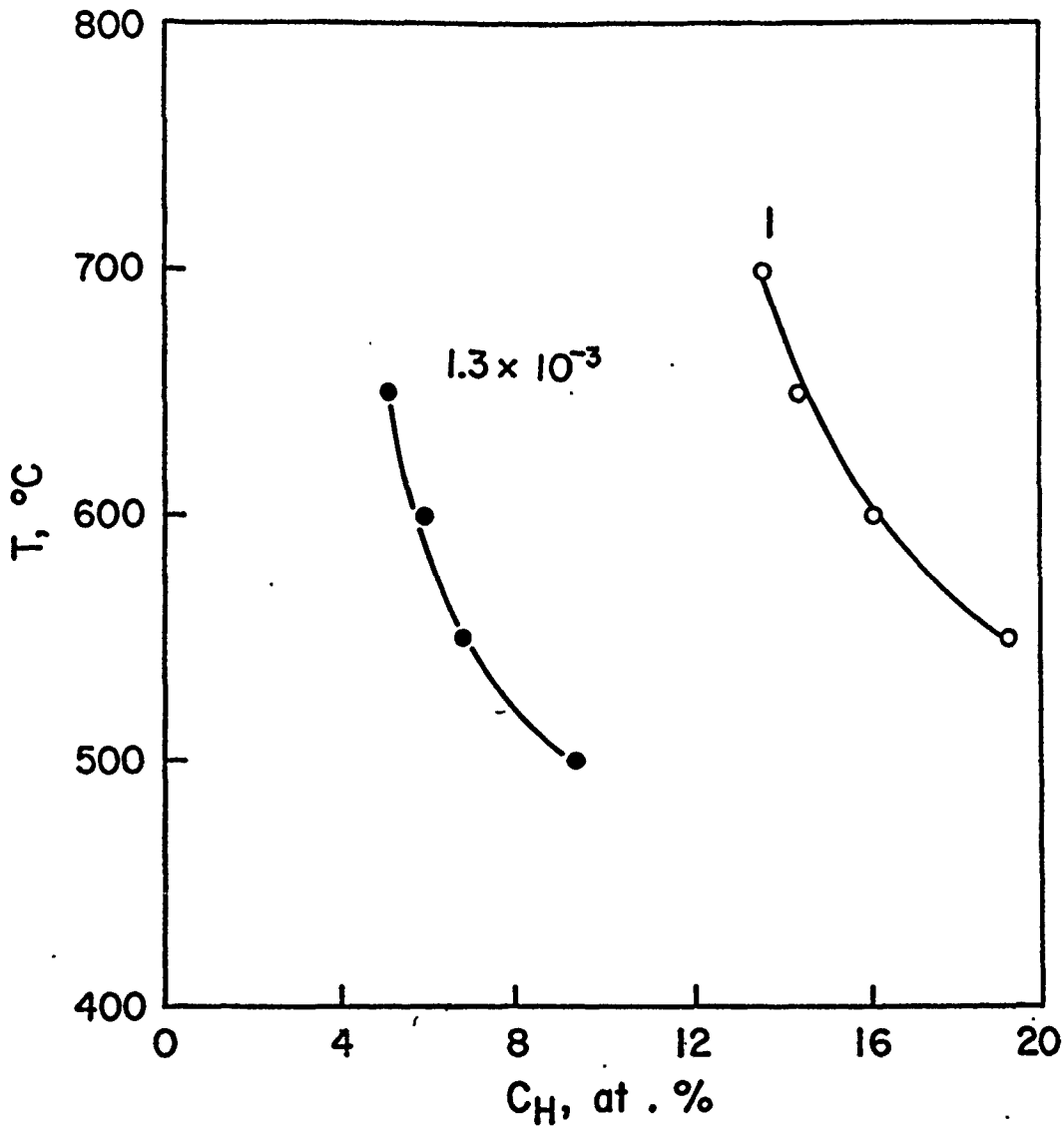

Fig. 5. Overall solubility (total uptake) of hydrogen in the α_2 phase vs 1/T, for two pressures shown on the curves in units of atm (or 130 Pa and 0.1 MPa).

Fig. 6. Hydride marking on the polished surface of the sample after cathodic charging in IN H_2SO_4 + 0.5 g/l $NaAsO_2$ solution with an applied current density of 0.2 A/cm^2.

Fig. 7. Hydride platelets precipitated during thermal charging in hydrogen gas; unetched surface viewed with polarized light. (a) C_H = 5.8 at %. (b) C_H = 11.2 at %.